ENGINEERING GAS DIFFUSION ELECTRODES FOR ELECTROCHEMICAL CARBON DIOXIDE UPGRADING

by

McLain E. Leonard

Master of Science in Chemical Engineering Practice, Massachusetts Institute of Technology, 2017
Bachelor of Science in Chemical Engineering, Montana State University, 2015

Submitted to the Department of Chemical Engineering
in partial fulfillment of the requirements for the degree of

Doctor of Philosophy in Chemical Engineering

at the

MASSACHUSETTS INSTITUTE OF TECHNOLOGY

February 2021

© Massachusetts Institute of Technology 2021. All rights reserved.

Author ....
Department of Chemical Engineering
January 14th, 2021

Certified by ....
Fikile R. Brushett
Cecil and Ida Green Career Development Chair
Thesis Supervisor

Accepted by ....
Patrick S. Doyle
Robert T. Haslam Professor of Chemical Engineering
Singapore Research Professor
Chairman, Committee for Graduate Students

Engineering Gas Diffusion Electrodes for Electrochemical Carbon Dioxide Upgrading

by

McLain E. Leonard

Submitted to the Department of Chemical Engineering on 14 January 2021, in partial fulfillment
of the requirements for the degree of
Doctor of Philosophy in Chemical Engineering

Abstract:

Electrochemical carbon dioxide reduction (CO2R) is increasingly recognized as a viable technology for the generation of chemicals using carbon dioxide (CO_2) recovered from industrial exhaust streams or directly captured from air. If powered with low-carbon electricity, CO2R processes have the potential to reduce emissions from chemicals production. Historically, three-electrode analytical cells have been used to study catalyst activity, selectivity, and stability with a goal of incorporating proven materials into larger devices. However, it has been recognized that the limited CO_2 flux through bulk volumes of liquid electrolyte limit the effective reaction rate of CO_2 when using promising catalyst systems. Gas-fed electrolyzers adapted from commercial water electrolyzer and fuel cell technologies have motivated researchers to explore combinations of porous electrodes, catalyst layers, and electrolytes to achieve higher areal productivity and favorable product selectivities. Present art demonstrates that high current density production (> 200 mA cm^{-2}) of valuable chemicals at moderate cell voltages (ca. 3–4 V) is achievable at ambient conditions using electrolysis devices with catalyst-coated gas diffusion electrodes (GDEs). However, beyond short durations (1–10 h) stable performance outcomes for flowing electrolyte systems remain elusive as electrolyte often floods electrode pores, blocking diffusion pathways for CO_2, diminishing CO2R selectivity, and constraining productivity. Systematic study of the driving forces that induce electrode flooding is needed to infer reasonable operational envelopes for gas-fed electrolyzers as full-scale industrial devices are developed.

In this thesis, I investigate GDE wettability as a prominent determinant of gas-fed flowing electrolyte CO_2 electrolyzer durability. To do this, I combine experimental and computational approaches. First, I use a flow cell platform to study transient evolution of activity, selectivity, and saturation to identify failure modes, including liquid pressurization, salt precipitation, electrowetting, and liquid product enrichment. Next, I use material wettability properties and reactor mass balances to estimate how enriched liquid product streams might defy non-wetting characteristics of current GDE material sets. Finally, I construct computational electrode models and vary surface chemistry descriptors to predict transport properties in partially saturated electrodes. Specifically, I consider how saturation evolves in response to relevant scenarios (i.e., electrowetting and liquid products) that challenge CO_2 electrolyzer durability.

Thesis Supervisor: Fikile R. Brushett
Title: Cecil and Ida Green Career Development Chair, Associate Professor of Chemical Engineering

Acknowledgments:

Thanking all the people in my life who helped me on this journey from Idaho to MIT is a challenging task, but I will try to do so here. I firmly believe that their continual emotional support has been the most important reason why I have been able to finish this doctoral thesis work.

I want to thank my research advisor, Fik, for encouraging me to dive into a challenging and exciting topic area. He provided me the needed space to grapple with my projects, independently, while still frequently making time to help me work through obstacles or even to just have long unstructured conversations about science. I now feel more comfortable with uncertainty and, in fact, I embrace this feeling, knowing that this means I might be onto something good.

I would also like to thank my thesis committee members, Yuriy and Klavs, for encouraging me to remember the richness of the concepts covered within the Chemical Engineering profession and to use that body of knowledge to propel my work. I now have an even greater appreciation for how fertile the interfaces between fields can be. Because of their support and advice, I look forward to using the wisdom of past scholars and thinkers to inform my present and future efforts.

I owe many thanks to the members of the Brushett Research Group and to all those who, directly and indirectly, supported my work at MIT over the past five years. I am privileged to have been a member of such a collaborative, fun, and innovative group of people. My hope is that the cooperative spirit fostered over the years might continue for generations to come.

I want to thank my friends both here in Cambridge, back home in the Rocky Mountains and the Pacific Northwest, and all other places in which I have been fortunate to live. My friends are amazing for using their time and energy to check in with me to make sure I am making time for my hobbies. During this long, arduous intellectual journey a frequent question I would receive from so many of them would be, “Are you doing anything for fun?” Even though our work gives us dignity and purpose, we should try to find time to make connections with others and to be present and enjoy this gift of life in all the small and large ways we can. My friends are the ones that keep me sane in a world that sometimes feels too big to comprehend.

I am fortunate to be part of a large family with roots spread both wide and deep. Even though this journey has taken me physically farther away from most of them, I still felt their energy here with me for the past five and a half years in Cambridge. My family seldom lobbied me to pick a certain profession or to chase increasing numbers of academic degrees, but they did what they could to help me achieve this milestone once I decided to pursue it. I cannot thank them enough for the sacrifices they have made to make sure I was prepared to do the most important work—the work of leaving the world in better shape than I found it.

Finally, I want to thank my partner, Sahar, for coming into my life, serendipitously, near the beginning of this doctoral journey. Sahar exerts a positive gravity on all those who meet her and I am, certainly, a prime beneficiary of her warmth. I am grateful for her companionship through the happiest achievements and the darkest periods of intense self-doubt. I cannot overstate how important it has been for me to have a partner who not only supports me but also challenges me, intellectually and emotionally, to question my prejudices and to live deliberately. Our adventures together, both near and far from home, have helped me to realize that my time in graduate school was not just a stepping stone to an eventual life, but life, itself, playing out in real time.

Table of Contents:

List of Figures:

List of Tables:

I. Introduction

Energy is of central importance to society and the abundance, availability, and affordability of liquid fossil fuels has been a key driver of the past century's progress. However, with global energy demand projected to increase by 28% by 2040, the world urgently needs to dramatically reduce greenhouse gas emissions while developing and deploying clean, reliable energy solutions[1]. Electrochemical processes are poised to play a pivotal role in the evolving global power system as the efficient interconversion of electrical and chemical energy can enable the deployment of renewable energy technologies (e.g., solar PV, wind) that support the decarbonization of the electric grid, power the automotive fleet, and offer new opportunities for chemical manufacturing. While considerable focus has been given to advancing electrochemical technologies such as batteries, fuel cells, and water electrolyzers for transforming electric and transportation sectors, there has been less focus on the role of electrochemistry in carbon dioxide (CO_2) utilization for sustainable hydrocarbon fuel production.

1. Carbon Dioxide as a Feedstock for Chemicals Manufacturing

Presently, CO_2 is widely considered an inconvenient waste stream, or not even considered at all. This perception could be challenged if we were to consider the potential utility for CO_2 as an alternative feedstock to petroleum for the purpose of industrial hydrocarbon production. Whether the CO_2 for this new industrial process should be captured at the emission source or if it can be extracted from air depends on the efficiency and feasibility of the capture technology used for either scenario. Direct air capture and utilization of CO_2, if achievable, might help to alleviate the climate changing effects causes by anthropogenic greenhouse emissions. However, the extremely low atmospheric concentration of CO_2 in the air (ca. 409 ppm in 2018) poses a significant technical challenge, especially for carbon negative schemes that rely on removal of CO_2 from the air.[2]

What can be achieved through electrochemical CO_2 upgrading depends on the scale of the emissions themselves and how much power electrified mitigation schemes will consume. In a 2015 perspective, Pletcher discusses the scale of the power inputs that would be required to electrochemically convert global CO_2 emissions in a given year.[3] He estimated that to offset annual emissions with a 2-electron CO_2 electrolysis process operating in a 3-V cell with 100% current efficiency would require power at a rate of ~10^{17} Wh/year, easily exceeding the current global electricity generating capacity that is ~10^{16} Wh/year. What is clear from this analysis is that technology alone cannot fix the CO_2 emissions problem and that changes in human behavior are necessary to reduce or prevent emissions at their sources.

Even at the scale of a single manufacturing plant, deploying CO_2 upgrading processes to replace thermochemical processes will require massive installations of capital in terms of footprint and cost. Smith et al. recently estimated that to replace one 10,000 tons/day methanol production plant with a "air-to-barrel" process would require nearly 0.22 km^2 of direct air capture surface area and 243 km^2 of dedicated solar photovoltaic area.[4] From this assessment it would appear that coupling direct air capture schemes with CO2R upgrading technologies may not be the most viable approach for closing the global carbon balance. However, these technologies may provide flexibility for chemicals producers that have access to high concentration point sources of CO_2 emissions already present in industry. By closing the carbon recycling loop, electrochemical CO_2 upgrading might help to prevent atmospheric emissions and reduce reliance on newly extracted petroleum as the only economically viable source of hydrocarbons. Techno-economic analyses such as these can provide a lens through which to understand which electrocatalytic pathways might be best to prioritize when scaling up CO2R technologies. In the next section, I present a techno-economic approach that can be helpful for understanding the economic viability of different target products as a function of the price of electricity.

2. *Techno-economic Analysis of Electrochemical CO_2 Upgrading*

As the world's largest economy with one of the largest per capita CO_2 emissions contributions, the U.S. with its relatively affordable electricity is a reasonable market in which to deploy CO_2 upgrading technologies.[5] Potential success for such schemes in a U.S. market will be driven by the marginal profitability of each CO_2 reduction pathway, which is a function of commodity market prices for chemicals and electricity. We initially use an optimistic scenario for electrochemical CO_2 upgrading to define the profit metric shown in Equation (I.1).

$$\text{Profit} = P_{\text{market}} - P_{\text{e}} \left| E_{\text{cell}} \right| zF \tag{I.1}$$

Revenue is represented by a market price, P_{market}, in \$/metric ton for a CO2R product. Chemical prices are taken from a previous techno-economic analysis that focused on cell-level performance metrics.[6] The price of industrial electricity in the U.S., P_{e}, reported in \$/kWh,[7] is used, although overall electricity prices may decrease as increasingly affordable renewable power generation capacity is added to the grid.[8] E_{cell} is the full cell potential for CO2R paired with the oxygen evolution reaction (OER). The stoichiometric constant, z, is the number of moles of electrons transferred per mole of product formed, dictated by the limiting half reaction. F is the Faraday constant (96485 C/mol e^-). Electron transfer is assumed to be 100% efficient towards each product. For this generous scenario, Equation (I.1) omits the prices of other necessary reactants, including CO_2 and water. E_{cell} is taken as the sum of the equilibrium cell voltage, E_{eq}, and the cell overpotential, η_{cell}, as shown in Equation (I.2).

$$E_{\text{cell}} = E_{\text{eq}} + \eta_{\text{cell}} \tag{I.2}$$

In general, E_{eq} is a function of the standard cell potential, E^0, temperature, T, pressure, P, chemical species activities, a_i, and electrons transferred, z, and can be calculated according to the Nernst equation shown in Equation (I.3).[9] It should be noted that standard conditions (T and P) and unit activities are assumed in this analysis.

$$E_{\text{eq}} = E^0 + \frac{RT}{zF}\ln\left(\prod_i \frac{a_{\text{ox},i}}{a_{\text{red},i}}\right) \tag{I.3}$$

E^0 defined as the difference between the standard reduction potentials of the cathode and anode half reactions as shown in Equation (I.4). In an electrolytic cell (i.e., CO2R paired with OER), $E^0 < 0$, while for a galvanic process $E^0 > 0$.

$$E^0 = E^0_{\text{cathode}} - E^0_{\text{anode}} \tag{I.4}$$

For an electrolytic process, cell overpotential, η_{cell}, represents the extra voltage that must be applied across the full cell, in excess of the thermodynamic minimum voltage, to reach a given current. This term includes the compounded cell inefficiencies that can be further deconvoluted into contributions from charge-transfer kinetics, chemical species mass-transport, and ohmic resistance.[9]

A representative selection of CO2R products was chosen for the economic analysis summarized in **Figure I-1**. Formic acid (HCOOH), carbon monoxide (CO), methanol (CH_3OH), methane (CH_4), ethylene (C_2H_4), and ethanol (C_2H_5OH) are well studied and being pursued for commercial scale production. The cathode half-reaction for each of these CO2R is listed in **Table I-1**. OER (E^0 = 1.23 V),[10] shown in Equation (I.5), is often the most convenient oxidation reaction to complement CO2R.

$$4\ \mathrm{OH^-} \rightarrow \mathrm{O_2} + 2\ \mathrm{H_2O} + 4\ \mathrm{e^-} \tag{I.5}$$

Additionally, OER's high overpotential in near-neutral to alkaline electrolytes common to CO2R makes it conservative input for process economics.[11,12] Other reactions, such as the partial oxidation of glycerol, have been proposed to reduce cell voltage and electricity costs, but these alternative scenarios were not a focus of this thesis.[13]

Table I-1: *Electrochemical CO2R reactions used for techno-economic analysis*

Product	**Chemical Formula**	*z*	**Half-reaction (alkaline)**
Formic acid/formate	$HCOOH/HCOO^-$	2	$CO_2 + 2\ e^- + H_2O \rightarrow HCOO^- + OH^-$
Carbon monoxide	CO	2	$CO_2 + 2\ e^- + H_2O \rightarrow CO + 2OH^-$
Methanol	CH_3OH	6	$CO_2 + 6\ e^- + 5\ H_2O \rightarrow CH_3OH + 6\ OH^-$
Methane	CH_4	8	$CO_2 + 8\ e^- + 6\ H_2O \rightarrow CH_4 + 8\ OH^-$
Ethylene	C_2H_4	12	$2\ CO_2 + 12\ e^- + 8\ H_2O \rightarrow C_2H_4 + 12\ OH^-$
Ethanol	C_2H_5OH	12	$2\ CO_2 + 12\ e^- + 9\ H_2O \rightarrow C_2H_5OH + 12\ OH^-$

In **Figure I-1**, revenue and cost are reported as clusters of 5 bars for each CO2R product. The leftmost (blue) bar is the revenue (i.e., market price) while the remaining cluster of 4 bars (shades of orange) to the right represent the increasing production costs associated with each percentage increase in E_{cell}. The cell potential is increased by 10%, 50%, and 100%, respectively, to identify scenarios where combinations of voltage-electricity price are profitable. The error bars for each production cost bar define the upper and lower limits of industrial electricity in each region (i.e., Alaska and Washington, respectively). In all cases shown here, methane is unprofitable because the U.S. market has been saturated with abundant, cheap natural gas extracted from the fracking boom in past decade.[14] Some chemicals like methanol and ethylene might be profitable, but they only approach feasibility near the thermodynamic potential. Formic acid and carbon monoxide are relatively profitable across all combinations of E_{cell} and P_{e} shown here. If electricity prices decrease below the lower bound reported here ($0.046/kWh), some of the marginal products such as methanol, ethanol, and ethylene may become more economically attractive.

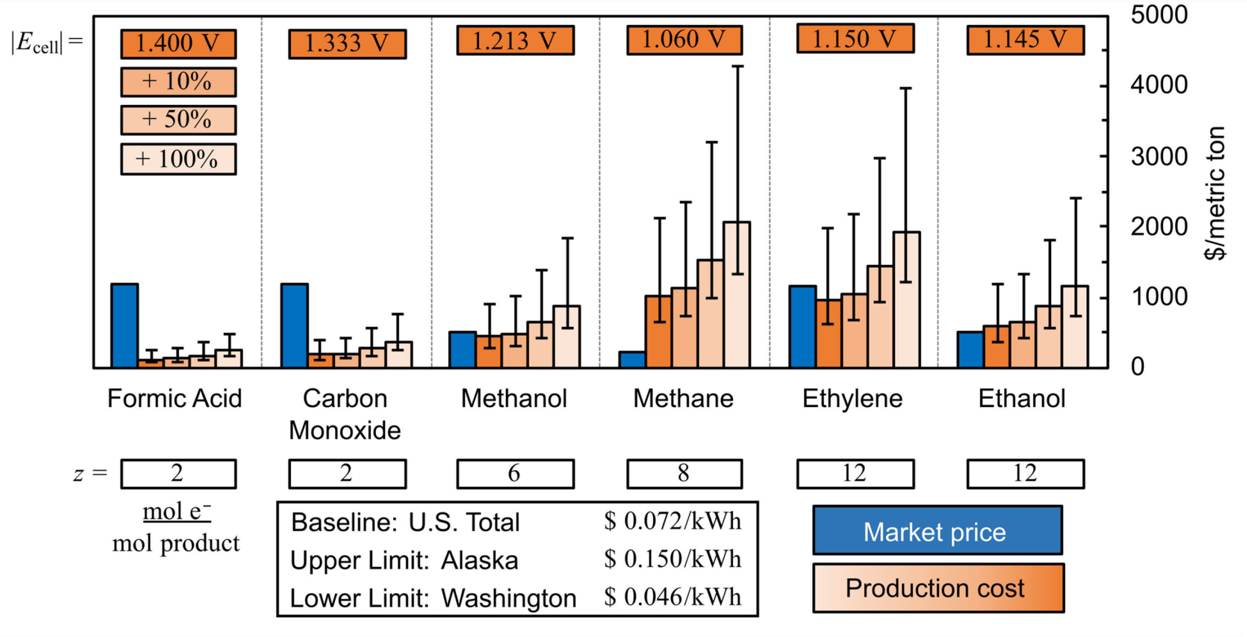

Figure I-1: *Techno-economic model results for electrochemical CO_2 upgrading to select products. We report each products commodity market price along with the production cost per metric ton to generate it electrochemically. Production cost is calculated using standard reduction potentials for each pair of full cell reactions, including various CO_2 reduction reactions paired with OER as the counter reaction for all cases. The upper and lower bounds for production cost show the range scenarios in the U.S. industrial electricity market. Increasing cell voltage demonstrates the production cost scales for deeper reduction products. Market prices are based on data from 2016 and earlier and electricity prices are taken from 2016.*

Reactions with fewer electron transfers could feasibly be pursued depending on market conditions according to this high-level economic analysis. Products like formic acid and carbon monoxide with lower z require lower energy inputs, which increases their profit margins. Deeper reduction products could still be reasonable to pursue if supply and demand shift in the future to either increase P_{market} or decrease P_{e}. It should be noted that this analysis implicitly assumes that introducing CO2R schemes at industrial scales would not detrimentally distort commodity markets for chemicals. However, the magnitude of this impact is presently difficult to determine since the future scale of these technologies and their potential to displace petroleum-centered chemicals production is still unknown.

Subsequent techno-economic modeling efforts must move beyond the simple profitability metric defined in this initial analysis to explore how reactor operating conditions, capital expenditures, and additional costs associated with operation and maintenance scale with process output. Inverted cost modeling, as recently demonstrated by Orella et al. for electrochemical CO2R,[15] is a reasonable extension of the coarse thermodynamics-centered approach highlighted in this work. By extending the scope of this techno-economic analysis to include cell-level details (e.g., operating conditions, geometric dimensions, and efficiencies), the sensitivity of process cost to various parameters can be articulated.

Installing economical electrochemical processes at a scale commensurate with the size of the chemicals sector will require significant advances in electrolyzer performance. Cells must be able to sustain high current densities to minimize capital expenditures and to generate output favorable distributions of products that can be utilized by existing chemical manufacturing schemes. Adopting operating strategies and components from adjacent and more mature electrochemical technologies such as chlor-alkali electrolyzers[16] and polymer electrolyte membrane fuel cells (PEFCs)[17] can provide insight into how to engineer porous electrodes for use at industrial scales.

3. *Engineering Gas Diffusion Electrodes for Electrochemical CO_2 Upgrading*

Establishing electrochemical CO_2 upgrading as a cornerstone technology within the chemicals industry will require us to engineer GDEs that are suited to the work of each unique reaction environment and production objective. To do this we would benefit from seeking to understand where porous electrodes have been used in the past, why they were (or why they were not) purpose-built for each application, and how we can apply to the effective utilization of CO_2. Approaches to this technological challenge are numerous, but in this thesis work I have taken the course described in **Figure I-2**. To start, I needed to identify which electrochemical platforms are effective models for representing the reaction environments that porous electrodes face once implemented within full-scale electrolyzers. In the second phase, I focused on electrode wettability as a key predictor of GDE durability. Wettability governs the extent to which a GDE can effectively manage multi-phase flow and, ultimately, determines overall device productivity, selectivity, and durability. In the final phase of this thesis, I used insights gathered from reactor studies and ex situ investigations of electrode wettability to begin constructing computational representations of GDEs to better understand relationships between wettability and functionality.

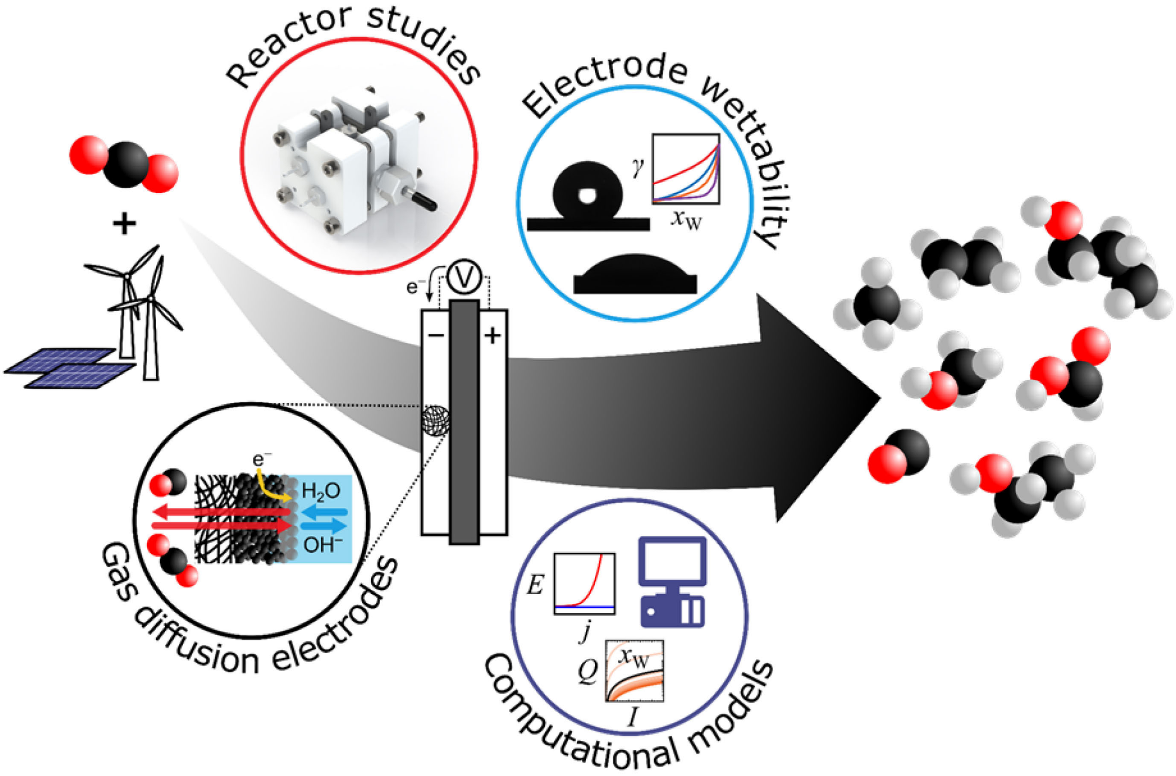

Figure I-2*: Conceptual thesis overview of Engineering Gas Diffusion Electrodes for Electrochemical* CO_2 *Upgrading. The work includes topics areas such as electrochemical reactor studies, electrode wettability characterization, and computational modeling of electrodes and cells.*

3.1. Gas Diffusion Electrodes

Carbon dioxide (CO_2) electrolyzers increasingly use gas diffusion electrodes (GDEs) to augment productivity and selectivity. GDEs separate gaseous and electrolyte phases while facilitating reactants/products/electrons transport to/from electrocatalytically active sites within the catalyst layer (CL). A material set that can manage diverse (e.g., electrical conductivity and electrocatalytic activity/selectivity) and contradictory (e.g., permeability and flooding resistance) functionalities is paramount for ensuring robust performance while targeting high product yields and efficiencies.

This thesis discusses how both experiments and modeling efforts are required to understand how components that were originally engineered for fuel cell applications might be translated to and adapted for use in CO_2 electrolyzers. As will be discussed in subsequent chapters, we should seek to understand the history of the development GDEs, primarily within the context of fuel cells, to determine which microstructural and compositional features of these advanced components are helping or hindering performance when applied to electrochemical CO_2 reduction.

3.2. Reactor Studies

Flow cell reactor platforms have largely been used to translate promising CO2R electrocatalysts to gas-fed configurations that resembled scaled-up electrolyzers. In this thesis, I used bulk electrolyte analytical reactors to characterize the mass transport limitations that emerge during CO2R. For most of the experimental work, I used a flow cells platform to systematically study the productivity afforded by using gas-fed reactor configurations for electrochemical CO_2 conversion and I characterized the dynamics of how these complex components fail when interfacing with liquid electrolytes. Extensive work to characterize gas diffusion electrode behaviors in small scale flow cell platform motivated later experimental and computational studies of how electrodes withstand challenging operating scenarios.

3.3. Electrode Wettability

Gas-fed CO_2 reduction schemes using gas diffusion electrodes must deal with the coexistence of both liquid and gaseous phases within porous materials. GDE wettability is a function of both porous media microstructure and surface chemistry, so contemplation of both aspects is necessary for predicting the interactions between the solid, liquid, gas phases and determining transport outcomes within cells. Ultimately, these microscopic interactions determine whether one phase (i.e., liquid) will occupy more of the pore volume than expected and constrain maximum achievable device performance. In this thesis, wettability is approached both with fundamental surface science studies as well as computational estimates of capillarity in porous media.

3.4. Computational Models

Taking empirical observations and constructing suitable models to capture real trends is at the heart of the acceleration of technology deployment at scale. We can use prior learnings from analogous electrochemical devices such as PEFCs to construct computational models of the gas diffusion electrodes and then evaluate them both ex situ (filling curves and “closure equations” for transport properties) and in situ (1D multiphysics transport models in COMSOL).

4. Outline of Thesis Document

The contents of **Chapter I** serve to contextualize the scale of the CO_2 problem and why CO_2 conversion technologies are not the only solution for anthropogenic emissions. I explain how CO_2 upgrading technologies could help to displace the need for petroleum inputs to industry because there are several hydrocarbon product pathways that could become economically viable according to techno-economic analysis. In **Chapter II** I present the progression of my CO2R studies from dissolved CO_2 cells to gas fed GDE flow cells that are the focus of my doctoral work. I discuss how the transition to gas-fed systems immediately results in high current densities and faradaic efficiencies but is challenged in flowing electrolyte systems. Borrowing technology and electrodes from PEFCs fuel cells and water electrolyzers can accelerate CO2R technology development, but their direct implementation into CO_2 electrolyzer environments can result in unanticipated failure modes. In **Chapter III** I present the result of a study in which I attempted to isolate the driving forces that cause premature GDE flooding. I explain how galvanostatic electrolysis reveal current-associated flooding and discuss further how a combination of electrochemical and chemical reactions result in diminished component durability and limited recoverability due to the intrusion of salt precipitation within the pore spaces of the electrode layers. In **Chapter IV** I investigate a hypothetical operating scenario in which pursuing high concentration liquid CO2R effluents will increase GDE wettability to the point of excessive electrode flooding. I study how the constituent materials of GDEs respond to different mixtures of water and organic CO2R products using contact angle goniometry on model surfaces. I couple this insight with simple mass balance models of electrolyzer and simple models for pore scale wettability to propose high level operational envelopes for CO_2 electrolyzers. In **Chapter V** I explore the implications of GDE wettability scenarios by using macro-homogeneous porous electrode models that originally developed for use in the study of water saturation in PEFC cathodes. I start with baseline models and modify the surface chemistry of the materials to understand how electrowetting and liquid CO2R products might challenge the assumptions of "hydrophobicity" that are often made about GDEs for CO2R. Finally, I integrate the computational GDE models into a 1D water transport model that is solved in COMSOL Multiphysics. I use the model to discuss how porous material saturation evolves as a function of wettability and operating pressure. In **Chapter VI,** I conclude by providing some perspective on why understanding the physical mechanisms at play within the GDE is necessary for enabling durable, reliable operation of gas-fed CO_2 systems. I also discuss how the experimental and modeling thrusts of this doctoral work might be continued in the future and why these new ways of using electrode wettability models should be validated by conducting new ex situ and in situ measurements of GDE saturation in challenging liquid environments.

II. Reactors for Electrochemical Carbon Dioxide Reduction

The choice of reactor configuration depends greatly upon the research objective. Three categories of electrochemical cells that are relevant to the work in this thesis are shown in **Figure II-1**. Kinetic studies of metallic electrocatalysts for electrochemical carbon dioxide reduction (CO2R) are often carried out in analytical cells that are represented by the leftmost icon in **Figure II-1**. For CO2R studies, the working electrode (WE) contains the catalytic surface to be evaluated, while the counter electrode (CE) facilitates a complementary oxidation reaction to complete the electrochemical circuit. Carbon dioxide (CO_2) is introduced is bubbled through the solution to reach a saturated state. In a three-electrode cell setup, a potentiostat is capable of precisely controlling the WE potential against the potential of a reference electrode (RE), which is a high impedance circuit element that undergoes a known reaction chemistry. All the electrodes are immersed in common bulk electrolyte solution. This cell type is well suited for reactions that take place completely in the liquid phase. However, depending on the catalyst CO2R can produce a mixture of both gas- and liquid-phase products. Gaseous products can be quantified using gas chromatography (GC) while liquid products can be identified by a variety of methods such as NMR and high-pressure liquid chromatography (HPLC), among others.

The two-chamber analytical cell, as shown in the rightmost icon in **Figure II-1**, was developed by Kuhl et al. to quantify gas and liquid phase CO2R products generated on metallic electrocatalysts.[18,19] A key feature of their device is the small liquid electrolyte volume relative to the WE surface area, which helps to enrich the concentration of liquid products for analysis. The cell design also includes headspace above the electrolyte that is continuously purged by gas introduced at the bottom of the cell as well as isolated cathode and anode chambers to prevent crossover and re-oxidation of species in the liquid phase.

The final reactor type, which is primary focus of this thesis, is the gas diffusion electrode (GDE) flow cell highlighted in the rightmost icon in **Figure II-1.** Flow cells can reach high geometric current densities because reactants (CO_2 and water) can be continuously fed in the gas phase through catalytically inactive electrode layers to dissolve in a thin electrolyte film within the catalyst layer, rather than through a bulk electrolyte solution. Therefore, GDEs are designed to simultaneously facilitate electrochemical CO_2 conversion while passively managing the interactions between the gas and liquid phases, as will be discussed at length in subsequent chapters.

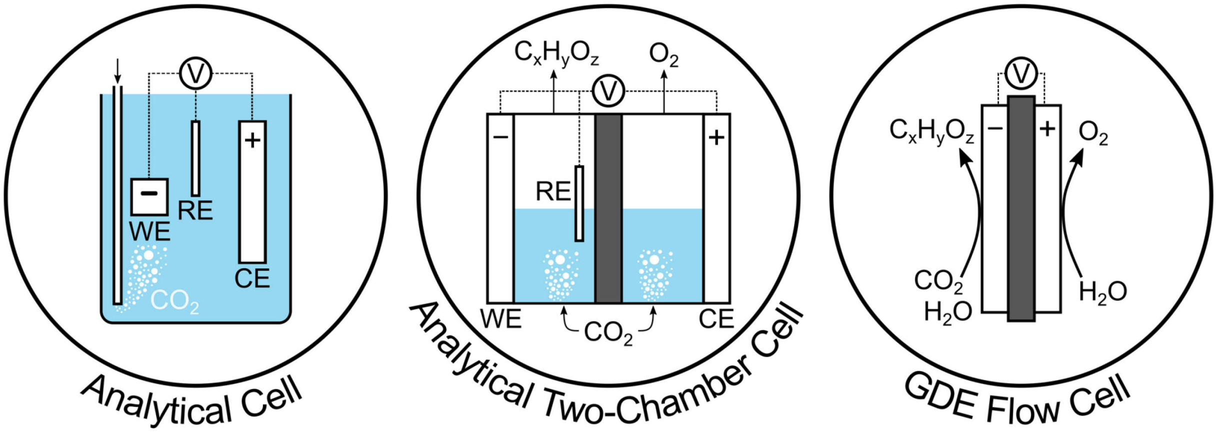

Figure II-1*: Electrochemical cell configurations for studying CO_2 reduction evolve to address emergent research questions.*

1. Bubble-Fed Two-Chamber Analytical Cell

Electroanalytical cells have been used extensively to study electrochemical CO_2 reduction (CO2R) in aqueous electrolytes. Devices like the one conceptualized in the leftmost icon of **Figure II-1** are ubiquitous in laboratories and are most often used to characterize catalyst activity and selectivity as a function of electrode potential. Because the typical electrode sizes are small, minimal catalyst loadings are required and the cell can be operated at low absolute currents, which reduces ohmic resistive losses ($V = IR$) between the WE-RE and WE-CE. Such cells are often suitable for studying catalysts in the kinetically-limited current-potential regime, assuming that mass transport limitations have been avoided or well characterized a priori. To properly characterize catalyst activity and selectivity, a cell should be operated at low currents and low reactant (i.e., CO_2) conversion. For the case of liquid CO2R products, it is also advantageous to maintain dilute species concentrations to maintain an aqueous electrolyte environment.

The initial cell studies in this thesis work were conducted in a two-chamber analytical cell fashioned after the device constructed by Kuhl et al.,[18,19] represented by the middle icon in **Figure II-1**. I designed, constructed, and operated my own version of the two-chamber analytical cell to be able to characterize CO2R selectivity and activity changes as a function of potential, prior to studying high-surface area electrocatalysts in a GDE flow cell. A digital representation of the cell was rendered in Solidworks is shown in **Figure II-2**. Using this type of cell, Kuhl et al. elucidated accurate product distributions for dilute reduction products generated on the same metal electrocatalysts as those identified in previous decades. In their pioneering work, Hori et al. first grouped metallic electrocatalysts into categories based on the dominant reduction products.[20] Intending to eventually transition to a flow cell platform to study GDEs, I chose to focus on silver (Ag), tin (Sn), and copper (Cu) as model electrocatalysts because they reliably produce carbon monoxide (CO), formate/formic acid (FA), and a mixture of hydrocarbons (HC), respectively.[20,21]

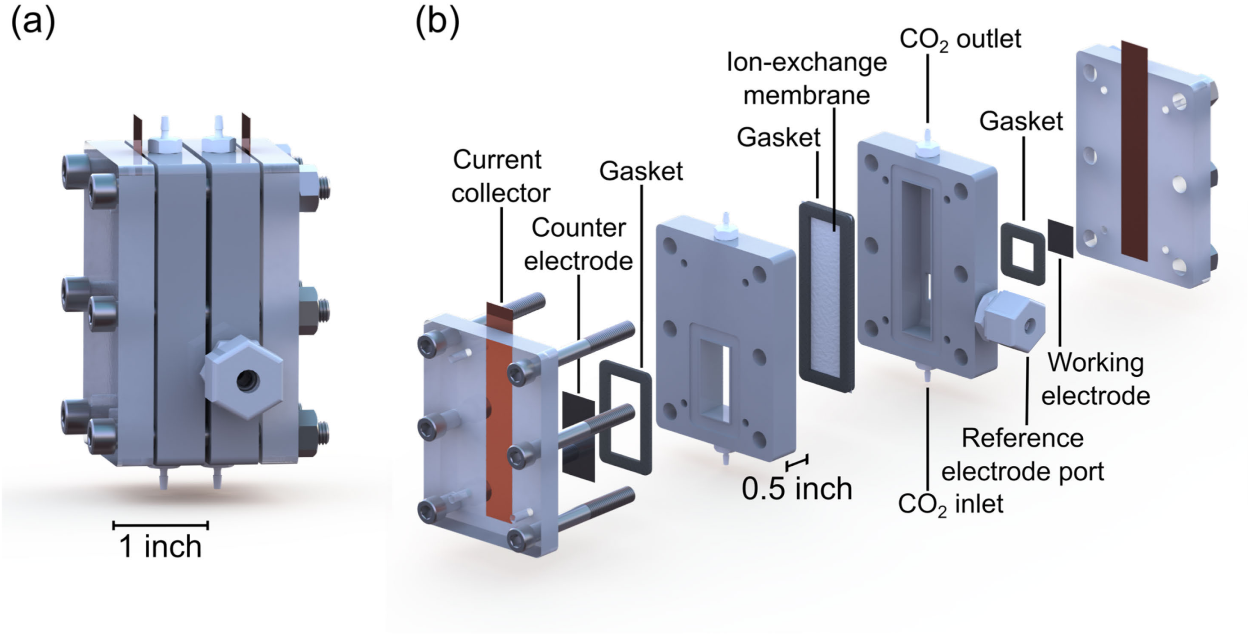

Figure II-2*: Solidworks rendering of the analytical two-chamber electrolysis cell for CO2R, including an (a) assembled view and an (b) exploded view of the components. Scale bars are provided for each panel and important components are labeled in panel (b). The reference electrode is not shown in this image.*

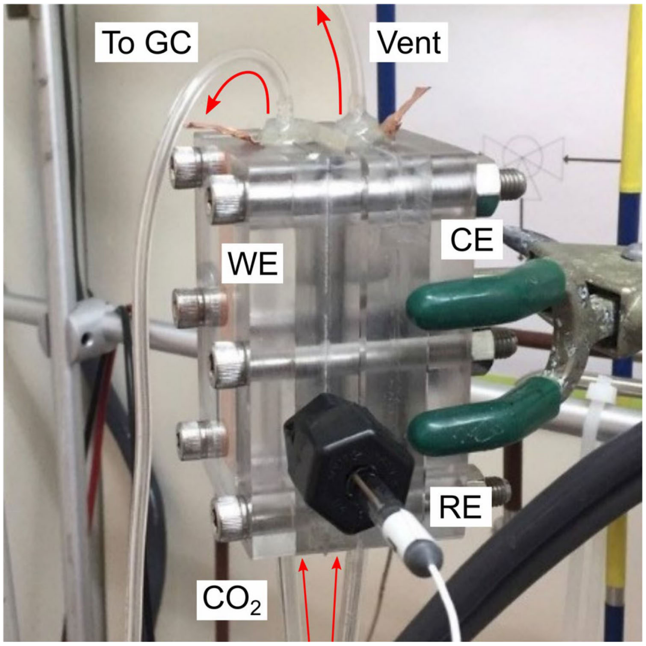

Figure II-3*: Photo of the analytical two-chamber cell, showing how CO_2 flows in through the bottom of the device and product gases exit at the top. The effluent gas mixture from the WE chamber (cathode) flows to a GC for compositional analysis, while O_2 and CO_2 from the CE chamber are vented to atmosphere in a fume hood. The RE pictured here is a glass bodied Ag/AgCl electrode. In this photo, the copper current collector tabs for the WE and CE are not yet connected to the potentiostat.*

1.1. Faradaic Efficiency Determination

Only short experiments (< 1 h) are necessary for each current-voltage set point to characterize a material's electrocatalytic activity and selectivity. Activity is defined as the current density, often measured in units of mA/cm^2 on a geometric area basis. If the roughness factor, or actual electrocatalyst surface area per geometric area, is known then the current density can be reported as the intrinsic activity of a material. Selectivity is represented by the faradaic efficiency, FE, or the fractional portion of the total current that is directed towards generating each reaction product. For practical purposes, the faradaic efficiency for each product, FE_i, must be defined both for a batch and continuous processes, as shown by Equations (II.1) and (II.2), respectively.

$$\mathrm{FE}_{i,\mathrm{batch}} = \frac{c_i V z_i F}{Q} \tag{II.1}$$

$$\mathrm{FE}_{i,\mathrm{continuous}} = \frac{x_i \dot{N} z_i F}{I} \tag{II.2}$$

The batch equation is most convenient for liquid CO2R products since they are quantified as part of small aliquots of the cathode chamber electrolyte. This batch equation can also be used if manual syringe injection into a GC device is the method of choice. Batch FE_i can be calculated from the concentration of species i, c_i, the sample volume, V, the charge number, z_i, and the total charge passed, Q, are known. The Faraday constant, F, is needed to convert from units of moles to C.

The continuous embodiment of the equation is convenient for experiments in which the cell headspace is periodically sampled by a GC device through an inline valve. Continuous FE_i can be determined once the mole fraction of species i, x_i, the molar flow rate, $\dot{N}$, charge number, z_i, and the total current at the time of the sampling, are known. $\dot{N}$ can readily be determined from the ideal gas law ($P\dot{V} = \dot{N}RT$) using information from a mass flow meter, which reports volumetric flow rate, $\dot{V}$, pressure, P, and temperature, T, for a preset carrier gas. If product concentrations are sufficiently low, the properties of the carrier gas (i.e., CO_2) should not vary enough to significantly affect the calculation of $\dot{N}$.

1.2. Experimental Material and Methods

Silver (Ag) electrodes with 1 cm^2 active geometric area were prepared from stock polycrystalline silver foil (0.1 mm thick, annealed, Premion®, 99.998% (metals basis)) that was first polished with sandpaper (3M, 400 grit) and then cut into ca. 1.2 cm x 1.2 cm squares. The additional geometric area is needed to hold the WE in place and the active area becomes ca. 1 cm^2 once compressed by a rubber gasket. Platinum counter electrodes with 3 cm^2 active geometric area were cut from platinum foil (0.025 mm thick, 99.9% (metals basis)). The Ag/AgCl reference electrode was filled with a saturated KCl fill solution (BASi, MF-2052). Prior to assembling the cell for each experiment, the Ag/AgCl RE potential was checked against a saturated calomel electrode (SCE, Fisher Scientific, nominally +242 mV vs SHE) that is dedicated for RE calibration and is stored in a saturated KCl solution. A commercial anion-exchange membrane (Selemion® AMV) was used to separate cathode and anode chambers while still allowing hydroxide (OH^-), bicarbonate (HCO_3^-), and carbonate (CO_3^{2-}) to move from cathode to anode during electrolysis. The anion-exchange membrane was soaked in a 0.1 M $KHCO_3$ electrolyte bath prior to use in electrolysis experiments. The 0.1 M $KHCO_3$ electrolyte used for each experiment was prepared by saturating a 0.05 M K_2CO_3 electrolyte (99.995% (metals basis), Sigma-Aldrich) solution with CO_2. All electrolyte solutions were prepared with deionized (DI) water (Millipore, 18.2 MΩ).

The analytical two-chamber cell was operated at ambient laboratory temperature and low backpressure (1–2 psig). CO_2 (Airgas, Research Grade 5.0) was fed to each side of the two-chamber cell by two independent mass flow controllers to set to their maximum-rated flow rates of 20 sccm (Brooks GF40 Series). The temperature, pressure, and volumetric flow rate of the gas stream exiting the cathode chamber was continuously monitored by a mass flow meter (Cole-Parmer, EW-17080-10, 50 sccm maximum). The gas stream exiting the anode chamber was submerged under an ca. 1 m water column to balance the backpressure of the cathode side caused by the narrow tubing running to the flowmeter and GC unit.

A VSP-300 (Bio-Logic) potentiostat was used for electrochemical measurements with a channel that is limited to current/voltage of ±500 mA/±12V. Data were collected and exported via EC-Lab software (Bio-Logic) to a text format (.csv) for processing. High-frequency resistance (HFR) between the WE and RE was measured using constant voltage electrochemical impedance spectroscopy with an amplitude of 20 mV and frequency of 10 kHz centered on the open-circuit voltage (OCV). Resistance between the WE and RE was compensated at 85% based on the HFR value measured prior to each constant potential experiment. The remaining 15% of compensation was applied while processing the electrochemical data in MATLAB using Equation (II.3).

$$E_{\mathrm{WE}} = E_{\mathrm{WE,applied}} - IZ_{\Omega} \tag{II.3}$$

The composition of the product gas mixture was measured using a gas chromatography (GC) system (Agilent 7890B) with HP-PLOT Q PT and HP-PLOT Molesieve columns (Agilent) and Argon carrier gas (Airgas, UHP Grade 5.0). Gas samples from a 1-mL sample loop were periodically injected at ca. 12 min intervals into the GC by a software-controlled 8-way valve driven by compressed air. A thermal conductivity detector (TCD) was used to quantify the concentrations of CO and H_2.

After cell assembly, gas lines are attached to the bottom ports of both the cathode and anode chambers. Once CO_2 is flowing through each chamber at 20 sccm, several mL of 0.1 M $KHCO_3$ electrolyte is injected through the top ports into each chamber of the cell with a syringe. If gas is not flowing at a sufficiently high mass flow rate at this point, the electrolyte will drain into the inlet gas lines. Next, CO_2 is bubbled through the electrolyte for at least 30 min to ensure that the electrolyte is saturated with CO_2. After the saturation step, the outlet gas lines are connected to the top ports of each chamber and the system is left to pressurize and equilibrate. At the end of each experiment, the gas flow rate is set to zero to depressurize the system. Once depressurized, the bottom gas inlet tubes are detached to let the electrolyte drain from both chambers into a common waste container since no liquid products were analyzed in this study.

Each electrolysis experiment was conducted for around 60 min, which is the time needed for 5 GC injections. Continuous FE for CO and H_2 is calculated using Equation (II.2) for each sampling time by taking an average of all relevant data (i.e., electrochemical, gas composition, and gas flow properties) ca. 1 min prior to each GC injection. The partial current density for each product is calculated by multiplying the FE by the total current density. To arrive at overall FE and partial current density data for each cathode potential set point, FE and partial current density were averaged over the entirety of the 60-minute experiment.

1.3. Results and Discussion

Constant potential (chronoamperometric) CO2R electrolysis experiments using roughened silver foil electrodes were conducted at set points ranging between –1.3 and –2.0 V versus the Ag/AgCl RE after compensating for ohmic resistance using Equation (II.3). FE and partial current density data are reported as a function of cathode potential in **Figure II-4** and **Figure II-5**, respectively. In addition to the FE data, quadratic functions are included for both CO and H_2 in **Figure II-4** to draw attention to the selectivity trends. Partial current density is reported on a logarithmic-scale in **Figure II-5**, as is typical for a Tafel analysis of kinetic behavior.[9]

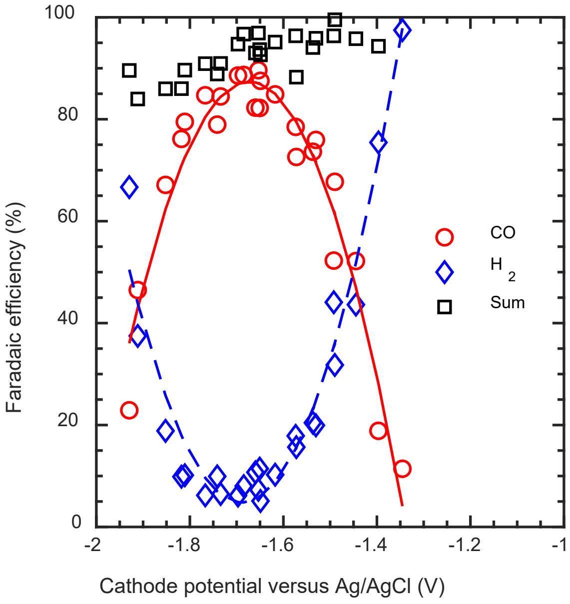

Figure II-4: *Faradaic efficiency data for CO_2 reduction to CO on a silver foil. The curves for CO and H_2 are fit with quadratic functions to demonstrate that CO efficiency reaches a peak before decreasing at higher applied cathodic potentials.*

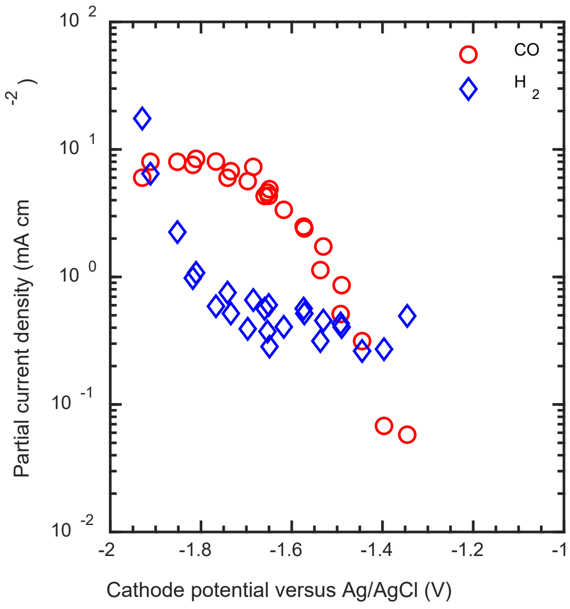

Figure II-5: *Partial current density data for CO_2 reduction to CO on a silver foil. The lower cathode potential region for CO qualitatively takes on a linear shape, but at higher cathode potentials the curve flattens, which can be reasonably attributed to mass transport limitations of CO_2 through the aqueous bicarbonate electrolyte.*

At low potentials, H_2 is the majority product, indicating that CO2R is the more kinetically limited reaction in this regime. However, CO FE increases at more negative potentials until peaking near a maximum of ca. 90% near –1.7 V vs Ag/AgCl. At more cathodic (negative) potentials the CO selectivity decreases and H_2 generation dominates again. Based on the reasonable initial assumption that many electrocatalytic reactions follow Butler-Volmer kinetics,[22] we might expect to observe a continual increase in CO partial current density as a function of cathode potential. If the reaction were kinetically-controlled and followed such a rate law, the data should appear linear when plotted on a logarithmic scale. In the absence of significant mass-transport limitations, the data could then be fit to forward reaction rate expression like the one shown in Equation (II.4) in order to extract useful empirical kinetic rate constants like exchange current density, i_0, and cathodic symmetry coefficient, α_c.

$$j_{\mathrm{CO}} = -i_o \exp\left(-\frac{\alpha_{\mathrm{c}} F}{RT}\eta\right) \tag{II.4}$$

However, the plateauing of the CO partial current density data in **Figure II-5** demonstrate that the limiting current density for CO2R to CO approaches ca. 10 mA/cm^2 in this reaction environment, which is consistent with results obtained using similar experimental cells and protocols.[19,23] In contrast, HER only requires water as a reactant, so its activity continues to increase at greater applied potentials. The most likely explanation for the diminishing CO FE at high cathodic potentials is that CO2R becomes mass transport limited in dissolved CO_2 even at seemingly mild current densities. Limited solubility and poor gas-electrolyte phase transfer contribute together to limit the rate of CO2R to CO. CO_2 solubility in water is already limited to around ca. 30 mM at standard conditions, but it decreases even further in electrolyte solutions as a function of increasing ionic strength according to “salting out” principles.[24] Additionally, insufficient mass transfer from gas bubbles to the electrolyte can result in undersaturation of CO_2 in the electrolyte. Lobaccaro et al. studied the effects of CO_2 depletion in analytical CO2R reactors with high electrode surface area to electrolyte volume ratios (> 0.5 cm^{-1}) by measuring chamber pH and product FE as a function of current density and CO_2 bubble size (as a proxy for gas-electrolyte mass transport rate). They concluded that by using glass frits to introduce small CO_2 bubbles into solution and by operating the cell at current densities beneath an upper limit of 10 mA cm^{-2} they could ensure that the cell was operating in a kinetically-controlled region for CO2R.[25] Despite these constraints, analytical cells are still useful for understanding how electrocatalysts respond to polarization in different electrolyte environments at low current densities, but their limitations should be acknowledged by researchers prior to use and adequately communicated when reporting experimental results.

2. Gas-Fed Electrochemical Flow Cell

Facile CO_2 transport from gas to catalyst surface is necessary to overcome the intrinsic activity and selectivity constraints of CO2R in aqueous electrolytes. Gas-fed electrochemical cells utilizing gas diffusion electrodes (GDEs) are suited to this task because their porous microstructures allow gaseous reactants/products to be introduced/removed to/from the catalyst layer primarily in the gas phase rather than through a bulk volume of electrolyte. The schematic in **Figure II-6** shows major components of the cathode GDE (diffusion layer and catalyst layer) along with representative material flows for CO2R to CO. In this configuration, CO_2 is introduced in the gas phase and moves through diffusion layer before dissolving in the electrolyte of the catalyst layer. Water (H_2O) necessary for CO2R can be fed in the gas phase (not shown), extracted from the aqueous electrolyte, or both. Reaction products (e.g., CO) are removed from the GDE either in the gas phase as shown here or in the liquid phase (not shown). Electrons current move through the conductive solid matrix of the diffusion layer before reaching the catalyst layer. The catalyst layer contacts and wets the electrolyte phase to facilitate ion transport. From these specified design requirements, it becomes evident that an effective GDE for CO2R must be engineered to simultaneously facilitate gas phase transport of reactants/products through the pore volume while allowing electronic current and heat to move through the solid matrix. Additionally, the wetting requirements of the solid components differ markedly between the layers: the catalyst layer must wet the electrolyte phase to conduct ions while the diffusion layer should be sufficiently non-wetting to prevent flooding of the pore space with liquid.

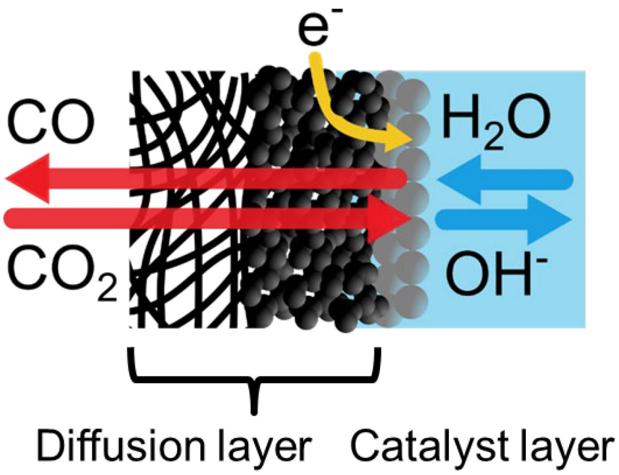

Figure II-6: *Cathode GDE schematic highlighting the core functionalities and material flows. In this device configuration, CO_2 is introduced in the gas phase and moves through diffusion layer before dissolving in the electrolyte of the catalyst layer. Water (H_2O) is either fed in the gas phase (not shown) or through the electrolyte as shown here. Electrons move through the conductive solid matrix of the diffusion layer before reaching the catalyst layer. The catalyst layer wets the electrolyte phase to facilitate ion transport. The diffusion layer should be sufficiently non-wetting of the liquids in the system to prevent flooding of the pore volume. Reaction products (e.g., CO) are removed from the GDE either in the gas phase as shown here or in the liquid phase (not shown).*

2.1. Developing a Flowing Electrolyte, Gas-Fed Carbon Dioxide Electrolyzer

The flow cell used in this thesis mimics design concepts from Kenis Research Group reactor while adopting the general architecture of Gen2 reactor platform developed in the Brushett Research

Group for redox flow battery studies. As shown in **Figure II-7**, a key feature of the cell is an added center channel that includes a reference electrode (RE) port, which enables 3-electrode GDE studies with flowing electrolyte. To date, several reactor embodiments of this GDE flow cell platform have been used to characterize the CO2R activity and selectivity of metallic nanoparticles, including Ag,[26] Sn/SnO_x,[27] and Cu.[28]

The reactor platform is modular, so components are chosen according to specifications of each compartment's reaction chemistries. In configurations where sufficiently non-wetting GDEs are included, independent control of gas/liquid stream flows through the cathode/electrolyte/anode compartments can be achieved. When using porous electrodes, reactant streams are typically moved in and out of the cell through the end plates/diffusers. To ensure a tight seal near the inlet and outlet, O-rings are compressed between the end plates and the polymer impregnated graphite current collectors, which also serve as flow fields. The components shown in **Figure II-7** are a version of "flow through" flow fields because they direct fluid to move in-plane through the porous electrode. Different current collector plates, such as graphite ones with a serpentine channel or titanium current collectors without channels, can easily be introduced depending on the experiment, as demonstrated in Chapter III. GDEs coated with catalyst are sealed against the current collector/flow field by planar rubber gaskets. As shown in **Figure II-7**, the cell is often constructed symmetrically, with GDEs on both sides, apart from changing the catalyst layers deposited on each electrode. However, different combinations of flow fields and electrodes can be combined to create hybrid gas-feed/liquid-feed cells. The RE shown in the graphic is a glass-bodied Ag/AgCl electrode. The full cell is kept in alignment during assembly using pins. Once fully assembled, the component stack is compressed with stainless steel bolts and nuts.

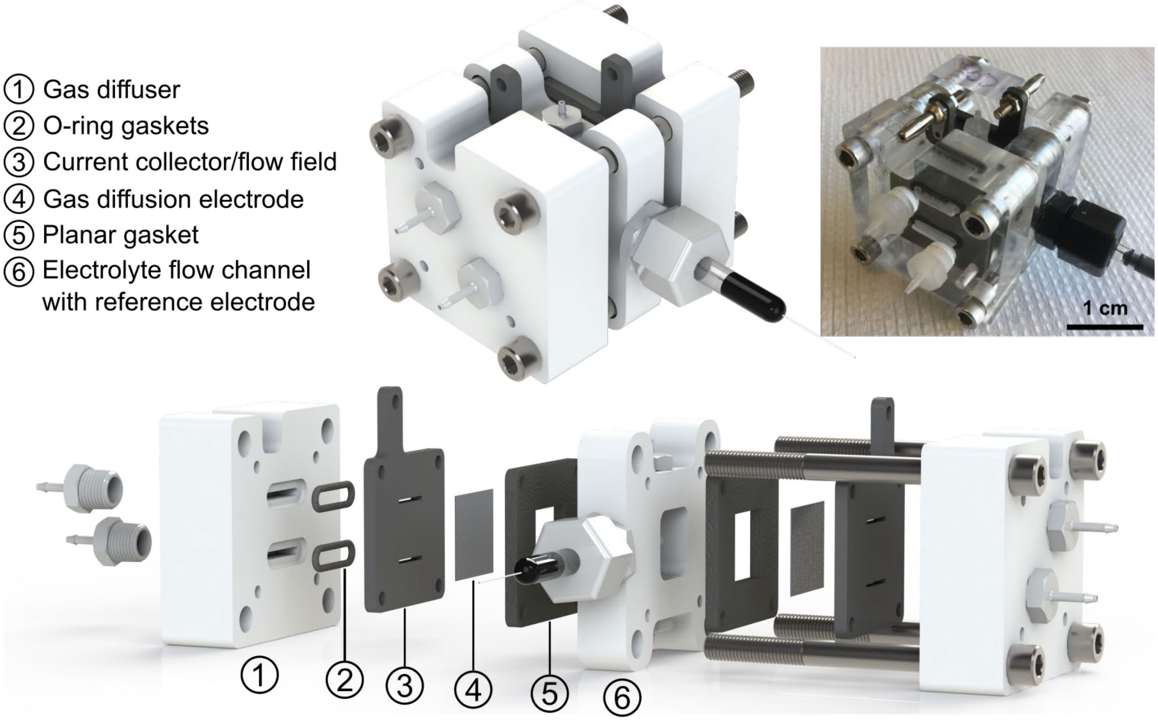

Figure II-7: *Solidworks rendering of the flow cell architecture used for GDE studies. This figure was originally reported in the article by Sen et al. and is reused here with permission.*[27]

GDEs provide a substantial activity advantage over planar electrodes as shown by the cathode polarization data in **Figure II-8**. The two order of magnitude increase in CO partial current density is immediately evident from a comparison of the Ag-foil results from Section II.1.3 against the Ag-GDE results to be contextualized in Chapter III. The data for each material were collected in different electrolytes, 0.1 M $KHCO_3$ and 1 M KOH, respectively. One immediate impact of switching to 1 M KOH is lower ohmic resistance, but this effect on polarization data is removed here by IR-correction of the cathode potential. A secondary effect of using an alkaline electrolyte is the slight positive shift in the onset potential for the CO2R activity in > 1 M KOH electrolyte, as discussed in more detail by Gabardo et al.[29]

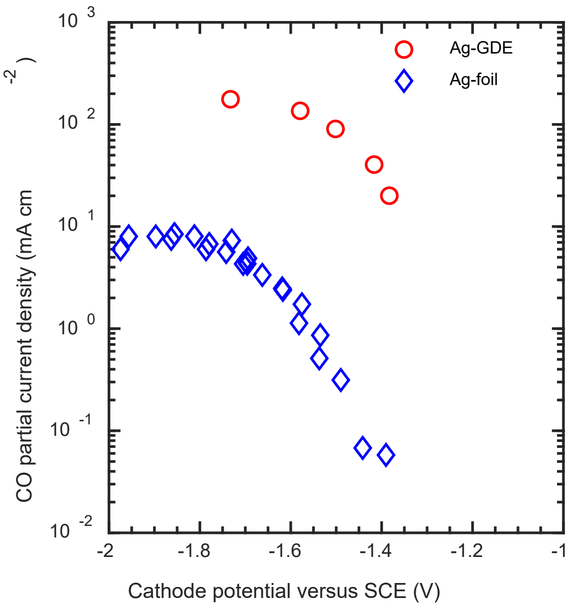

***Figure II-8**: Comparison of CO2R activities achieved using a Ag-foil versus a Ag-GDE. The partial current density of the Ag-foil plateaus near ca. 10 mA/cm^2 while the Ag-GDE reaches an activity of ca. 100 mA/cm^2. The Ag-foil data were collected in 0.1 M $KHCO_3$ saturated with CO_2 and the Ag-GDE data were collected in 1 M KOH.[26] Although the polarization curves were measured in different electrolytes, the two sets of conditions are typical of those that have been used to evaluate electrocatalysts in each reactor platform.*

2.2. High Current Density Operating is Stifled by Electrolyte Flooding

Although the use of GDE flow cells leads to substantial increases in CO2R geometric current densities as compared to bulk electrolyte cells with foil electrodes, liquid flooding and blockage of gas transport poses a significant challenge to extended operation. Much of the motivation for the studies in later chapters of this thesis stems from the consistent observation of flooding while studying several catalysts, including Ag, Sn/SnO_x, and Cu nanoparticles, that had been deposited onto carbon-based gas diffusion layers (GDLs).

In one representative study, electrolysis experiments were conducted using the flow cell pictured in **Figure II-7** to determine whether there were significant CO2R FE and partial current density differences between Cu-GDEs prepared using different catalyst deposition protocols. Optical images of the different Cu-GDEs can be seen at the top of **Figure II-9**. The set of electrodes includes (from left to right) spray-coated commercial nanoparticles (SP), electroplated nanoparticles on a plasma-treated GDL substrate (EC-P); electroplated nanoparticles on an ionomer-treated GDE substrate (EC-I), and electroplated nanoparticles on ionomer-treated GDL substrate with post-deposition plasma treatment (EC-I-P). The anode GDE was a Pt/C electrolyst deposited on a carbon GDE. A detailed description of catalyst deposition protocols for this study in our group are reported by Sen et al.[28]

During the experiments, dry CO_2 gas was fed at 20 sccm to the cathode compartment, while dry H_2 gas was fed at less than 10 sccm to the anode. The hydrogen oxidation reaction (HOR) was chosen as the anode reaction to reduce the overall cell potential. A Nafion 117 membrane was pressed against the Pt/C anode GDE to prevent penetration of H_2 gas bubbles into the center flow channel. 1 M KOH electrolyte was recirculated at 2 mL min^{-1} using a peristaltic pump. Cathode potential was held at −1.8 V against a Hg/HgO reference electrode (+140 mV versus SHE, CH Instruments Inc., Austin, TX) for all experiments. 85% IR-correction of the cathode potential was applied during the experiment and the remaining 15% was compensated during data processing. Gaseous products from the cathode chamber were analyzed with GC for CO, CH_4, C_2H_4, and H_2 using the method described for the two-chamber analytical cell.

Selectivity and activity results for the Cu-GDEs are reported in **Figure II-9a** and **b**. Partial current densities for each product are calculated by multiplying the species FE by the total current density at each time point. Species partial current densities at the 12 min and 60 min time points are stacked in **Figure II-9a** to show both activity and selectivity in the same plot. What is notable from these data is that total current densities decrease by up to ca. 50% for all samples over the course of the 60-minute electrolysis runs. Additionally, the FE of C_2H_4, often a target product when using Cu-

GDEs, decreased over the experiment as well, as shown in **Figure II-9b**. The diminishing CO2R selectivity at a constant potential indicates that CO_2 transport through the GDE. In most experiments, liquid electrolyte or salt precipitates were found to have penetrated through the GDE and into the CO_2 stream, leading to the development of the hypothesis that electrolyte flooding is a primary cause of CO2R activity loss, as opposed to catalyst deactivation.

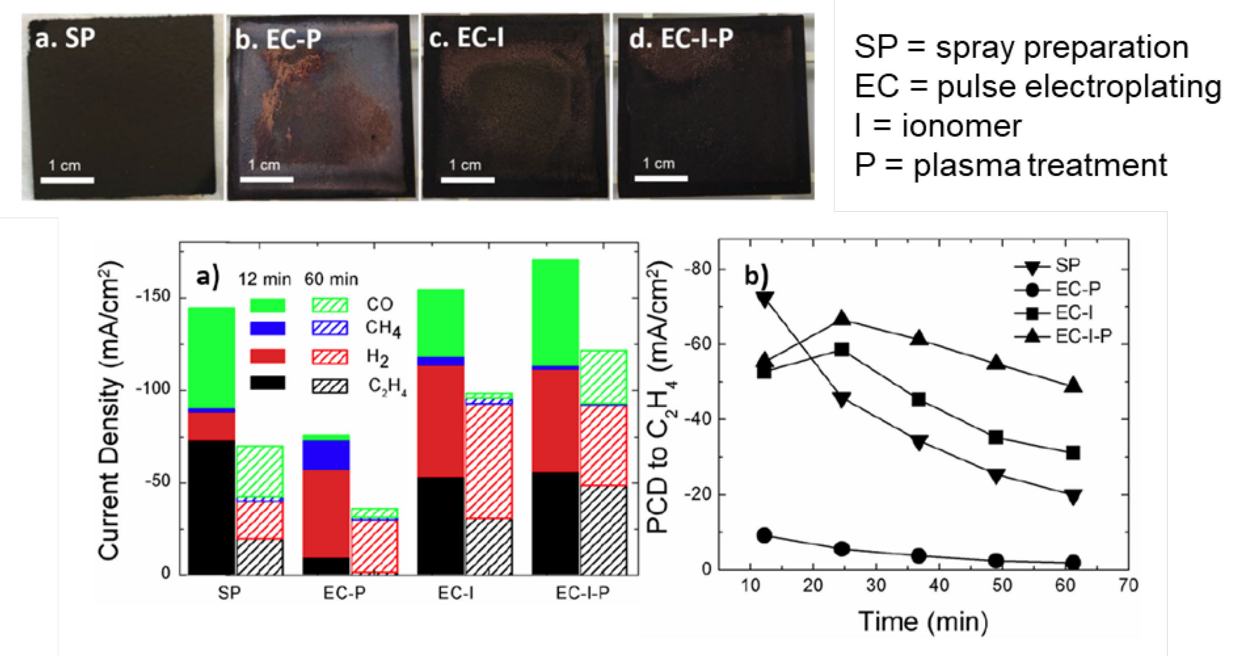

Figure II-9: *Cu-GDE activity and selectivity towards CO2R declines rapidly in the flow cell. The contents of this figure were originally reported in the article by Sen et al. and have been adapted for use here with permission.*[28]

The results of this study provoke deeper considerations of GDE properties and how we might engineer them to better withstand the reaction environments inherent to CO2R. Understanding whether GDEs placed in contact with flowing electrolytes are durable enough to reach high current densities (> 100 mA/cm^2) for extended durations, especially as they increase in scale, will dictate, in part, if this flow cell configuration can be used successfully for industrial CO2R. The answer to this question depends heavily on the nature and magnitude of the fundamental forces that underly flooding and how they tend to emerge because of operating conditions, materials properties, or both. Thus, there is need for deliberate studies of flooding dynamics in GDEs and determination as to whether its impacts on CO2R activity and selectivity are reversible.

III. Investigating Electrode Flooding in a Flowing Electrolyte, Gas-Fed Carbon Dioxide Electrolyzer

Managing the gas-liquid interface within gas diffusion electrodes (GDEs) is key to maintaining high product selectivities in carbon dioxide electroreduction. By screening silver-catalyzed GDEs over a range of applied current densities, we observe an inverse correlation between carbon monoxide selectivity and the electrochemical double-layer capacitance, a proxy for wetted electrode area. We find that plotting current-dependent performance as a function of cumulative charge leads to data collapse onto a single sigmoidal curve indicating that the passage of faradaic current accelerates flooding. We hypothesize that high cathode alkalinity, driven by both initial electrolyte conditions and cathode half-reactions, promotes carbonate formation and precipitation which, in turn, facilitates electrolyte permeation. This mechanism is reinforced by the observations that post-test GDEs retain less hydrophobicity than pristine materials and that water rinsing and drying electrodes temporarily recovers peak selectivity. This knowledge offers an opportunity to design electrodes with greater carbonation tolerance to improve device longevity.

1. Background

Developing efficient carbon dioxide (CO_2) electroreduction processes, which leverage renewable electrons, can provide sustainable pathways to a range of fuels, chemicals, and plastics while also displacing anthropogenic greenhouse gas emissions.[30] Aqueous-phase CO_2 delivery has been the preferred method for evaluating electrocatalytic materials at ambient conditions (298 K, 1 atm).[18–20] However, electrochemical performance in such configurations is constrained by low CO_2 solubility (33 mM)[31] and diffusivity (1.9×10^{-5} $cm^2 \cdot s^{-1}$),[10] which, in turn, lead to mass transport limitations that set an upper limit on current density of ca. 20 $mA \cdot cm^{-2}$.[25] Gas-phase delivery is an alternative approach whereby CO_2 is fed into an electrolysis cell through a gas diffusion electrode (GDE) whose catalyst layer (CL) interfaces with an electrolyte layer. In this configuration, the higher diffusivity of gaseous CO_2 ($\sim 10^{-1}$ $\mathrm{cm^2 \cdot s^{-1}}$)[10] and the reduced diffusion lengths within the CL enable increased current densities, typically an order of magnitude or greater over atmospheric aqueous-phase cell designs.[32–34] Indeed, gas-fed devices have demonstrated high geometric-area-specific current densities with a variety of carbon monoxide (CO) and hydrocarbon-selective metal electrocatalysts.[34–39] However, most emerging gas-fed CO_2 electrolyzers often exhibit limited durability, with performance decay after only a few hours of operation,[40,41] in part because these cell formats employ GDEs based on repurposed polymer electrolyte fuel cell (PEFC) materials that are not tailored to electrolysis applications.

Gas diffusion layers (GDLs) in PEFCs are responsible for facilitating gas, liquid, electron, and heat transport in the presence of the reactant gases and water, so material composition and microstructures have been optimized accordingly. For example, removing water from the cathode CL is crucial to device operation, especially at high currents when generated liquid water inhibits oxygen flux. To this end, densely-packed partially-hydrophobized microporous layers (MPLs) coated onto carbon-fiber substrates (CFSs) serve both as high-surface-area, electronically-conductive contacts to the CL and as effective media for water management.[42–44] Studies focused on water transport in PEFCs, enhanced by advanced operando imaging techniques, have motivated engineering both GDL microstructure and surface chemistry to achieve high power operation under water-saturated conditions.[45–52]

Recently, the need to understand electrolyte wetting phenomena at the gas-liquid interface within the GDE has been identified as an important area of investigation towards improving electrode durability for CO_2 reduction.[53] While PEFC GDLs embody desirable properties for CO_2

electrolyzers (e.g., geometry, permeability, electrical conductivity), these materials are not designed to meet all requirements for device longevity (e.g., resistance to liquid electrolyte percolation, stability in alkaline pH, durability under deeply cathodic potentials). Specifically, the efficacy of the MPL as a barrier to liquid electrolyte permeation, as is the case in liquid-electrolyte-based CO_2 electrolyzers, is limited by increasing apparent hydrophilicity over time.[36] Often, hydrophobicity/-philicity is measured via sessile drop contact angles (θ) between a surface (e.g., graphite) and a test fluid (e.g., water). High contact angles ($\theta > 90°$) are indicative of hydrophobicity, whereas low contact angles ($\theta < 90°$) describe hydrophilicity. Because water can exhibit a range of solid-liquid contact angles, $65° < \theta < 95°$, across an assortment of graphitic and carbon-fiber surfaces,[54–57] wet-proofing material, e.g., polytetrafluoroethylene (PTFE), is coated onto the carbon components to ensure that GDLs are hydrophobic.[57,58] Translating this concept to alkaline CO_2 electrolysis, a previous study by Kim et al. showed that tuning MPL PTFE loading to control electrolyte wetting improved CO selectivity over the parasitic hydrogen (H_2) evolution reaction (HER).[59] Although this work demonstrated promising CO_2 reduction activity with Ag-coated GDEs (Ag-GDEs), the short runs typical of catalyst screening experiments (i.e., several minutes to an hour) may not allow enough time for the detrimental effects of electrode flooding to become apparent. Longer-term operation in the gas-fed, flowing electrolyte format is sometimes explored, but stable performance remains elusive. In these cases, electrode flooding along with a changeover from CO to H_2 in the product gas stream are consistently reported.[35,40]

Pursuant to the goal of better understanding the dynamics of GDE flooding in a flowing electrolyte CO_2 electrolyzer, we conducted a systematic study of electrode stability across a range of current densities in an alkaline electrolyte. In addition to voltage-current and product composition measurements, we quantify the electrochemical double-layer capacitance (EDLC) to track electrolyte ingress into the GDE during electrolysis. We hypothesized that EDLC, proportional to wetted electrode area, is inversely correlated with cell performance and that measurable deviations from the desired steady state, specifically the transition from CO to H_2 production, may be captured by this metric. Recently, EDLC measurements have been used to quantify the wetted surface area of macroporous, fibrous carbon GDLs when subjected to a range of capillary pressures with electrolyte on one side and air at ambient conditions on the other.[60] While direct measurement of wetted surface areas is desirable, it is best suited for homogenous materials with a defined specific capacitance (in units of F/unit area) extracted from a representative sample of a known geometric area and minimal roughness. In contrast, catalyst-coated GDEs are composite materials with regions of distinct surface chemistry that preclude quantitative deconvolution through a single EDLC measurement.[61] Despite this constraint, meaningful performance comparisons can still be made between consistently prepared electrodes. Accordingly, EDLC measurements are a powerful technique for tracking electrolyte penetration for CO_2 electrolyzers and other electrochemical devices that rely on stable gas-liquid interfaces (e.g., metal-air batteries, water electrolyzers, chlor-alkali electrolyzers).

2. *Experimental Methods*

2.1. Gas-Fed Flowing Electrolyte CO_2 Electrolyzer

A gas-fed, flowing-electrolyte electrolyzer design (**Figure III-1**) adapted from a low-volume redox flow battery platform was used for all electrolysis experiments.[62] The projected electrode area is 2.55 cm^2 (1.7 cm × 1.5 cm) and the electrolyte chamber volume is 3.24 cm^3 (1.7 cm × 1.5 cm × 1.27 cm). A polymer-impregnated graphite plate with serpentine flow channel (MWI, G347B) serves as both the current collector and CO_2 distributor to the cathode.

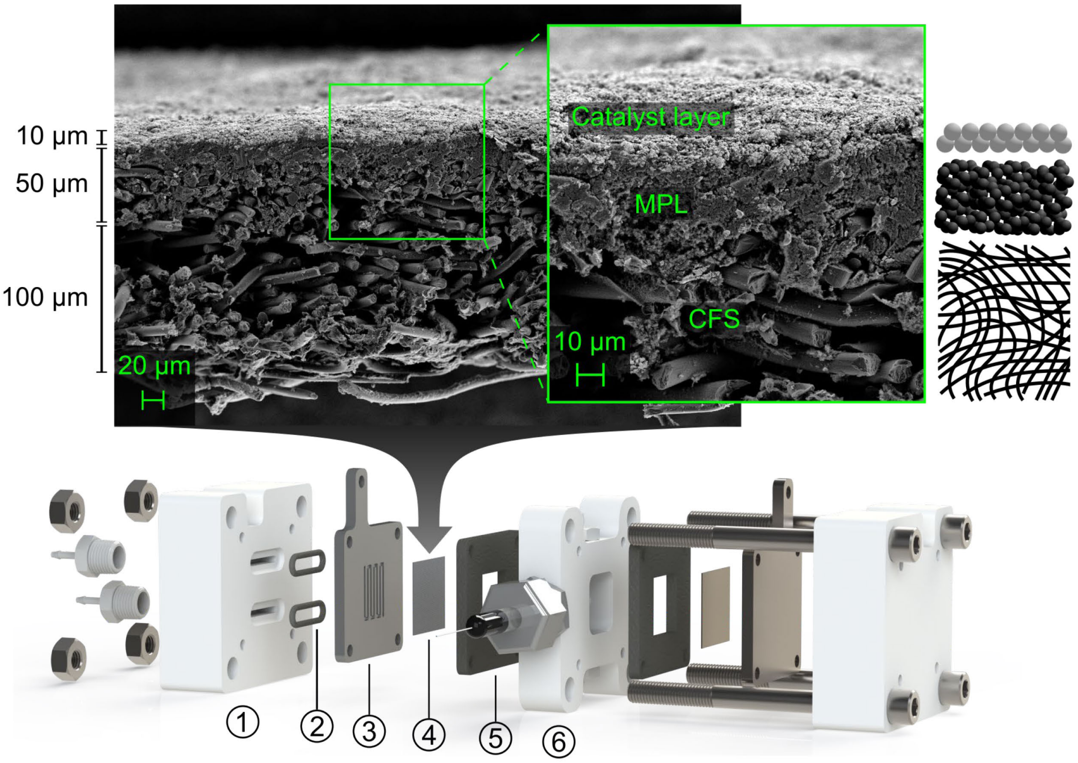

Figure III-1*: Exploded view of the flow reactor and cross-section SEM images of a Ag-GDE. Gas diffusion electrodes (top, Freudenberg H23C6) with a silver (Ag) catalyst layer (CL), a microporous layer (MPL), and a carbon fiber substrate (CFS) are loaded into a custom-built gas-fed, flowing-electrolyte electrolyzer (bottom) with a Hg/HgO reference electrode. An exploded view of the cell shows the (1) diffuser plates, (2) O-ring gaskets, (3) current collectors/flow fields, (4) gas diffusion electrode (cathode)/metal electrode (anode), (5) planar gaskets, (6) and electrolyte flow channel with reference electrode.*

The working electrodes for all experiments were carbon-based, Freudenberg H23C6 (FuelCell Store) GDLs featuring a CFS with PTFE wet-proofing and an MPL. CLs were applied to the GDLs to make GDEs by spraying an ink containing Ag nanoparticles with a nominal size of 20-40 nm (Alfa Aesar, 45509-06), XA-9 alkaline ionomer (Dioxide Materials™), isopropyl alcohol (IPA), and deionized water onto the MPL with an airbrush (Speedaire, 48PX91) utilizing nitrogen as a propellant. The ink formulation was 38 µL water/mg Ag, 38 µL IPA/mg Ag, and 1.3 µL XA-9 solution/mg Ag and was sonicated for 20 min to disperse the nanoparticles in solution prior to spraying. Each sprayed batch contained 20 GDEs. Representative SEM images of the CFS, MPL, and CL are shown in **Figure III-2**. Each GDE had a total area of 2.0 cm × 2.0 cm with a catalyzed area of 1.5 cm × 1.7 cm. The total batch loading was determined by subtracting the initial carbon paper mass from the final mass. The average catalyst loading was measured by taking the total batch loading and dividing it by the catalyzed (active) area (2.55 cm^2) per electrode. The catalyst loading for all GDEs was between 0.2–0.35 mg·cm^{-2}. SEM images show that the metal particle sizes were larger than 20–40 nm due to agglomeration during airbrush spray deposition (**Figure III-2c**). The counter electrode for the oxygen evolution reaction (OER) is a nickel foam (Alantum, pure compressed single sheet with initial 800 μm cell size) contacting a titanium (McMaster-Carr, Grade 2) current collector selected to withstand highly anodic potentials in the system. A mercury/mercury oxide (Hg/HgO, CHI152) reference electrode was used for alkaline-compatibility with a pH 13.6 KOH (Sigma-Aldrich, ACS reagent grade and/or Puriss. Grade) fill solution to match the conditions in the flowing electrolyte channel. The Hg/HgO reference electrode was checked against a saturated calomel electrode (Fisher Scientific, nominally +242 mV vs SHE) dedicated for calibration.

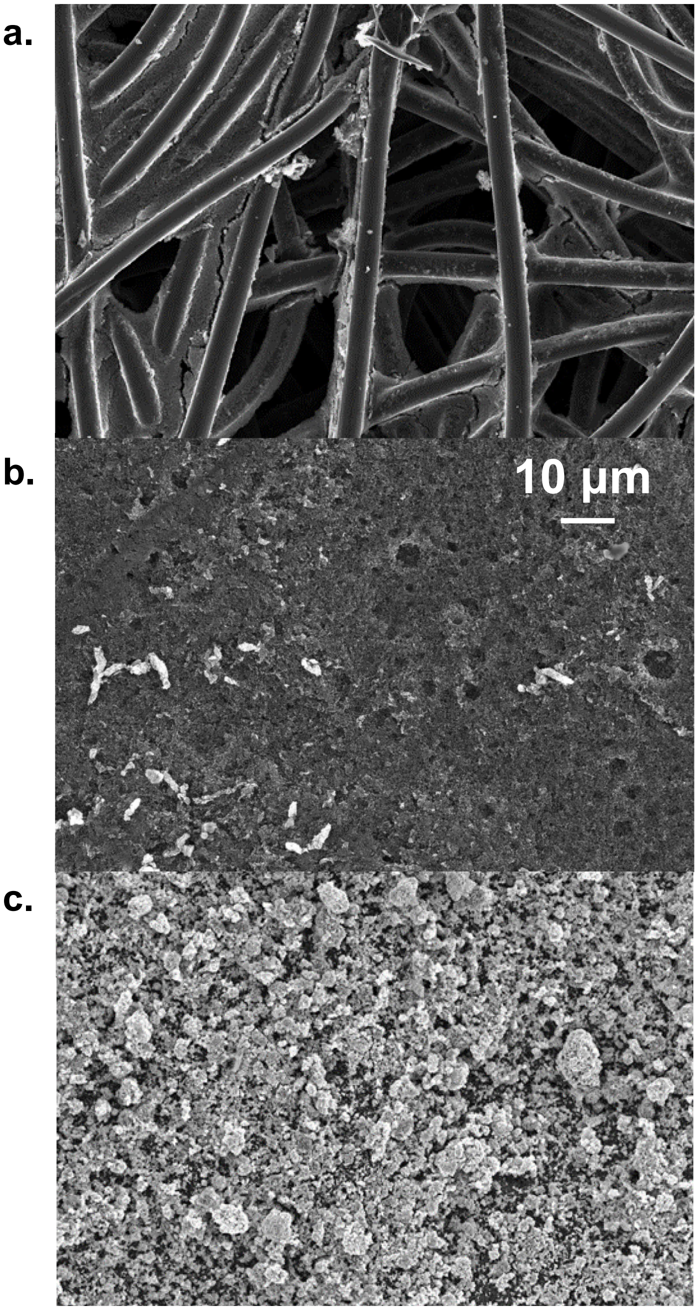

***Figure III-2**: SEM images of a representative Ag-GDE, including the (a) carbon fiber substrate (CFS), (b) microporous layer (MPL), and (c) Ag catalyst layer (CL). The MPL and CFS are part of a Freudenberg H23C6 gas diffusion layer. The 10 µm scale bar applies to all three panels.*

2.2. Material Flows and Pressure Regulation

The electrolyzer was operated at ambient laboratory temperature and at low back pressure (1–2 psig). CO_2 (Airgas, Research Grade 5.0) was fed to the cell by a mass flow controller with a maximum-rated flow rate of 20 sccm (Brooks GF40 Series). The temperature, pressure, and volumetric flow rate of the exiting gas stream was continuously monitored by a mass flow meter (Cole-Parmer, EW-17080-10, 50 sccm maximum). Electrolyte was flowed once (i.e., "single-pass") through Norprene tubing (Saint Gobain, L/S 14) to the cell with a peristaltic pump (Masterflex® L/S® Standard Digital Pump) set at 1 $mL\cdot min^{-1}$. All nominally 1 M KOH solutions were prepared with deionized (DI) water (Millipore, 18.2 MΩ). The residual moisture content of the KOH pellets was not considered during preparation, so the pH of all solutions was measured to be 13.6 with a Metrohm 914 pH/Conductometer. Single-pass operation was used to avoid carbonation-induced pH changes to KOH electrolyte across the GDEs during multi-hour experiments. Back pressure was maintained at the outlet of the gas and liquid streams with dome-loaded, low-flow rate back pressure regulators (Equilibar, LF1SNN12B-NSMP10T100F4KK) set between 1.5–2.0 psig with compressed air to the reference port.

2.3. Electrochemical Measurements

A VSP-300 (Bio-Logic) potentiostat was used for all electrochemical measurements. The channel used for all experiments is limited to current/voltage of ±500 mA/±12V. The maximum current density for the electrolysis experiments (196 $mA\cdot cm^{-2}$) was determined by the upper current limit of the potentiostat. Data were collected and exported by EC-Lab software (Bio-Logic) to a text format (.mpt) for processing. High-frequency resistance (HFR) between the reference and working electrodes was measured using constant voltage electrochemical impedance spectroscopy with an amplitude of 20 mV and frequency of 100 kHz centered on the most recently measured working electrode (cathode) potential.

2.4. Product Quantification

Product gas composition was measured using a gas chromatography (GC) system (Agilent 7890B) with HP-PLOT Q PT and HP-PLOT Molesieve columns (Agilent) and Argon carrier gas (Airgas, UHP Grade 5.0). Gas samples from a 1-mL sample loop were periodically injected into the GC by a software-controlled 8-way valve driven by compressed air. A thermal conductivity detector (TCD) was used to quantify all gases of interest. The method can detect permanent gases and light hydrocarbons such as methane, ethane, and ethylene. However, only CO and H_2 were included when calculating product gas mole fractions.

2.5. Capacitance Measurements

Capacitance is estimated by regressing the measured working electrode charging current as function of potential sweep rate. Sweep rates ranged from 50–500 $mV\cdot s^{-1}$ in increments of 50 $mV\cdot s^{-1}$. The voltage range was chosen to avoid both HER and OER, which are anticipated to occur at ca. –0.70 V and +0.53 V vs Hg/HgO (pH = 13.6), respectively. For an ideal capacitor, the charging current is a plateau, however for porous rough electrodes a non-zero resistive contribution leads to a sloped charging current. Therefore, for consistent calculations, the charging current, i_C, was determined at the center of the voltage window (–25 mV vs Hg/HgO) by taking the average of the absolute values of the anodic, $i_{C,\text{anode}}$, and cathodic, $i_{C,\text{cathode}}$, charging currents according to Equation (III.1),

$$i_C = \frac{\left|i_{C,\text{anode}}\right| + \left|i_{C,\text{cathode}}\right|}{2} \tag{III.1}$$

The slope of the charging current as a function of sweep rate plot is taken to be the capacitance, while the *y*-intercept is taken to be the baseline faradaic current. There is some increase in the *y*-intercept over time (**Figure III-3**) that can be attributed to H_2 oxidation. For reference, the equilibrium potential for H_2 oxidation at pH 13.6 is ca. –0.7 V vs Hg/HgO, so it follows that a small amount of background faradaic current would be recorded in this voltage region when H_2 is present in the GDE.

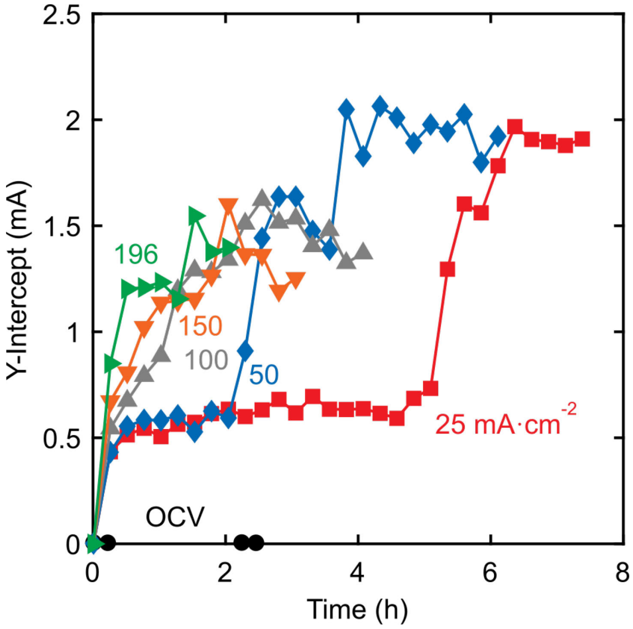

Figure III-3*: Y-intercept (mA) from capacitance fitting as a function of time and applied current density.*

2.6. Breakthrough Pressure Measurements

Breakthrough pressures was measured using a custom-built capillary pressure imbibition apparatus (**Figure III-4**). Samples with 7-mm diameters were punched from the parent materials and then sealed inside a custom sample holder with O-rings (McMaster-Carr, 1171N119) for each measurement. A syringe pump (Harvard Apparatus Pump 11 Pico Plus Elite) set at 7.5 µL·min^{-1} and loaded with two 5-mL BD (Becton Dickinson) syringes was used to apply DI water pressure to one side of the porous sample, while the gas side pressure matched that of the ambient air in the laboratory. Samples were oriented with MPLs contacting the liquid chamber. A USB camera (Celestron Handheld Digital Microscope Pro) was set to record time-lapse 2.1-megapixel images of the CFS side of the GDE. The images were used to determine the locations of the liquid droplets that penetrated the sample and emerged on the air side of the sample. Liquid-side pressure was measured with a pressure transducer with an operating range of 0–1 bar and a 4–20 mA current output (OMEGA, MMG015C1B3A0T3A5), transmitted via a National Instruments DAQ, and logged with LabView. The hydraulic head (8.5 mbar) due to the transducer position below the sample was subtracted from all measurements.

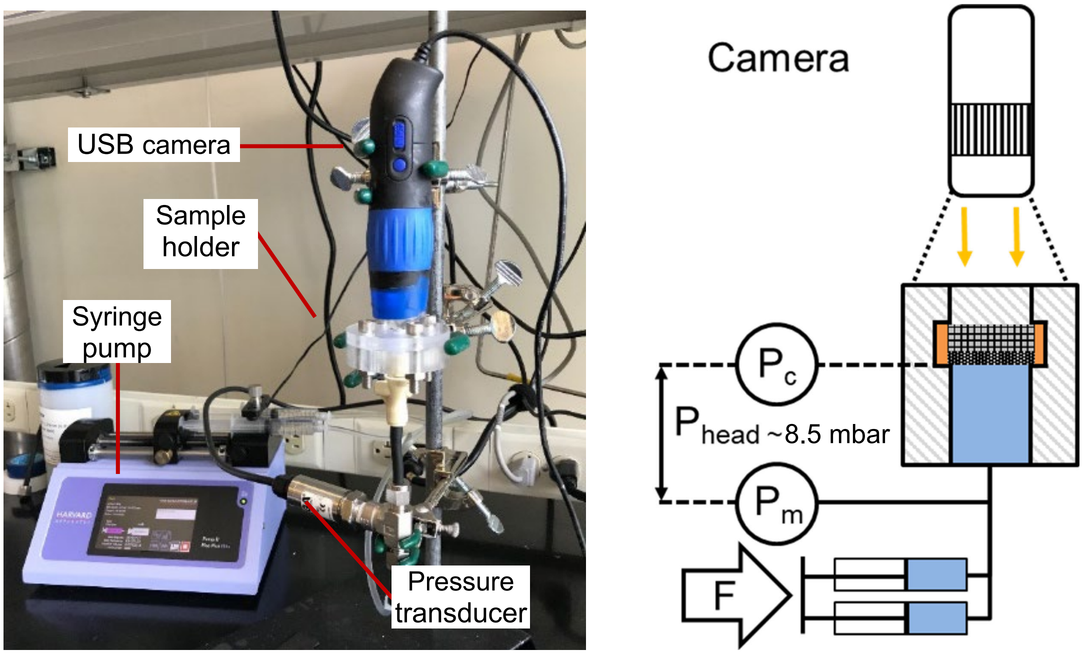

Figure III-4*: Image and schematic of the capillary pressure imbibition apparatus used to quantify breakthrough pressures. Capillary pressure (*P_C*) is computed by *$P_C = P_m - 8.5$* mbar.*

2.7. Scanning Electron Microscopy (SEM)

Surface images of the GDE components (**Figure III-2**) were taken using a Zeiss Merlin scanning electron microscope (SEM) equipped with an Inlens detector and operated at an accelerating voltage of 10 kV. Cross-section images (**Figure III-1**, **Figure III-11**, **Figure III-12**, and **Figure III-13**) were taken using a Zeiss Gemini Ultra55 SEM equipped with secondary electron (SE) and energy dispersive spectroscopy (EDS) detectors for imaging and qualitative elemental analysis, respectively. Elemental mapping (**Figure III-11**, **Figure III-12**, and **Figure III-13**) within a 512 × 400 pixel working area was performed using a 15-kV accelerating voltage, ca. 8.5 mm working distance, 60.0 μm aperture, and 200 μs dwell time. A total of 20 frames were used to generate each elemental map including carbon (C), oxygen (O), fluorine (F), potassium (K), and silver (Ag).

3. Results and Discussion

3.1. CO_2 Electrolysis and Capacitance Measurements

We employed the electrochemical reduction of CO_2 to CO on silver (Ag) as a model reaction due to its high selectivity, gaseous reactants/products, and robustness across multiple catalysts and cell configurations.[19,23,37,39,63–66] We evaluated catalyst-coated Freudenberg GDLs in a custom-built, gas-fed electrolyzer with a flowing electrolyte (**Figure III-1**). GDLs with MPLs (Freudenberg H23C6) were airbrush coated with an ink containing Ag nanoparticles ($\sim 0.5\ \mathrm{mg \cdot cm^{-2}}_{\mathrm{geo}}$) and an alkaline ionomer from Dioxide Materials™ to create GDEs with an active area of $2.55\ \mathrm{cm^2}_{\mathrm{geo}}$ as shown in the representative scanning electron microscopy (SEM) cross-section in **Figure III-1** (top). Freudenberg GDLs were selected for their mechanical flexibility and relatively defect-free MPL,[67] which we anticipated may improve the flooding tolerance of the cathode.

For all experiments, Ag-GDE cathodes were loaded into the cell shown in **Figure III-1** (bottom) along with a metallic nickel (Ni) anode and a mercury/mercury oxide (Hg/HgO) reference electrode to enable independent measurement of individual electrode polarizations. The cell geometry was originally developed by our group as a small-scale redox flow battery testing platform[62] and was recently adapted for a catalytic study of tin and tin oxide GDEs for electroreduction of CO_2 to formate in a gas-fed, flowing alkaline electrolyte configuration.[27] In this study, the cathode side was outfitted with a serpentine flow field machined from polymer-impregnated graphite and operated in gas-phase delivery mode. The serpentine flow field both provides electrical contact to the GDE and facilitates liquid removal by flowing gas, which allows experiments to continue until the advanced stages of electrode flooding. The anode side is outfitted with a titanium (Ti) current collector that is stable at the highly oxidizing potentials required for the oxygen (O_2) evolution reaction (OER). Evolved O_2 gas and unrecovered cathode gas bubbles are removed from the cell by the flowing electrolyte stream and vented to atmosphere. The cell assembly protocol is described in Appendix A. A schematic (**Figure III-27**) and images (**Figure III-28**) of the experimental setup along with a description of electrolyzer startup can be found in Appendix B.

Pure (99.999%) CO_2 was fed at 20 sccm to the CFS-side of the Ag-GDE. An alkaline potassium hydroxide electrolyte (KOH, pH = 13.6) was chosen instead of a neutral to mildly alkaline pH potassium carbonate (K_2CO_3)/bicarbonate ($KHCO_3$) electrolyte to minimize solution resistance across the full cell.[10] Higher pH also enables lower overpotentials for converting CO_2 to CO and/or hydrocarbons.[29,37] To control the effects of carbonation, which consumes up to 5% of the feed CO_2 at open circuit voltage (OCV) (Figure III-5), the electrolyte stream was not recirculated but rather was passed once through the cell at 1 $mL \cdot min^{-1}$. These operating conditions mirror those commonly reported in the field and, therefore, illuminate the challenges of GDE durability in present-day flowing alkaline electrolyte configurations.[36,37,59,63,68–71]

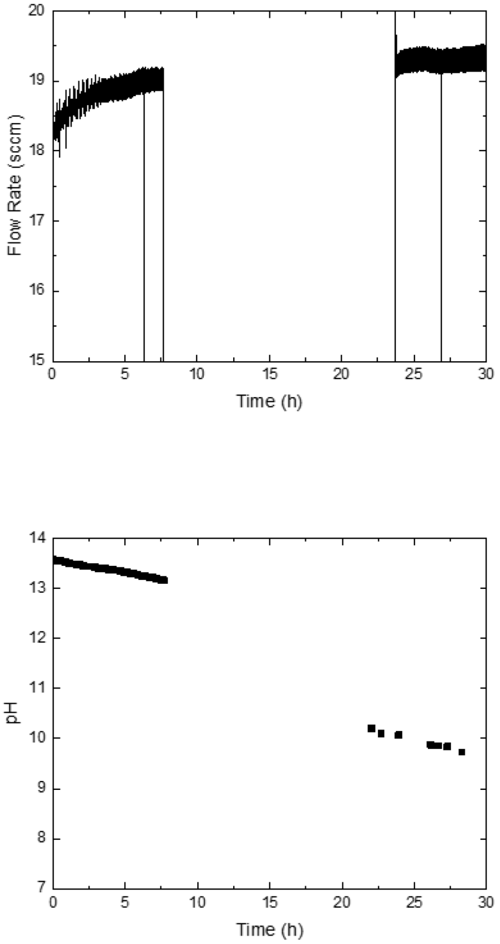

Figure III-5*: Visualizing trans-GDE carbonation by tracking the CO_2 mass flow rate over time for an uncoated GDE held at OCV. For this test, 55 mL of 1 M KOH solution was recirculated through the reactor at a flow rate of 1 mL·min^{-1}. We plot the mass flow rate of CO_2 (units of sccm) and the pH of the electrolyte as a function of time. The nominal feed mass flow rate is close to 20 sccm, but the mass flow meter records a maximum of ca. 19.5 sccm. We initially observe a lower flow rate (ca. 18.5 sccm) due to carbonation. Over time, the pH trends towards neutral and the CO_2 flow rate approaches a maximum of 19.5 sccm. By subtracting the initial flow rate from the maximum, we can estimate a per-pass carbonation rate from the initial CO_2 consumption rate that by* $\frac{\mathbf{19.5-18.5}}{\mathbf{19}}\mathbf{.5 = 0.051 \approx 5}\%$.

Each experiment was divided into 15-minute segments that are composed of a high-frequency resistance measurement (10 s) to determine solution resistance between the cathode and the Hg/HgO reference electrode, a series of voltammetric sweeps between -100 and +50 mV vs Hg/HgO to estimate cathode EDLC (50 s total), and, finally, a galvanostatic hold (14 min 15 s).

At the end of every time segment, the effluent gas from the cathode half-cell was sampled by a gas chromatography (GC) system. The effluent electrolyte was not analyzed for the presence of liquid-phase products because Ag electrocatalysts are anticipated to generate primarily gaseous CO and H_2 at the conditions tested.[19,20]

Constant current electrolysis, i.e., galvanostatic, experiments were run to probe the effect of current density on CO mole fraction in the effluent gas over time. An advantage of galvanostatic operation, as compared to potentiostatic operation, is that the total product gas generation rate should remain constant because both reaction products, CO and H_2, require 2 moles of electrons per mole of product as shown in the following half-reaction equations, Equation (III.2) and Equation (III.3), that are also provided in Appendix C with the anode half-reaction and full cell reactions,

$$\mathrm{CO_2(aq) + H_2O(l) + 2\ e^- \rightarrow\ CO(g) + 2\ OH^-(aq)}\ (E^0 = -0.10\ \mathrm{V\ vs\ RHE}) \qquad \text{(III.2)}$$

$$\mathrm{2\ H_2O(l) + 2\ e^- \rightarrow\ H_2(g) + 2\ OH^-(aq)}\ (E^0 = 0.00\ \mathrm{V\ vs\ RHE}) \qquad \text{(III.3)}$$

The graphical representation of gas-fed CO_2 electrolysis shown in **Figure III-6a** depicts both desired and flooded operational states within a Ag-GDE. As described earlier, nominally hydrophobic GDLs are used to limit electrolyte intrusion into the gas stream, while maintaining CO_2 flux. However, once electrolyte floods the GDE the liquid diffusion length for CO_2 to the CL increases to the point that the CO_2 flux cannot support the current demand for CO production and HER becomes favored throughout the wetted portions of the electrode.

The evolution of electrode performance as a function of time across a series of current densities (25, 50, 100, 150, and 196 $\mathrm{mA{\cdot}cm^{-2}}$) is shown in **Figure III-6b**. Across all current densities tested, the peak CO mole fraction was >90%, which agrees with performance from previous reports using

Ag-catalyzed GDEs.[37,63] After the first 15 min of operation, notable differences emerge when applying different current densities. For low to moderate current densities there is a period of steady CO production, ranging from 1–5 h and inversely dependent on the magnitude of the applied current density, followed by a catastrophic failure evinced by a rapid decrease in the CO product mole fraction, while for the higher current densities of 150 and 196 $mA \cdot cm^{-2}$, the electrode transitions from CO to H_2 production within 30 min of operation. The cathode potential grows more negative during stable operation but becomes more positive as the dominant product transitions CO to H_2 (**Figure III-29**) and more of the GDE carbon becomes wetted by electrolyte. As the accessible area for HER increases, the cathode potential is anticipated to decrease in magnitude. The HFR traces do not show a clear trend among the current densities tested (**Figure III-30**).

EDLC (hereafter referred to as capacitance) measurements provide additional insight into the cathode state as the product gas mole fraction transitions from CO- to H_2-rich. As shown in **Figure III-6c**, we observe that the currents from cyclic voltammetry increase over time, indicating changes at the electrode-electrolyte interface. After extracting and processing the capacitive currents at each time point, we plot the capacitance as a function of time in **Figure III-6d**. We find that when we hold the cell at OCV for at least 8 h as a zero-current baseline and observe relatively steady capacitance between 0.5–1.0 mF over time, indicating that the electrode-electrolyte interface is stable before electrolysis begins. After passing faradaic current through the cell for 15 min, the capacitance increased to 1.5–2.0 mF for all current densities. Similar to the product composition traces in **Figure III-6b**, we observe steady capacitance for low to moderate current densities until a sudden increase that coincides with performance failure.

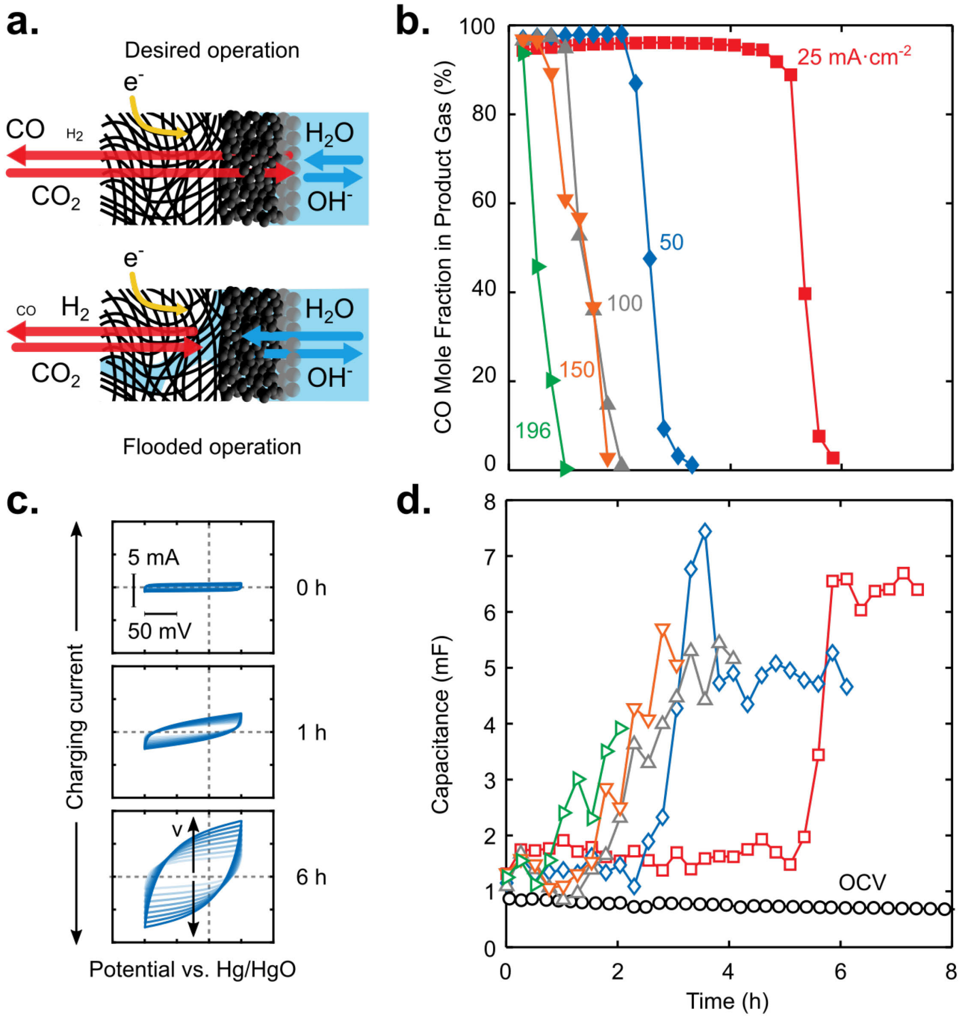

Figure III-6*: Galvanostatic CO_2 reduction using a gas-fed flowing electrolyte reactor. (a) GDE flooding limits CO_2 flux to the catalyst layer and promotes HER. (b) Increasing current densities (mA·cm^{-2}) applied to Ag-GDEs are associated with a decreasing CO mole fraction in the product gas mixture (%). (c) As operation proceeds the capacitive currents extracted from cyclic voltammetry every 15 min increase (d) Sudden catastrophic losses in CO production qualitatively correlate inversely with sharp increases in capacitance (mF) across all current densities.*

In general, we observe a qualitatively inverse correlation between CO mole fraction in the product gas and cathode capacitance (**Figure III-31**). We also see that changes in capacitance lag behind changes in CO mole fraction by at least 15 min. This delay coupled with the observation that the capacitance subtly decreases prior to each catastrophic flooding event suggests that liquid electrolyte penetration into the GDE may not be the sole cause of performance failure.

From the collection of traces in **Figure III-6b** and **Figure III-6d**, we see that the rate of GDE failure is positively correlated with increasing current. Exploring the possibility that faradaic processes influence the time to failure, we plot CO mole fraction (**Figure III-7a**) and capacitance (**Figure III-7b**) as a function of the cumulative charge passed (Q) in **Figure III-7**, where $Q = I \times t$, I is absolute current (mA), and t is time passed (h). While reporting electrochemical data as a function of charge passed (units of mAh), as opposed to time, is more commonly associated with energy storage devices, in the present context, quantifying charge passed until failure may provide insight into the "capacity" of the GDE. Interestingly, we observe a collapse of the CO mole fraction data onto a single sigmoidal curve (**Figure III-7a**), with especially good agreement at low charges (ca. 0–400 mAh), suggesting that current-dependent changes to the electrolyte (e.g., increased cathode alkalinity leading to accelerated carbonation), may influence the rate of flooding. Furthermore, the capacitance data (**Figure III-7b**) reveals a similar onset charge to flooding across experiments, although there is scatter at higher charges (> 400 mAh) after the onset of product changeover. The capacitance data, plotted either as a function of time (**Figure III-6d**) or charge (**Figure III-7b**), do not appear to approach a consistent maximum value at the advanced stages of electrode failure. We reason that flooding pathways are stochastic in both the MPL and CFS and that the extent of observable GDE saturation resulting from electrolyte permeation throughout the CFS varies due to microstructural differences between individual electrodes. Enlarged plots of the **Figure III-7a** and **Figure III-7b** data from 0–500 mAh (**Figure III-32**) along with a description of the sigmoid function used for qualitatively fitting each data set are provided in Appendix D.

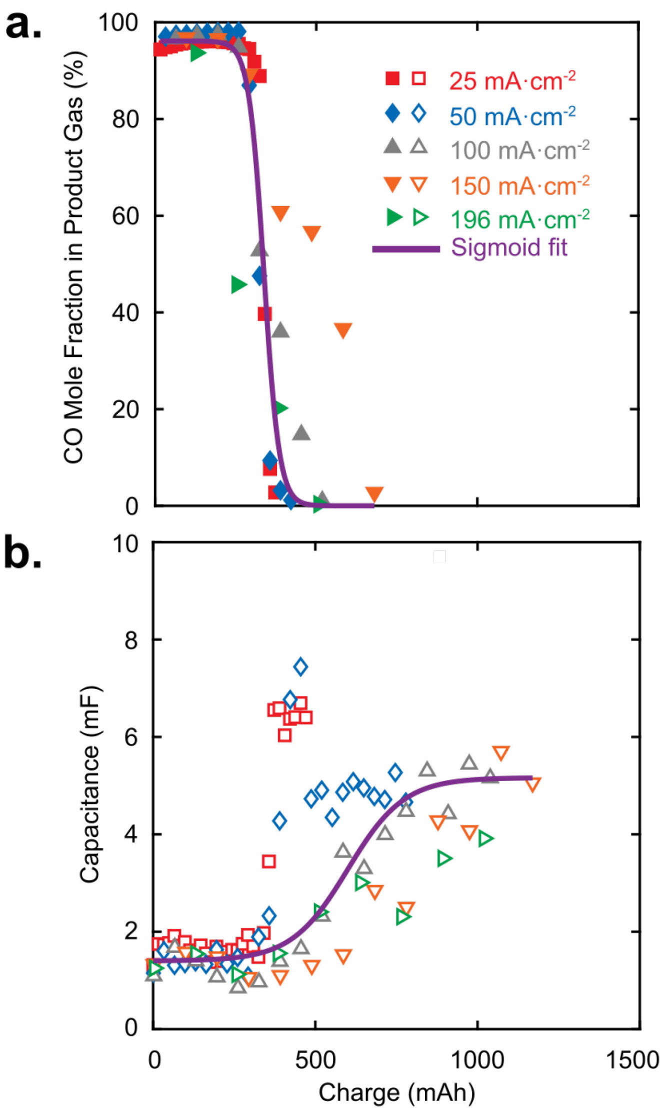

Figure III-7: *Current-associated GDE failure. Plotting (a) CO mole fraction in the product gas (%) and (b) capacitance (mF) as functions of cumulative charge (mAh) results in some collapse of the performance data. This indicates that faradaic processes, i.e., CO_2 reduction and HER, likely contribute to the onset of GDE failure.*

The chemical and physical mechanisms that underlie these trends are not yet fully understood and, to our knowledge, have neither been extensively reported nor discussed in the context of gas-fed CO_2 electrolyzers. Although GDE flooding may be caused by a variety of phenomena (e.g., macroscopic pressure imbalances, evolutions in surface wettability, evaporation-condensation), for this study, we focus on the connections between carbonation and flooding since we consistently observe salt crystallites on the backside of flooded GDEs and at the inlet of the cathode flow field (**Figure III-8**). Specifically, we postulate that the transition from CO to H_2 production within GDEs is driven by phenomena that occur in parallel with electrolysis but manifest and negatively impact performance at different rates.

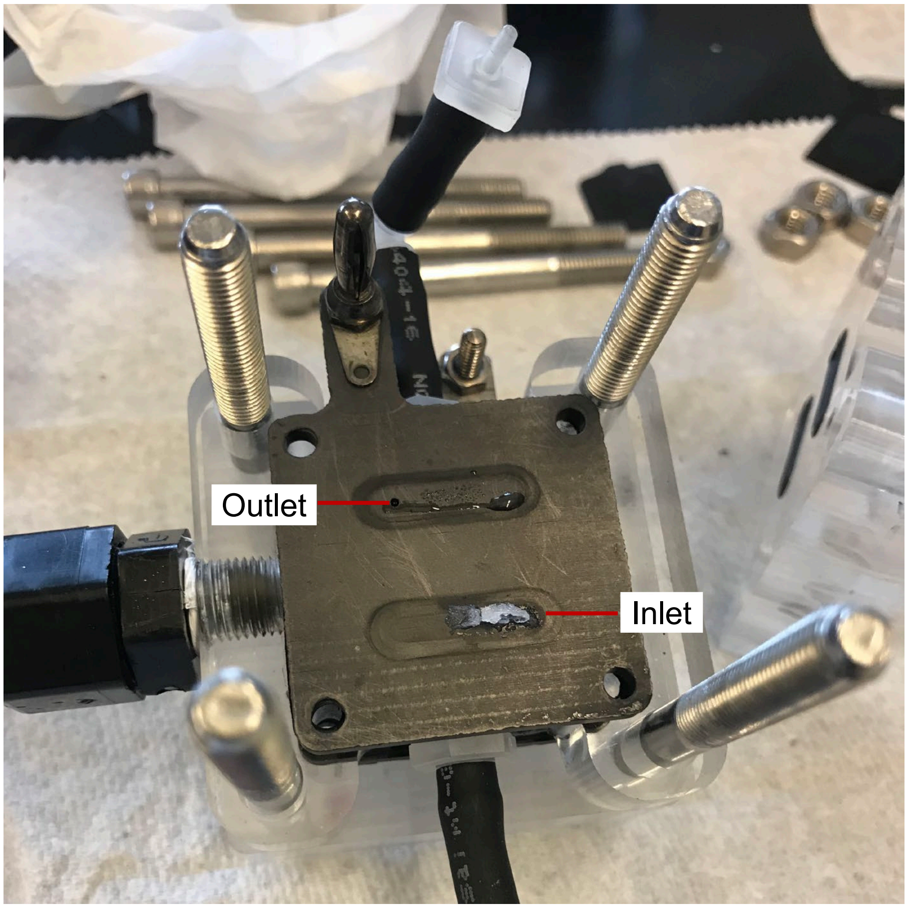

Figure III-8*: Salt near the inlet of the serpentine flow field and liquid at the outlet after GDE flooding and failure.*

The first phenomenon is electrolyte carbonation, which occurs wherever dissolved CO_2 and hydroxide (OH^-) ions co-exist. This effectively includes all electrolyte-wetted regions of the Ag-GDE. Indeed, such CO_2 chemisorption is deliberately leveraged in direct air capture processes to selectively remove dilute CO_2 from the atmosphere.[72] First, CO_2 reacts with one OH^- to form a bicarbonate (HCO_3^-) intermediate, then the newly formed HCO_3^- reacts with a second OH^- to produce one carbonate (CO_3^{2-}) and one water (H_2O) molecule as shown by Equations (III.4) and (III.5),

$$CO_2(aq) + OH^-(aq) \rightarrow HCO_3^-(aq) \tag{III.4}$$

$$HCO_3^-(aq) + OH^-(aq) \rightarrow CO_3^{2-}(aq) + H_2O(l) \tag{III.5}$$

A kinetic study reported by Schulz et al. shows that the forward rate for Equation (III.5) is faster than that for Equation (III.4), so most CO_2 that reacts with the OH^--rich electrolyte is effectively converted to CO_3^{2-}.[73] We see that this parasitic loss is initially overcome to sustain high selectivity for CO production, likely because CO_2 is fed in stoichiometric excess. However, carbonation of the electrolyte not only increases single-pass conversion to the undesired products of HCO_3^- and CO_3^{2-}, but also indirectly slows CO_2 reduction kinetics by initiating an unfavorable shift towards more neutral pH.[69] Furthermore, galvanostatic operation ensures that HER, which also produces OH^- ions according to Equation (III.3), will substitute for any lost CO_2 reduction within the CL. Therefore, as the rate of CO_2 electrolysis decreases, the persistently high local pH due to HER in the presence of any excess CO_2 will accelerate the carbonation rate in a positive feedback loop. This performance drift is mirrored by negative/cathodic drift in the electrode potential trace that emerges before the onset of catastrophic flooding (**Figure III-29**). When operating galvanostatically, such increases to the cathode potential can be attributed to some combination of increased kinetic overpotential due to local electrolyte neutralization and increased CO_2 mass transport resistance as liquid blocks gas diffusion pathways.

The second phenomenon is the emergence of physical blockages within the GDE that inhibit CO_2 flux and promote HER. Both solid (i.e., salt crystallites) and liquid (i.e., electrolyte) species emerge on the gas side of the cathode flow field (**Figure III-8**) once liquid electrolyte breaks through the GDE. After partially filling the CFS, liquid electrolyte is trapped until sufficient convection is applied to physically displace the droplets or until the water evaporates leaving behind salt crystals that hinder gas flux to the CL.[74] As the pure CO_2 feed contacts the electrolyte, carbonation together with water evaporation synergistically increase the likelihood of precipitation because $KHCO_3$ (3.62 mol/kg H_2O) and K_2CO_3 (8.03 mol/kg H_2O) have lower solubilities than KOH (21.57 mol/kg H_2O) on a molal basis.[10] Furthermore, both hydrated and dehydrated alkali carbonates in the solid phase (e.g., K_2CO_3) can also consume additional CO_2 to produce bicarbonates (e.g., $KHCO_3$) per the following equations,[75]

$$K_2CO_3 \cdot 1.5\ H_2O(s) + CO_2(g) \leftrightarrow 2\ KHCO_3(s) + 0.5\ H_2O(g) \tag{III.6}$$

$$K_2CO_3(s) + CO_2(g) + H_2O(g) \leftrightarrow 2\ KHCO_3(s) \tag{III.7}$$

As our ability to measure species concentrations at relevant length scales (~µm) within GDEs is limited, precise accounting of chemical and electrochemical reaction dynamics is difficult to achieve experimentally. Nonetheless, due to the mass action reflected by Equations (III.2)–(III.7) we anticipate that complex dynamic equilibria between ionic species emerge near the CO_2-electrolyte interface during electrolysis, depending on the operating conditions and the movement of species within the electrode microstructure.

The collapse of the performance data when plotted as a function of cumulative charge (**Figure III-7**) suggests that the electrode has a charge threshold that, if exceeded, will lead to failure. Charge directly translates to newly formed OH^- ions that become available for carbonation reactions (Equations (III.4) and (III.5)) near the gas-liquid interface of the GDE. By considering the electrolysis data in **Figure III-6** and **Figure III-7** together with the stoichiometry of Equations

(III.2)–(III.5), we can infer that carbonation rate at the cathode increases with current density. Indeed, electrochemically-mediated CO_2 separation schema leveraging this phenomenon have been proposed.[76–78] Accordingly, we hypothesize that GDE failure is initiated by carbonate salt precipitation followed by rapid electrolyte percolation through the crystallites which retards CO_2 transport sufficiently as to necessitate H_2 generation via water splitting to meet imposed galvanostatic requirements. A similar electrode degradation mechanism has previously been proposed for air-fed, flowing electrolyte alkaline fuel cells.[79] This hypothesis is further supported by results from fundamental porous media evaporation studies, which show that once salt crystallites effloresce at the MPL-CFS interface, they can pump water through the MPL via capillary action due to their hygroscopic character.[80]

Managing the parasitic capture of CO_2 by aqueous electrolytes and the precipitation of carbonate salts, thereafter, may benefit from electrode-level models that can predict precipitation events in response to selected operating conditions such as the ionic strength of the electrolyte, the bulk electrolyte pH, the pH of the electrode-electrolyte interface, and the water vapor content in the feed gas.[81] Given the diversity of porous media available, the characteristic behavior for the Freudenberg GDLs presented here may not be representative of or predictive for all GDEs, but the underlying chemical and physical phenomena associated with CO_2 electrolysis, OH^- generation, and carbonation are expected to persist for all electrodes and for all mild to strong alkaline aqueous electrolytes used in a gas-fed, flowing electrolyte configuration. For the remainder of this work, we seek to validate the proposed carbonate-driven flooding mechanism and to explore the possibility of restoring electrode functionality after failure.

3.2. Capillary Pressure Breakthrough Measurements

To explore the extent to which the magnitude of the faradaic current impacts the severity of electrode failure, we characterized the post-test ex situ flooding resilience of Ag-GDEs used in the electrolysis experiments. We employed capillary pressure imbibition with deionized water to quantify and map the apparent loss of hydrophobicity of Ag-GDE samples. Water is an appropriate test liquid for these experiments because the KOH solution used in the electrolysis experiments (ca. 5 wt%) has similar density ($1.05\ \mathrm{g{\cdot}cm^{-3}}$) and surface tension ($0.075\ \mathrm{N{\cdot}m^{-1}}$) to water ($0.99\ \mathrm{g{\cdot}cm^{-3}}$, $0.073\ \mathrm{N{\cdot}m^{-1}}$) at room temperature (20 °C).[82] Capillary pressure imbibition is a method by which gas-liquid pressure differences ($P_L - P_G$) are applied across a porous material to induce intrusion or withdrawal of liquid. It has been utilized extensively to characterize the wettability/saturation characteristics of PEFC cathode GDLs.[83–86] In the CO_2 electrolysis field, carbon-based GDLs with MPLs adopted from PEFCs have been understood to be macroscopically hydrophobic and, therefore, are considered suitable candidates for catalyst scaffolds and gas-liquid barriers.[87] However, because carbonate salts are hygroscopic, any embedded crystallites left behind after electrolyte flooding events would decrease the resilience of the electrode to liquid intrusion.

To quantify the possible effects of electrolysis on apparent electrode hydrophobicity, we measure the breakthrough pressure of water through GDLs and GDEs with the MPL (if applicable) facing the water in a custom-designed apparatus (**Figure III-4**) inspired by analogous setups in the literature.[74,85,88,89] First, circular samples of pristine carbon-paper GDLs with (Freudenberg H23C6) or without (Freudenberg H23) MPLs were screened as comparisons for the Ag-GDE samples. As reported in the two leftmost data in **Figure III-9a**, the average breakthrough pressure ($N = 5$) for the CFS (**Figure III-2a**) is (23 mbar). After adding an MPL (**Figure III-2b**) to the

CFS, the average breakthrough pressure (*N* = 5) increases by an order of magnitude (642 mbar). Next, the same Ag-GDEs used for the experiments reported in **Figure III-6**, were screened post-test. Prior to imbibition, Ag-GDE samples were removed from the electrolysis cell, thoroughly rinsed with deionized water to remove any surface salts and excess electrolyte, and then left to dry in ambient laboratory air. For these electrodes we expect the breakthrough pressures to decrease in the base case due to the application of a Ag CL that includes hydrophilic ionomer (**Figure III-2c**), which may seep into the MPL during airbrush deposition (**Figure III-10**).[90] The low surface tension of organic-aqueous mixtures that constitute the carrier solvents for catalyst inks may be responsible for the formation of hydrophilic regions within the GDE near the CL-MPL interface. However, embedded crystallites are anticipated to have a more drastic effect on flooding resilience (vide supra). Indeed, the breakthrough pressures for these samples (*N* = 2 for OCV, 25, 100, 150, 196 mA·cm^{-2} and *N* = 1 for 50 mA·cm^{-2}) decrease to less than 100 mbar, except for the 25 mA·cm^{-2} samples, which retain more of the breakthrough resistance. The 196 mA·cm^{-2} samples exhibit the lowest average breakthrough pressure (22 mbar), which is equivalent to that of the CFS in isolation (23 mbar). The samples held at OCV retain an average breakthrough pressure (446 mbar) that is closer to a pristine GDL with MPL than to any of the post-run samples, suggesting that immersing GDEs in electrolyte without passing faradaic current may not compromise the hydrophobicity, at least not at these experimental timescales.

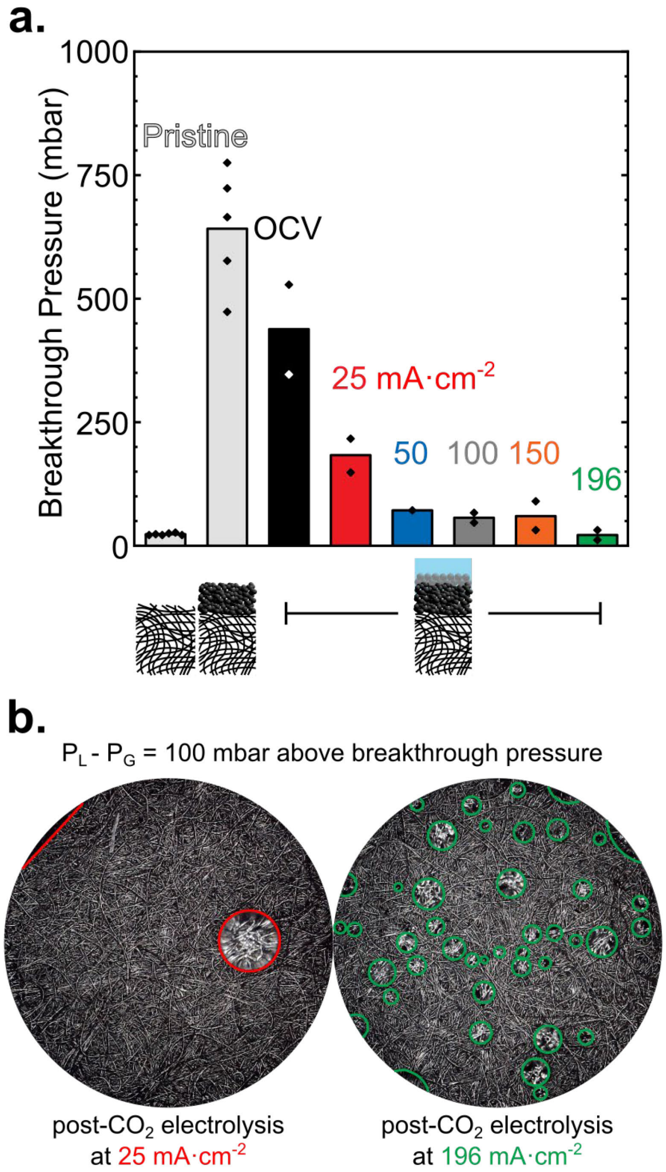

***Figure III-9**: Capillary pressure breakthrough pressure results. (a) Breakthrough pressures for Ag-GDEs decrease with increasing current density (25–196 mA cm^{-2}) and approach the value for the bare CFS (H23), while the Ag-GDE held at OCV retains breakthrough resistance that is closer to the value for uncoated GDL with an MPL (H23C6). (b) Representative images of the CFS while applying a capillary pressure 100 mbar in excess of the breakthrough point to the MPL side of Ag-GDEs demonstrate the greater extent of liquid percolation for Ag-GDEs after operation at disparate current densities.*

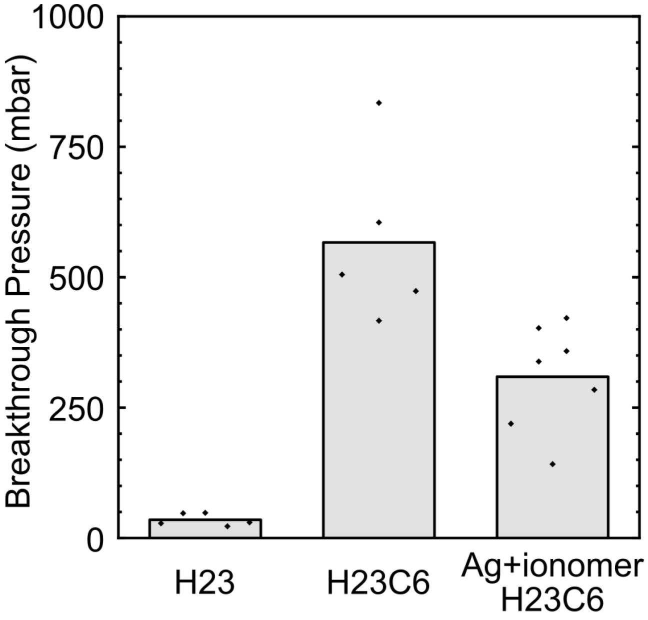

Figure III-10*: Average breakthrough pressure for H23C6 decreases after applying a CL that includes Ag nanoparticles and ionomer. Breakthrough pressure for H23 is included for comparison against a fibrous GDL material without an MPL. The data reported here were collected with a separate but similarly prepared Ag-GDE batch from the ones used in the primary data set.*

The lower breakthrough pressures for used GDE samples could be explained by either irreversible mechanisms, such as chemical degradation of PTFE, or reversible mechanisms, such as efflorescent salt deposits within the GDL. Although PTFE degradation has been reported under cathodic potentials in aqueous electrolyte,[91] additional spectroscopic, microscopic, and chemical analyses may be required in the future to evaluate the extent to which this failure mode impacts performance. Strengthening the hypothesis of carbonation-accelerated electrode failure, is the observation of well-distributed liquid breakthrough points on the CFS that likely correspond to the locations of salt deposits left behind by electrolyte flooding and carbonate precipitation. Representative CFS images under positive capillary-pressure conditions are shown in **Figure III-9b**. Although we observe a diminishing resilience to the initial liquid breakthrough with increasing current density, water eventually percolates through multiple points simultaneously at sufficiently high capillary pressures across all samples. The carbonate-driven flooding mechanism is quantitatively supported by the observation that flooding resistance of each sample generally decreases with increases in applied current density. This aligns with the notion that higher current density produces higher alkalinity and, therefore, increased carbonation within the wetted regions of an electrode (vide supra). Because we observe that water eventually percolates at multiple locations for all post-test samples, we can also infer that this failure mechanism is common to all Ag-GDEs used in this work.

We confirm the presence of crystallized salts in the pores of flooded GDEs by combining cross-sectional SEM images with elemental mapping of carbon (C), Ag, fluorine (F), potassium (K), and oxygen (O). We see from maps of the pristine (**Figure III-11**), post-test 25 mA·cm^{-2} (**Figure III-12**), and post-test 196 mA·cm^{-2} (**Figure III-13**) samples that the K signal conformally covers the MPL-regions of both flooded samples, but not the pristine sample. Discrete K nodules are visible for the 196 mA·cm^{-2} sample, but not for the 25 mA·cm^{-2} sample, suggesting that the carbonation rates, which vary with applied current density, impact the size, location, and likely growth dynamics of the salt deposits. Overall, we see from both imaging and ex situ breakthrough pressure measurements that the favorable barrier properties of the MPL are nullified by the presence of embedded salts left behind after electrolyte flooding. To complement the findings from this ex situ study, we sought to test our hypothesis of carbonation-driven flooding by probing the reversibility of electrode failure.

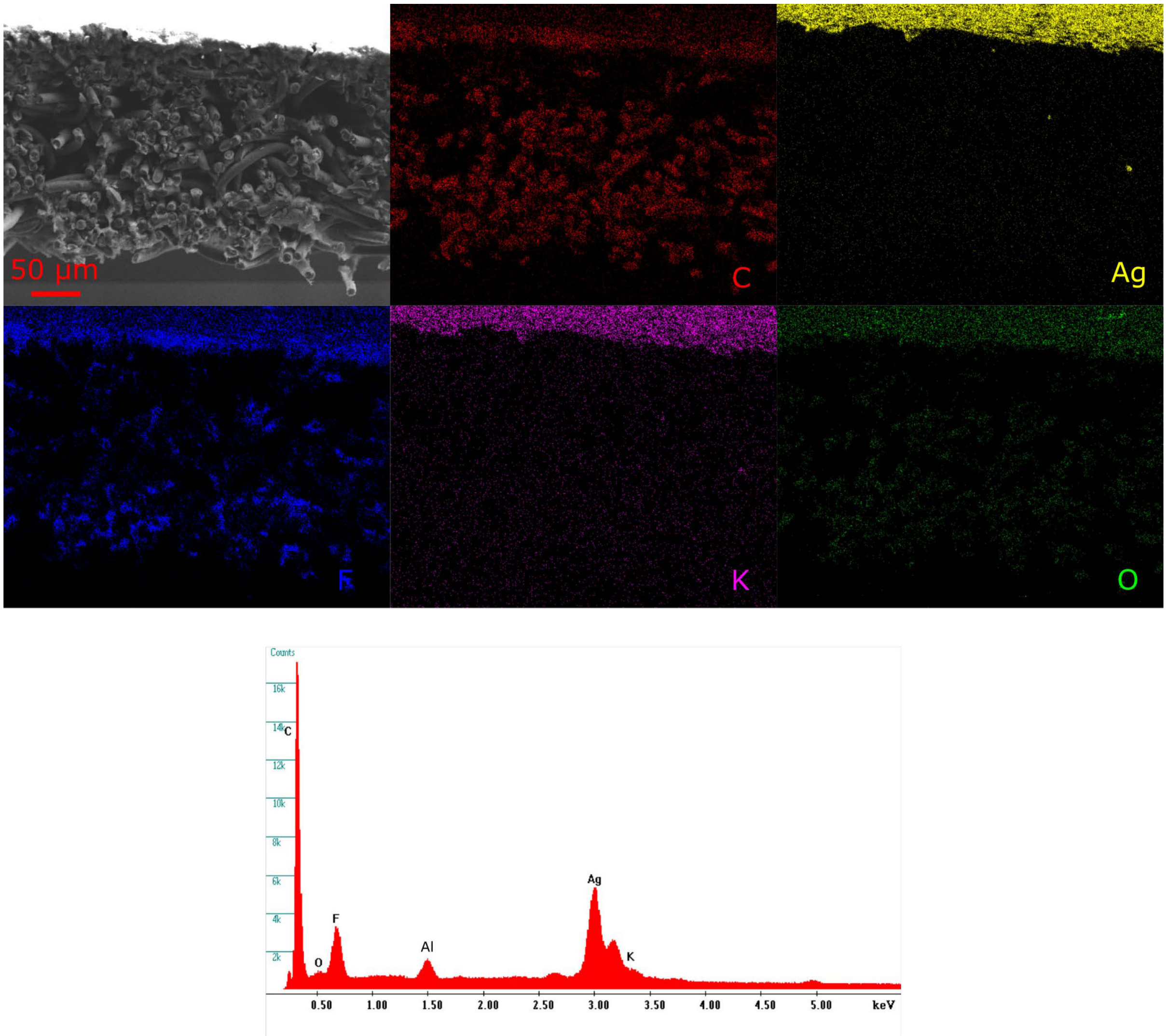

Figure III-11*: Pristine Ag-GDE cross-section SEM image with EDS map and spectrum. The potassium (K) signal that coincides with Ag on the top surface of the sample can be explained by the proximity to the Ag peak close to 3.20 keV. The aluminum (Al) peak comes from the SEM sample holder.*

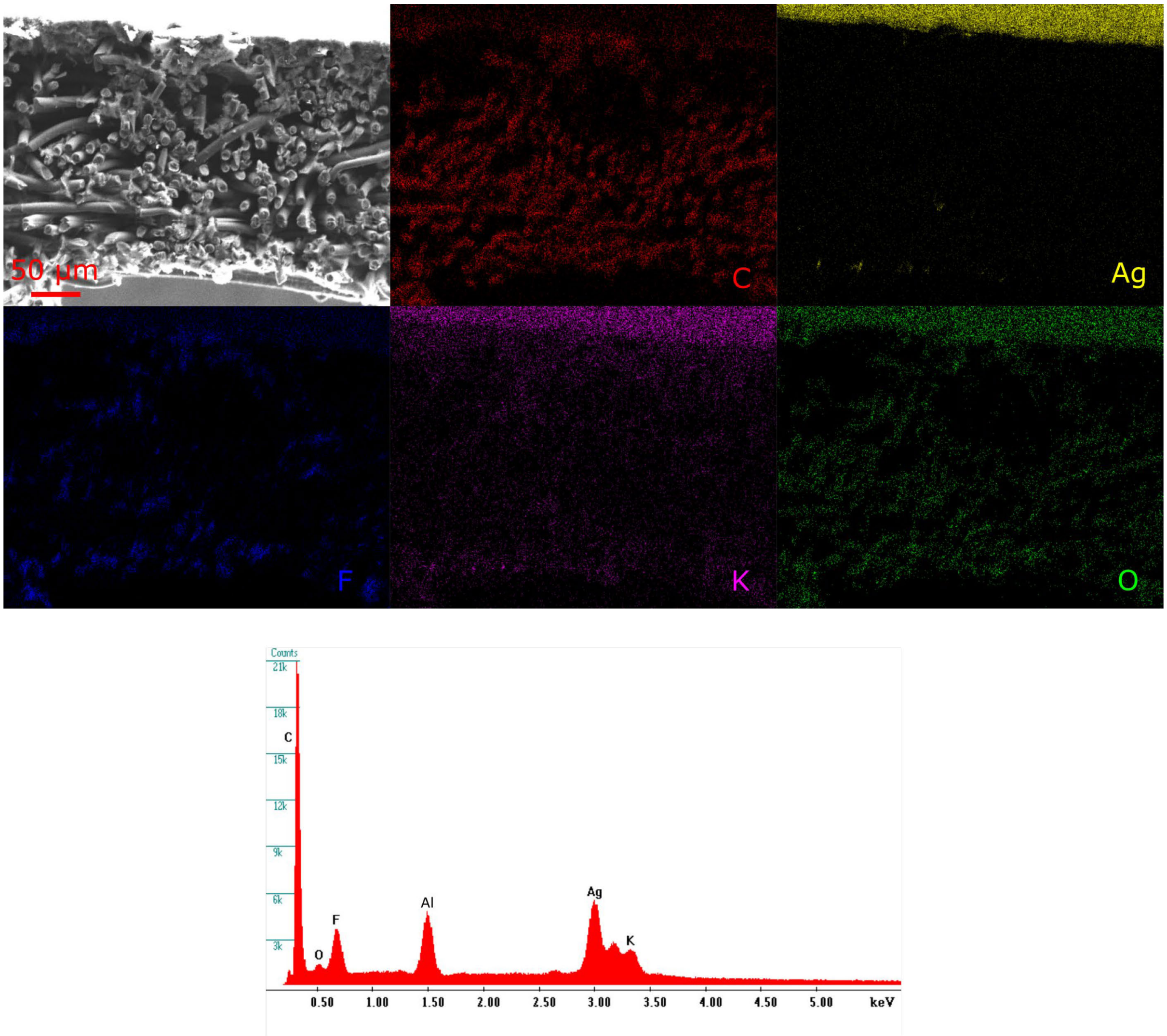

Figure III-12: *Post-test Ag-GDE (25 mA·cm^{-2}) cross-section SEM image with EDS map and spectrum. The potassium (K) signal that coincides with Ag on the top surface of the sample can be explained by the proximity to the Ag peak close to 3.20 keV. The aluminum (Al) peak comes from the SEM sample holder.*

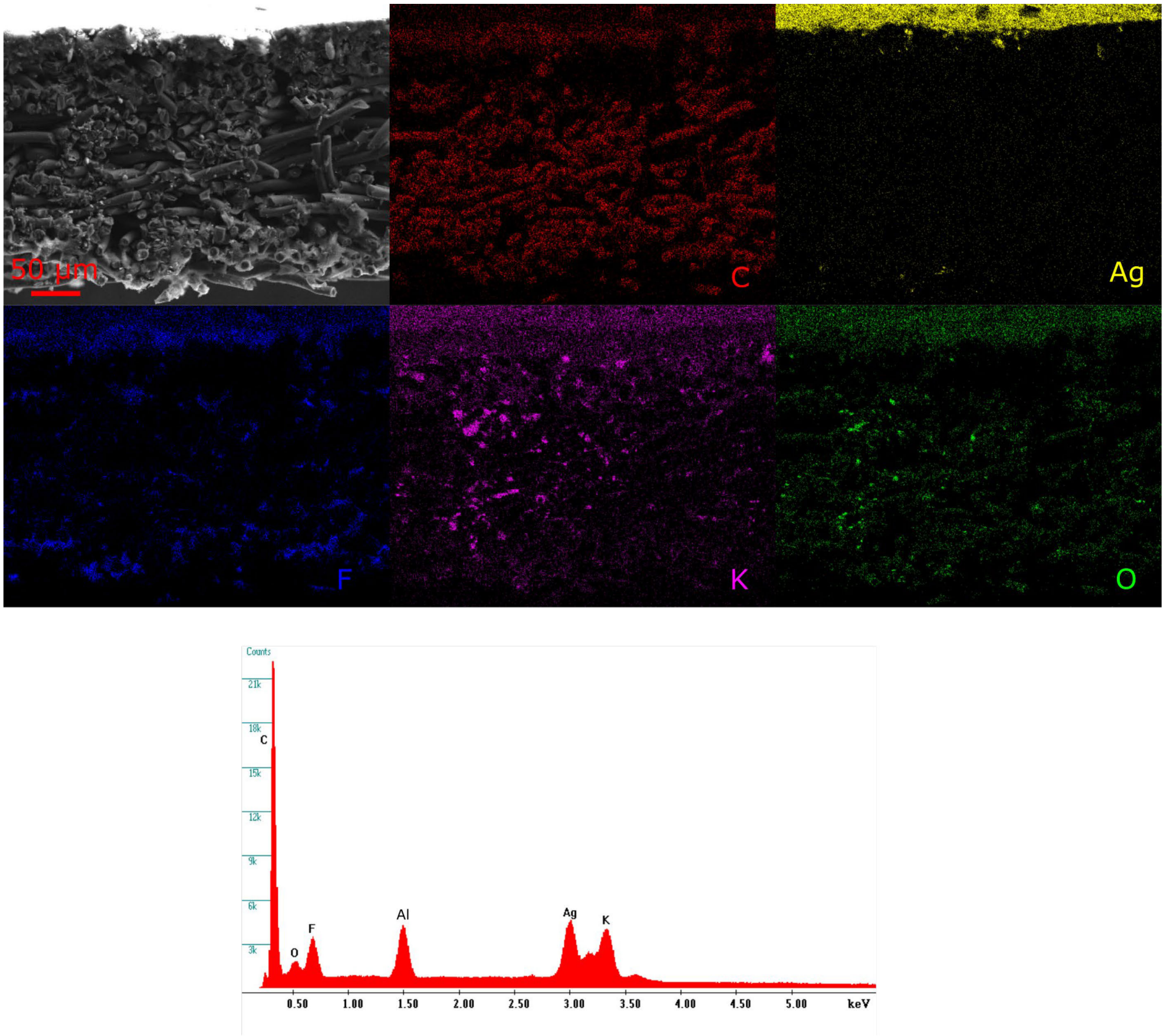

Figure III-13: *Post-test Ag-GDE (196 mA·cm*$^{-2}$*) cross-section SEM image with EDS map and spectrum. The potassium (K) signal that coincides with Ag on the top surface of the sample can be explained by the proximity to the Ag peak close to 3.20 keV. The aluminum (Al) peak comes from the SEM sample holder.*

3.3. Gas Diffusion Electrode Recovery

Based on the results from both electrolysis (**Figure III-6** and **Figure III-7**) and breakthrough pressure (**Figure III-9**) measurements, we explored the possibility of recovering electrode performance through either in situ OCV holds or ex situ electrode restoration. If periodic restoration is required, then in situ recovery facilitated by switching to OCV would be the more appealing operating strategy because it avoids cell disassembly.

First, we operated the cell galvanostatically at 50 mA·cm^{-2} for 1 h at the same conditions as the previous electrolysis experiments (**Figure III-6**) before switching the cell to OCV for an extended hold. The peak CO mole fraction (**Figure III-14a**) remains over 95% during the initial 1-h galvanostatic period, confirming that substantial flooding has yet to occur. This is also supported by the capacitance trace, which shows that the GDE is stable during the initial hour and for the next 48 h while at OCV. During this extended hold, the gas outlet stream is not flooded with electrolyte, but some condensation is visible through the acrylic backing plate near the gas outlet. The moisture may either come from evaporation of water in the electrolyte or from water liberated as a product of the HCO_3^- to CO_3^{2-} reaction at the gas-electrolyte interface as shown in Equation (III.5). Regardless of the source, if not managed appropriately, moisture buildup in the gas channel without the passage of current is anticipated to be problematic for electrolyzer longevity. After current is restored, the performance is only stable for ca. 30 min before catastrophic failure. The total time on stream before failure was ca. 2 h of galvanostatic operation when including a current pause, which is somewhat shorter than the uninterrupted experiment (**Figure III-6**) that lasted around 2.5 h. Even though there are no detectable changes to the cathode capacitance after 1 h of electrolysis, it appears that carbonation compromises the electrode performance even when the cell is held at OCV. Because carbonation persists in the absence of current, in situ restoration strategies like the one explored here may ultimately be ineffective.

Depending on the frequency of intervention, ex situ electrode rinses may be a viable approach for removing salt from porous electrodes. To this end, we tested if rinsing and/or drying GDEs could recover the same CO_2 conversion performance as pristine ones. Previous works report rinsing GDEs after CO_2 reduction to restore electrochemical activity, but the wetted state of the electrode during operation beyond the achievable current density and faradaic efficiency was not discussed.[40,92,93] Continuing with the same electrolysis protocol, we started by running experiments at 50 mA·cm^{-2} until the onset of GDE failure, defined here as the inflection in the CO mole fraction trace. Next, we shut down the electrolyzer, removed the Ag-GDE, and either (1) dried or (2) rinsed and dried the electrode before reinstalling it in the cell. First, we observe from the CO mole fraction and capacitance traces in **Figure III-14b** that vacuum drying alone results in GDE failure within 30 min of starting the subsequent run. After partial flooding we observe electrolyte measured to be ca. pH 10, via a pH test strip (0–14 scale, VWR International), on the CFS closest to the gas inlet of the serpentine flow field as indicated by the darker regions of a representative image (**Figure III-14c**). In this pH range, the electrolyte likely contains both $KHCO_3$ and K_2CO_3.[73] The liquid distribution on the CFS suggests a non-uniform permeation rate across the electrode area. Notably, flooding is concentrated where the CO_2 concentration is the highest and the flowing gas humidity is lowest, which aligns with conditions that most strongly shift chemical and physical equilibria towards carbonation and precipitation of K_2CO_3/$KHCO_3$ crystallites.

Next, we used the same electrolysis conditions but rinsed the GDE with deionized water after each run and prior to vacuum drying. As shown in **Figure III-14d** we observe that rinsing and drying a partially flooded GDE between each run restores much of the performance. However, the maximum CO mole fraction continually decreases, albeit by relatively minor amounts on subsequent runs, demonstrating that each rinse/dry cycle does not fully restore peak performance. These observations agree with a recent report by Endrődi et al. for a multi-cell CO_2 electrolyzer stack study in which they injected water into cathode gas stream to wash away K_2CO_3 precipitates that block CO_2 flux and they observed that peak current density decreased over time at a fixed voltage.[92] In both their study and our own, we observe that once the electrode has flooded it can only be partially restored to its initial peak performance with superficial rinsing. Interestingly, we see that capacitance increases on the second run as compared to the first and remains relatively stable after subsequent uses, suggesting that it is difficult to completely remove salt crystallites that are deeply embedded in the GDE using our current washing methods. The inability to remove all residual salts aligns with the reduced breakthrough pressure values measured for post-run Ag-GDE samples that were also rinsed and dried prior to analysis (**Figure III-9a**). Another possible, but untested, hypothesis is that crystallization irreversibly damages the porous structure of an electrode leading to higher permeability and reduced hydrophobicity. Additional electrode imaging analysis would be required to unambiguously confirm or refute this supposition.[94] We confirm with this study that periodically restoring the electrode by an ex situ rinse prolongs electrolyzer lifetime, albeit at the expense of process of feasibility. Specifically, removal and refurbishment of electrodes from within industrial electrolyzer stacks would likely require repeated equipment disassembly and reassembly leading to additional maintenance costs and compromised reliability. Ultimately, technical solutions will be needed to minimize flooding during high-current operation in gas-fed flow electrolyte systems.

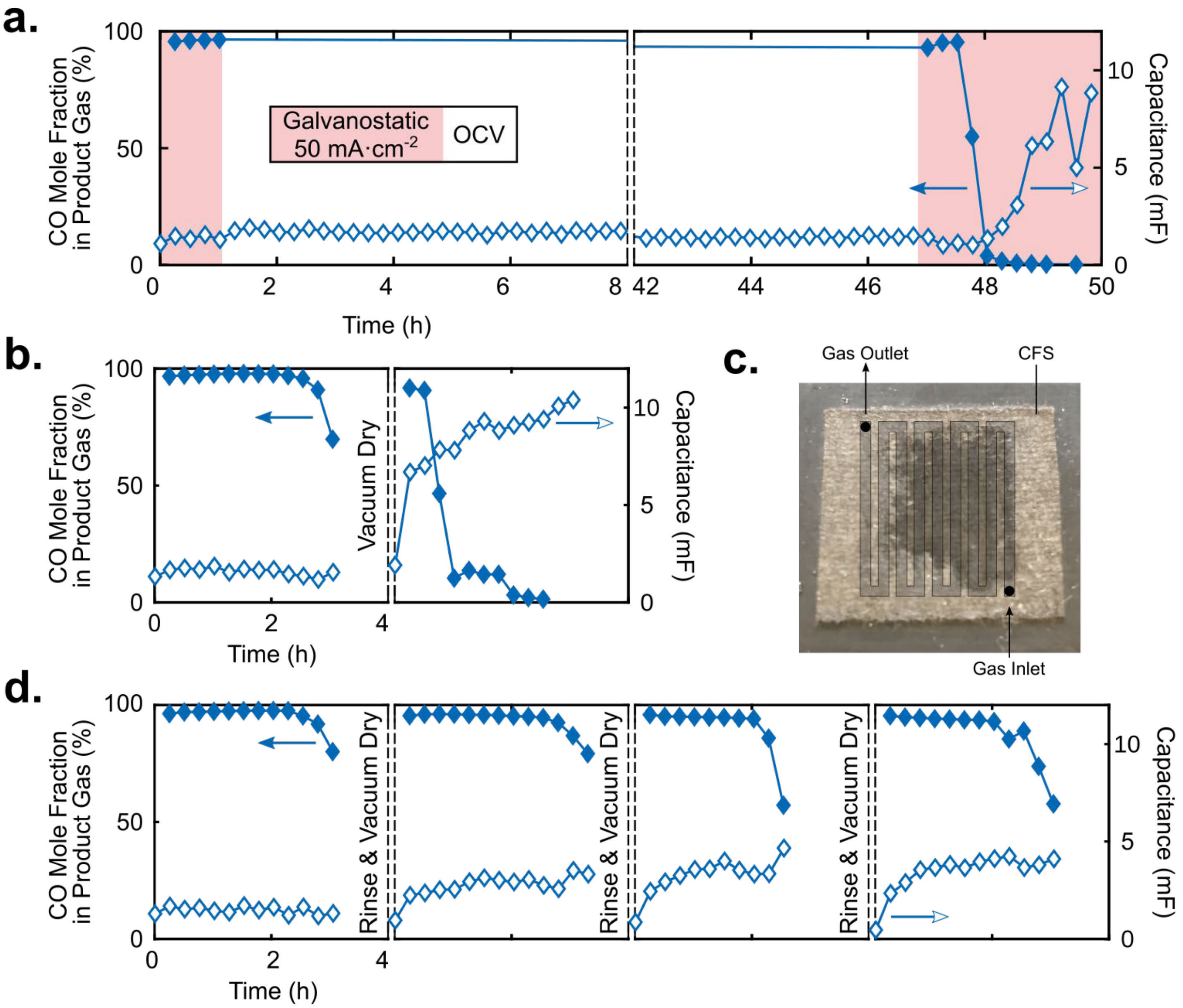

Figure III-14: *Probing the recoverability of GDEs. (a) Operating the cell at 50 mA·cm*$^{-2}$ *for 1 h and then switching to OCV for 48 h results in nearly immediate performance failure after restoring current. This indicates that flooding may occur slowly at OCV but is likely accelerated by faradaic processes. (b) Drying a partially flooded GDE after operating at 50 mA·cm*$^{-2}$ *does not restore the initial performance. (c) The portion of the GDE closest to the serpentine channel inlet, where* CO_2 *concentration is highest and humidity is lowest, floods first as indicated by the darker portion of the CFS. (d) Rinsing partially flooded GDEs in DI water then drying restores much of the peak performance although it gradually decreases after repeated uses.*

4. Conclusions

Systematic screening of Ag-GDEs in a gas-fed, flowing-electrolyte CO_2 electrolyzer revealed that electrode flooding rate correlates with applied current density. GDEs used at the lowest current density (25 $mA \cdot cm^{-2}$) demonstrate peak CO mole fraction in the product gas near 95% for over 5 h while those used at the highest current density (196 $mA \cdot cm^{-2}$) maintain this peak performance for less than 15 min. Recognizing that faradaic current accelerates electrode flooding and failure, we propose that carbonation serves not only as a parasitic sink for reactant gas but also as a promoter of GDE flooding by way of crystallite precipitation within the nominally hydrophobic GDL materials. Ex situ measurements of water breakthrough pressures for electrodes used in the electrolysis experiments reveal that GDEs exposed to higher currents retain less of their initial hydrophobicity. Successful attempts to recover peak CO mole fractions in the product gas by rinsing electrodes affirm that carbonation and salt crystallization within the electrode are associated with performance failure. In our system, the collapse of the electrolysis performance data onto a single curve when plotted as a function of cumulative charge passed suggests that each electrode may have a material-dependent carbonate threshold that, if exceeded, will lead to precipitation and failure.

We note that reports identifying associations between carbonation and electrode failure exist within the alkaline fuel cell literature.[79,95–97] Specifically, previous studies explored the impact of CO_2 contamination on gas-fed alkaline electrolyte systems, albeit at lower concentrations. Specifically, Rolla et al. reported that feeding laboratory air to cathodes for the oxygen reduction reaction resulted in reduced current densities and gradual electrolyte flooding through the GDE along with detectable precipitates at the gas-electrolyte interface after several hundred hours on stream.[79] The authors also suggested that feeding dehumidified air streams to the cathode accelerates “ageing” of both carbon and PTFE-based GDEs through electrolyte dry out and salt precipitation. Thus, although seemingly counterintuitive, humidified CO_2 streams may offer a pathway to extending electrode lifetime even though the CL is wetted by an aqueous electrolyte.

Despite the fact that operating lifetime can be extended by adjusting operating conditions, the persistence of the carbonation problem has hampered market adoption of alkaline fuel cells for critical areas such as mobility, in which PEFCs are now the dominant fuel cell technology.[98] Instead, alkaline fuel cells are limited to stationary applications where CO_2 scrubbing from the air feed stream is more tractable or to niche applications such as space, marine, or military where the use of pure reactant gases like H_2 and O_2 is practical.[99]

Although this work focuses on Ag-GDEs in contact with a flowing alkaline electrolyte for CO_2 to CO conversion, we anticipate that persistent cathode alkalinity will broadly impact the performance of both liquid and solid-electrolyte systems. For example, current-accelerated parasitic uptake of CO_2 has been reported for membrane-based CO_2 electrolysis systems with both weak carbonate electrolytes[100] or DI water[101] fed to the anode. Polymer electrolytes feature immobile cation moieties that facilitate anion (i.e., OH^-, HCO_3^-, and CO_3^{2-}) transport and remove the need for the mobile alkali metal cations (e.g., Na^+, K^+, Cs^+) responsible for the salt precipitation that diminishes the effectiveness of GDEs in flowing electrolyte devices. However, carbonation still occurs at the alkaline interface of the cathode and anion-exchange membrane facilitating the undesirable transport of CO_3^{2-} and HCO_3^- across the cell and resulting in the discharge of CO_2 at the locally acidic anode. Consequently, the relationship between current density and carbonation remains relevant for this electrolyzer configuration.

We anticipate that insights from the electrochemical and ex situ results presented here for a gas-fed flowing electrolyte CO_2 electrolyzer will direct attention towards the complex interplay between faradaic and homogenous reactions on and within GDEs and how these processes influence electrolyte ingress over a range of current densities and operating conditions (e.g., temperature, humidity). Quantifying electrolyte saturation in GDEs via direct operando imaging would complement this work by elucidating and perhaps confirming the physical origins of flooding at the interfaces between charged porous media and electrolytes. Furthermore, past findings from mature adjacent technologies aid in the interpretation of new experimental observations and may inspire emergent GDE designs and cell configurations for CO_2 electrolysis. Specifically, incorporating application-tailored microstructures and wettability into GDEs may facilitate carbonate clearance from the gas-liquid interface that mitigates precipitation/flooding events and promotes high CO_2 conversion rates for extended operation.

ACKNOWLEDGMENTS

This work made use of the MRSEC Shared Experimental Facilities at Massachusetts Institute of Technology, supported by the National Science Foundation under award number DMR-1419807, as well as the Center for Nanoscale Systems at Harvard University. The authors acknowledge the financial support of DOE SBIR Contract #DE-SC0015173. A.F.C. acknowledges the SNSF for funding a postdoctoral fellowship (PZEZP2_172183). The authors also thank Katharine Greco and Michael Orella of the Brushett Research Group as well as Dr. Brian Skinn and Dr. Timothy Hall of Faraday Technology, Inc. for insightful discussions.

5. *Appendix A: Reactor Assembly Protocol*

1. Gather the parts to assemble the flowing electrolyte CO_2 electrolyzer/reactor that are shown below and include: two end-pieces/diffusers, four O-rings, graphite serpentine flow field / current collector, Ti current collector, Ag-GDE cathode, Ni anode, two rubber gaskets, electrolyte flow channel / reference electrode port, Hg/HgO reference electrode, and four 1/4-28 UNF bolts with corresponding nuts.

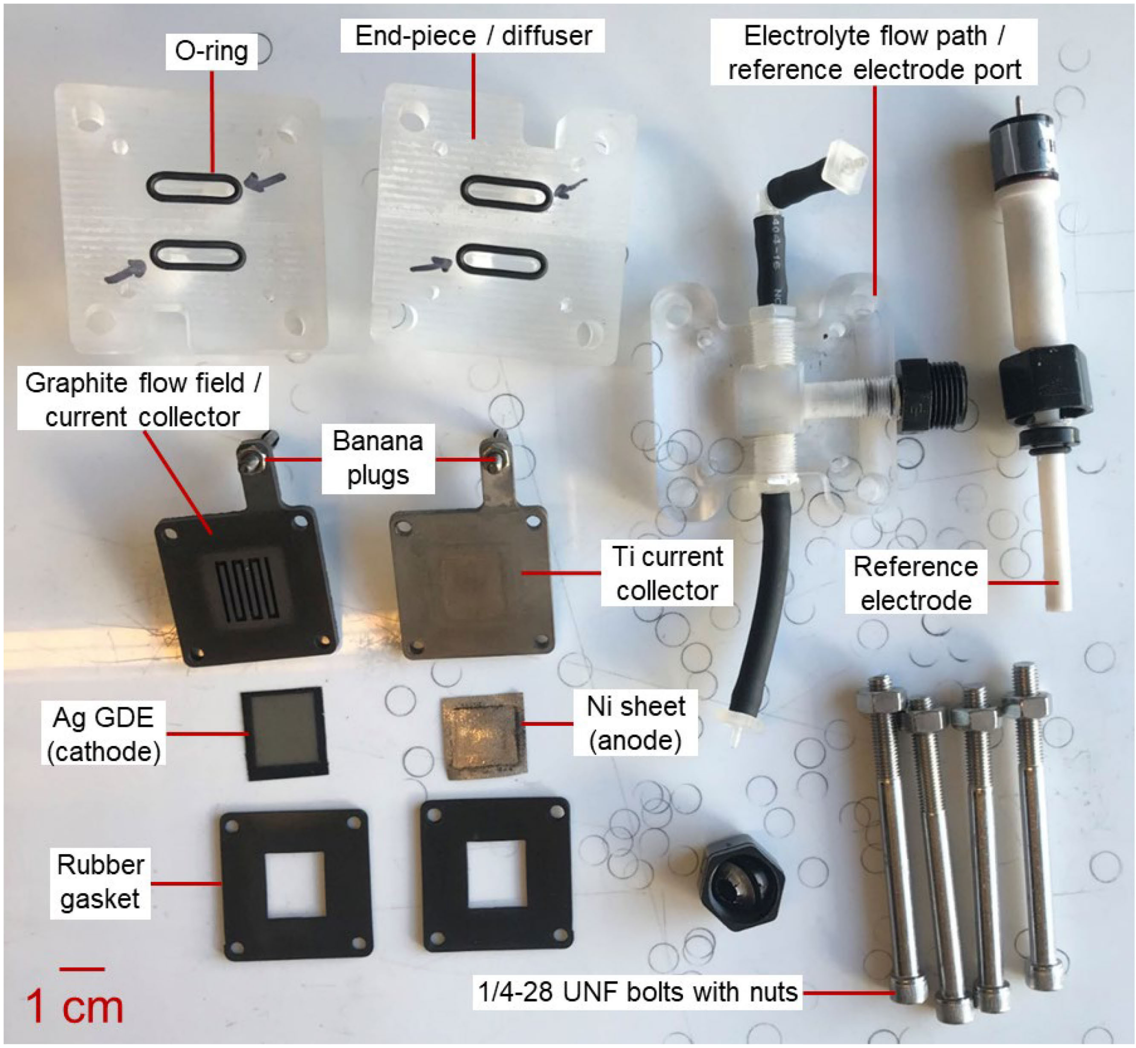

Figure III-15: *Flow reactor components labeled and arranged prior to assembly.*

2. Insert 1/8” diameter alignment pins into a cell assembly platform (typically there are 4 pins but only 3 are pictured below).

3. Place one end-piece onto the platform such that the gas inlet and outlet are facing downwards and the O-rings are facing upwards. The alignment pins should go through the smaller holes.

4. Place the current collector on top of the end-piece such that the banana plug is facing downwards.

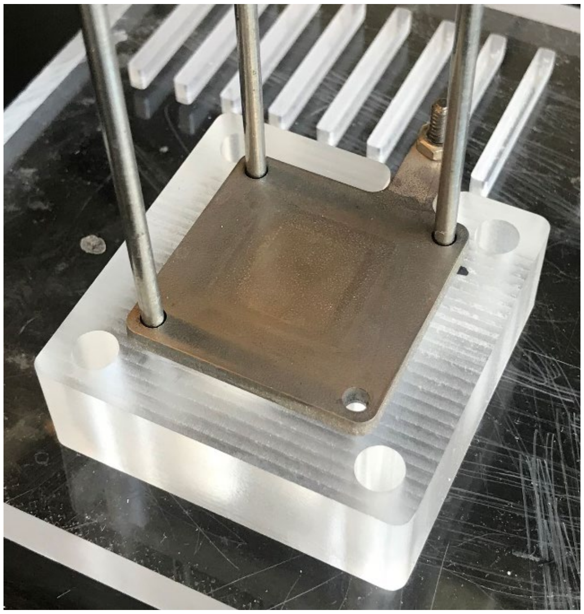

Figure III-16*: Titanium alloy anode current collector plate.*

5. Place the anode in the center of the current collector (either side can be facing up).

6. Place one rubber gasket on top (to seal in the anode).

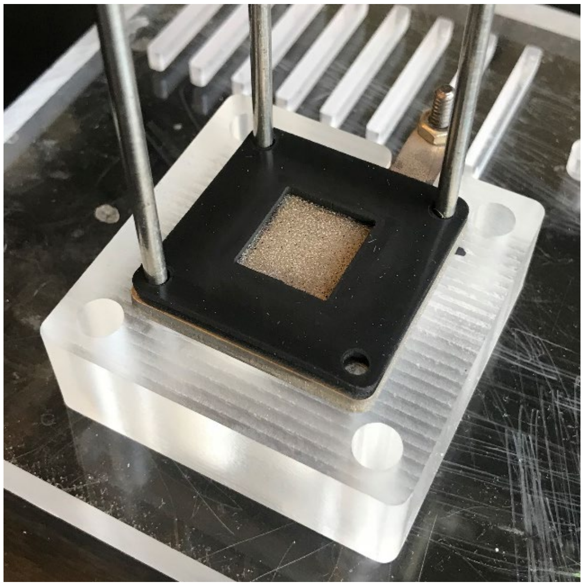

***Figure III-17**: Nickel foam anode sealed against the current collector by a rubber gasket.*

7. Place the electrolyte flow channel / reference electrode port on top of the rubber gasket. From this viewpoint, the reference electrode port should be to the left, the electrolyte inlet should be below the rubber gasket and the electrolyte outlet should be above the rubber gasket.

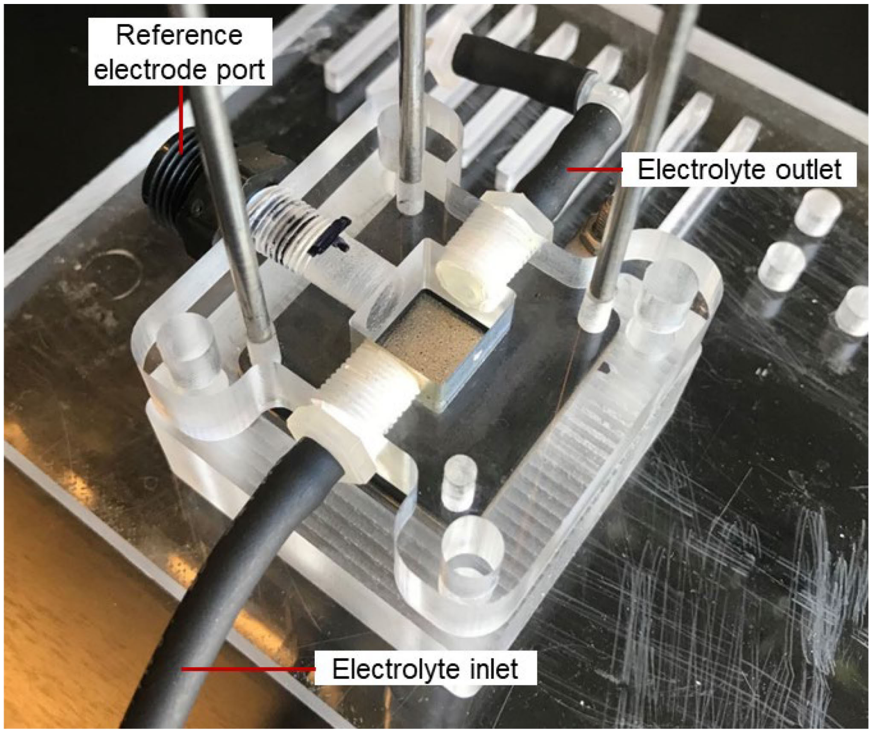

Figure III-18*: Electrolyte flow channel, including reference electrode port, placed on top of the anode components. Electrolyte flows from inlet at the bottom to the outlet at the top.*

8. Place the second rubber gasket on top of the electrolyte flow path / reference electrode port.

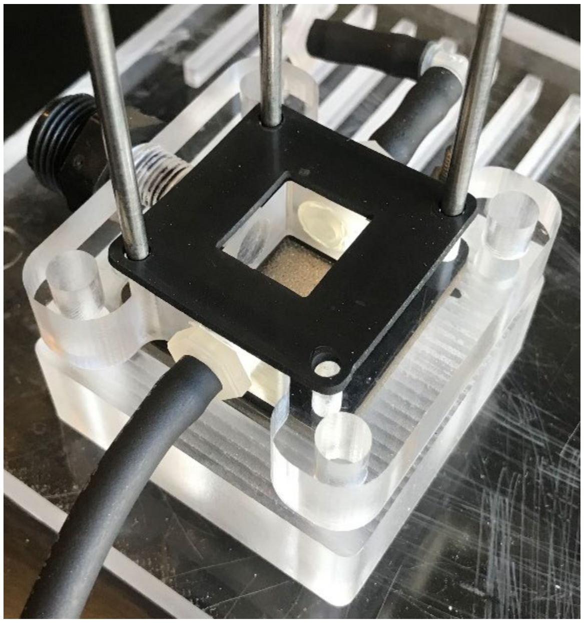

Figure III-19*: Cathode compartment gasket placed against the electrolyte flow channel.*

9. Insert the reference electrode into the reference electrode port such that the tip is just visible in the electrolyte flow channel. Then, thread the cap onto the corresponding fitting and hand tighten.

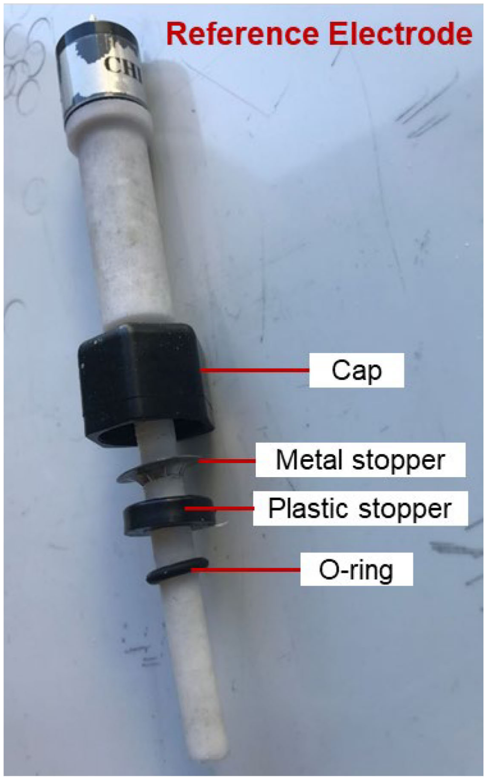

Figure III-20: *Hg/HgO reference electrode with a 1 M KOH fill solution. Compression fitting components needed to fasten and seal the reference electrode to its port in electrolyte flow channel are labeled for reference.*

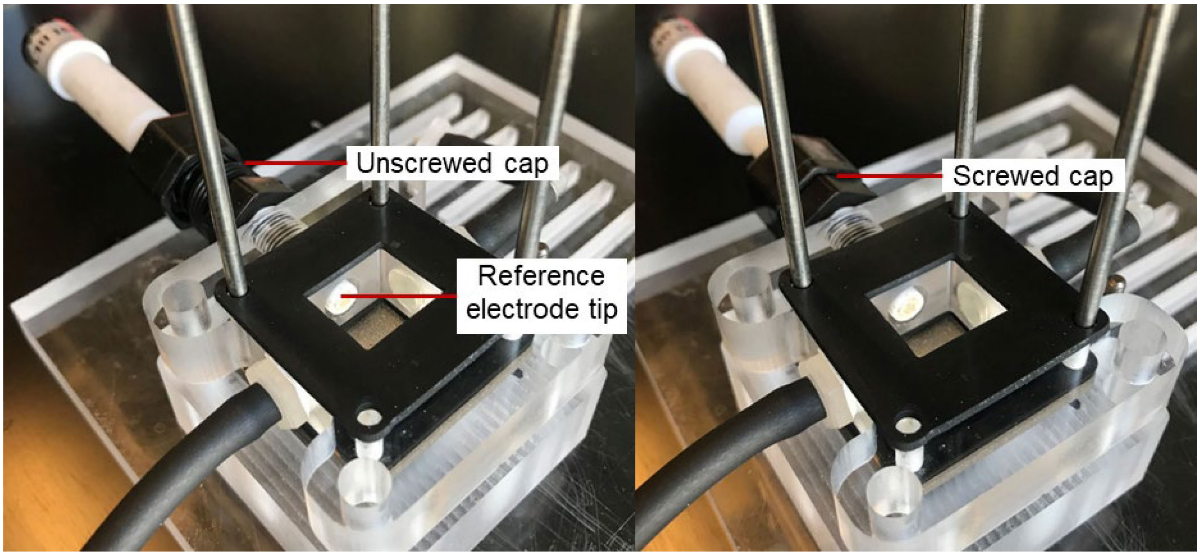

Figure III-21: *Reference electrode inserted and fastened to the electrolyte flow channel*

10. Place the Ag-GDE cathode in the center of the rubber gasket such that the catalyst layer is facing down (towards the electrolyte flow field). Then, place the flow field / current collector on top such that the flow path is facing downwards toward the electrode (banana plug facing upwards).

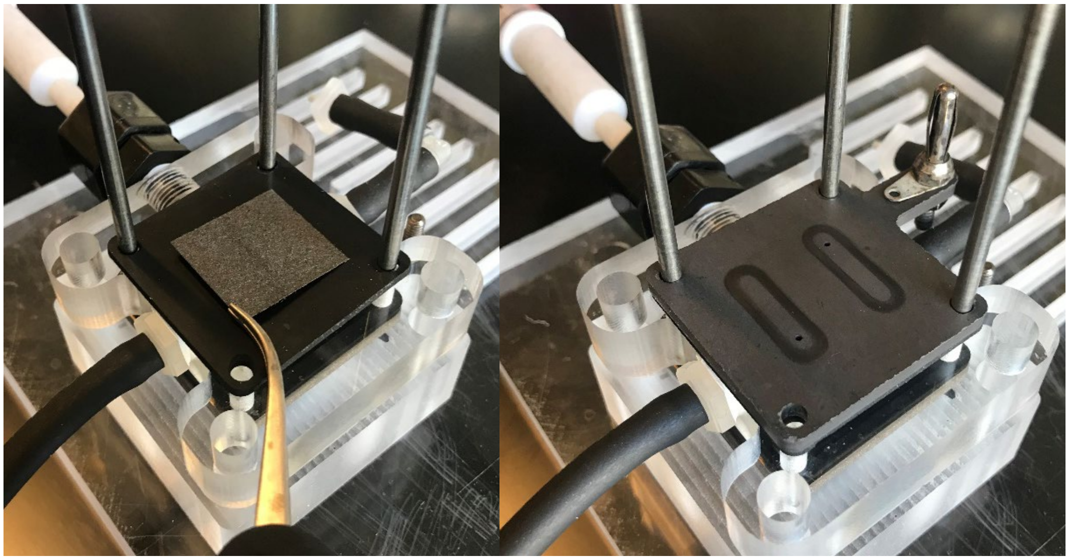

Figure III-22: *Ag-GDE sealed against a gasket by a carbon gas flow channel/current collector*

11. Place the second end-piece on top such that the O-rings are facing down towards the flow field / current collector.

12. Insert the four bolts through the outer (large) holes.

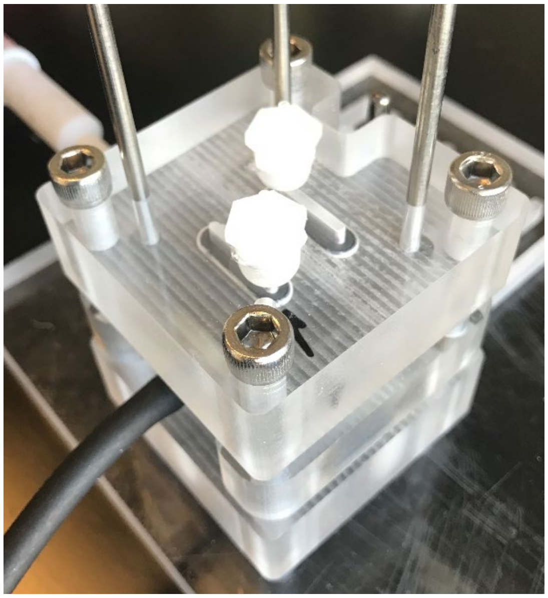

Figure III-23*: Cathode end piece and bolts in place prior to tightening*

13. Place two fingers across the bolt heads (as pictured below) and then screw on the nuts until they are hand tight.

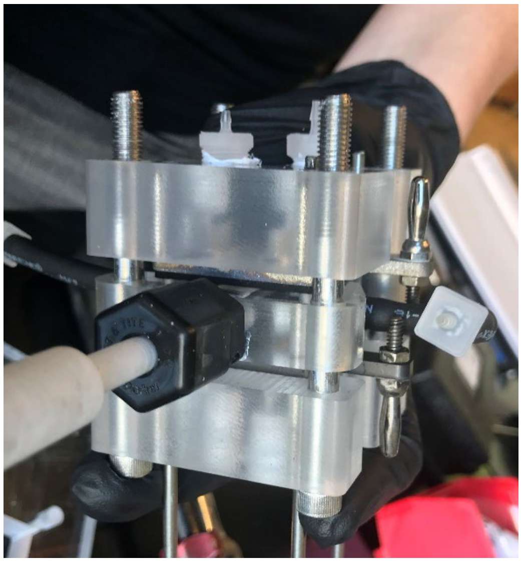

Figure III-24: *Aligned flow reactor components held in hand prior to tightening/compression*

14. Using a 7/16” wrench and a torque screwdriver (set to 15 lbf-in), first tighten each bolt (in an x-formation) until resistance is felt. Then, tighten each bolt until torque is felt (do this two times).

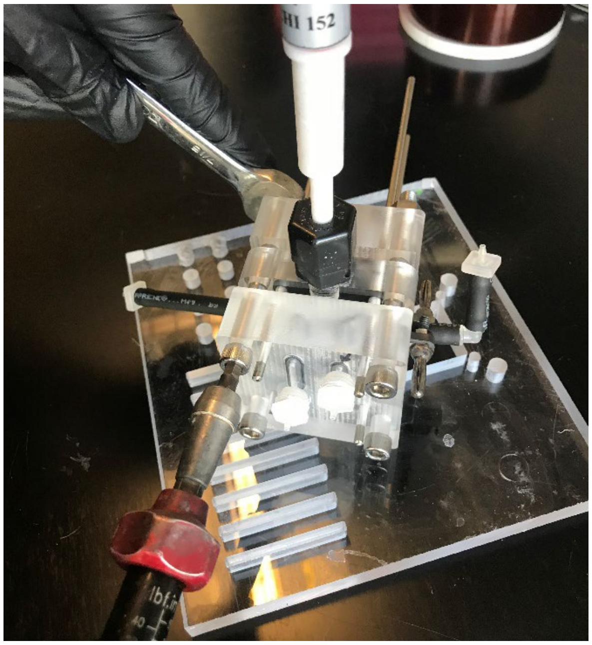

Figure III-25: *Flow reactor being tightened using a torque screwdriver*

15. Remove alignment pins to complete the assembly.

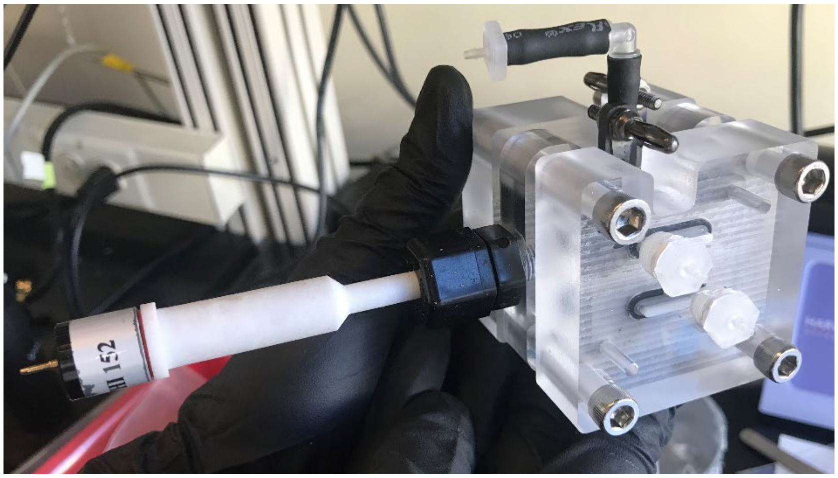

Figure III-26: *Flow reactor assembled and compressed shown with reference electrode*

6. *Appendix B: Electrolyzer Schematic and Startup Protocol*

First, the electrolyzer was mounted into a fume hood at the same height as the liquid back pressure regulator to minimize pressure differences due to hydraulic head. Next, the electrochemical leads from the potentiostat (working, counter, and reference electrodes) were connected to the cell. After the gas lines were connected and the gas mass flow controller (MFC) is set to 20 sccm, the peristaltic pump was set to 1 $mL \cdot min^{-1}$ to fill the central chamber with electrolyte from the feed reservoir bottle. The schematic shown in **Figure III-27** shows the flow of materials and electrons through the experimental setup. Images of the setup are shown in **Figure III-28** After filling the chamber, the outlet from the chamber was connected to the inlet of the liquid-side back pressure regulator. The system was left untouched until the liquid filled the backpressure regulator and droplets were observed downstream entering the waste container. After the gas and liquid were both flowing through the system, the mass flow meter (MFM) registered measurable CO_2 gas flow rates. The MFM reading was never expected to reach 20 sccm because there is carbonation that occurs when contacting CO_2 with a KOH electrolyte (**Figure III-5**). Once gas flow is observed, the electrolysis can begin. First the electrochemical method is started. Next the MFM recording script is started. Finally, the GC sequence is started and a blank GC sample is taken near time point zero.

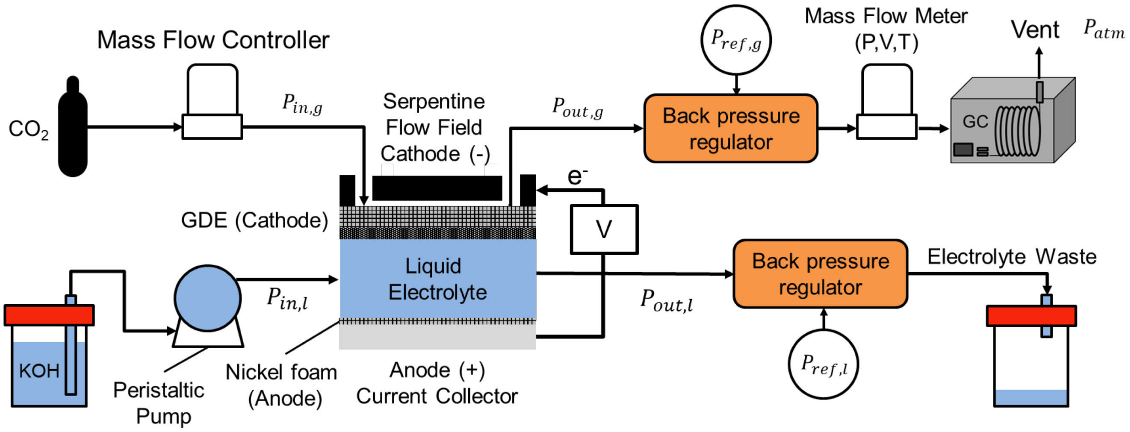

Figure III-27: *Schematic of the gas-fed, flowing liquid electrolyte* CO_2 *electrolyzer setup.*

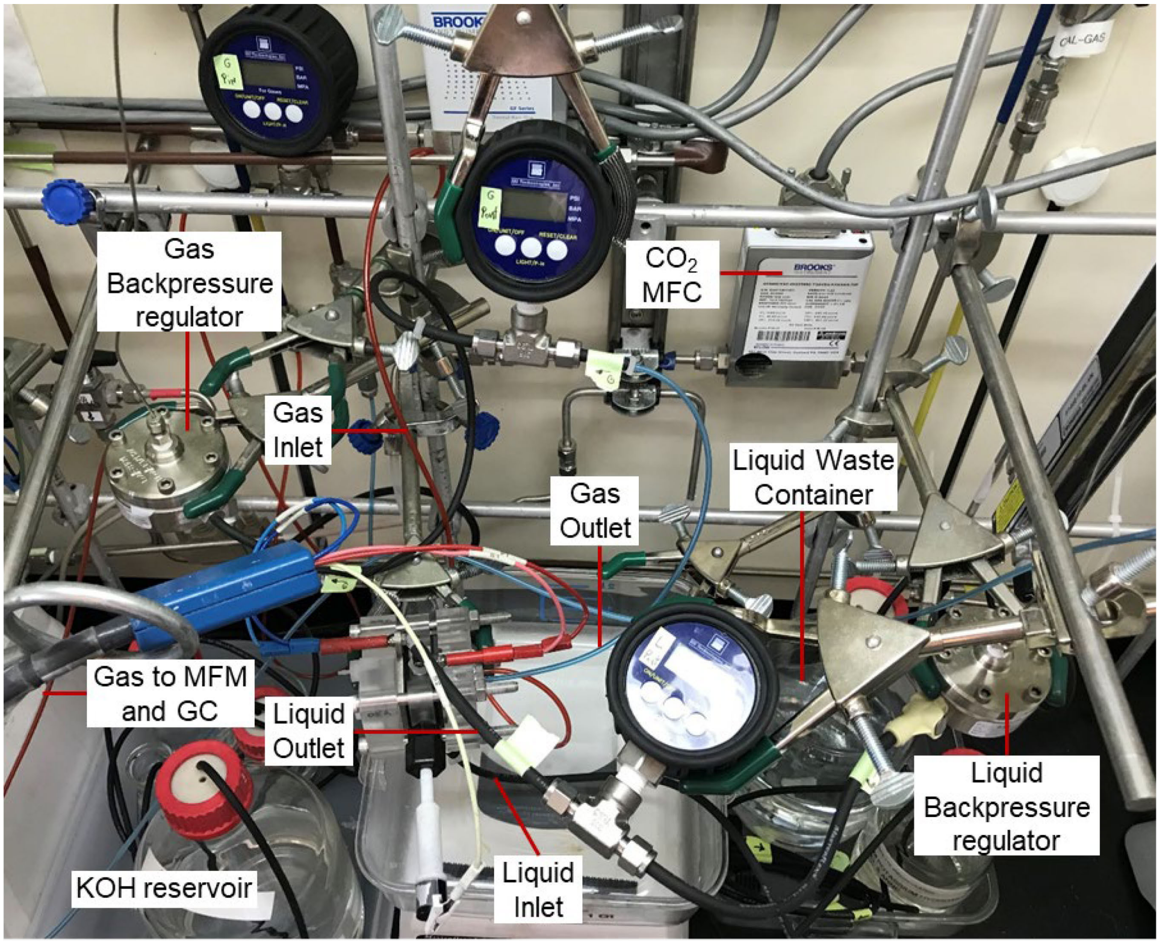

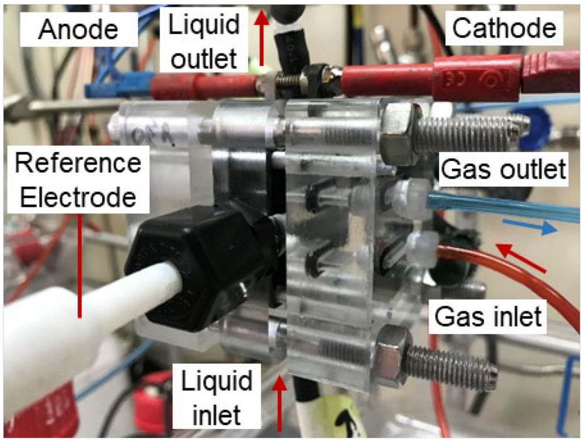

***Figure III-28**: Images of the gas-fed, flowing liquid electrolyte experimental setup (top) and the electrolyzer (bottom).*

7. *Appendix C: Electrochemical Reactions*

Relevant half- and full-cell electrochemical reactions are provided along with the associated standard reduction potential, E^0.

7.1. Cathode Half-Cell Reactions

When using Ag-GDEs in a 1 M KOH electrolyte the only appreciable CO_2 reduction product is CO, which is produced according to Equation (III.2). HER is the only side reaction considered and H_2 is produced according to Equation (III.3).

$$\mathrm{CO_2 + H_2O + 2\ e^- \rightarrow\ CO + 2\ OH^-}\ (E^0 = -0.10\ \mathrm{V}) \tag{III.2}$$

$$\mathrm{2\ H_2O + 2\ e^- \rightarrow\ H_2 + 2\ OH^-}\ (E^0 = 0.00\ \mathrm{V}) \tag{III.3}$$

7.2. Anode Half-Cell Reactions

A nickel anode facilitates the oxygen evolution reaction (OER) as shown in Equation (III.8).

$$\mathrm{4\ OH^- \rightarrow\ O_2 + 2\ H_2O + 4\ e^-}\ (E^0 = 1.23\ \mathrm{V}) \tag{III.8}$$

7.3. Full-Cell Reactions

Combining each of the cathode half-cell reactions with the anode half-cell reaction results in the following full-cell reactions for CO and H_2 generation in Equation (III.9) and Equation (III.10), respectively. The minimum full-cell voltages for each reaction pair by taking the difference between the cathode and anode standard reduction potentials, $E^0_{\text{cell}} = E^0_{\text{cathode}} - E^0_{\text{anode}}$.

$$\mathrm{CO_2\ \rightarrow\ CO + 1/2\ O_2}\ (E^0_{\text{cell}} = -1.33\ \mathrm{V}) \tag{III.9}$$

$$\mathrm{H_2O\ \rightarrow\ H_2 + 1/2\ O_2}\ (E^0_{\text{cell}} = -1.23\ \mathrm{V}) \tag{III.10}$$

8. Appendix D: Galvanostatic CO_2 Reduction Addendum

Supplemental visualizations of the galvanostatic CO_2 reduction results are provided in the following figures.

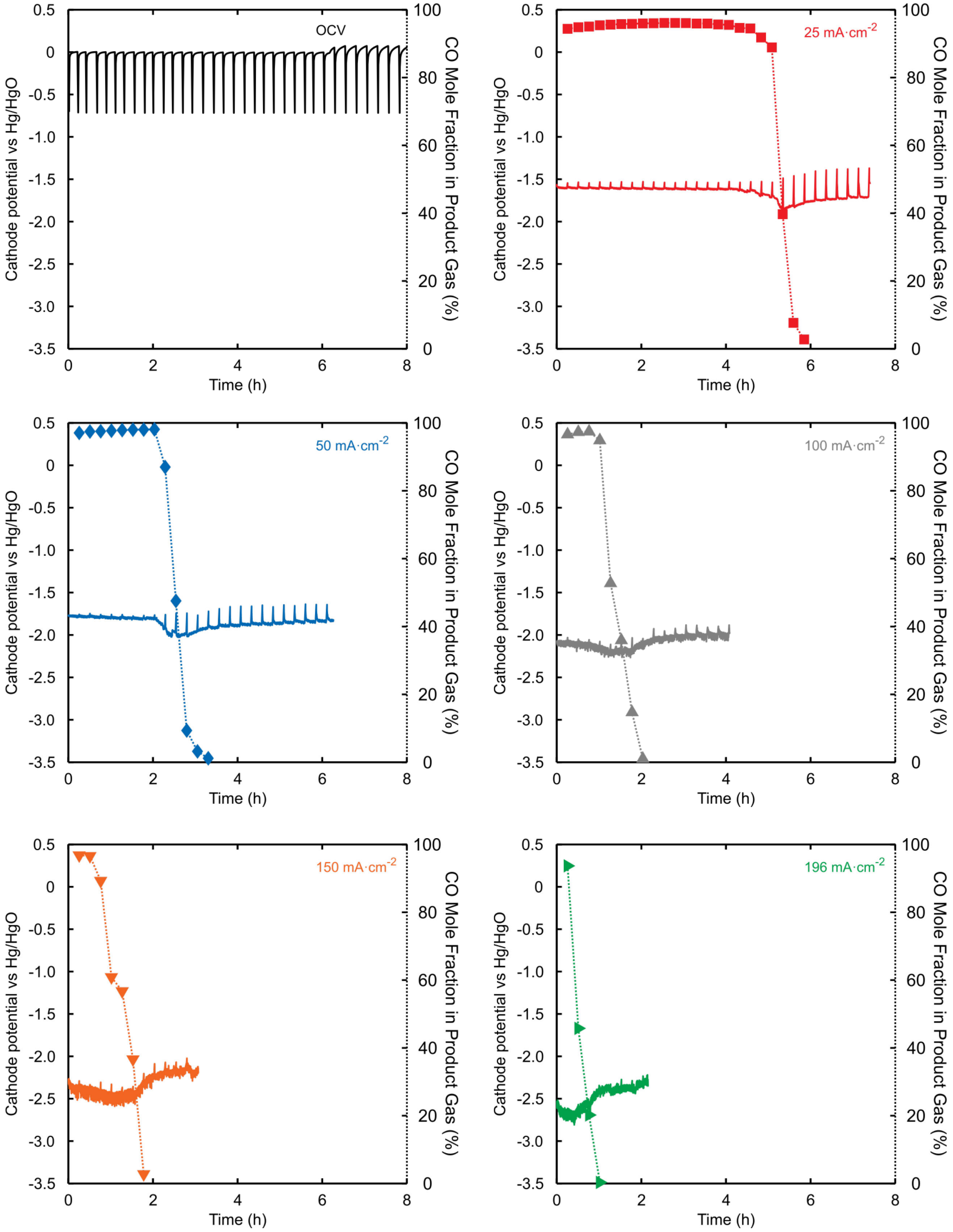

Figure III-29*: Uncompensated cathode potential vs Hg/HgO and CO mole fraction in the product gas as functions of time and applied current density.*

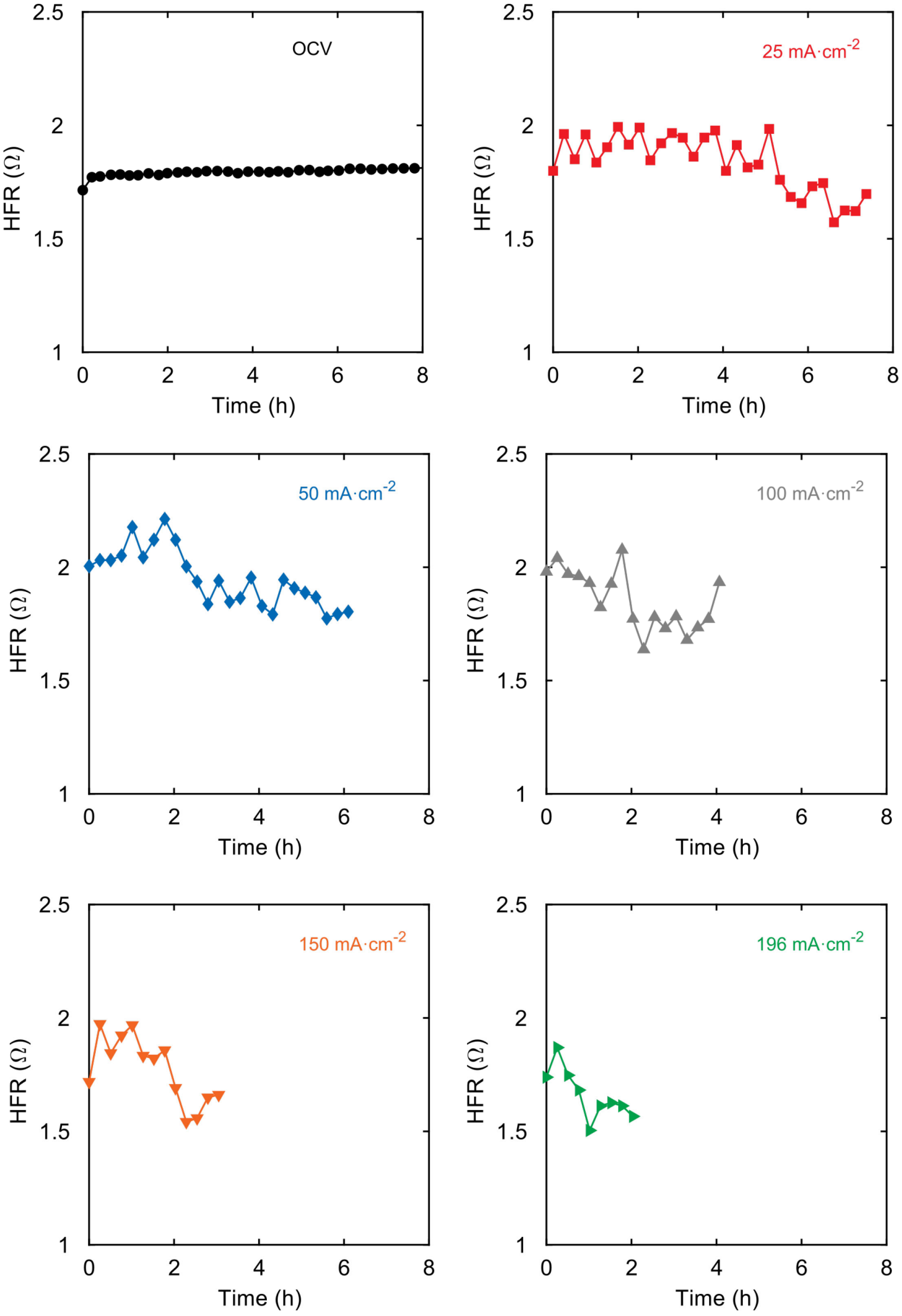

***Figure III-30**: High frequency resistance (HFR) between the cathode and reference electrode as a function of time and applied current density.*

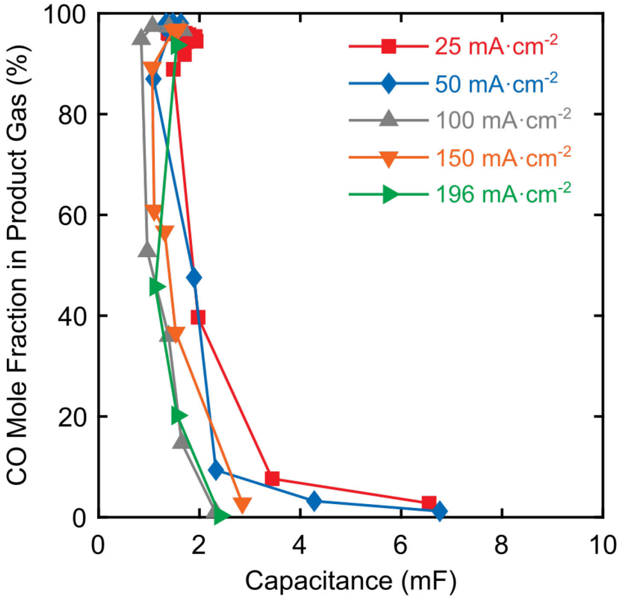

Figure III-31: *CO mole fraction in the product gas as a function of capacitance and applied current density.*

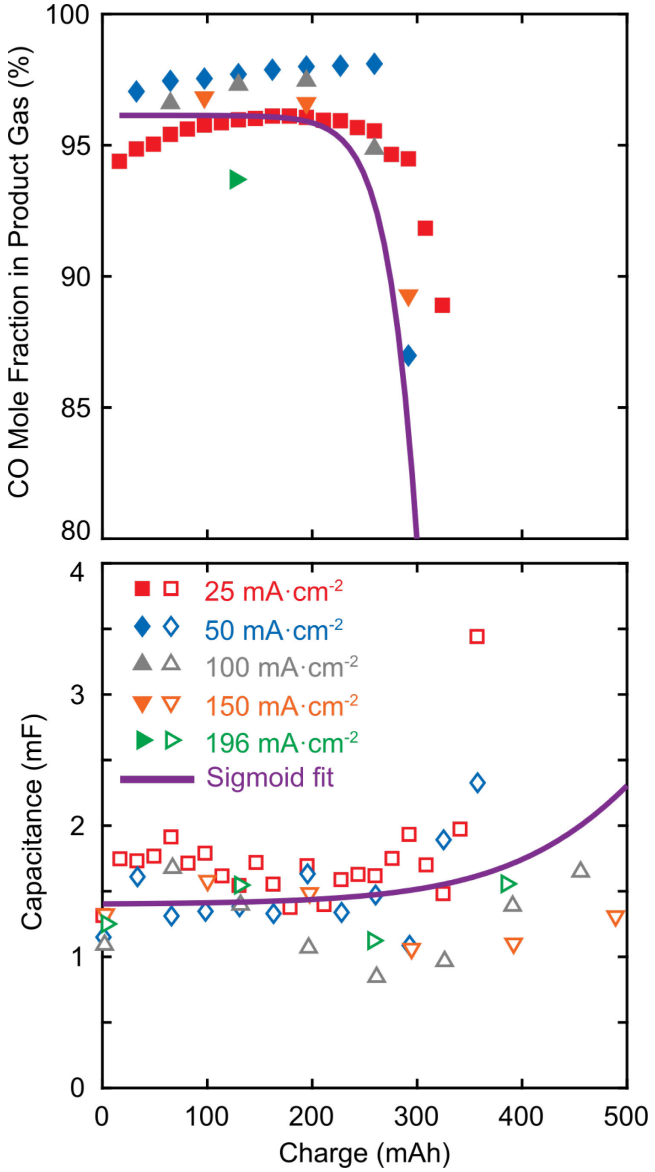

Figure III-32: *Enlarged plots of the CO mole fraction and capacitance as functions of charge and applied current density from* ***Figure III-7****. The logistic function used for fitting has the general form* $\boldsymbol{f(x) = a + \frac{b}{1+e^{-k(x-x_0)}}}$*, where a and b are the lower and upper bounds of the function, respectively, k is the logistic growth rate, and* x_0 *is the curve midpoint. The parameter sets,* $[\boldsymbol{a, b, x_0, k}]$*, for the CO mole fraction and capacitance data are* $[\boldsymbol{0\ , 96.1\ , 337, -0.0184}]$ *and* $[\boldsymbol{1.50, 4.50\ , 425\ , 0.00592}]$*, respectively.*

IV. Flooded by Success: On the Role of Electrode Wettability in CO_2 Electrolyzers that Generate Liquid Products

Economic operation of carbon dioxide (CO_2) electrolyzers generating liquid products will likely require high reactant conversions and product concentrations, conditions anticipated to challenge existing gas diffusion electrodes (GDEs). Notably, electrode wettability will increase as lower surface tension products (e.g., formic acid, methanol, ethanol, and 1-propanol) are introduced into electrolyte streams, potentially leading to flooding. To understand the hydraulically stable operating envelopes in mixed aqueous-organic liquid domains, we connect intrinsic electrode wettability descriptors to operating parameters such as electrolyte flow rate and current. We first measure contact angles of water-organic product dilutions on polytetrafluoroethylene (PTFE) and graphite surfaces as planar analogues for GDE components. We then use material balances around the reactive gas-liquid-solid interface to calculate product mass fractions as functions of water sweep rate and current. Product composition maps visualize the extent to which changes in cell performance influence capillary pressure, a determinant of GDE saturation. Analyses suggest that formic acid mixtures pose little risk for GDE flooding across a wide range of sweep-rate/current combinations, but effluents containing <30% alcohol by mass may cause flooding. This study reveals opportunities to integrate microstructural features and oleophobic surface treatments into GDEs to repel mixtures of aqueous and organic liquids and expand the window of stable operating conditions.

1. Background

Electrochemical carbon dioxide reduction (CO2R) is increasingly recognized as a viable technology for flexible generation of chemicals using carbon dioxide (CO_2) recovered from industrial exhaust streams or directly captured from air.[102,103] When coupled with affordable electricity generated from renewable sources, CO2R has the potential to displace petroleum-based chemicals production in a low-carbon economy.[30] Given that the form factors of electrochemical technologies evolve as they transition from benchtop prototypes in the laboratory to engineered unit operations integrated into an industrial process, it is reasonable to anticipate commensurate shifts in the objectives and challenges for each scale. Historically, three-electrode analytical cells have been used to study catalyst activity, selectivity, and stability with a goal of incorporating proven materials into larger devices.[20,104,105] However, it has been recognized that the limited CO_2 flux through bulk volumes of liquid electrolyte suppresses the reaction rate of CO_2 and inhibits the performance of otherwise promising catalytic systems.[25,41,106] Gas-fed electrolyzers adapted from commercially successful water electrolyzer and fuel cell technologies have motivated CO2R researchers to explore various combinations of porous electrodes, catalyst layers, liquid electrolytes, and polymeric membranes to achieve higher areal productivity while maintaining steady fluxes of species between flow channels and active sites.[33,59,101,107,108] For example, state-of-the-art devices achieve high current density (>200 mA cm^{-2}) production of valuable intermediates, such as carbon monoxide (CO), at moderate cell voltages (ca. 3 V) and ambient conditions for relatively extensive durations (>100 h) using cell configurations similar to polymer electrolyte water electrolyzers.[109]

Such impressive prototype performance begs the question: Could operation of electrolyzers at high product generation rates result in reaction environments so extreme that they challenge the flooding thresholds of existing porous electrode materials sets? We posit that the conditions necessary for industrial CO2R may render GDEs composed of hydrophobic materials incompatible with lower-surface-tension mixed aqueous-organic phases generated at the reactive gas-liquid-solid interface. Note that flooding occurs across a range of gas-to-gas and gas-to-liquid electrolyzers for a variety of reasons (e.g., electrolyte carbonation and salt precipitation,[26] electrowetting,[93] and uneven GDE pressure distributions[93]). In this work, we consider the wettability of GDE components, evinced by sessile drop contact angles on planar analogues, in contact with aqueous-organic liquid mixtures representative of potential product stream compositions. Subsequently, we use a simple mass balance model paired with contact angle measurements to estimate electrolyzer operating limits, represented by the capillary pressure, beyond which product streams would be anticipated to spontaneously flood conventional GDEs without deploying additional pressure control strategies. By connecting readily obtainable measures of electrode-liquid affinity to cell operating conditions, we aim to develop insights into operating regimes for CO_2 electrolyzers that generate liquid products and to address critical questions, such as: (i) What are threshold compositions for liquid product mixtures that may lead to spontaneous electrode flooding under pressure-balanced conditions? (ii) Do current state-of-the-art effluent compositions fall within a stable region for PTFE-containing GDEs? (iii) Can we design porous electrodes with flooding resilient structures and surface energies to withstand high product concentrations?

2. *Industrial CO_2 to Liquids Electrolyzers Will Move Beyond Differential Operation*

At the bench-scale, where component validation and performance benchmarking are typically the desired outcomes, electrochemical cells with active areas of ca. 1–10 cm^2 are often operated to generate dilute product streams that are conducive to quantitative analyses. Under differential conditions, in which species concentration gradients are assumed to be negligible,[110] electrochemical kinetic parameters can be determined in the absence of mass transfer limitations that may obscure results at higher degrees of reactant depletion. When targeting gas-phase products, such as CO, differential conditions are generally achieved by feeding CO_2 in stoichiometric excess to the cathode compartment to ensure low single-pass CO_2 conversion ($<$ 20%) for a given total current (**Figure IV-9**, Appendix A). For cells with flowing electrolytes, water-miscible liquid products can be diluted either by increasing the total electrolyte volume for batch operation or increasing flow rate in single-pass operation. As an added benefit, generating dilute products can reduce the risk of creating dangerous concentrations and/or quantities of hazardous reaction products that are more appropriately handled in industrial settings where suitable hazard management protocols exist.

In contrast, the choice of operating conditions and reactor architecture for commercial CO2R systems will be driven by application economics to the point that the set of idealized scenarios explored at the bench-scale may not reflect practical device set points. Indeed, it may be more cost-effective to operate electrolyzers so that both gaseous and liquid effluents are highly enriched in CO2R products. Results from our previously reported technoeconomic model indicate that separations could constitute a larger fraction of overall CO2R process cost when generating liquid products as opposed to gaseous products.[15] Based on this coarse analysis, we postulate that process economics, driven by the desire to minimize downstream separations of liquid products from the carrier phase, will likely dictate that future at-scale CO2R systems generate higher product concentrations than those contemplated at the laboratory-scale today. Accordingly, publications focused on scale-up have begun to highlight electrolyzers which operate with high current densities,[111] large total currents,[92] and concentrated product streams.[38,112,113]

As CO2R cell prototypes begin to traverse these new operating regimes, challenges can be anticipated due to shifts in chemical compatibility requirements for reactor components (catalysts, electrodes, periphery), significant deviations from low-concentration kinetic behavior, and greater process safety concerns arising from concentrated toxic products. Here, we elect to focus on irregularities expected to arise for gas diffusion electrodes (GDEs) while operating gas-fed CO2R devices at high liquid product generation rates. Recent reports of flowing electrolyte CO2R cells with extended durability (ca. 10–100 h) have generally espoused the importance of incorporating fluorinated polymers (i.e., polytetrafluoroethylene (PTFE)) in the GDEs, either as an additive or a structural component, to maintain a stable gas-liquid-solid interface between the liquid product/electrolyte phase and gaseous reactant phase.[36,37,111] Historically, fluorinated polymers have been used as *hydro*-phobic coatings for carbon gas diffusion layers to assist in water management in polymer electrolyte fuel cells[17] and as structural components in oxygen depolarized GDEs to maintain stable gas-electrolyte interfaces.[114] Initial investigations by Haas *et al.* and Dinh *et al.* suggest that fluoropolymer-rich GDEs can significantly improve the operating lifetimes of a variety of CO2R cell architectures.[36,115] While PTFE as a GDE support has expanded the envelope for high-current electrolysis, it is reasonable to expect that the assumed equilibrium state of the cathode-electrolyte interface could be perturbed by high concentrations of liquid products, such as alcohols. High alcohol generation rates have also been reported to dissolve some anion-exchange polymer membranes in situ.[112] Although this observation is relevant for understanding the limits of specific component durability, we will not focus on this aspect of chemical compatibility in this work.

3. *Gas Diffusion Electrode Flooding Is Governed by Capillary Pressure and Wettability*

In CO2R, the GDE is an interfacial cell component that separates the gaseous and electrolyte phases and facilitates flux of reactants/products/electrons to/from the catalytically active sites. A key challenge is the rational selection of GDE materials that can manage diverse (e.g., electrical conductivity and electrocatalytic activity/selectivity) and often contradictory (e.g., permeability and flooding resistance) functionalities across a range of operating modes. Equilibrium between two immiscible mobile phases (i.e., gas and electrolyte) in a porous medium depends on a trans-interfacial pressure differential that is defined both by surface wettability, fluid physical properties, and pore dimensions. If we consider an idealized porous medium to be composed of cylindrical pores, or capillaries, we can use Equation (IV.1), as proposed by Washburn,[116] to calculate the capillary pressure, P_C, as a function of the solid-liquid-gas contact angle, θ, the pore radius, r, and the liquid-gas surface tension, γ. The capillary pressure defines the difference at equilibrium between the gas and liquid phase pressures (P_G and P_L, respectively).[117]

$$P_\mathrm{C} = P_\mathrm{L} - P_\mathrm{G} = \frac{-2\gamma\cos\theta}{r} \qquad \text{(IV.1)}$$

The relationships between parameters in **(IV.1)** are generally valid for understanding high-level capillarity trends. However, in order to more accurately predict the complex filling behaviors of real porous materials, this simple model for capillary pressure should be paired with additional macroscopic descriptors such as porosity, tortuosity, pore size distribution, and pore accessivity.[118]

Understanding the effects of material selections on wettability properties of the electrodes requires consideration of surface energetics. Porous electrodes are often composite materials, consisting of high energy constituents (i.e., metal or carbon) that provide electrical and thermal conductivity[119] and low energy adjuncts (e.g., polymer coatings) that contribute additional functionalities, such as mechanical durability or wet-proofing to manage liquid saturation. Modifications to electrode surfaces can drastically change wettability characteristics regardless of the bulk material.[119] In the 1960s, pioneering work by Zisman characterized the spreading and adhesion of liquids on solids as a function of surface energy/surface tension.[120] In the context of fluid droplets on planar solids, (i) macroscopic solid-liquid-gas contact angles track with the composition of test fluids according to the surface tension and (ii) test fluids transition from non-wetting ($\theta > 0°$) to wetting ($\theta = 0°$) on a given solid at a surface energy (surface tension) threshold value that depends on the chemical character and physical structure of the surface.

Commonly pursued CO2R products like organic acids (i.e., formic acid) and C1–C3 primary alcohols (i.e., methanol, ethanol, 1-propanol) are water-miscible at ambient conditions. When these organic species are introduced into aqueous solution, even at dilute concentrations, they can greatly affect physical properties such as density, viscosity, and liquid-gas surface tension (**Figure IV-10**, Appendix A). Changes to density and viscosity affect pressure drops within flowing electrolyte-based cells; however, we choose not to focus on pumping duties in this work. Changes to surface tension/contact angle, in combination with electrode geometries, most directly influence GDE wetting and saturation, which acutely impact reactant fluxes and, therefore, electrocatalytic performance. Surface tension in electrolyte solutions can be influenced by several factors including ionic strength, anion-cation pairs, and temperature.[82,121–124] Given the breadth of the compositional space and potential testing conditions, here we elect to focus on the introduction of organic components into solution as they are anticipated to most drastically impact surface tension. Further analyses may explore how these effects are amplified or suppressed depending on electrolyte composition or operating conditions.

Measuring the *apparent* contact angles of sessile droplets is an effective method for characterizing the wettability of candidate porous electrode materials with a variety of test liquids reminiscent of CO2R product streams. Although this macroscopic approach is often applied to study non-ideal substrates, *intrinsic* contact angles can only be measured on smooth, non-porous surfaces (Young's theory).[125] Appropriate corrections to contact angles measured on textured materials, which appear distorted when compared to flat materials with equivalent surface chemistry,[119] can be made for both homogeneous (Wenzel) and heterogeneous (Cassie-Baxter) wetting regimes.[126,127] Despite the obscurations introduced by roughness and entrapped fluids when determining quantitative measures of wettability on porous substrates, droplet-based protocols are widely practiced to evaluate the resistance of textiles and other electrochemically functional materials to wetting.[45,128–132]

4. Experimental

4.1. Contact Angle Measurements with Sessile Drop Goniometry

To better understand the wettability of aqueous-organic mixtures in the context of CO2R, we selected formic acid (FA; reagent grade, ≥ 95% purity, Sigma-Aldrich), methanol (MeOH; HPLC grade, ≥ 99.9%, Sigma-Aldrich), ethanol (EtOH; anhydrous, 200 Proof, KOPTEC), and 1-propanol (PrOH; ACS reagent, ≥ 99.5%, Sigma-Aldrich) for analysis. We prepared solutions across a range of dilutions from 0 to 100% by mass with deionized (DI) water (18.2 MΩ, Milli-Q). Salt-free solutions were used to isolate the interaction between each test liquid and water. Subsequent studies may elucidate the impacts of the chemistry and concentration of dissolved salts on relevant physical properties. FA mixtures were used in place of formate salt solutions because this study focuses on the effect of introducing organic solvent components into aqueous solutions. Although formate salt product mixtures are typically reported in the literature, some electrolyzer variants utilizing porous solid electrolytes can generate salt-free, concentrated acid product streams, making a focus on FA applicable.[38,133] Additionally, organic acid solutions are known to have lower surface tension than electrolyte solutions, so FA has utility for a bounding study focused on negative surface tension deviations from water.[121,122] PTFE (FP303050, Goodfellow) and graphite (99.997%, 867-421-20, Goodfellow) sheets were used as the primary solid substrates for droplet studies. PTFE sheets were cleaned with DI water and isopropyl alcohol (IPA; ≥ 99.5%

ACS, VWR Chemicals BDH®) and dried using compressed air prior to analysis. Graphite sheets were prepared by removing the top layer of material with Scotch® tape (MFR#: 810, 3M). 5-µL droplets[134] were dispensed onto substrates using an automatic pipetting unit. Measurements were taken in ambient air where the temperature and relative humidity remained between 20–24 °C and 10–40%, respectively. Videos of 30–60 s duration were captured at 30 frames per second using a contact angle goniometer system (Model 200, ramé-hart) and processed using DropPy V1.0.0a0, a Python ≥3.6-based goniometer software.[135] Substrates were spot-cleaned before dispensing and imaging new droplets. Contact angles were determined by fitting edges with a two-parameter Bashforth-Adams model that accounts for the effects of gravity on droplet shape. To minimize the influence of evaporation on measurements, only the first 10 s of each recorded video were used for contact angle fitting. As a result of these practical constraints, the reported contact angles may not strictly reflect the equilibrium state. Additional descriptions of experimental procedures as well as the data collected for each trial (**Table IV-2** and **Table IV-3**) are provided in Appendix B.

4.2. Contact Angle Measurements with Select CO2R Products as Test Liquids

To determine the qualitative impact of mixed organic-aqueous product streams on electrode wettability, we measured the contact angles for the solutions described above as a function of water content, as shown in **Figure IV-1**. The markers for each product represent the average contact angle from 5 trials at each concentration and the error bars are one standard deviation of the same measurements. The water contact angle on PTFE is found to be 112° ± 1.5°, which is consistent with previous work.[136] The water contact angle on the graphite sheet is measured at 131° ± 1.8°. As expected, the contact angles of the mixtures on both surfaces decrease with increasing mass fraction of organic species due to the reductions in surface tension. The tendency to wet the solids is directly proportional to the carbon chain length of the product which is associated with decreased polarity and surface tension (PrOH < EtOH < MeOH < FA < water), especially for the primary alcohols.[10] The ability for each solid to prevent spontaneous liquid imbibition by a porous electrode can be assessed, at a high level, by comparing the point at which the test fluid would be neutrally wetting in the context of a cylindrical capillary (i.e., has a contact angle of 90°). When studying graphite, solutions with more than 10% alcohol fall below the 90°-threshold; however, the alcohols can be mixed in higher proportions before neutrally wetting conditions are reached on PTFE. In both cases, the FA mixtures reach neutrally wetting conditions at much greater mass fractions than the alcohols, suggesting that such product streams will not lead to significant changes in capillarity relative to pure aqueous solutions in PTFE-containing GDEs. As such, CO2R to FA appears to have a wide range of feasible operating compositions, exceeding the highest reported concentrations to date (ca. 15–30% by mass).[38,133] In contrast, the transition concentrations for alcohols are significantly lower and we anticipate that such compositions will be readily-achievable in practical CO2R-to-liquids electrochemical processes, posing a stability challenge for PTFE-containing GDEs.

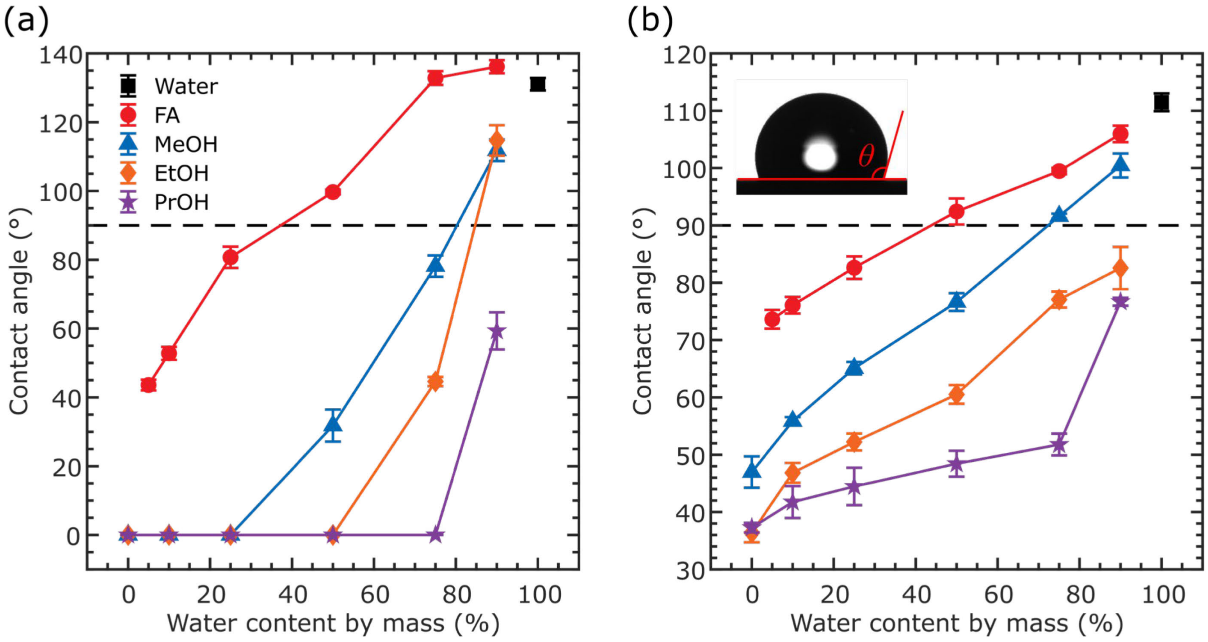

Figure IV-1*: Sessile drop contact angles, θ, on (a) graphite and (b) PTFE for an array of liquid CO2R products as a function of water content by mass. An example image of a sessile water droplet on PTFE is provided in panel (b) to demonstrate the position of θ.*

Beyond experimental measurements of the apparent contact angles of test fluids, γ can be used as a common predictor for the wettability of different fluid mixtures.[119] With the previous θ measurements, we can construct Zisman plots (**Figure IV-2**) to predict the critical surface tension, γ_{C0}, for complete wetting ($\theta = 0°$) and the surface tension at the cylindrical capillary transition composition, γ_{C90}, ($\theta = 90°$) for both graphite (**Figure IV-2a**) and PTFE (**Figure IV-2b**). We fit the data (black open circles) for each surface with quadratic functions (red lines), which is reasonable based on previous analyses that used similar empirical fits.[120] We then predict γ_{C0} values of 34.8 mN m^{-1} for graphite ($R^2 = 0.93$, $RMSE = 4.1$ mN m^{-1}) and 21.9 mN m^{-1} for PTFE ($R^2 = 0.97$, $RMSE = 2.4$ mN m^{-1}). We performed a similar analysis using a secondary set of well-defined test fluids and determined γ_{C0} to be 14.8 mN m^{-1} for PTFE. These data (**Table IV-4**) along with an additional Zisman plot and linear empirical fit (**Figure IV-12**) can be found in Appendix B. As can be seen for graphite, the data below 34.8 mN m^{-1} represent the product compositions that completely spread when contacting the solid. Note that none of the liquids tested had sufficiently low surface tensions to completely wet PTFE, so the empirical fit is needed to estimate γ_{C0}. The γ_{C90} for graphite and PTFE are predicted to be 45.2 mN m^{-1} and 47.2 mN m^{-1}, respectively. These values are useful for predicting sign changes in P_{C}, as will be considered in the next section. For comparison, Zisman reported a γ_{C90} of ca. 40 mN m^{-1} for PTFE,[120] but did not report a value for graphite, which is reasonable given that wettability of carbon surfaces vary widely depending on allotrope.[54] As such, microscopically smooth bulk materials that can serve as proxies for carbon particles or fibers remain elusive.[55]

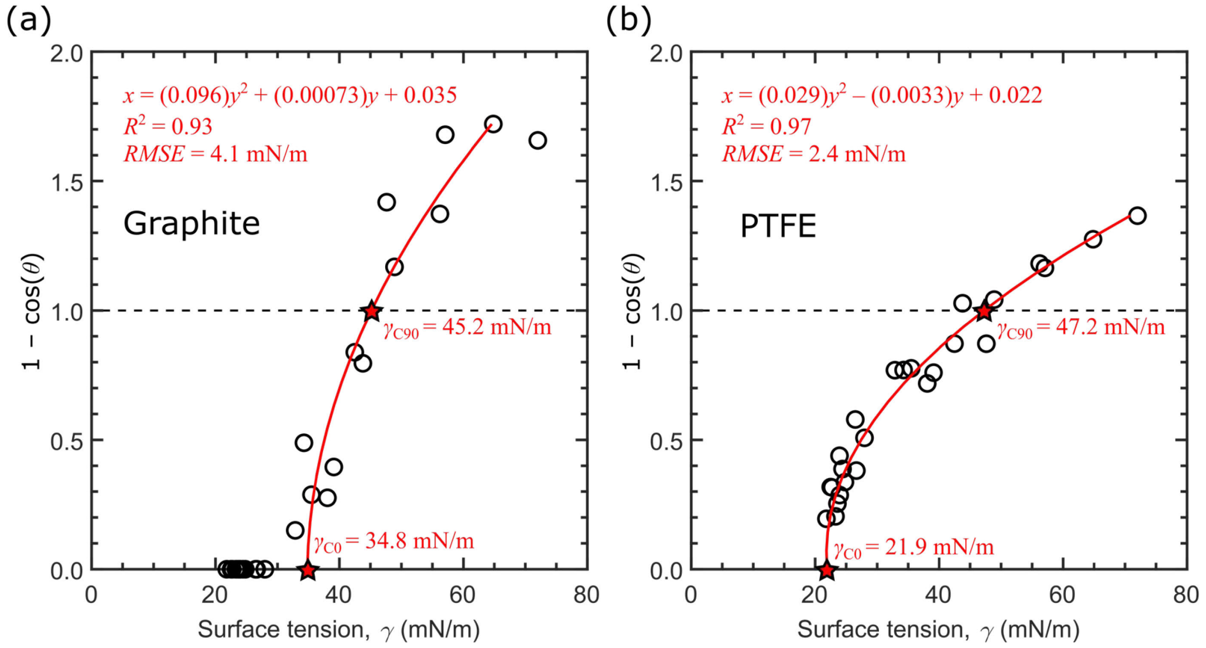

***Figure IV-2**: Zisman plots for (a) graphite and (b) PTFE with all the CO2R test liquids are used to predict wettability with surface tension, γ, as a common descriptor. Empirical quadratic fits (x = γ, y = 1 – cos(θ)) are plotted in red and are used for determining critical surface tensions (☆ markers), such as γ_{C0} and γ_{C90}, associated with each material.*

5. *Operating Envelopes Are Mapped Using Electrolysis Mass Balances*

5.1. Model Formulation

While ex situ contact angle data only provide qualitative insights on wettability for porous electrodes, such understanding informs materials selection for different classes of reactions. Here, we use wettability data in combination with a simple mass balance model around the cathode reaction zone to estimate ranges of feasible operating conditions before liquid product enrichment near the gas-liquid-solid interface would be expected to induce electrode flooding. A mass balance model represented by the schematic in **Figure IV-3** accounts for the mass flow rates of water and organic products to/from a well-mixed liquid phase control volume. The results and possible implications of changing electrolyzer set points are primarily discussed in the context of the widely studied flowing liquid electrolyte configuration.[29,36,37,40,70,106,107,115,137–146] However, some recently reported cell configurations can generate salt-free aqueous-organic mixtures by integrating polymer electrolyte components (dense polymer electrolyte membrane,[112] porous polymer electrolyte,[133] or ionomer-coated packed beads[38]). Although the model framework is inspired by cells that use a flowing electrolyte, the zero-dimensional mass balance approach can serve to bound the operating space of CO2R systems without assuming device-specific geometry. It should also be noted that this model cannot predict location-specific flooding susceptibility based on operating conditions and cell geometry.

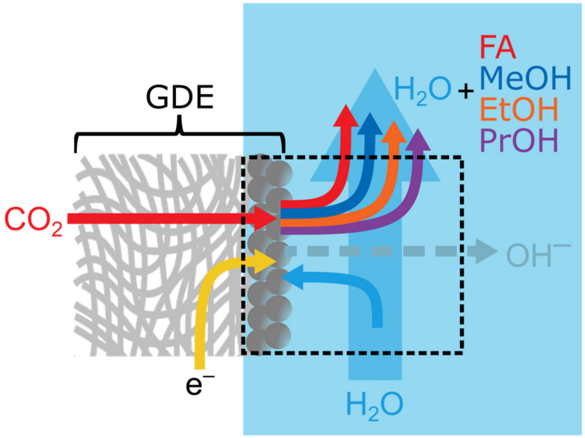

Figure IV-3: *Electrolyzer mass balance model schematic. Water is fed to the cathode GDE where* CO_2*, water (*H_2O*), and electrons (*e^-*) are consumed within the catalyst layer to produce liquid organic components. The exiting stream contains an aqueous-organic mixture. We do not include the contributions of hydroxide (*OH^-*) ions and other anions on the overall mass balance or liquid phase properties.*

As shown by Equations (IV.2) and (IV.3), respectively, Faraday's law of electrolysis connects the mass flow rates for product generation, $\dot{m}_{\mathrm{P,rxn}}$, and water consumption, $\dot{m}_{\mathrm{W,rxn}}$, at the cathode to the current (I) and one of the two stoichiometric constants, z_{P} and z_{W}, which correspond to the number of electrons per mole of product generated and water consumed, respectively.

$$\dot{m}_{\mathrm{P,rxn}} = \frac{I}{z_{\mathrm{P}}F} M_{\mathrm{P}} \tag{IV.2}$$

$$\dot{m}_{\mathrm{W,rxn}} = \frac{I}{z_{\mathrm{W}}F} M_{\mathrm{W}} \tag{IV.3}$$

In these equations, F is the Faraday constant, M_{P} is the molar mass (kg mol^{-1}) of a product species, and M_{W} is the molar mass of water. The mass flow rate of feed water, $\dot{m}_{\mathrm{W,in}}$, shown by Equation (IV.4), is defined as a function of the inlet volumetric sweep rate, Q, and the density of water, ρ_{W}.

$$\dot{m}_{\mathrm{W,in}} = \rho_{\mathrm{W}} Q \tag{IV.4}$$

Generally, the *sweep rate* of liquid electrolyte impacts product flux away from the catalyst layer to the bulk electrolyte and, by extension, the distribution of product concentrations along the reactor length and at the exit. In this treatment, we select Q directly (mL min^{-1}) to regulate product dilution for a given current (mA), but this ability to independently control product removal and tune dilution would be hampered in polymer-electrolyte-based cells as alternative flux mechanisms, like evaporation and membrane transport, are less readily controllable.[112]

We implement material balances around electrons, water, and liquid reaction products to directly calculate the total mass flow rate exiting the reactor, $\dot{m}_{\text{out}}$, as defined by Equation (IV.5), while ignoring dissolved gases (e.g., CO_2, CO, hydrogen, etc.) and dissociated ions such as hydroxide (OH^-) produced from the cathodic half-reactions as well as bicarbonate (HCO_3^-) and carbonate (CO_3^{2-}) that form as a result of carbonation reactions.[73] We also choose to set the product feed rate, $\dot{m}_{\text{P,in}}$, to zero in this study.

$$\dot{m}_{\text{out}} = \left(\dot{m}_{\text{W,in}} - \dot{m}_{\text{W,rxn}}\right) + \left(\dot{m}_{\text{P,in}} + \dot{m}_{\text{P,rxn}}\right) \tag{IV.5}$$

Through substitution, we arrive at Equation (IV.6), which defines the product mass fraction, x_{P}, as the total product mass divided by the total mass exiting the reaction zone as a function of total current, I, and inlet water volumetric sweep rate, Q.

$$x_{\text{P}} = \frac{\dot{m}_{\text{P,in}} + \dot{m}_{\text{P,rxn}}}{\dot{m}_{\text{out}}} = \frac{\dot{m}_{\text{P,in}} + \dfrac{I}{z_{\text{P}}F} M_{\text{P}}}{\left(\rho_{\text{W}} Q - \dfrac{I}{z_{\text{W}}F} M_{\text{W}}\right) + \left(\dot{m}_{\text{P,in}} + \dfrac{I}{z_{\text{P}}F} M_{\text{P}}\right)} \tag{IV.6}$$

Here, I can either represent a partial current towards a target product or, assuming 100% faradaic efficiency, a total current. The water mass fraction, x_{W}, is readily determined from x_{P} by using Equation (IV.7) because we assume a binary mixture in the liquid phase.

$$x_W = 1 - x_P \tag{IV.7}$$

Each cathodic half reaction consumes CO_2, H_2O, and electrons and produces hydrogenated products and OH^- as shown in **Table IV-1**. Included are the relevant stoichiometric constants—n_P (the number of moles of CO_2 per mole of product), z_P, and z_W—as well as M_P for each product. We convert from a molar basis to a mass basis because it can be more convenient to work in a laboratory setting with mass (or weight) fractions at high solute concentrations.

***Table IV-1**: CO2R half-reaction stoichiometry for liquid products*

Half reaction	n_P **(mol CO_2/mol P)**	z_P **(mol e/mol P)**	z_W **(mol e/mol W)**	M_P **(g/mol P)**
$CO_2 + 2\ e^- + H_2O \rightarrow HCOO^- + OH^-$	1	2	2	46.03
$CO_2 + 6\ e^- + 5\ H_2O \rightarrow CH_3OH + 6\ OH^-$	1	6	6/5	32.04
$2\ CO_2 + 12\ e^- + 9\ H_2O \rightarrow C_2H_5OH + 12\ OH^-$	2	12	12/9	46.07
$3\ CO_2 + 18\ e^- + 13\ H_2O \rightarrow C_3H_7OH + 18\ OH^-$	3	18	18/13	60.09

This simple mass balance analysis enables consideration of the cumulative impact of water consumption and organic product generation on the physical properties of the solution and the wettability of the electrode. Note that the stoichiometric constants used in this model only account for the water consumption in cathode half-reactions, as the microenvironment local to the electrode-electrolyte interface will determine flooding. However, in a full cell water is generated at the anode during the oxygen evolution reaction. Depending on the cathode reaction stoichiometry, this source could offset some or all the water consumption (**Table IV-7**). For example, there is no net water consumed for the conversion of CO_2 to formate/FA, but CO2R-to-alcohols reactions still result in net water consumption. By focusing on the cathode water consumption, this model estimates a conservative upper bound for organic product concentrations anticipated for a given chemistry, current, and liquid sweep rate.

5.2. Model Results and Discussion

We have constructed composition contour plots for FA, MeOH, EtOH, and PrOH (**Figure IV-4**) by calculating x_P across many currents and flow rates. The *y*-axes are reported on a base-10 log scale for clarity across several magnitudes of flow rates. Composition isoclines, reported in product content mass (%, solid lines), start at 0.1, 1, and 10% and then continue from 10–100% in increments of 10%. According to Equation (IV.2), sweeping the current from 0–1000 mA at fixed Q results in a linear increase in the production rate, while increasing Q from 0.001–1 mL min^{-1} at fixed I decreases x_P due to their inverse relation. The product composition contours generally shift downward with increasing number of electrons transferred (i.e., deeper reduction products) and increasing molar mass. The exception is FA, which has a similar molar mass to EtOH. FA composition is less sensitive to Q at fixed I, whereas the alcohols are more likely to reach high concentration through modest changes to Q.

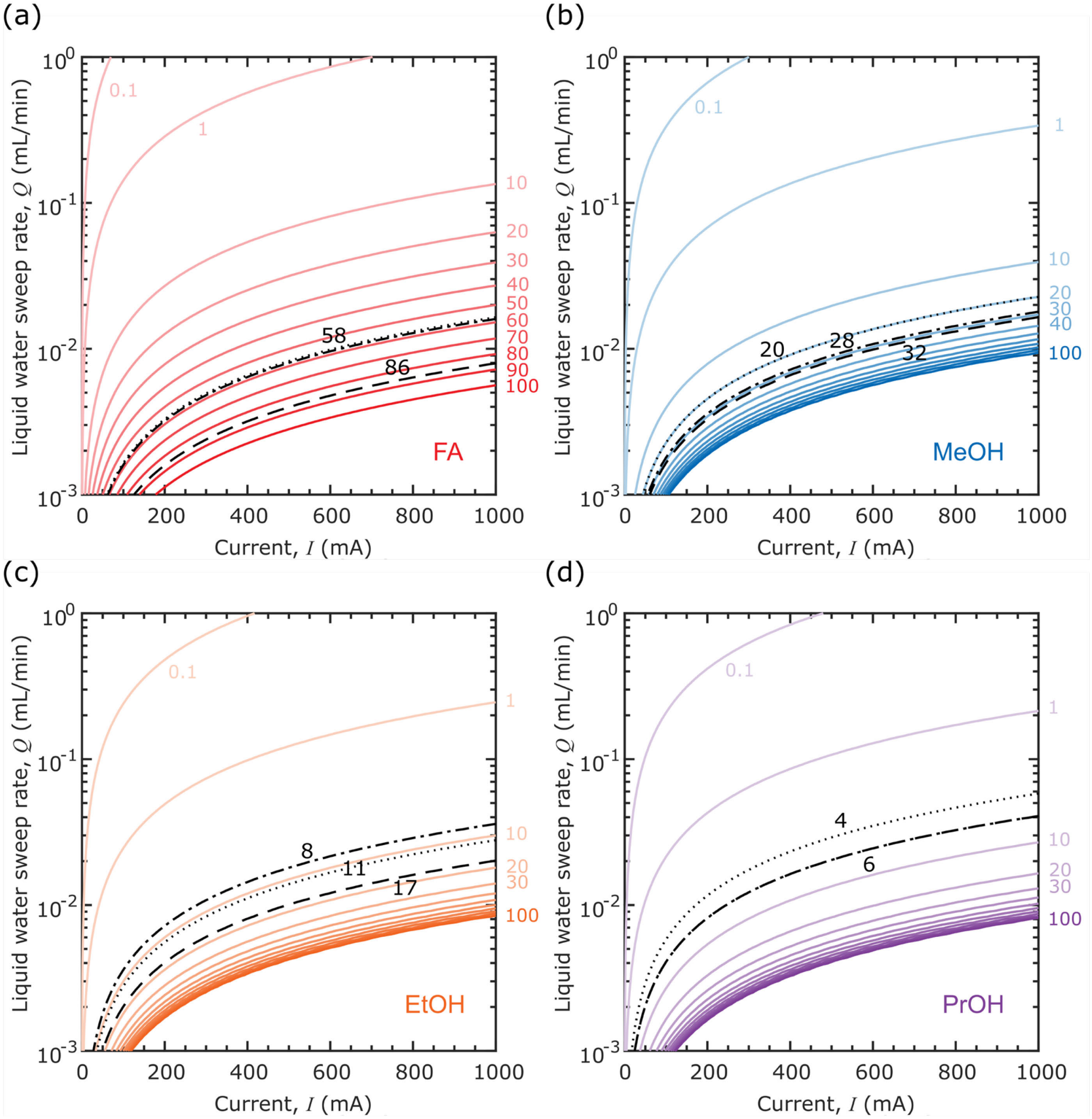

***Figure IV-4**: Liquid product concentration contours, x_P, reported in product content by mass (%), is calculated for (a) FA, (b) MeOH, (c) EtOH, and (d) PrOH as a function of liquid inlet water flow rate and current by using a mass balance around a hypothetical CO_2 electrolyzer with a flowing electrolyte stream. The additional black dashed lines correspond to the measured (– · –) and theoretically predicted (47 mN/m from this work, · · · and 40 mN/m from Zisman,*[120] *– – –) $\theta = 90°$ point on PTFE at which the mixture transitions from non-wetting to wetting.*

Determining 90°-threshold compositions from ex situ contact angle data allows us to estimate a band of operating conditions that may lead to an unfavorable P_C sign change (i.e., from positive to negative). We use wettability metrics for PTFE to represent GDE stability because they are assumed to be invariant to mild voltage biases within the electrode. In contrast, graphite is the more polarizable GDE component, so we may anticipate that its wettability will increase as a function of electrode voltage in accordance with electrowetting phenomena.[147,148] The measured transition composition, here, corresponding to a measured 90° contact angle on planar PTFE, is indicated with a black dot-dash (– · –) line for each of the product subpanels in **Figure IV-4**. These compositions were determined by interpolating between measured data points (**Figure IV-11**, Appendix B). If making predictions using a Zisman rule, all liquids with γ below that of a transition value, which is either 47 mN/m (this work, · · ·) or 40 mN/m (Zisman, – – –)[33], should wet PTFE with a contact angle less than 90°. We estimate the transition composition for each CO2R product by finding the water composition at which the γ curves (**Figure IV-10b**, Appendix A) reach the 90°-threshold. While there are discrepancies between the measurements and predicted isoclines, the differences between the operating conditions needed to achieve each composition are relatively minor. At flow rates above each transition line, the sweep stream provides enough water to the reaction zone at a given current to keep the product composition below the critical imbibition point. Put another way, for a given sweep rate, the electrochemical conversion rate is slow enough that enrichment of organic species in the reaction zone is not so great as to lead to flooding.

In agreement with the contact angle measurements, the ordering and position of the transition composition isoclines in *Q-I* space align with the γ and polarity of the organic species (**Figure IV-10b**, Appendix A). Plotting the isoclines for different liquid species together (**Figure IV-5**) is an effective way for determining if electrolyzer operating conditions need to be tailored according to product identity. For example, although FA mixtures reach the threshold at much higher concentrations as compared to the alcohol mixtures, the operating conditions required to reach zero capillary pressure are similar for species of equivalent polarity. At the extremes of species wettability (i.e., PrOH versus FA), however, the Q required to induce a contact angle transition varies by nearly an order of magnitude at the same I.

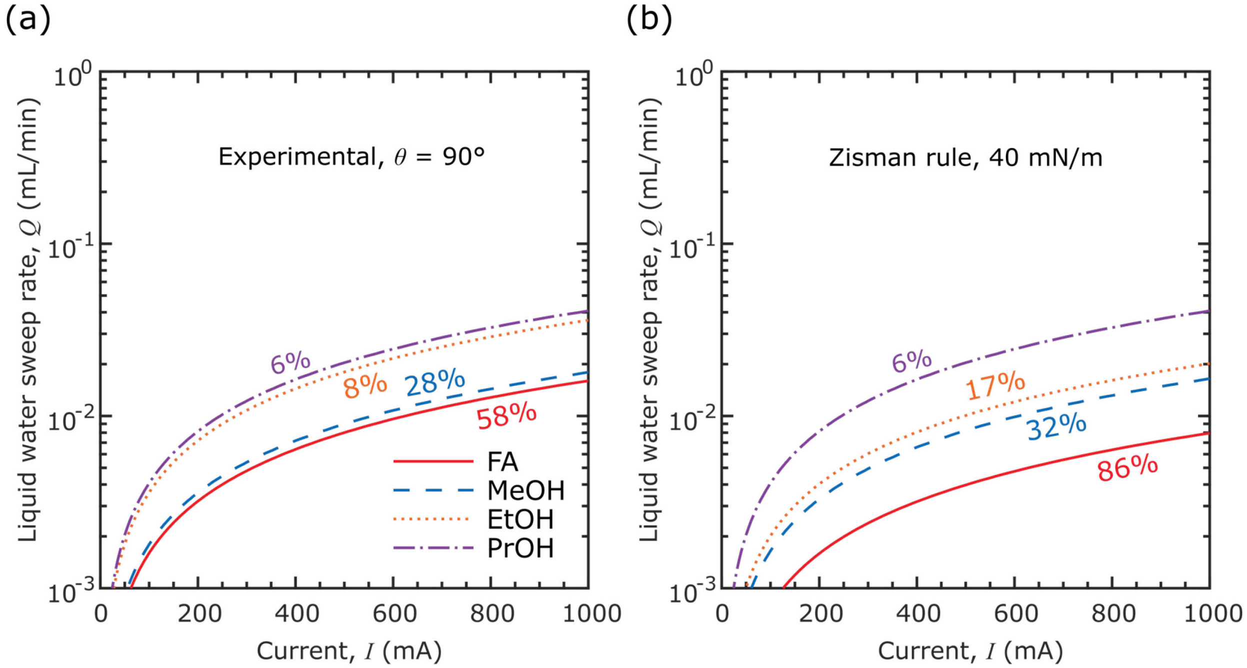

Figure IV-5*: Transition CO2R product mixture composition contours corresponding to $\theta = 90°$ on PTFE (when $P_C = 0$ bar) as (a) measured in this work and (b) predicted from a Zisman rule surface tension threshold ($\theta = 90°$) of 40 mN m^{-1} for nonpolar solvents on PTFE.*[120]

Now with x_P mapped to different operating conditions, we can connect the wettability of the various liquid mixtures to a simple prediction of equilibrium P_C using Equation (IV.1), which is helpful for understanding the pressure differentials required to maintain a stable gas-liquid-solid interface in a gas fed CO_2 electrolyzer. Again, here we do not initially consider complex physical and geometric features evident in real GDE materials (e.g., thickness, pore size distribution, fiber spacing, particle sizes, mixed wettability)[46,149] to determine P_C or flooding dynamics because simplified models suffice for capturing general trends in capillarity. However, further analyses explicitly considering saturation or wetting dynamics in electrodes with finite volume could expand from these zeroth-order analyses of interfacial P_C and refine predictions of stable operating envelopes.

We compute P_C at various levels of water content, x_W, (**Figure IV-6**) in order to translate product composition to equilibrium interfacial pressure along the contours in **Figure IV-4**. The P_C data associated with this figure are reported in **Table IV-8** in Appendix C. We employ interpolated PTFE contact angle values (**Figure IV-11**) to calculate P_C with diameters of 30 µm and 0.1 µm as representative of the effective pore dimensions for macroporous carbon fiber substrates and microporous layers, respectively.[46] As the pore diameters differ by a factor of 300, the P_C scales accordingly. Results can be interpreted for each pore by using the left (30 µm) and right (0.1 µm) vertical axes of **Figure IV-6**. Generally, the smaller pores characteristic of a microporous layer—assuming it is crack-free—exhibit greater capillary pressure values as compared to the larger pores characteristic of a carbon fiber substrate.[150] For a given set of intrinsic solid-liquid affinities (specified by γ and θ), the pore diameter can serve to modulate the driving force for imbibition. If we were to overlay the P_C outputs onto the corresponding composition contours of **Figure IV-4**, these new isoclines would serve to approximate the magnitude of the maximum liquid-gas pressure differential that a GDE could withstand while still maintaining interfacial stability. For example, once P_C becomes negative, a porous electrode may spontaneously imbibe the liquid phase and become flooded. This coarse approach allows for the insertion of P_C models that are uniquely suited to specific electrode microstructure, layer composition, and surface functionalization. Comparing the operating envelope for each liquid-PTFE combination as a function of current and flow rate is useful for predicting if any notable physical changes to the system pressure equilibrium emerge when targeting different CO2R products. The critical composition lines generally shift upward from FA to PrOH, according to chain length, depth of electroreduction, and decreasing polarity, which taken together indicate that the allowable operating space will narrow as the deeper CO2R products considered in this subset are pursued.

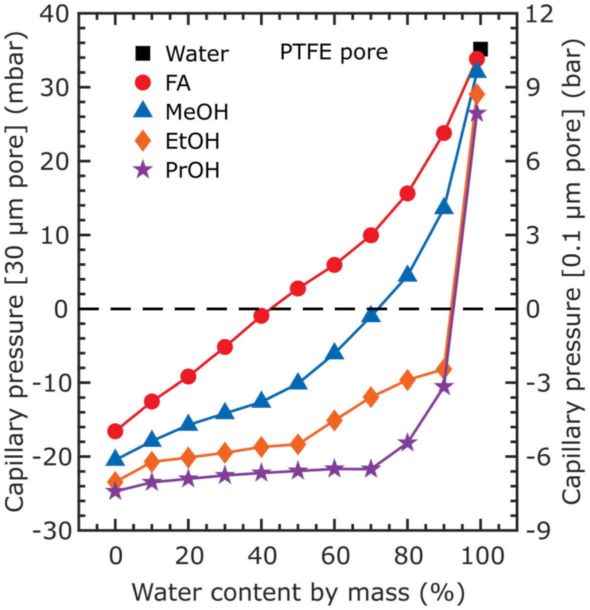

Figure IV-6*: Capillary pressure, P_C, is calculated as a function of water content by mass, x_W, and CO2R liquid product for cylindrical PTFE pores with diameters of 30 µm (left axis) and 0.1 µm (right axis), which are representative of characteristic pore sizes in carbon fiber substrates and microporous layers, respectively.*

These results suggest that the operating envelope for FA is likely to be wider than for alcohols for PTFE-containing GDEs. However, when considering that many existing commercial GDEs are composite materials (conductive metal and hydrophobic PTFE components) with mixed wettability properties (*vide supra*, oxygen depolarized cathodes), these contours may constitute an *optimistic* set of conditions correlating to P_C transition. Using composite GDEs may ultimately prove necessary when scaling to larger cell areas due to enhanced through-plane conductivity as compared to the PTFE-supported electrodes. Despite the greater flooding risk inherent to this category of GDEs, which are necessarily composed of high energy conductive constituents, there are still opportunities to tune wet-proofing content to achieve favorable P_C envelopes[70] as well as high CO2R activity and faradaic efficiency.[59,106]

This mass balance analysis serves to estimate P_C thresholds for porous electrodes in contact with low surface tension liquid mixtures. However, what is not evident from the results until now is that pore geometry and surface wettability *together* determine P_C in real porous media. Therefore, in the next two sections we briefly discuss the potential for leveraging microstructure and surface chemistry to engineer more robust porous electrodes for CO2R-to-liquids electrolyzers.

6. *Opportunities for Selecting Electrode Microstructure to Prevent Spontaneous Flooding*

Using idealized cylindrical pore geometry alone to determine electrode stability thresholds suggests that liquid mixtures spontaneously enter porous media precisely at the 90° threshold. However, porous electrodes often consist of non-ideal material geometries, such as packed particles or entangled fibers, that can exhibit non-intuitive filling and draining behaviors.[149] Inspired by the earlier works of Purcell[149] and Mason & Morrow[151], Forner-Cuenca and colleagues developed a constricted pore model and used it, in part, to explain why patterned hydrophilic channels in fibrous gas diffusion media do not necessarily spontaneously fill with water.[46,152] This adaptation of the Washburn model framework shown in Equation (IV.8) appears similar to Equation (IV.1), but allows for a pore radius, $r = r(z)$, that varies as a function of longitudinal position, z, and introduces a new variable called the filling angle, $\alpha = \arctan(\mathrm{d}r/\mathrm{d}z)$, which changes according the local derivative of the pore profile.

$$P_{\mathrm{C}} = P_{\mathrm{L}} - P_{\mathrm{G}} = \frac{-2\gamma\cos(\alpha+\theta)}{r} \qquad \text{(IV.8)}$$

It is important to note that $P_C = P_C(z)$ since the pore diameter varies according to the longitudinal position along the pore channel. Therefore, the operable output of this model is the *maximum* *capillary pressure* along the channel length, since the location of highest resistance determines whether the liquid will tend to spontaneously advance into, or flood, the pore. For this analysis, we use a maximum pore diameter, d_{max}, of 30 μm, and fiber diameter, d_{fiber}, of 10 μm as representative of carbon fiber substrates.[46] A schematic of the pore geometry (**Figure IV-13**) along with more details about the modified capillary pressure expression and the model's parameter sensitivities (**Figure IV-14, Figure IV-15**, and **Figure IV-16**) are provided in Appendix D.

Exploring the resistive effect imparted by α, we calculate the maximum P_{C} as a function of the constriction aspect ratio, $d_{\mathrm{min}}/d_{\mathrm{max}}$, or the ratio between minimum and maximum pore diameters. Each contour in **Figure IV-7** corresponds to a generic CO2R liquid aqueous-organic mixture in contact with PTFE surface. The surface tension and PTFE contact angle combinations (γ, θ) for each contour are functionally defined by the polynomial fit shown in **Figure IV-2b**. The results reported in this plot indicate that, as might be expected, solutions with $\theta_{\mathrm{PTFE}} > 90°$ have a maximum $P_{\mathrm{C}} > 0$ for all constriction ratios. However, mixed results emerge for solutions with $\theta_{\mathrm{PTFE}} < 90°$. From this plot, we see that the maximum P_{C} values for solutions with contact angles slightly lower than 90° start negative but eventually cross the zero capillary pressure line. These results support the previously validated observation that positive pressure differentials ($P_{\mathrm{L}} - P_{\mathrm{G}} > 0$) are sometimes required to fill constricted ($d_{\mathrm{min}}/d_{\mathrm{max}} < 1$), hydrophilic pores.[46] Through this simple analysis, we can see the inherently protective effect of constricted pore geometry with regards to electrode flooding. Considering this possibility, we suggest that porous media be selected according to specifics of the pore geometry (i.e., packed particles or fibers) in addition to other factors (e.g., pore size distribution, pore connectivity, thickness, etc.). However, we cannot neglect the fact that adding constrictions to the porous substrate (i.e., decreasing $d_{\mathrm{min}}/d_{\mathrm{max}}$) could negatively impact other transport phenomena in the GDE (e.g., gas phase effective diffusivity) by increasing the tortuosity and/or decreasing overall permeability.[153] The extent of this tradeoff has yet to be determined in this context.

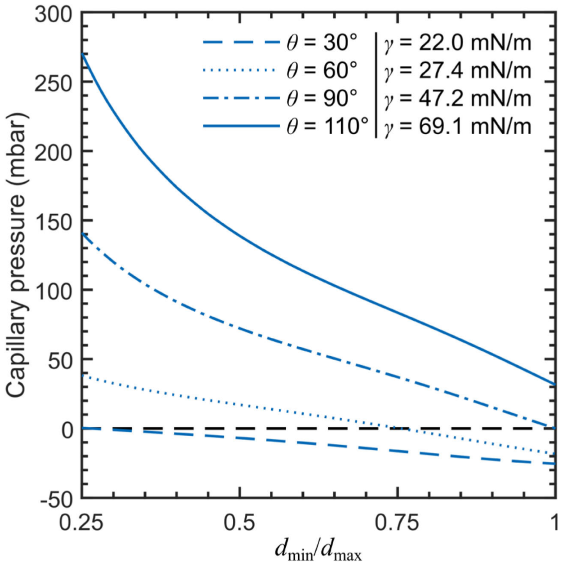

Figure IV-7: *Maximum capillary pressure is calculated for a constricted cylindrical pore (d_{max} = 30 µm, d_{fiber} = 10 µm) as a function of the ratio between minimum and maximum pore diameters, d_{min}/d_{max}. The contour lines correspond to different combinations of (γ,θ) for a generalized liquid CO2R product on PTFE as defined by the (red) Zisman plot polynomial fit line shown in* ***Figure IV-2b****. By adding a constriction (d_{min}/d_{max} < 1) to an otherwise cylindrical channel, we see that a positive pressure difference is required to flood the pore for liquid mixtures with θ < 90°.*

7. Opportunities for the Integration of Oleophobic Materials

Oleophobic treatments constitute a readily-available modification to GDEs that may better suit aqueous-organic environments.[120] Introducing oleophobicity to PTFE membranes has enabled their use as venting materials in electronic devices filled with organic solvents, such as lithium-ion batteries.[154] Although we cannot necessarily measure the intrinsic wettability of porous materials with macroscopic sessile drop methods,[45,155] apparent contact angles enable comparisons between different samples. Using the same methods as described for solid PTFE (vide supra), we measured the apparent contact angles (**Figure IV-8**) of the test liquids on two different porous sheets: untreated PTFE (PM21M, Porex®) and oleophobic PTFE (PMV15T, Porex®). The raw data are reported in **Table IV-5** and **Table IV-6**, which can be found in Appendix B. The non-wetting envelope (ca. $\theta > 90°$) for all the test liquids is expanded for the porous materials as compared to the dense, flat PTFE sheet shown in **Figure IV-1**. As mentioned earlier, surface roughness and entrapped gases can increase the apparent phobicity/philicity of a given solid-liquid-gas combination. However, while the untreated porous PTFE is eventually wetted by lower surface tension mixtures, the oleophobic PTFE does not exhibit any $\theta < 90°$. These initial results demonstrate that appropriate modifications to extant and proven material sets may greatly improve wettability characteristics. While the oleophobic treatment here was applied to a PTFE substrate,[156] it could, in principle, be expanded to other polymer, metal, or carbon substrates to improve liquid repellency or tune wettability, ideally with a covalent bond to improve adhesion.[157] Durability under alkaline CO_2 electrolysis conditions is paramount, so it is advantageous that disclosed compositions for oleophobic fluoropolymer coatings are already functionally compatible with proven polymer additives such as PTFE.[156,158,159] However, validation of coating compatibility in this application requires the development of rigorous protocols that emulate a variety of extreme scenarios (solvent exposure, elevated temperatures, physical abrasion, etc.).[160,161] Finally, although the optimal distribution of oleophobicity throughout the GDE subdomains (i.e., macroporous substrate, microporous layer, and/or catalyst layer) is not explored in this work, it should be considered in future studies.

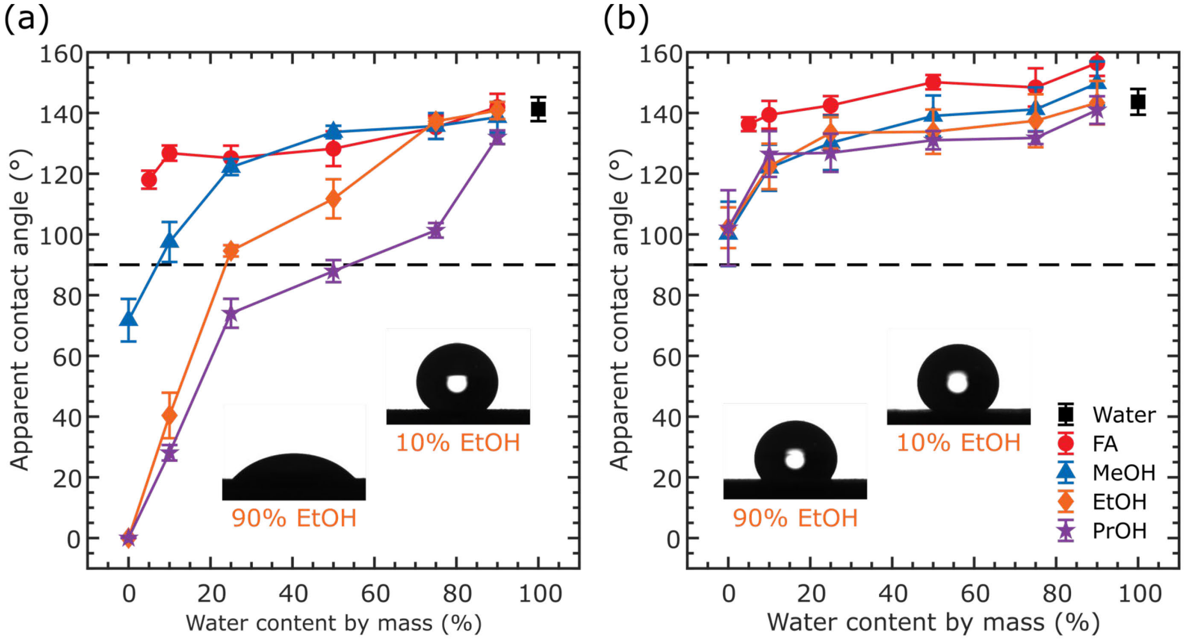

Figure IV-8*: Apparent sessile drop contact angles for selected CO2R product liquids as a function of water content by mass on (a) Porex® PM21M expanded PTFE and (b) Porex® PMV15T oleophobic treated sintered PTFE sheets.*

8. *Conclusions and Outlook*

The generation of concentrated liquid products in CO_2 electrolyzers is an economically attractive operating objective that may be attainable by targeting high current to liquid sweep rate ratios. Under such conditions, the propensity to flood cathode GDEs may increase, in part, due to enrichment of low-surface-tension liquid products. Thus, connecting electrolyzer set points to gas diffusion media wettability/capillarity is paramount for understanding device durability. By combining sessile drop contact angle measurements, electrolyzer mass balances, and capillary pressure models, we can map CO2R liquid product compositions to cell operating conditions (liquid sweep rate and applied current) and, subsequently, estimate the liquid-gas pressure differentials that might result in electrode flooding. Using this simple framework, we predict that FA-generating electrolyzers could be more resistant to flooding than the equivalent alcoholproducing electrolyzers when targeting high-mass-fraction effluents. In fact, we predict that alcohol concentrations <30% by mass could flood a GDE in the absence of additional pressure control. After expanding the capillary pressure model to include pore constrictions, we observe that it may be possible to exploit the complex capillarity behavior of realistic microstructures to engineer more robust GDEs. We also see an opportunity to tune the wettability characteristics of current GDE material sets via oleophobic treatments, with the goal of expanding the stable operating envelope for CO2R-to-alcohols electrolyzers. By exploring some of the material challenges that face CO2R during the necessary scale-up phase, we hope to inspire additional researchers in this field to consider these obstacles at an early stage of technology development.

ACKNOWLEDGMENTS

The authors acknowledge the financial support of DOE SBIR Contract #DE-SC0015173. The authors kindly thank Prof. Karen K. Gleason and the members of her group for access to and support using their goniometer system to measure contact angles. The authors also thank Lauren E. Clarke and Charles T.-C. Wan of the Brushett Research Group for insightful discussions. Finally, we would like to thank Porex® for providing us with samples of its porous PTFE and oleophobic-treated PTFE materials that were used in this study.

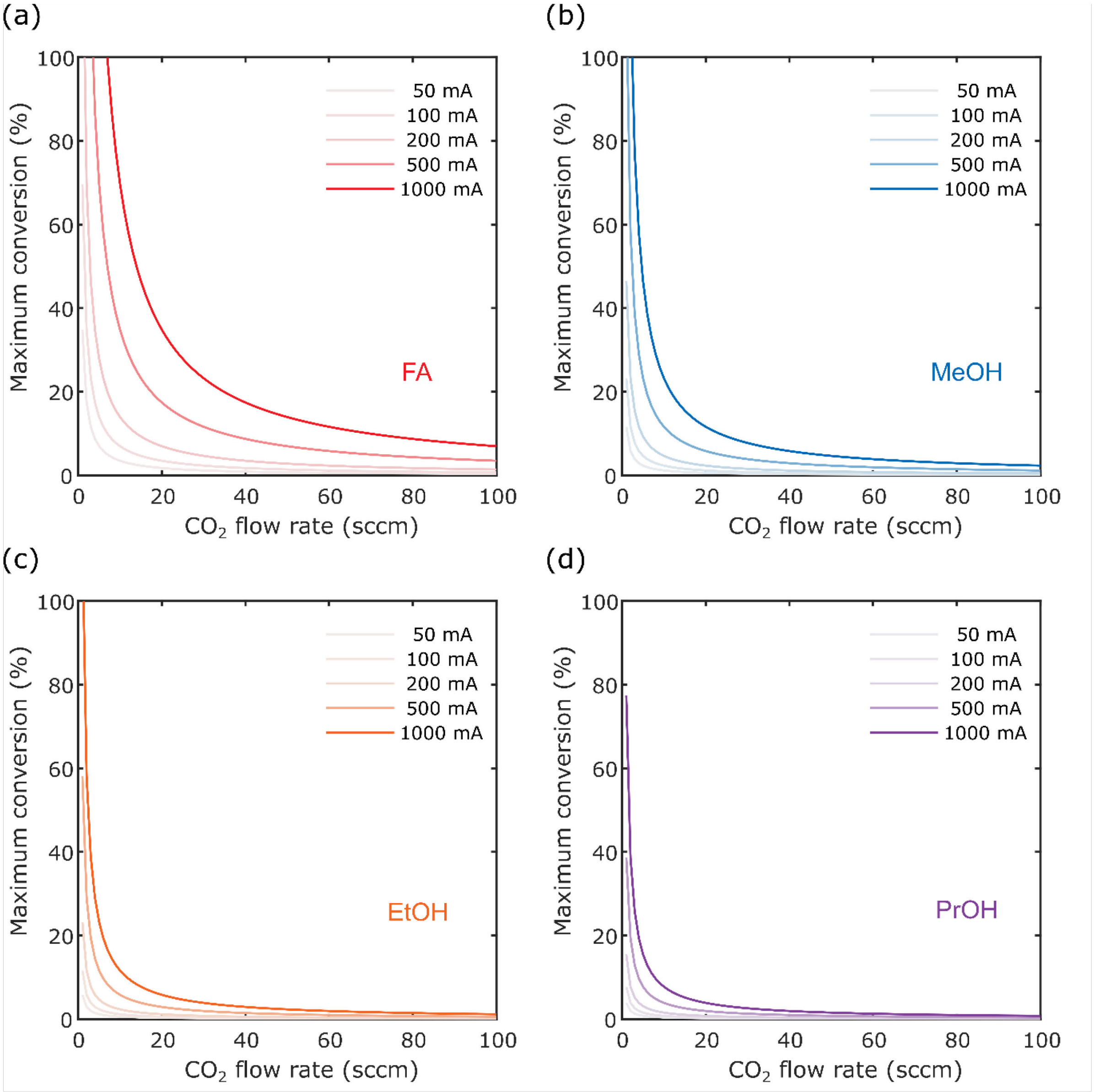

Figure IV-9: *Maximum single pass conversion of CO_2 (i.e., 100% faradaic efficiency) as a function of inlet CO_2 mass flow rate and current for (a) FA, (b) MeOH, (c) EtOH, and (d) PrOH.*

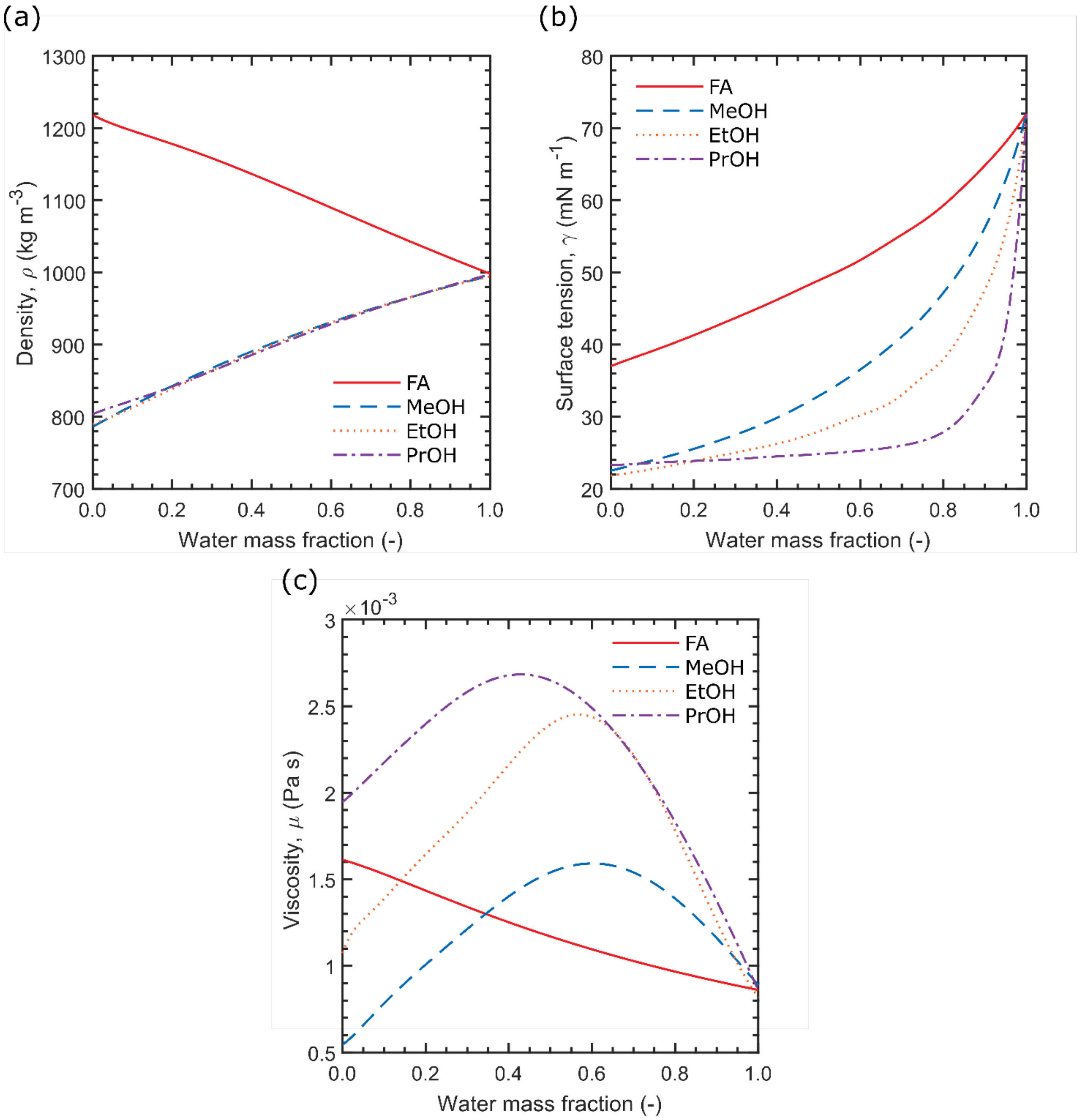

***Figure IV-10**: Physical properties: CO2R product liquid mixtures. Mixture properties spline and/or polynomial fits for (a) density, (b) surface tension, (c) and viscosity as a function of water mass fraction for FA, MeOH, EtOH, and PrOH. These physical data not measured by the authors were reportedly collected at ambient conditions (298.15 K and 1 atm).[10] Curves for interpolation were generated with either polynomial or spline fits.*

10. Appendix B: Contact Angle Measurements

10.1. Droplet Dispensing and Image Capture

The base plate containing the sample was taped to the goniometer stage using carbon tape. The camera, light, and automatic pipetting unit powered on, and the software was initialized for data collection. A 5-μL droplet was dispensed from the DI water reservoir and micro-transformers were used to focus the camera. Next, the pipet tip (200 μL Gel-Saver® Round Gel Loading Tip, USA Scientific) was rinsed three times with 250 μL of DI water. When working with liquids other than water, a 40-μL air pocket was pulled into the pipette tip created to provide separation between the DI water supply and the test liquid. Test liquid was pulled into the pipette tip in 40 μL batches prior to dispensing and droplet imaging.

The Drop Volume Control module within the DROPimage Advanced V2.7.02 software (rame-hart) was used to dispense 5-μL droplets. The embedded video capture module was used to record .avi video files for between 30–60 seconds at a rate of 30 frames per second. Droplets were transferred from the pipette tip to the sample surface using the micro-transformers to raise the goniometer stage up until liquid-solid contact was established. Once the droplet was in place, the stage was lowered back into focus with both the droplet and stage in focus for the video capture. A clean portion of the solid sample was used for each droplet trial by using the micro-transformers to laterally adjust the stage position. An aerosol duster was used to clean the surface of the samples so that more data could be collected.

10.2. Image Processing and Angle Determination

Contact angles were determined from recorded video files using DropPy V1.0.0a0, a Python-based goniometer software,[162] that was constructed and published by some of the authors. Contact angles were determined by fitting droplet edges with a two-parameter Bashforth-Adams model that is used to account for the effects of gravity on droplet shape. This approach is more robust than linear fits between the baseline and droplet tangent lines, especially when utilizing dense test liquids like diiodomethane (3.32 g cm^{-3}) or superhydrophobic (contact angles great than 145°) surfaces.[163] The reported contact angles averages from the first 10 seconds of each captured video at a processed image frequency of 1 frame per 2 seconds. For most droplets, a σ value of 1.0 was used for the edge detection Gaussian filter and a circle threshold of 10 pixels above the baseline was selected.

10.3. Processed Data

Table IV-2: *Contact angle data for graphite with an array of test liquids corresponding to CO2R products. These are the raw data corresponding to* ***Figure IV-1a***.

Test Surface	z_p	Test Liquid	Water mass fraction (%)	Contact angle (°)						
				Droplet 1	Droplet 2	Droplet 3	Droplet 4	Droplet 5	Mean (°)	Standard Deviation (°)
Graphite	--	Water	100	130.2	129.0	130.8	131.3	133.9	131.1	1.8
Graphite	2	FA	5	42.8	41.5	45.7	44.4	43.5	43.6	1.6
Graphite	2	FA	10	52.8	50.7	51.9	55.9	52.6	52.8	1.9
Graphite	2	FA	25	77.6	80.7	78.0	85.0	82.4	80.7	3.1
Graphite	2	FA	50	100.3	100.1	99.6	99.9	98.6	99.7	0.7
Graphite	2	FA	75	133.2	133.2	134.8	133.5	129.5	132.8	2.0
Graphite	2	FA	90	135.6	133.1	136.7	137.3	138.0	136.1	1.9
Graphite	6	MeOH	0	0.0	0.0	0.0	0.0	0.0	0.0	0.0
Graphite	6	MeOH	10	0.0	0.0	0.0	0.0	0.0	0.0	0.0
Graphite	6	MeOH	25	0.0	0.0	0.0	0.0	0.0	0.0	0.0
Graphite	6	MeOH	50	35.1	37.5	27.5	26.8	32.2	31.8	4.7
Graphite	6	MeOH	75	78.1	73.4	82.1	78.4	78.9	78.2	3.1
Graphite	6	MeOH	90	109.5	115.4	114.4	108.1	111.9	111.9	3.1
Graphite	12	EtOH	0	0.0	0.0	0.0	0.0	0.0	0.0	0.0
Graphite	12	EtOH	10	0.0	0.0	0.0	0.0	0.0	0.0	0.0
Graphite	12	EtOH	25	0.0	0.0	0.0	0.0	0.0	0.0	0.0
Graphite	12	EtOH	50	0.0	0.0	0.0	0.0	0.0	0.0	0.0
Graphite	12	EtOH	75	45.8	43.0	43.5	44.7	46.0	44.6	1.3
Graphite	12	EtOH	90	115.2	110.4	110.3	120.5	117.2	114.7	4.4
Graphite	18	PrOH	0	0.0	0.0	0.0	0.0	0.0	0.0	0.0
Graphite	18	PrOH	10	0.0	0.0	0.0	0.0	0.0	0.0	0.0
Graphite	18	PrOH	25	0.0	0.0	0.0	0.0	0.0	0.0	0.0
Graphite	18	PrOH	50	0.0	0.0	0.0	0.0	0.0	0.0	0.0
Graphite	18	PrOH	75	0.0	0.0	0.0	0.0	0.0	0.0	0.0
Graphite	18	PrOH	90	53.4	58.1	55.2	65.3	64.7	59.3	5.4

Table IV-3*: Contact angle data for PTFE with an array of test liquids corresponding to CO2R products. These are the raw data corresponding to* ***Figure IV-1b****.*

Test Surface	z_p	Test Liquid	Water mass fraction (%)	Contact angle (°)						
				Droplet 1	**Droplet 2**	**Droplet 3**	**Droplet 4**	**Droplet 5**	**Mean (°)**	**Standard Deviation (°)**
PTFE	--	Water	100	114.0	110.7	111.3	111.5	109.8	111.5	1.5
PTFE	2	FA	5	70.9	74.7	73.5	73.8	75.2	73.6	1.6
PTFE	2	FA	10	74.9	76.1	77.7	77.3	74.4	76.1	1.4
PTFE	2	FA	25	79.2	83.3	84.0	83.1	83.6	82.6	2.0
PTFE	2	FA	50	94.3	90.5	95.2	90.0	92.2	92.4	2.3
PTFE	2	FA	75	99.3	99.4	100.1	99.9	98.7	99.5	0.6
PTFE	2	FA	90	103.6	107.1	107.3	105.9	106.0	106.0	1.4
PTFE	6	MeOH	0	42.3	47.2	49.5	48.0	47.9	47.0	2.7
PTFE	6	MeOH	10	55.0	56.9	55.5	55.9	56.1	55.9	0.7
PTFE	6	MeOH	25	65.9	63.7	66.4	64.6	64.9	65.1	1.1
PTFE	6	MeOH	50	75.0	75.6	78.7	77.8	76.1	76.6	1.5
PTFE	6	MeOH	75	91.4	91.2	91.3	92.0	92.1	91.6	0.4
PTFE	6	MeOH	90	99.6	102.2	99.1	98.2	103.1	100.4	2.1
PTFE	12	EtOH	0	37.6	37.7	37.4	34.6	34.6	36.4	1.7
PTFE	12	EtOH	10	46.8	46.1	46.3	49.8	45.3	46.8	1.7
PTFE	12	EtOH	25	52.2	52.3	54.5	51.6	50.5	52.2	1.5
PTFE	12	EtOH	50	60.9	61.6	59.8	62.2	58.1	60.5	1.6
PTFE	12	EtOH	75	75.0	77.6	76.5	77.6	78.7	77.1	1.4
PTFE	12	EtOH	90	78.4	79.0	84.6	84.0	86.8	82.6	3.7
PTFE	18	PrOH	0	36.6	36.3	38.1	37.2	38.1	37.3	0.8
PTFE	18	PrOH	10	38.2	43.4	45.5	40.8	40.9	41.7	2.8
PTFE	18	PrOH	25	49.1	41.4	46.7	42.4	42.7	44.5	3.3
PTFE	18	PrOH	50	50.7	50.2	45.2	48.9	47.3	48.4	2.3
PTFE	18	PrOH	75	52.1	54.3	52.7	49.4	50.5	51.8	1.9
PTFE	18	PrOH	90	76.5	76.3	77.2	77.6	75.9	76.7	0.7

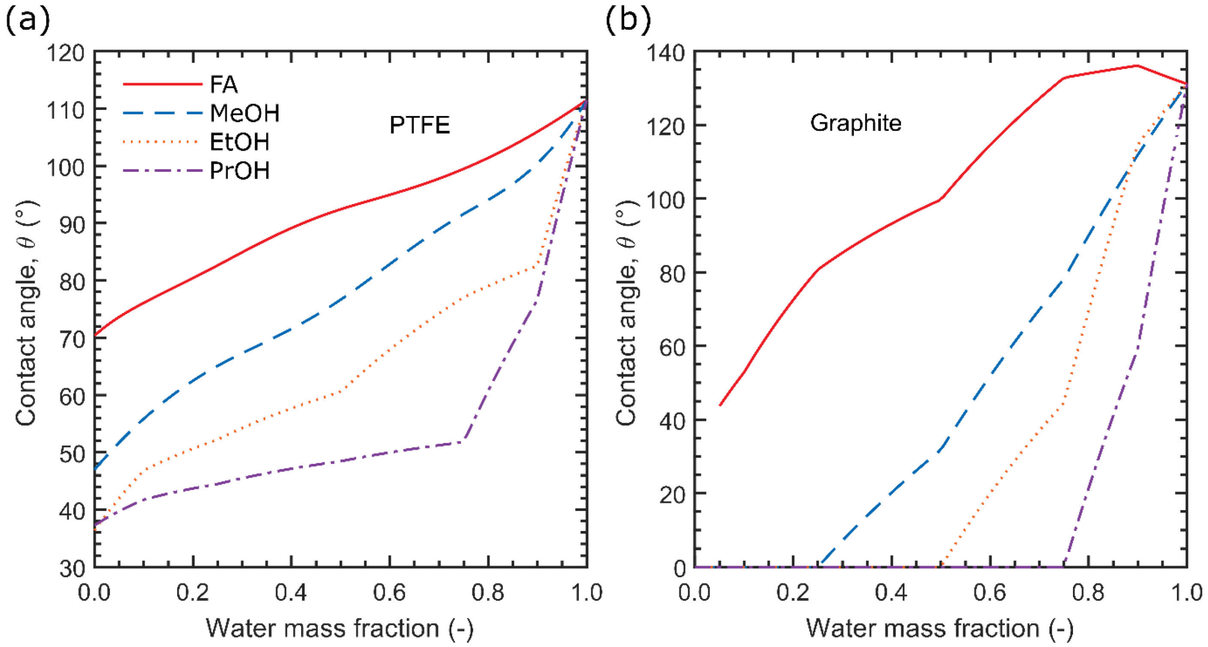

Figure IV-11*: Spline and/or polynomial fits for contact angleson (a) PTFE and (b) graphite as a function of water mass fraction for FA, MeOH, EtOH, and PrOH. These fits correspond to the data reported in* ***Figure IV-1****.*

***Table IV-4**: Contact angle data and relevant surface tension values for a validation set of test liquids are used to determine the surface energy of PTFE with a linear empirical fit.*

Test Surface	Test Liquid	Surface tension, γ (mN/m) [10]	Contact angle (°) Droplet 1	Droplet 2	Droplet 3	Droplet 4	Droplet 5	Mean (°)	Standard Deviation (°)
PTFE	Water	72	110.98	109.54	110.56	108.70	108.34	109.62	1.15
PTFE	Glycerol	64	98.36	101.96	99.56	98.84	100.22	99.79	1.41
PTFE	Diiodomethane	51	82.12	82.91	82.73	84.11	81.64	82.70	0.93
PTFE	1-propanol	23	30.30	33.61	32.10	39.68	41.72	35.48	4.96

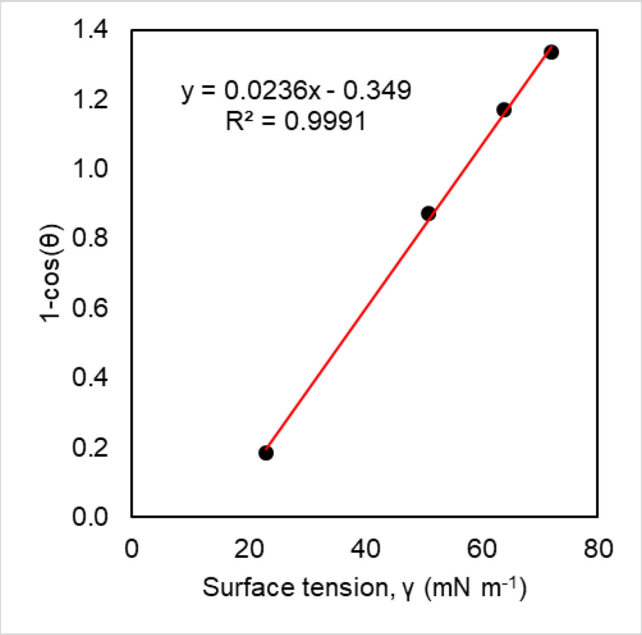

***Figure IV-12**: Zisman plot for PTFE using a validation set of test liquids. Test liquids ranging from low to high surface tensions were used. The test fluid identities, surface tensions, and contact angles measurements are reported in **Table IV-4**. The γ_C for PTFE, which is determined to be the x-intercept was determined to be 14.8 mN/m.*

***Table IV-5**: Apparent contact angle data for porous Porex® PM21M with an array of test liquids corresponding to CO2R products. These are the data corresponding to **Figure IV-8a**.*

Test Surface	z_p	Test Liquid	Water mass fraction (%)	Contact angle (°)						
				Droplet 1	Droplet 2	Droplet 3	Droplet 4	Droplet 5	Mean (°)	Standard Deviation (°)
PM21M	--	Water	100	144.6	137.6	137.6	140.4	146.2	141.3	3.9
PM21M	2	FA	5	118.3	120.2	119.9	112.9	118.8	118.0	3.0
PM21M	2	FA	10	130.9	126.7	124.5	126.7	125.1	126.8	2.5
PM21M	2	FA	25	123.0	120.1	131.1	126.3	125.2	125.1	4.1
PM21M	2	FA	50	123.9	137.4	130.4	125.3	124.3	128.2	5.7
PM21M	2	FA	75	128.8	135.7	138.6	136.0	137.4	135.3	3.8
PM21M	2	FA	90	146.6	144.7	143.9	137.4	137.3	142.0	4.4
PM21M	6	MeOH	0	60.1	72.1	72.8	75.1	78.6	71.7	7.0
PM21M	6	MeOH	10	87.5	94.6	102.0	99.7	103.8	97.5	6.6
PM21M	6	MeOH	25	118.2	121.3	123.5	125.2	122.7	122.2	2.6
PM21M	6	MeOH	50	132.3	132.8	134.1	137.2	132.4	133.7	2.1
PM21M	6	MeOH	75	128.3	138.5	138.3	135.8	137.6	135.7	4.3
PM21M	6	MeOH	90	129.9	140.5	139.1	140.8	142.8	138.6	5.1
PM21M	12	EtOH	0	0.0	0.0	0.0	0.0	0.0	0.0	0.0
PM21M	12	EtOH	10	39.1	28.9	49.5	41.4	43.0	40.4	7.5
PM21M	12	EtOH	25	93.2	92.6	94.4	97.4	95.2	94.6	1.9
PM21M	12	EtOH	50	107.3	112.8	122.5	107.1	108.9	111.7	6.4
PM21M	12	EtOH	75	136.1	137.0	137.4	138.9	137.1	137.3	1.0
PM21M	12	EtOH	90	142.7	141.9	139.1	136.8	143.6	140.8	2.8
PM21M	18	PrOH	0	0.0	0.0	0.0	0.0	0.0	0.0	0.0
PM21M	18	PrOH	10	30.7	29.1	24.6	NaN	28.0	28.1	2.5
PM21M	18	PrOH	25	81.6	73.2	68.9	74.7	71.7	74.0	4.8
PM21M	18	PrOH	50	81.5	90.4	89.0	90.0	88.7	87.9	3.6
PM21M	18	PrOH	75	101.3	98.6	101.0	100.7	105.2	101.4	2.4
PM21M	18	PrOH	90	129.6	132.1	134.4	130.0	134.1	132.0	2.2

Table IV-6*: Apparent contact angle data for porous Porex® PMV15T with an array of test liquids corresponding to CO2R products. These are the data corresponding to* ***Figure IV-8b****.*

Test Surface	z_p	Test Liquid	Water mass fraction (%)	Contact angle (°)						
				Droplet 1	Droplet 2	Droplet 3	Droplet 4	Droplet 5	Mean (°)	Standard Deviation (°)
PMV15T	--	Water	100	143.1	139.1	141.9	143.6	150.6	143.7	4.2
PMV15T	2	FA	5	136.6	134.8	133.4	137.6	139.2	136.3	2.3
PMV15T	2	FA	10	132.0	138.7	144.1	141.0	141.2	139.4	4.6
PMV15T	2	FA	25	141.6	138.7	140.8	145.2	146.1	142.5	3.1
PMV15T	2	FA	50	148.0	152.9	149.1	152.5	148.3	150.2	2.4
PMV15T	2	FA	75	151.6	144.3	148.9	156.7	140.6	148.4	6.3
PMV15T	2	FA	90	149.9	156.2	158.7	156.1	161.4	156.5	4.2
PMV15T	6	MeOH	0	85.6	94.1	101.4	107.4	112.3	100.2	10.6
PMV15T	6	MeOH	10	109.3	120.9	124.9	128.5	126.1	122.0	7.6
PMV15T	6	MeOH	25	114.6	133.9	131.2	137.5	133.6	130.2	9.0
PMV15T	6	MeOH	50	139.2	132.6	132.3	143.6	147.6	139.0	6.7
PMV15T	6	MeOH	75	135.9	137.3	134.8	147.7	150.2	141.2	7.2
PMV15T	6	MeOH	90	144.1	160.0	141.9	150.0	152.9	149.8	7.2
PMV15T	12	EtOH	0	94.9	97.7	100.0	110.4	108.1	102.2	6.7
PMV15T	12	EtOH	10	111.5	119.8	122.0	129.5	129.3	122.4	7.5
PMV15T	12	EtOH	25	125.2	133.6	134.6	139.4	134.6	133.5	5.2
PMV15T	12	EtOH	50	129.3	129.0	127.5	142.8	140.7	133.8	7.3
PMV15T	12	EtOH	75	124.6	134.2	137.6	146.8	143.9	137.4	8.7
PMV15T	12	EtOH	90	139.7	138.4	136.6	150.3	151.9	143.4	7.2
PMV15T	18	PrOH	0	81.4	101.8	107.1	105.8	114.5	102.1	12.4
PMV15T	18	PrOH	10	114.2	124.3	130.9	130.5	132.6	126.5	7.5
PMV15T	18	PrOH	25	117.2	126.3	126.0	132.1	132.8	126.9	6.3
PMV15T	18	PrOH	50	126.0	133.4	133.0	132.1	130.7	131.0	3.0
PMV15T	18	PrOH	75	131.7	128.5	133.6	133.3	131.8	131.8	2.0
PMV15T	18	PrOH	90	133.2	141.2	142.2	144.9	143.3	141.0	4.5

11. Appendix C: Mass Balance Model Addendum

***Table IV-7**: CO2R half-reaction stoichiometry for liquid-phase products along with oxygen evolution stoichiometry. The net moles of water produced per mole of product for a full cell is reported in the rightmost column.*

Half reaction	n_P (mol CO_2/mol P)	z_P (mol e/mol P)	z_W (mol e/mol W)	M_P (g/mol)	Full-cell net water (mol W/mol P)
$CO_2 + 2\ e^- + H_2O \rightarrow HCOO^- + OH^-$	1	2	2	46.03	0
$CO_2 + 6\ e^- + 5\ H_2O \rightarrow CH_3OH + 6\ OH^-$	1	6	6/5	32.04	–2
$2\ CO_2 + 12\ e^- + 9\ H_2O \rightarrow C_2H_5OH + 12\ OH^-$	2	12	12/9	46.07	–3
$3\ CO_2 + 18\ e^- + 13\ H_2O \rightarrow C_3H_7OH + 18\ OH^-$	3	18	18/13	60.09	–4
$2\ OH^- \rightarrow 0.5\ O_2 + H_2O + 2\ e^-$	-	4	–2	32.00	-

Table IV-8*: Capillary pressure, P_C, as a function of product mass fraction, x_P, for each CO2R product. P_C was calculated using the Young-Laplace expression (Equation (IV.1)) with pore radius, r, was set to 15 µm and 0.05 µm for the left and right axes in* ***Figure IV-6****, respectively. The surface tension of each mixture, γ, was taken from the set of data plotted in* ***Figure IV-10b****.*

Product content by mass, x_P (%)	**Capillary pressure, $P_C = P_L - P_G$ (mbar)**							
	FA		**MeOH**		**EtOH**		**PrOH**	
	r = 15 µm	r = 0.05 µm	r = 15 µm	r = 0.05 µm	r = 15 µm	r = 0.05 µm	r = 15 µm	r = 0.05 µm
0	35.1	10500	35.1	10500	35.1	10500	35.1	10500
0.1	35.0	10500	34.8	10400	34.5	10400	34.2	10300
1	33.8	10100	32.0	9610	29.1	8720	26.5	7940
10	23.8	7140	13.6	4080	–8.2	–2450	–10.5	–3160
20	15.6	4690	4.5	1340	–9.6	–2890	–18.1	–5440
30	10.0	2990	–1.0	–305	–11.9	–3580	–21.7	–6510
40	5.9	1780	–6.1	–1820	–15.1	–4530	–21.7	–6500
50	2.7	824	–10.1	–3040	–18.3	–5500	–21.9	–6580
60	–0.9	–279	–12.6	–3780	–18.7	–5610	–22.2	–6660
70	–5.2	–1550	–14.1	–4240	–19.5	–5850	–22.5	–6760
80	–9.2	–2750	–15.7	–4720	–20.1	–6040	–23.0	–6900
90	–12.5	–3760	–17.9	–5370	–20.7	–6220	–23.5	–7040
100	–16.6	–4970	–20.5	–6140	–23.4	–7030	–24.7	–7410

12. Appendix D: Capillary Pressure Calculations for a Constricted Pore

This analysis follows the framework proposed by Forner-Cuenca et al.[46,152] We assume the pore channel to be axisymmetric, so that $r = r(z)$ only. A graphic depicting variable-radius, pore profile is shown in **Figure IV-13**. Note that this schematic is not drawn to scale.

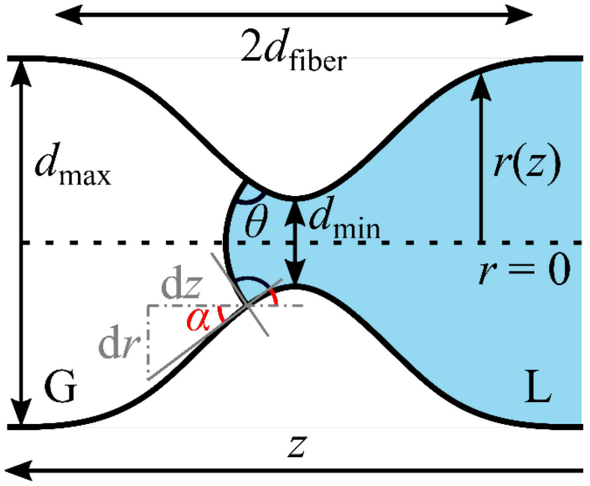

Figure IV-13*: Constricted pore model: Schematic. A sinusoidal pore profile is shown along with associated geometric parameters. The model concept is adapted from Forner-Cuenca et al.*[46] *This schematic is not drawn to scale. L = liquid phase, G = gas phase.*

To account for the possibility of constrictions in the pore channel, a sinusoidal profile as shown in Equation (IV.9) is used.

$$r(z) = \underbrace{\frac{1}{2}\left(\frac{d_{\text{max}}}{2} + \frac{d_{\text{min}}}{2}\right)}_{\text{average pore radius}} - \underbrace{\frac{1}{2}\left(\frac{d_{\text{max}}}{2} - \frac{d_{\text{min}}}{2}\right)}_{\text{amplitude}} \cos\left(\pi \frac{z}{d_{\text{fiber}}}\right) \tag{IV.9}$$

The period of the sinusoid was set to the equivalent of two fiber diameters, $2d_{\text{fiber}}$. The sinusoid offset is taken to be the average pore radius. The amplitude is taken to be one-half of the midpoint between the maximum, $d_{\max}$, and minimum, $d_{\min}$, pore diameters. As shown by Equation (IV.10) the instantaneous slope of the pore wall is a function of z.

$$\frac{\mathrm{d}r(z)}{\mathrm{d}z} = \frac{1}{2}\left(\frac{d_{\max}}{2} - \frac{d_{\min}}{2}\right)\left(\pi \frac{1}{d_{\text{fiber}}}\right)\sin\left(\pi \frac{z}{d_{\text{fiber}}}\right) \tag{IV.10}$$

The filling angle, α, is computed from the slope using Equation (IV.11).

$$\alpha(z) = \arctan\left(\frac{\mathrm{d}r(z)}{\mathrm{d}z}\right) \tag{IV.11}$$

Finally, we compute the P_C as a function of position in pore channel using Equation (IV.12). We plot the *maximum capillary pressure* over the entire domain, $-d_{\text{fiber}} < z < d_{\text{fiber}}$, as this constitutes the greatest resistance to imbibition.

$$P_{\mathrm{C}}(z) = P_{\mathrm{L}} - P_{\mathrm{G}} = \frac{-2\gamma\cos(\alpha(z)+\theta)}{r(z)} \tag{IV.12}$$

For the following calculations we set the base case parameters to be $\gamma = 0.072$ N/m (water), $\theta = 80°$ (water on some slightly hydrophilic surface), $d_{\text{fiber}} = 10$ µm, and $d_{\max} = 30$ µm. Sensitivities of the calculated P_C to θ, $d_{\max}$, and d_{fiber} are reported in **Figure IV-14**, **Figure IV-15**, and **Figure IV-16**, respectively.

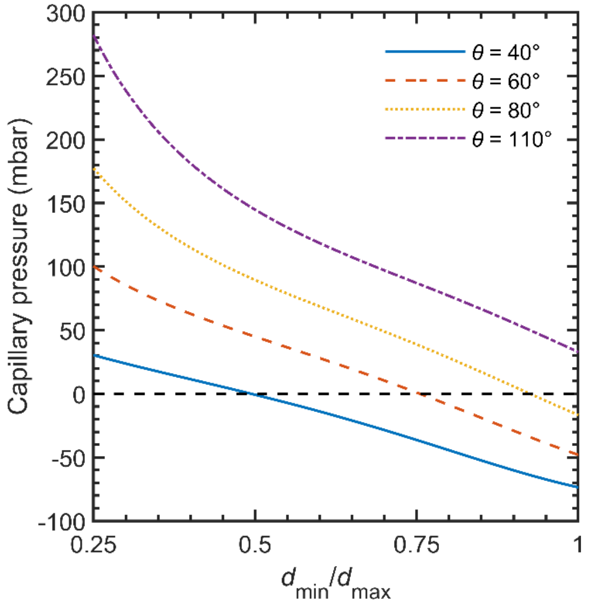

Figure IV-14: *Constricted pore model: Max capillary pressure as a function of contact angle. Water contacting the pore walls at varying contact angles, θ. Maximum capillary pressure is calculated for a constricted cylindrical pore (d_{max} = 30 µm, d_{fiber} = 10 µm) as a function of the ratio between minimum and maximum pore diameters, d_{min}/d_{max}.*

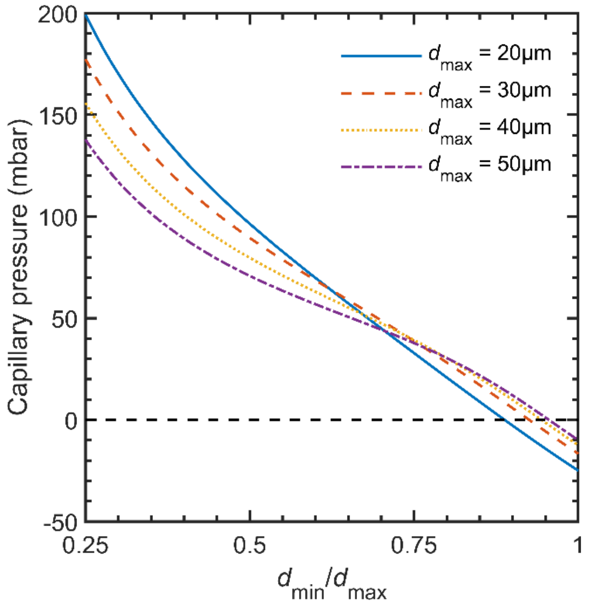

Figure IV-15: *Constricted pore model: Max capillary pressure as a function of max diameter. Water contacting pore walls at θ = 80° with d_{fiber} = 10 µm and varying d_{max}. Maximum capillary pressure is calculated for a constricted cylindrical pore as a function of the ratio between minimum and maximum pore diameters, d_{min}/d_{max}.*

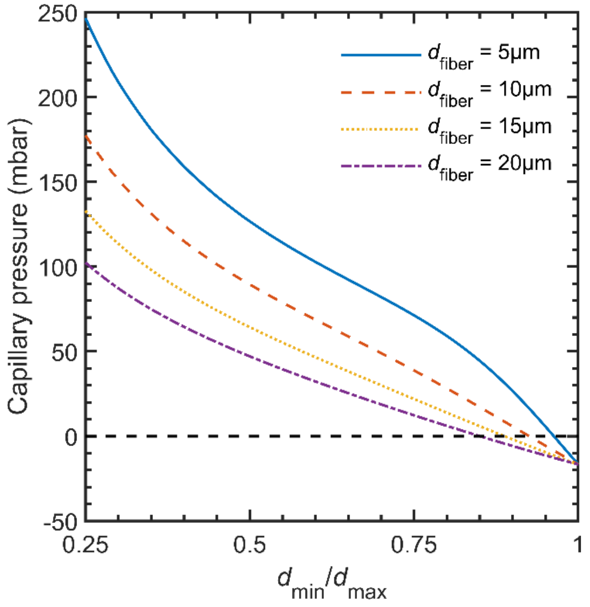

Figure IV-16*: Constricted pore model: Max capillary pressure as a function of fiber diameter. Water contacting pore walls at $\theta = 80°$ with d_{max} = 30 μm and varying d_{fiber}. Maximum capillary pressure is calculated for a constricted cylindrical pore as a function of the ratio between minimum and maximum pore diameters, d_{min}/d_{max}.*

13. Appendix E: List of Symbols

Table IV-9*: List of constants*

Constant	Value	Unit	Description
F	96485	C mol e^{-1}	Faraday constant
M_P	FA 0.04603 MeOH 0.03204 EtOH 0.04607 PrOH 0.06009	kg mol^{-1}	molar mass of a CO2R product
M_W	0.01802	kg mol^{-1}	molar mass of water
n_P	(**Table IV-1**)	mol CO_2 mol P^{-1}	carbon ratio
z_P		mol e mol P^{-1}	electron-product ratio
z_W		mol e mol W^{-1}	electron-water ratio
ρ_W	998.2071	kg m^{-3}	density of water at STP

Table IV-10*: List of variables*

Variable	Unit	Description
d_fiber	m	fiber diameter
d_max	m	maximum pore diameter
d_min	m	minimum pore diameter
I	A	current
$\dot{m}_\text{out}$	kg s^{-1}	total mass flow rate exiting the reactor
$\dot{m}_\text{P,in}$	kg s^{-1}	product feed rate
$\dot{m}_\text{w,in}$	kg s^{-1}	water feed rate
$\dot{m}_\text{P,rxn}$	kg s^{-1}	product generation rate
$\dot{m}_\text{W,rxn}$	kg s^{-1}	water consumption rate
P_C	bar	capillary pressure
P_G	bar	gas phase pressure
P_L	bar	liquid phase pressure
Q	mL min^{-1}	volumetric flow rate of feed water
r	m	cylindrical pore radius
x_P	-	mass fraction of product
x_W	-	mass fraction of water
z	m	longitudinal cylindrical coordinate

***Table IV-11**: List of Greek letter variables*

Greek letter	Unit	Description
α	°	filling angle
γ	mN m^{-1}	liquid-gas surface tension
γ_{C0}	mN m^{-1}	critical surface tension for complete wetting ($\theta = 0°$)
γ_{C90}	mN m^{-1}	cylindrical capillary transition surface tension ($\theta = 90°$)
θ	°	intrinsic solid-liquid-gas contact angle

V. Computational Model Representations of Gas Diffusion Electrodes

In this work, I describe how macro-homogeneous porous electrode models can be constructed for predicting the impacts of gas diffusion electrode (GDE) liquid saturation on CO_2 electrolyzer performance. Specifically, partially saturated porous media models that were introduced for the study of polymer electrolyte fuel cells (PEFCs) are adapted for CO_2 electrolyzers to explore relevant GDE flooding scenarios introduced and discussed in previous chapters.

1. Background

Electrochemical CO_2 reduction (CO2R) models have been developed to validate the fact that GDEs enable greater current densities and improved faradaic efficiencies in CO_2 electrolyzers by increasing gaseous species fluxes as compared to flooded electrodes.[81,164] These models assume that gas diffusion layers (GDLs) used to support the catalyst layer remain dry during operation; however, flooding of GDEs in contact with liquid electrolytes has been reported at moderate operating conditions (< 200 mA cm^{-2}).[26,40] While spatially-variant liquid saturation in porous materials is necessarily considered in PEFC models, where liquid water is both a product of the cathodic oxygen reduction reaction and present in humidified gas streams, liquid intrusion scenarios remain unarticulated for CO2R. Thus, there is a need to conceptualize, construct, and experimentally validate porous electrode two-phase flow models that are tailored for the environments inherent to CO2R electrolyzers.

We use macro-homogeneous descriptions of porous materials as reported by Weber et al.[165,166] because they permit variation of microstructure (i.e., pore size distribution, PSD) and surface chemistry (i.e., contact angle distribution, CAD) in order to define constitutive relations that describe simultaneous two-phase (gas and liquid) coexistence and transport within different porous electrode components. This approach has been integrated into 1D multiphysics transport models and successfully validated against experimental results for polymer electrolyte fuel cells (PEFC) and CO_2 electrolyzers according to the abbreviated workflow shown in **Figure V-1**. [167–170] Within this model framework, Weber et al. were able to systematically vary carbon fiber substrate and microporous layer properties to deconvolute the role of each in managing water transport in the cathode GDL of a PEFC. However, the (electro)chemical environment of CO2R challenges the electrode wettability assumptions established during contemplation of PEFCs. More specifically, two phenomena that emerge as possible contributors to GDE flooding during CO2R are (i) electrowetting, which reduces the solid-liquid-gas contact angle, θ, when liquid electrolyte contacts polarizable electrode surfaces,[171,172] and (ii) lowered gas-liquid surface tension, γ, when organic reduction products (e.g., ethanol) enter aqueous electrolytes.[173]

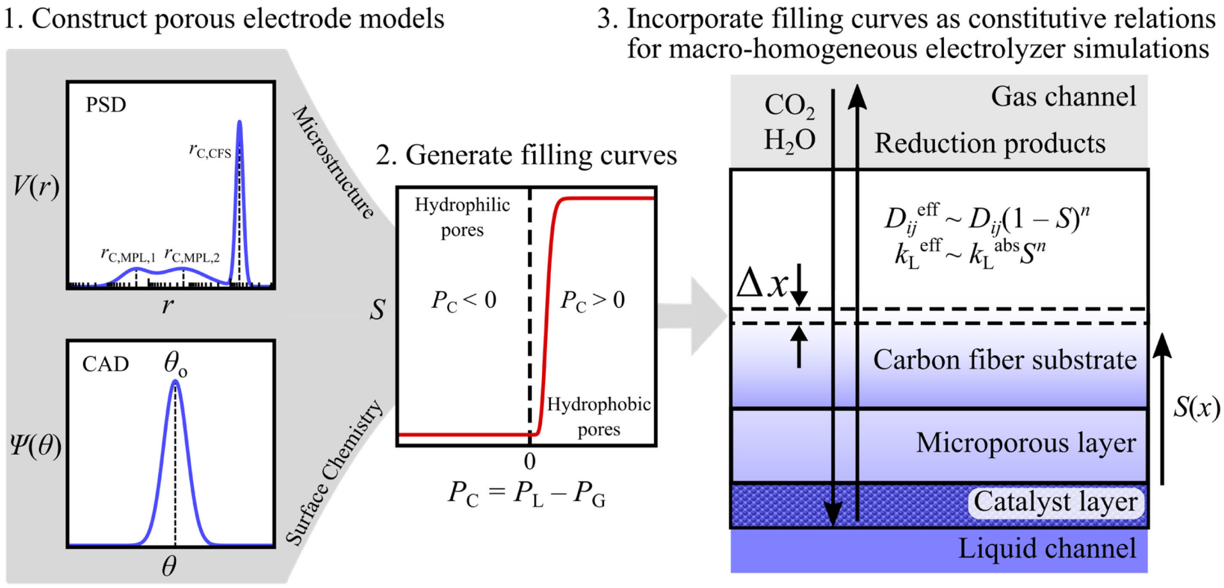

***Figure V-1**: Workflow for integrating GDE models into transport simulations. Statistical descriptions of porous media, which consider both microstructure (pore size distribution, PSD) and surface chemistry (contact angle distribution, CAD), are used to generate filling curves. $V(r)$ and $\Psi(\theta)$ represent pore volume and contact angle probability density functions, which are taken to be log-normal and normal distributions, respectively.*[166] *These constitutive relations can be used to determine the local GDE saturation as a function of the liquid-gas pressure differential or capillary pressure, $P_C = P_L - P_G$, in a one-dimensional CO_2 electrolyzer transport model. Local saturation, $S(x)$, scales the transport coefficients for gaseous and liquid species (i.e., binary diffusivity, D_{ij}, and Darcy permeability, k_L^{abs}) to yield effective values (D_{ij}^{eff} and k_L^{eff}) in the presence of liquid.*

Electrode wettability is a function of both microstructure and surface chemistry, represented by a pore size distribution (PSD) and a contact angle distribution (CAD), respectively. At each location within a porous material, the "saturated" pore volume fraction is determined by the critical pore radius, r_c, which is calculated from a version of Washburn's equation, shown in Equation (V.1).

$$r_c = -\frac{2\gamma\cos(\theta)}{P_C} \tag{V.1}$$

r_c is a function of the liquid-gas pressure differential, or capillary pressure ($P_C = P_L - P_G$), as well as the surface tension, γ, and the intrinsic contact angle, θ, formed between the solid and fluid phases.

Saturation, S, mapped to P_C on a "filling curve" forms a constitutive relationship can be constructed for each GDE component and integrated into a macro-homogeneous transport model. The fraction of liquid filling the pore volume, S, is crucial for calculating effective transport coefficients (i.e., diffusivities and Darcy permeabilities) according to empirical relations generally taking forms similar to $D_{ij}^{\mathrm{eff}} \sim D_{ij}(1 - S)^n$, where n is a fitting parameter that is valued between 2–3 for typical carbon fiber substrates used in PEFCs, for example.[86,166] In this example equation, the effective binary diffusivity of a gaseous species, $\mathrm{D}_{ij}^{\mathrm{eff}}$, decreases as the fraction of the pore volume occupied by gas, $(1 - S)$, decreases. Within the macro-homogeneous framework, increasing liquid saturation promotes liquid percolation and diminishes gaseous species diffusion, resulting in hindered performance for gas-fed systems such as CO2R.

Although this macro-homogeneous mathematical framework lacks pore-scale resolution, it is computationally expedient and useful for conducting parametric investigations of GDE properties across different operating scenarios involving challenging reaction environments.[166] Scenarios that benefit from resolution of flooding and blockage events at the pore scale are perhaps handled by tools that more directly account for the irregularities inherent to real porous media such as pore network modeling (PNM) or Lattice Boltzmann methods.[174–176] For example, this account for materials with heterogeneously applied coatings or with microstructural features that vary as a function of position. Additional phenomena, such as the electrolyte dry-out and salt creep highlighted in Chapter III, could be handled by PNM approaches.[177]

In the following sections, I will explain how mathematical expressions can be formulated to describe two-phase flow and coexistence within of porous materials and then be used to calculate relevant equilibrium and transport properties as a function of P_C and S. By the end of the chapter, I will use this model framework to discuss practical scenarios in which GDE wettability might shift during operation of CO_2 electrolyzers, including the generation of enriched aqueous-organic product mixtures and electrowetting when using liquid electrolytes.

2. Macro-homogeneous GDE Component Model Construction

Empirical fits of experimentally measured capillary pressure-saturation (P_C-S) curves are easily used to determine local porous media liquid saturation values, but they are less useful for investigating property-performance relationships. Constructing analytically tractable mathematical descriptions of electrodes based on well-defined functions, such as Gaussian distributions, provides opportunities to parametric studies of GDE component wettability.[166] Following the approach of Weber et al., the PSD and CAD of each GDE component are described by the log-normal distribution of pore volume, $V(r)$, as a function of pore radius, r, and a normal distribution of contact angles, $\Psi(\theta)$, respectively.[165,166] Combining information from these functions allows us to define expressions for a macro-homogeneous property, Y, as a function of r_c and θ, as shown in Equation (V.2).

$$Y\left(r_c,\theta\right)=\int_0^{90}\Psi(\theta)\int_0^{r_c}W(r)V(r)drd\theta+\int_{90}^{180}\Psi(\theta)\int_{r_c}^{\infty}W(r)V(r)drd\theta \qquad \text{(V.2)}$$

A weight function, $W(r)$, along with the bounds of integration to define analytical expressions for different relevant porous media properties, such as liquid saturation, S, and relative Darcy permeability, k_r, of a fluid phase. Practically, each expression for Y is evaluated in two steps. First, the product of $W(r)V(r)$ is integrated analytically in two parts for the hydrophilic and hydrophobic portions of the material. For a given r_c, which, itself, is determined from P_C and θ using Equation (V.1), the resulting analytical expression is numerically integrated over the range of the CAD, $0° \leq \theta \leq 180°$ in two parts. Thus, using this approach may properties, Y, can be defined as a function of P_C.

2.1. Microstructure

The microstructure of each porous component of the GDE is described by a PSD, which can be determined either via fluid intrusion experiments or direct imaging. Mercury intrusion porosimetry (MIP) is a widely-practiced analytical method for estimating total pore volume, pore sizes, surface area, bulk densities, absolute densites of porous materials.[178] In this method, mercury as a non-wetting fluid is pressurized against a porous sample contained inside a previously evacuated chamber. Once applied pressure data are converted to pore sizes using a form of Washburn's equation, Equation (V.1), the incremental volume of mercury reported versus pore size constitutes the PSD. Alternatively, PSDs can be calculated from 3D X-ray tomography representations of porous materials by using open-source software such as PoreSpy.[179]

Each material PSD is converted to an equivalent mathematical description by using log-normal distributions, which are characterized by well-defined parameters and can be integrated analytically. The total PSD distribution for a material can be described by normalized pore volume distribution, $V(r)$, which, as shown by Equation (V.3), is a weighted sum of log-normal distributions, with each curve corresponding to a different pore size mode.

$$V(r) = \sum_k f_{r,k} \left\{ \frac{1}{r s_k \sqrt{2\pi}} \exp\left[-\left(\frac{\ln(r) - \ln(r_{\mathrm{o},k})}{s_k \sqrt{2}} \right)^2 \right] \right\} \tag{V.3}$$

Key fitting parameters for each component curve, V_k, are the characteristic pore radius of mode k, $r_{\mathrm{o},k}$, the spread of the distribution for mode k, $\underline{s_k}$, and the component weight for mode k, $f_{r,k}$. The sum of the component weights sum to one.

For this work, I used PSDs determined for the same Freudenberg manufactured family of materials that were used in Chapter III. The PSD for each GDE component material is taken from the incremental mercury volume data obtained from MIP. MIP measurements were performed by Particle Testing Authority (Norcross, GA), using method MIP-04, which includes intrusion and extrusion analysis to measure pore sizes in the range of 360 to 0.003 μm. Overlayed plots of the GDL, CFS, and computed MIP PSDs are included in **Figure V-25** in Appendix B.

Freudenberg H23C6 and H23I2 carbon papers are used to represent the full GDL and carbon fiber substrate (CFS), respectively. H23C6 is a composite material including both polytetrafluoroethylene (PTFE)-coated CFS with a microporous layer (MPL) applied to one side. H23I2 is a PTFE-coated CFS and is used to understand which pore size modes in the full GDL are attributed to the fibrous matrix. Only pore size less than 100 μm were used for analysis of the GDL and CFS layers because their thickness is ca. 200 μm. For similar reasons, pore sizes less than 1 μm were used for the MPL, which is ca. < 50 μm. Select classification information for both commercial carbon fibers materials are provided in **Table V-1**.

***Table V-1**: General properties of gas diffusion layer materials used to deconvolute the microstructural contributions of the CFS and MPL.*

Property	**GDL**	**CFS**	**MPL (assumed from citation)**
Manufacturer	Freudenberg	Freudenberg	Freudenberg
Product name	H23C6	H23I2	-
PTFE Treated	✓	✓	✓
MPL	✓		✓
Thickness (μm)	250	210	< 50 (SEM)

The PSDs for the CFS and MPL were manually fit using Equation (V.3) in Microsoft Excel. First, the raw incremental volume data (mL g^{-1}) for both the full GDL and the CFS were normalized by their respective total intrusion volumes from MIP (1.2809 mL and 1.4751 mL) to get a volume normalized incremental volume (g^{-1}) data set. Next, the PSD for the MPL was calculated by taking the difference between the GDL and CFS PSDs. The full GDL PSD is no longer needed once the MPL information has been extracted from the GDL PSD by subtracting signal contributed by the CFS.

Before fitting log-normal distributions to the CFS and MPL microstructural data, each PSD is rescaled so that the total area under the curve is equal to one. This is done in two steps. First, a maximum pore size cutoff is applied for each phase. The rescaling factor is determined by trapezoidal numerical integration using the `trapz` function in MATLAB from pore radii of 0 μm to the maximum cutoff radius for each material (CFS: 100 μm and MPL: 1 μm). Second, each PSD is divided by its rescaling factor and parameters are determined manually. The fitting parameters for each material are provided in **Table V-2**. The normalized PSD data for the full GDL (H23C6) are reported in **Figure V-2** while the normalized PSD data and log-normal curve fits for the CFS (H23I2) and MPL (calculated by H23C6 – H23I2) are both provided in **Figure V-3**.

The fitted parameters for the CFS and MPL generally align with expectations of the characteristic pore size required for each layer. By design, the MPL has characteristic pore sizes in the range of 1 μm and smaller, while the CFS has mostly larger pores that are on the order of 10 μm and larger. However, after fitting the normalized MIP data, we can observe that a pore radius mode of 90 μm emerges in the CFS. While this mode is needed to accurately fit the incremental pore volume data in this case, we must recognize that this pore size is fictitious. The total thickness of the CFS is ca. 200 μm, so this larger pore radius mode would imply that the material has some pores that are nearly as large (ca. 180 μm) as the total material thickness. Because this is unrealistic given the actual observed microstructure of the H23C6 and H23I2 materials, we must assume that the true dominant pore radius mode for the material is ca. 10 μm. As will be shown subsequently, the P_C-*S* behavior of the CFS would not be accurately predicted accurately by the initial set of microstructural fitting parameters so a unimodal PSD with a characteristic pore radius of 10 μm is used. Although the CFS microstructure is simplified for further analysis, the volume normalization process used in this section was still needed to extract a representation of the MPL PSD from H23C6 MIP data. Plots of the PSD fits for each material are provided in Appendix C.

Table V-2*: Preliminary microstructural PSD parameters for each GDE component as determined by MIP measurements.*

PSD Parameter	**Value**		**Unit**
	CFS	**MPL**	
$r_{o,1}$	10	0.025	µm
$r_{o,2}$	90	0.12	µm
$r_{o,3}$	0.03	2.2	µm
$r_{o,4}$	1.0	-	µm
s_1	0.30	0.12	
s_2	1.37	0.80	
s_3	0.20	2.00	
s_4	1.70	-	
$f_{r,1}$	0.38	0.025	
$f_{r,2}$	0.61793	0.100	
$f_{r,3}$	0.00007	0.875	
$f_{r,4}$	0.002	-	

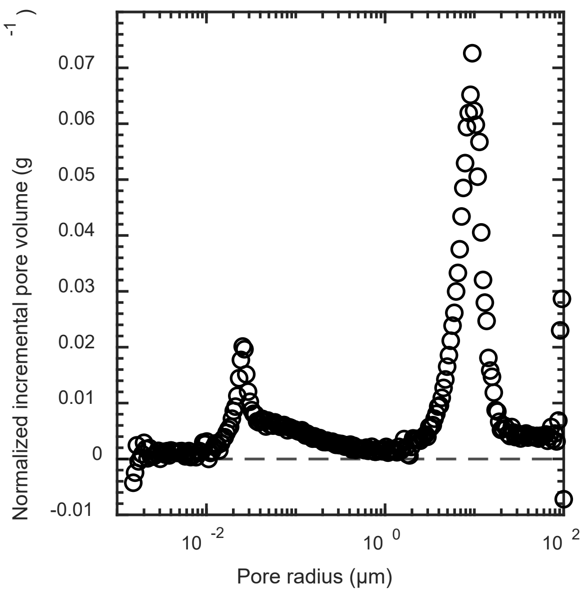

Figure V-2*: PSD for H23C6, a composite GDL material consisting of a CFS coated with PTFE combined with an MPL that applied to one side. The PSD consists of normalized incremental pore volume per unit mass data as measured by MIP.*

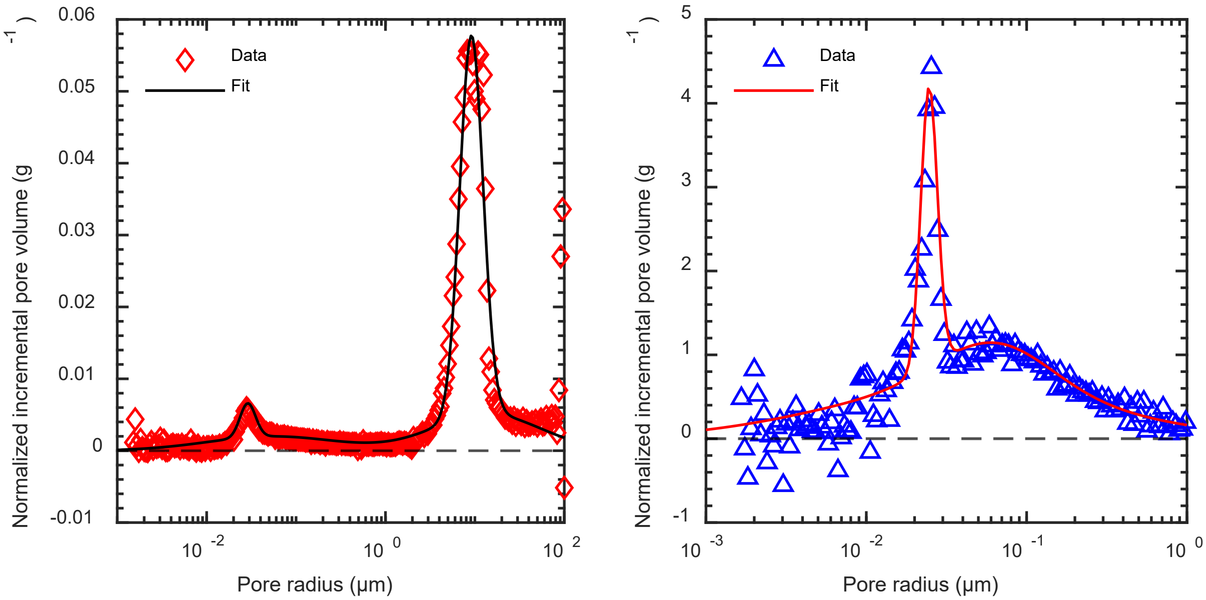

Figure V-3: *PSDs for CFS (H23I2) and MPL (H23I2 subtracted from H23C6). Each PSD consists of normalized incremental pore volume per unit mass data as measured by MIP.*

2.2. Surface Chemistry

The surface chemistry of a material's pore walls is described by a CAD, $\Psi(\theta)$, which is described by a weighted sum of normal distributions as shown in Equation (V.4).

$$\Psi(\theta) = \sum_{n} f_{\theta,n} \left\{ \frac{1}{\sigma_n \sqrt{2\pi}} \exp\left[-\frac{1}{2} \left(\frac{\theta - \theta_{\mathrm{o},n}}{\sigma_n} \right)^2 \right] \right\} \tag{V.4}$$

Each component curve n corresponds to a different contact angle mode described by a characteristic contact angle, $\theta_{\mathrm{o},n}$, and spread, σ_n. The curves weights are described by characteristic fractions, $f_{\theta,n}$, which together sum to one.

Physically the CAD corresponds to the distribution of constituent materials throughout the GDE. If the distribution of materials (e.g., carbon and PTFE) were precisely known then it might be possible to directly assign a CAD. For example, we could attempt estimate the material distribution from elemental mapping information of the GDE as shown in **Figure V-4**. However, since experimentally measured P_C-S data is readily measurable, we can adjust the characteristic parameters of a CAD to fit a computational saturation curve against the experimentally measured one. Furthermore, by fitting a distribution of contact angles to real filling data, we can implicitly incorporate the effects of pore-scale non-idealities (e.g., pore constrictions, dead-end pores, non-conformal coating coverage) that produce hysteresis loops during filling and draining cycles.[166]

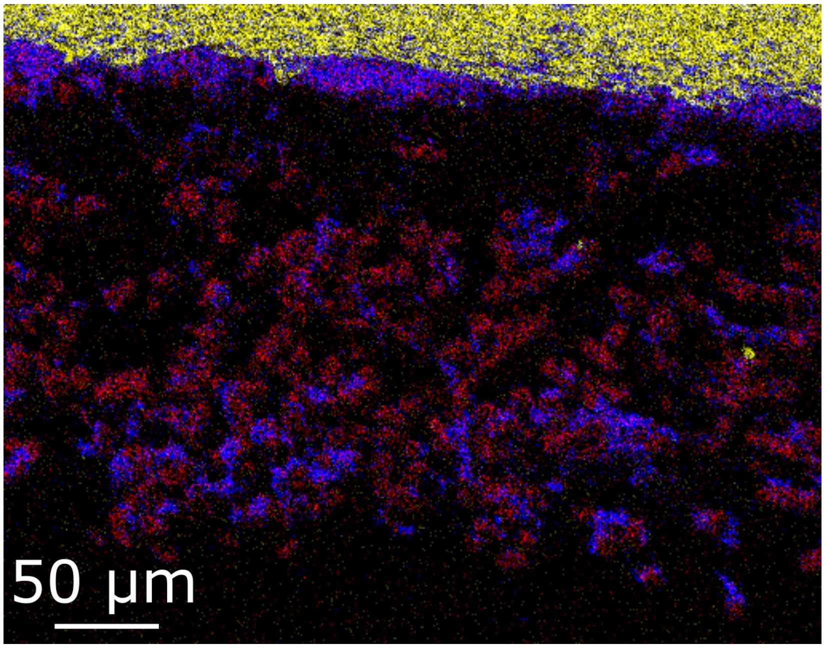

***Figure V-4**: Elemental mapping (EDS) overlay for a Ag-GDE cross-sectional SEM image, including carbon (red), fluorine (blue), and silver (yellow). This image was created by overlaying selected subpanels shown in **Figure III-11**. This composite image shows that MPL (top layer) below the silver catalyst is composed of a relatively homogeneous and balanced mixture of PTFE and carbon particles while the CFS (bottom layer) has heterogeneous distributions of PTFE amongst the carbon fibers.*

With a working definition of the CAD, $\Psi(\theta)$, in place, we can extend the definition of the pore volume distribution by substituting Washburn equation's, Equation (V.1), into Equation (V.3) to define a PSD in terms of P_C and θ as shown in Equation (V.5).

$$V\left(P_{\mathrm{C}},\theta\right)=\sum_{k} f_{r,k}\left\{\frac{1}{\left(-2\gamma\cos(\theta)/P_{\mathrm{C}}\right)s_k\sqrt{2\pi}}\exp\left[-\left(\frac{\ln\left(-2\gamma\cos(\theta)/P_{\mathrm{C}}\right)-\ln\left(r_{\mathrm{o},k}\right)}{s_k\sqrt{2}}\right)^2\right]\right\} \tag{V.5}$$

3. *Models and Data: Fitting the Macro-homogeneous Electrode Model to P_{C}-S Data*

As discussed earlier, we choose to adjust the parameters of the CAD to fit the computed P_{C}-S curve against empirical water filling data. To do this, we must define an expression for liquid saturation based on the pore volume distribution introduced previously. We can use non-linear least squares fitting to determine the characteristic wettability parameters of the CAD while holding constant the microstructural parameters obtained from MIP. Importantly, this process of comparing computed saturation predictions against real saturation data allows us to determine which characteristic pore sizes are representative of the real microstructure and check which of those might be unphysical artifacts of the porosimetry method.

3.1. Liquid Saturation (S* and S)

The liquid saturation is taken directly as the filled pore volume for a given r_{c}. Thus, the unscaled saturation, S^*, is calculated from Equation (V.2) using $W(r) = 1$, as shown in Equation (V.6).

$$\begin{aligned} S^* = & \int_0^{90} \Psi(\theta)\left\{\sum_k \frac{f_{r,k}}{2}\left[1+\operatorname{erf}\left(\frac{\ln\left(r_{\mathrm{c}}\right)-\ln\left(r_{\mathrm{o},k}\right)}{s_k\sqrt{2}}\right)\right]\right\}d\theta \\ & +\int_{90}^{180} \Psi(\theta)\left\{\sum_k \frac{f_{r,k}}{2}\left[1-\operatorname{erf}\left(\frac{\ln\left(r_{\mathrm{c}}\right)-\ln\left(r_{\mathrm{o},k}\right)}{s_k\sqrt{2}}\right)\right]\right\}d\theta \end{aligned} \tag{V.6}$$

To fit the model saturation curve against an experimental capillary pressure-saturation curve, we need to substitute the expression in Equation (V.1) for r_{c}. From this we derive an analytical expression for S^* as a function of P_{C} as shown in Equation (V.7).

$$\begin{aligned} S^* = & \int_0^{90} \sum_n f_{\theta,n} \left\{ \frac{1}{\sigma_n \sqrt{2\pi}} \exp\left[-\frac{1}{2}\left(\frac{\theta - \theta_{\mathrm{o},n}}{\sigma_n} \right)^2 \right] \right\} \\ & \times \left\{ \sum_k \frac{f_{r,k}}{2} \left[1 + \operatorname{erf}\left(\frac{\ln\left(-2\gamma\cos(\theta)/P_\mathrm{C}\right) - \ln\left(r_{\mathrm{o},k}\right)}{s_k\sqrt{2}} \right) \right] \right\} d\theta \\ & + \int_{90}^{180} \sum_n f_{\theta,n} \left\{ \frac{1}{\sigma_n \sqrt{2\pi}} \exp\left[-\frac{1}{2}\left(\frac{\theta - \theta_{\mathrm{o},n}}{\sigma_n} \right)^2 \right] \right\} \\ & \times \left\{ \sum_k \frac{f_{r,k}}{2} \left[1 - \operatorname{erf}\left(\frac{\ln\left(-2\gamma\cos(\theta)/P_\mathrm{C}\right) - \ln\left(r_{\mathrm{o},k}\right)}{s_k\sqrt{2}} \right) \right] \right\} d\theta \end{aligned} \quad \text{(V.7)}$$

It is known that after filling some porous materials retain residual fluid that cannot easily be removed by capillary forces alone and, especially for the case of entrapped water, requires removal by evaporation.[85] Thus, the final expression for liquid saturation, S, is bound between minimum ("residual") and maximum saturation values, S_{min} and S_{max}, respectively, and is scaled by Equation (V.8).

$$S = S_{\mathrm{min}} + S^*\left(S_{\mathrm{max}} - S_{\mathrm{min}}\right) \quad \text{(V.8)}$$

3.2. Non-linear Least Squares Fitting of P_C-S Curves

A non-linear least squares fitting routine was executed in MATLAB to determine CAD parameters for each GDE component that result in the best agreement between computational and experimental P_C-S curves. I determine two sets of wettability parameters for the CFS by fitting the saturation model against both the H23 and H23I2 water P_C-S data. The data for each material was collected and provided to me by Dr. Yongwook Kim and Prof. Jeff Gostick of PMEAL at the University of Waterloo. For the MPL, I assume a characteristic contact angle, $\theta_{\mathrm{o},1}$ = 110°, and spread, $\sigma_1 = 1$, based on a previous report by Weber et al.[166] This choice is made because fully saturated P_C-S curves for microporous materials are practically difficult to measure. Relatively large water pressures (ca. 10 bar) are required to penetrate the smallest (< 1 μm) hydrophobic pores. The residual saturation is assumed to be zero for the MPL since we do not have experimental saturation data for that component. The CFS residual saturations is set to $S_{\mathrm{min}} = 0$ because the materials are initially dry. The maximum saturation is assumed to be $S_{\mathrm{max}} = 1$ for both components.

Non-linear least squares fitting was used to determine the best fit CAD parameters for the CFS. As mentioned earlier, by performing this analysis I was able to justify reducing the initial set of four characteristic pore radii in the CFS PSD down to one. As demonstrated by the poor visual fits between model and data in **Figure V-5**, the presence of the large (ca. 90 μm) pores in the initial PSD does not accurately predict filling data for the bare fibrous CFS (H23) or the PTFE-coated CFS (H23I2) materials. Characteristic contact angles of $\theta_{\mathrm{o}} = 120°$ ($\sigma = 0.024$) and $\theta_{\mathrm{o}} = 180°$ ($\sigma = 0.21$) are calculated for H23 and H23I2, respectively. Apparently, the presence of a 90-μm pore size in the initial model leads to high root mean square errors (RMSE(H23) = 0.1222, RMSE(H23I2) = 0.1625) due, in part, to the unphysically high model predicted saturation near $P_{\mathrm{C}} = 0$. Such large pores cannot physically exist given the material thickness and so we can justifiably omit them from the CFS PSD. This choice is reinforced numerically by the fact that the predicted angle for H23I2 is maximized to $\theta_{\mathrm{o}} = 180°$ by the non-linear least squares routine. We can conclude that the MIP PSD for the CFS is principally characterized by the 10-μm pore radius mode. I also ignore the smallest pore modes for the remainder of the study and assume the entirety of the CFS microstructure can be represented by a unimodal PSD centered on a 10-μm pore radius. An updated and simplified set of PSD parameters for the CFS and MPL are reported in **Table V-3**.

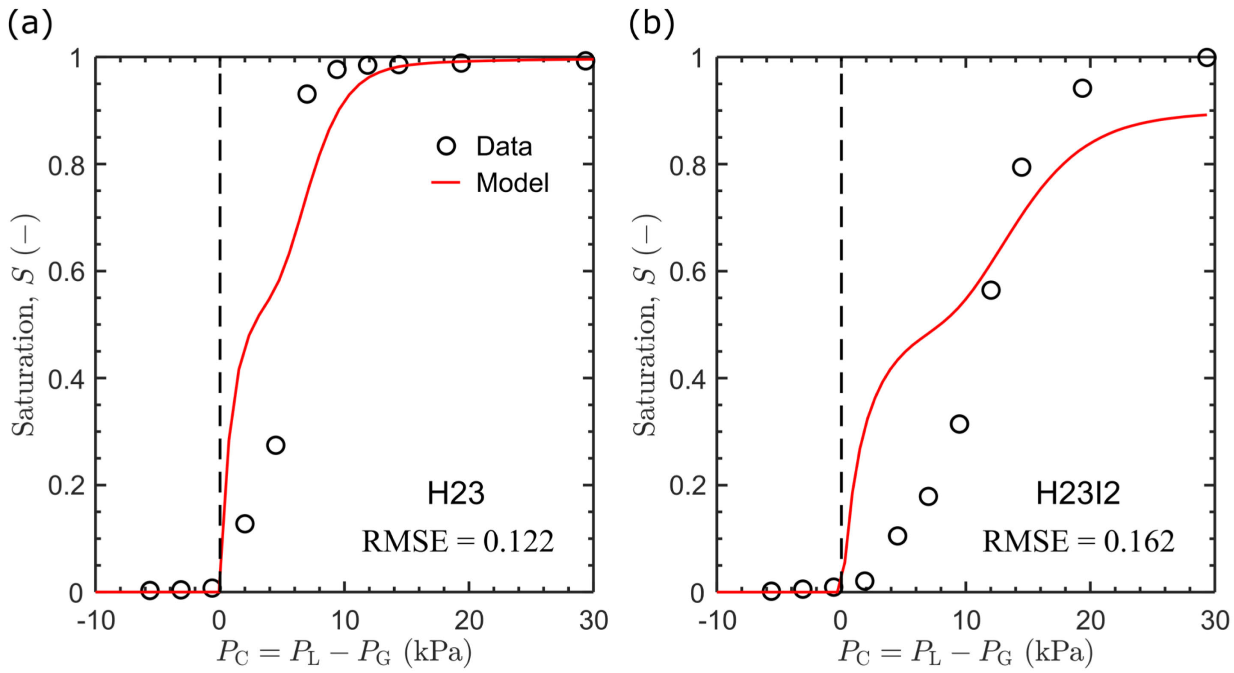

***Figure V-5**: Inaccurate saturation trends are predicted using initial CFS PSD parameters. The presence of a 90 µm pore size in the initial model leads to unphysically high saturation near $P_C = 0$ even when using $\theta_o = 180°$. The RMSE for the uncoated CFS (left, H23) and PTFE-coated CFS (right, H23I2) model prediction are 0.122 and 0.162 saturation units. Because of this result, we can conclude that the MIP PSD for the CFS is mostly characterized by a 10 µm pore radius mode. Data was collected by Dr. Yongwook Kim and Prof. Jeff Gostick of PMEAL at the University of Waterloo.*

***Table V-3**: Simplified set of PSD parameters for the CFS and MPL after CAD analysis*

PSD Parameter	Value		Unit
	CFS	MPL	
$r_{o,1}$	10	0.025	µm
$r_{o,2}$	-	0.12	µm
$r_{o,3}$	-	2.2	µm
s_1	0.30	0.12	
s_2	-	0.80	
s_3	-	2.00	
$f_{r,1}$	1	0.025	
$f_{r,2}$	-	0.100	
$f_{r,3}$	-	0.875	

Now with a simplified set of PSD parameters established for the CFS (rc = 10 µm, s = 0.3), we can use non-linear least squares fitting in MATLAB to determine a more accurate set of CAD parameters. Using the same routine, I fit two distinct CADs for the uncoated (H23) and PTFE-coated (H23I2) CFS samples. The set of best fit CFS CAD parameters with their associated RMSE values along with the assumed MPL CAD parameters are reported in **Table V-4**.

Table V-4*: CAD parameters representing the internal CFS and MPL surface chemistries*

CAD parameter	**Value**			**Unit**
	CFS (H23)	**CFS (H23I2)**	**MPL**	
θ_o	111	143	110	°
σ	5.6	19.1	1	
P_C-S *RMSE*	0.051	0.026	N/A	-

Characteristic contact angles of $\theta_o = 111°$ ($\sigma = 5.6$) and $\theta_o = 143°$ ($\sigma = 19.1$) are calculated for H23 and H23I2, respectively. CAD plots for the CFS and MPL are shown together in **Figure V-6**. The addition of a PTFE coating with H23I2 predictably shifts the best fit CAD towards higher characteristic angles as compared to H23. In addition, the spread of the distribution increases indicating that more of the pore volume only becomes accessible at higher pressures. As noted previously, the generally higher-than-expected intrinsic contact angles determined from P_C-S data in fibrous media can be attributed to the combined effects of surface chemistry, tortuosity, and complex filling phenomena within pores and at intersections.[86,166]

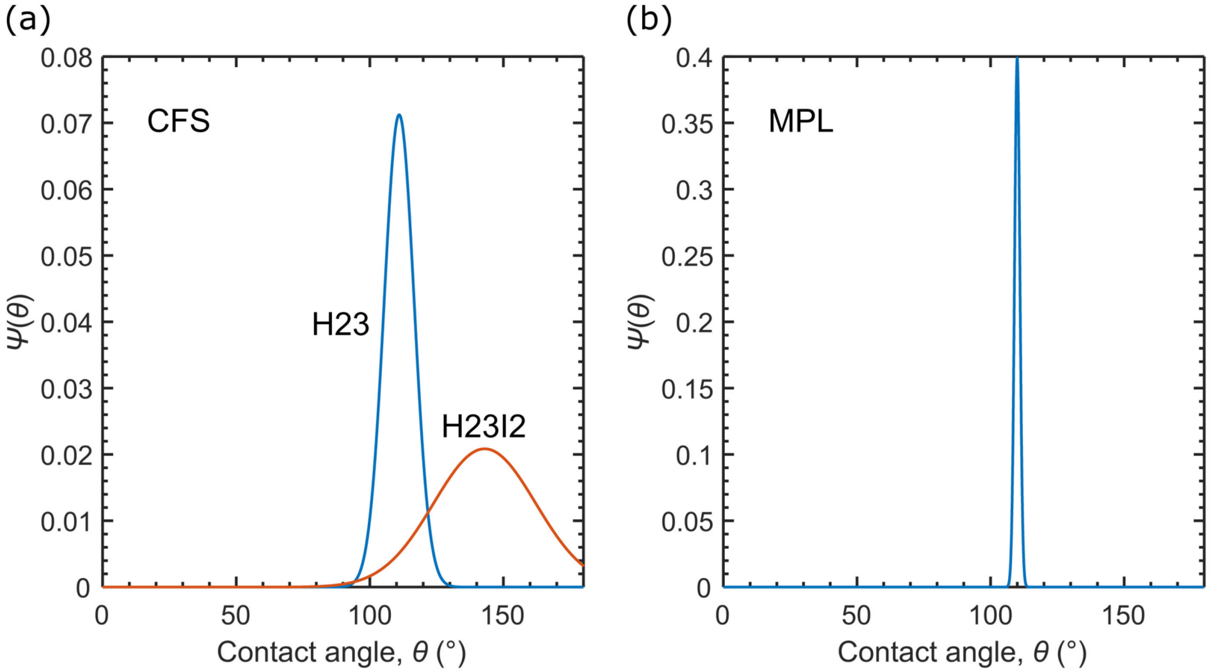

Figure V-6*: Contact angle distributions for (a) CFS (H23 and H23I2) and (b) MPL.*

Once the fictitious large pores are removed from the PSD, the model predicted RMSE values improve. The RMSE for H23 and H23I2 are 0.051 and 0.026, respectively, which are notable improvements from the naïve initial fit to the original PSD data. Improved visual agreement between the models and the data are demonstrated in **Figure V-7**.

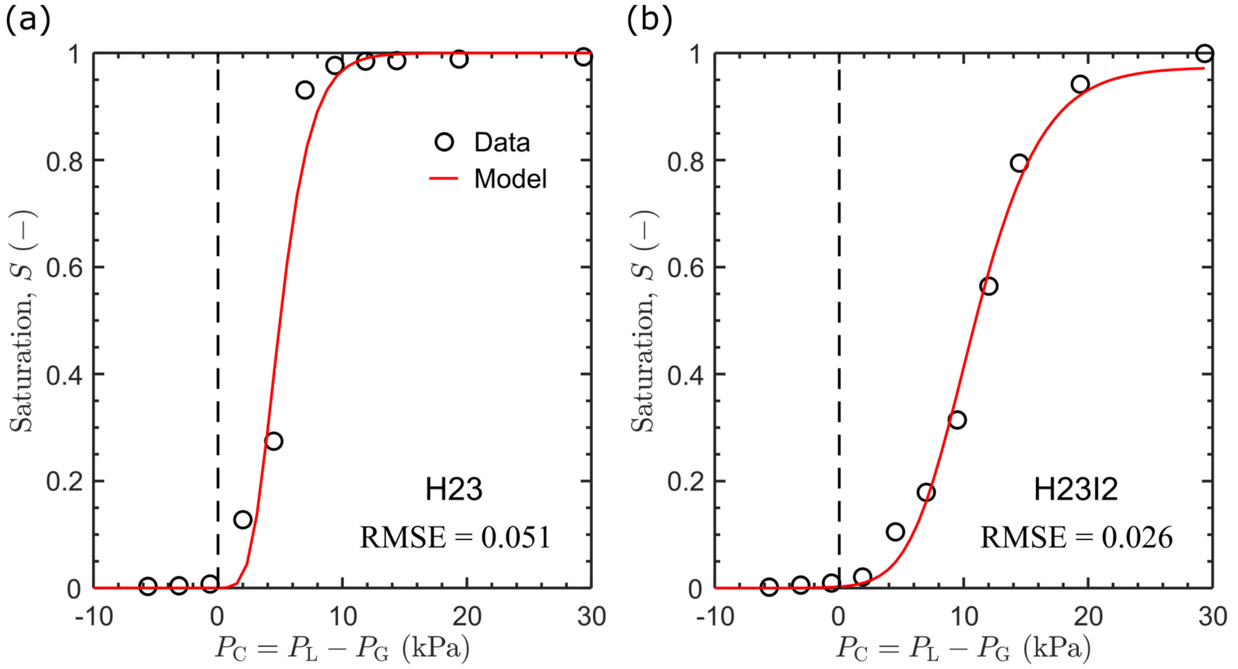

***Figure V-7**: Saturation trends are predicted using simplified CFS PSD parameters. The RMSE for the (a) uncoated CFS (H23) and (b) PTFE-coated CFS (H23I2) model predictions are 0.051 and 0.026 saturation units, respectively. The addition of PTFE wet proofing shifts the curve towards more positive P_C values, indicating that higher liquid pressures (lower gas pressures) are required for the liquid to saturate the CFS. Data was collected by Dr. Yongwook Kim and Prof. Jeff Gostick of PMEAL at the University of Waterloo.*

The final P_C-S model predictions for the CFS (H23) and MPL are shown together for comparison in **Figure V-8**. I elect to use the H23 CAD for the remaining analysis for simplicity since it is uncoated and, thus, a more well-defined material than H23I2. As expected, greater pressures are required to reach similar MPL saturation values as in the CFS. In future work, equivalent P_C-S data should be collected for the MPL as were collected for the isolated CFS materials. In practice, such MPL intrusion experiments are difficult to execute because high pressures are required and the MPL should ideally be isolated from the CFS (i.e., freestanding).

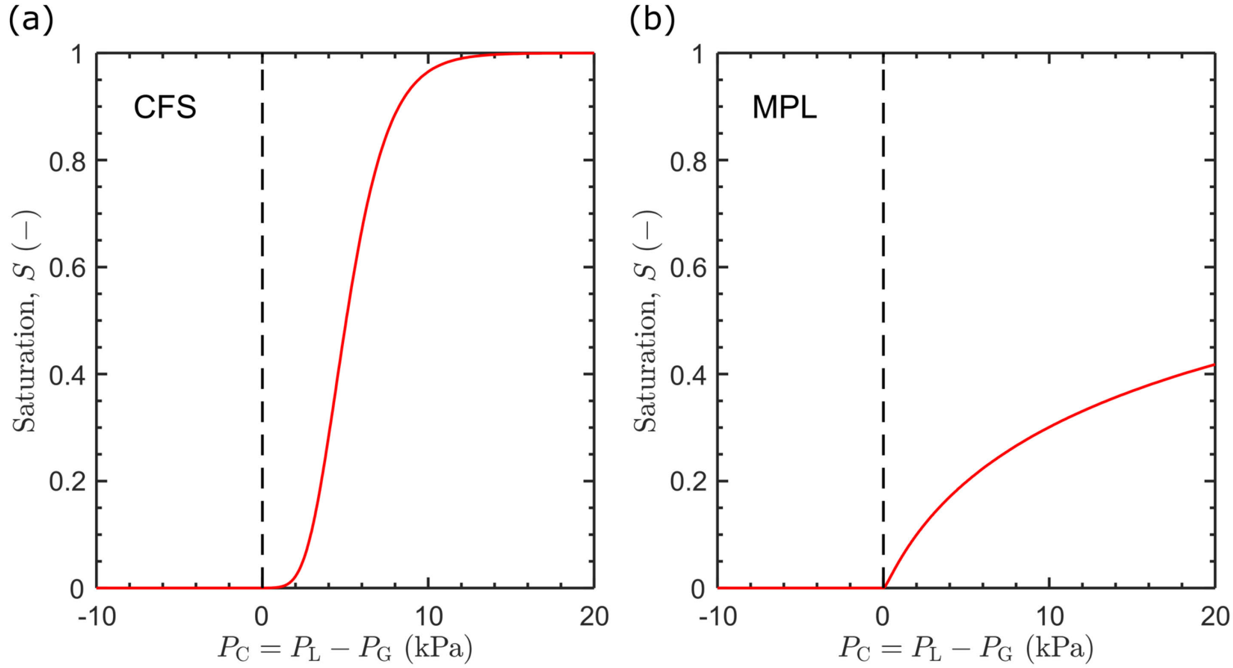

***Figure V-8**: Saturation versus capillary pressure for each GDE component. Different filling trends for the (a) CFS (H23) and (b) MPL are demonstrated by plotting their curves within the same pressure range.*

While fitting using a CAD to fit a saturation model against experimental P_C-S filling data does not provide quantitative information about pore-scale filling or connectivity, it can, in part, capture high level wettability effects, such as adding a PTFE-coating to increase the flooding resistance of GDE layers. Further study of the filling behavior of both the CFS and MPL using operando imaging can illuminate with more detail how local water saturation and trans-GDE percolation evolve. For now, I use this macro-homogeneous framework to probe how contact angle variation leads to changes in the P_C-S curves for the CFS (H23) and MPL along with other selected properties.

4. Calculated Properties: Equilibrium and Transport Properties

Once the PSD and CAD are defined for each GDE component, we can use Equation (V.2) to develop analytical expressions for equilibrium properties, such as the average pore radius for

Knudsen diffusion of gaseous species and volume-specific liquid-gas interfacial area, as well as transport properties like the relative permeabilities of liquid and gas phases. Each expression is defined in the following sections and representative plots for each GDE component are reported.

4.1. Average Knudsen Radius (r_{Kn})

Effective gas diffusivity through porous materials with small pore sizes, such as the MPL and CL, is calculated according to a parallel resistance as shown in Equation (V.9).[180]

$$D_i^{\mathrm{eff}} = \frac{1}{\dfrac{1}{D_i} + \dfrac{1}{D_{\mathrm{Kn},i}}} \tag{V.9}$$

Therefore, the effective diffusivity of species *i*, D_i^{eff}, is taken as the inverse sum of the bulk species diffusivity, D_i, and the Knudsen diffusivity, $D_{\mathrm{Kn},i}$, which is calculated from Equation (V.10).

$$D_{\mathrm{Kn},i} = \frac{2r_{\mathrm{Kn}}}{3}\left(\frac{8RT}{\pi M_i}\right)^{\frac{1}{2}} \tag{V.10}$$

Intrinsically, the Knudsen diffusivity is derived by considering the mean free path of a molecule according to the kinetic theory of gases, so it is determined, in part, by from the molar mass of species *i*, M_i, temperature, T, and the ideal gas constant, R. The average pore radius for Knudsen diffusion, r_{Kn}, is calculated from the average radius of gas-filled pores as a function of P_{C} by using Equation (V.2) with $W(r) = r$. The final expression for r_{Kn} is taken from the average radius normalized by the total gas filled pore volume $(1 - S)$ as shown in Equation (V.11).

$$r_{\mathrm{Kn}} = \frac{\begin{array}{c}\displaystyle\int_0^{90} \Psi(\theta)\left\{\sum_k \frac{f_{r,k}}{2} r_{\mathrm{o},k} \exp\left[s_k^2/2\right]\left[1 - \mathrm{erf}\left(\frac{\ln\left(r_{\mathrm{c}}\right) - \ln\left(r_{\mathrm{o},k}\right)}{s_k\sqrt{2}} - \left(s_k/\sqrt{2}\right)\right)\right]\right\} d\theta \\ \displaystyle + \int_{90}^{180} \Psi(\theta)\left\{\sum_k \frac{f_{r,k}}{2} r_{\mathrm{o},k} \exp\left[s_k^2/2\right]\left[1 + \mathrm{erf}\left(\frac{\ln\left(r_{\mathrm{c}}\right) - \ln\left(r_{\mathrm{o},k}\right)}{s_k\sqrt{2}} - \left(s_k/\sqrt{2}\right)\right)\right]\right\} d\theta\end{array}}{1 - S} \tag{V.11}$$

With this equation established, r_{Kn} as a function of P_{C} can be reported for each GDE component as shown in **Figure V-9**.

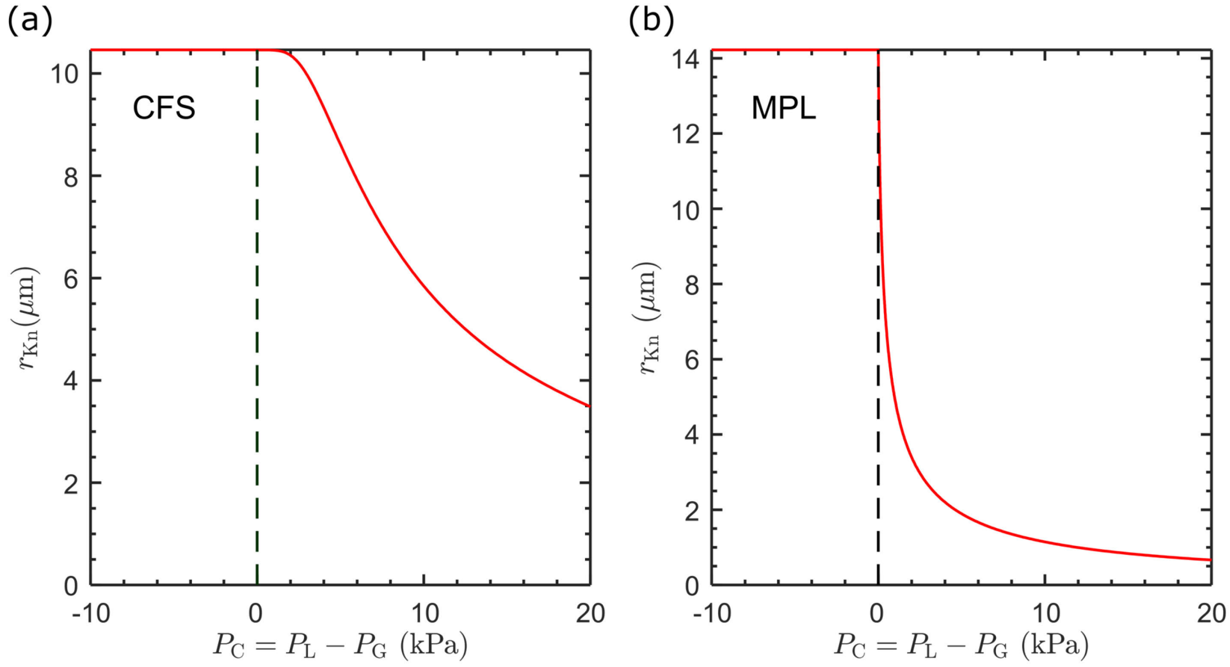

***Figure V-9**: Average Knudsen radius versus capillary pressure for each GDE component. Different average radius trends for the (a) CFS (H23) and (b) MPL are demonstrated by plotting their curves within the same pressure range.*

For $P_{\mathrm{C}} < 0$, the r_{Kn} is unimportant important for both materials as Knudsen diffusion is calculated to be most impactful for pore radii less than 1 µm. However, for $P_{\mathrm{C}} > 0$, the average radius of gas-filled pores decreases to a size where it begins to constrain diffusivity, according to Equation (V.10). This 1 µm approximation can be determined by recalling that the typical bulk phase gas species binary diffusivity at standard conditions is around ~10^{-5} cm^2 s^{-1}. Therefore, according to Equation (V.10) and plot in **Figure V-10**, the magnitude of D_{Kn} becomes roughly equivalent to this bulk value at pore radiuses close to 1 µm, using CO_2 with a molar mass of $M_{\mathrm{CO2}} = 44.01$ g mol^{-1} as an example. Knowing this, we can see from the plots in **Figure V-9** that the impacts of Knudsen diffusion are more apparent in microporous materials such as the MPL and CL.

Additionally, the constraints of Knudsen diffusion are largely negligible in macroporous materials since their characteristic pores sizes mostly exceed 1 µm, so the CFS results are only reported here for completeness.

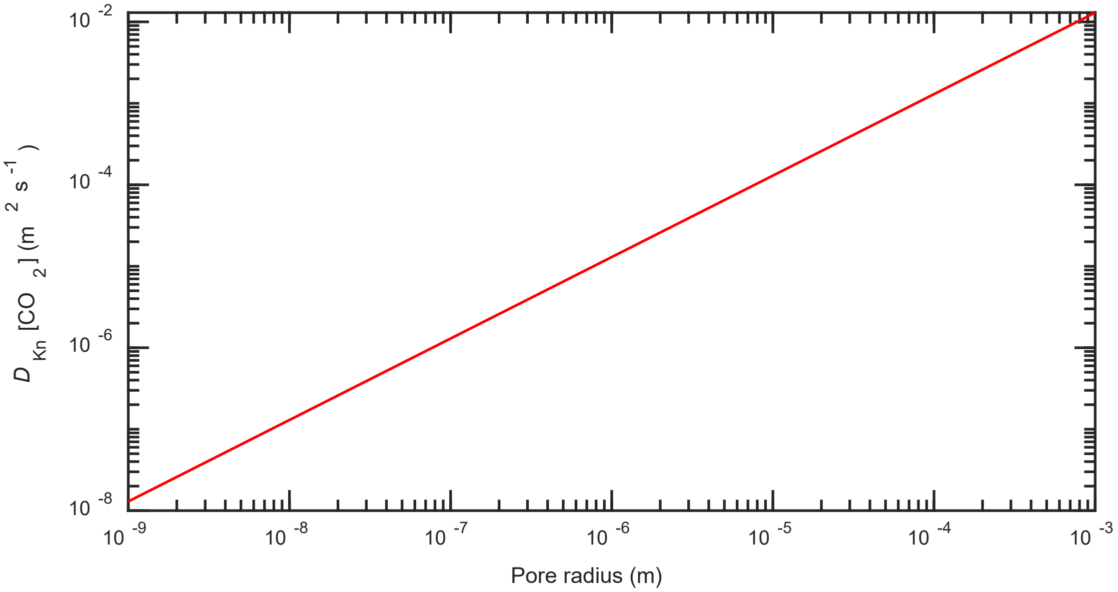

Figure V-10: *Knudsen diffusivity for CO_2 reported as a function of pore radius. The effect of Knudsen diffusion only becomes comparable to typical gas phase bulk diffusivities (~10^{-5} cm^2 s^{-1}) for pore radii at or less than 1 µm.*

4.2. Volume-Specific Liquid-Gas Interfacial Area ($a_{\mathrm{v,LG}}$)

The facile exchange of reactant and product species between gas and liquid phases within a GDE dictates the maximum electrocatalytic productivity in an CO_2 electrolyzer. The rate of mass transfer, or flux, of species across the liquid-gas phases is defined on a per area basis. To convert the flux expression to a mass transfer rate per unit volume for porous electrode modeling, an interfacial liquid-gas area per unit volume, $a_{\mathrm{v,LG}}$, (units of m^{-1}) is required. As defined by Zhou et al., this interfacial area, $a_{\mathrm{v,LG}}$, is estimated at a given r_{c} by Equation (V.12).[168]

$$a_{\mathrm{v,LG}} = a_{\mathrm{c}}\left(1 - \frac{a_{\mathrm{c}}}{a_{\mathrm{c,max}}}\right) \tag{V.12}$$

The total cross-sectional area per unit volume, $a_{\mathrm{c,max}}$, is given by Equation (V.13).

$$a_{\mathrm{c,max}} = \sum_k \frac{f_{r,k}\exp\left(s_k^{\ 2}/2\right)}{4r_k} \tag{V.13}$$

The cross sectional area per unit volume a_{c} is determined by the expression in Equation (V.14), which is determined by taking the ratio between the pore cross-sectional area and pore volume ($\pi r^2/\ \pi r^2 L \sim 1/4r$).

$$\begin{aligned} a_{\mathrm{c}} = & \int_0^{90} \Psi(\theta)\left\{\sum_k \frac{f_{r,k}}{8r_{\mathrm{o},k}}\exp\left[s_k^2/2\right]\left[1+\operatorname{erf}\left(\frac{\ln\left(r_{\mathrm{c}}\right)-\ln\left(r_{\mathrm{o},k}\right)}{s_k\sqrt{2}}+\left(s_k/\sqrt{2}\right)\right)\right]\right\}d\theta \\ & + \int_{90}^{180} \Psi(\theta)\left\{\sum_k \frac{f_{r,k}}{8r_{\mathrm{o},k}}\exp\left[s_k^2/2\right]\left[1-\operatorname{erf}\left(\frac{\ln\left(r_{\mathrm{c}}\right)-\ln\left(r_{\mathrm{o},k}\right)}{s_k\sqrt{2}}+\left(s_k/\sqrt{2}\right)\right)\right]\right\}d\theta \end{aligned} \tag{V.14}$$

Plots of $a_{\mathrm{v,LG}}$ as a function of P_{C} for GDE components are provided in **Figure V-11**, respectively. We can see from the curve that contact area reaches a maximum unlike the curves for other properties, which either monotonically increase or decrease, depending on the phase.

Contemplating the shape of the $a_{\mathrm{v,LG}}$ curve provides insight into the how the optimum P_{C} for maximizing mass transfer might shift as a function of a porous medium's wettability. Of course, maximizing the interfacial area might only be advantageous for some GDE components, such as the catalyst layer.

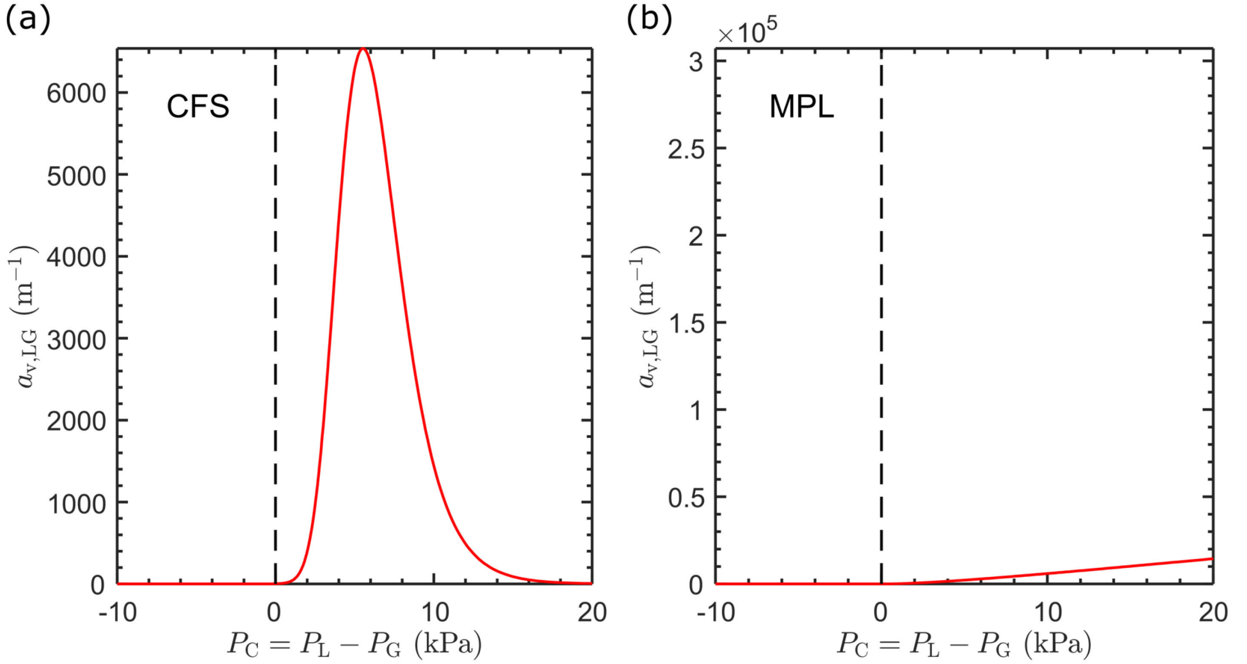

Figure V-11*: Liquid-gas interfacial area versus capillary pressure for each component. Different volume-specific liquid-gas interfacial area trends for the (a) CFS (H23) and (b) MPL are demonstrated by plotting their curves within the same pressure range.*

4.3. Relative Permeabilities for Darcy Flow ($k_{\mathrm{r,L}}$ & $k_{\mathrm{r,G}}$)

Within the macro-homogeneous framework used here, the pressure driven flow of liquid and gas phases through the GDE components is assumed to follow Darcy's Law. A general expression for the superficial velocity as a function of the pressure gradient is given by Equation (V.15).

$$\mathbf{u} = -\frac{k}{\mu}\nabla P \tag{V.15}$$

The velocity field of the fluid, $\mathbf{u}$, is calculated from negative of the pressure gradient, $-\nabla P$, which is multiplied by the effective Darcy permeability of the porous medium, k^{eff}, and divided by the dynamic viscosity of the fluid, μ. As the permeability decreases with increasing liquid saturation, we can determine k^{eff} by taking the product of the saturated Darcy permeability, k_{sat} and the relative permeability, k_{r}.

$$k^{\mathrm{eff}} = k_{\mathrm{r}} k_{\mathrm{sat}} \tag{V.16}$$

We can calculate k_{r} for each phase according to the approach of Weber et al. that assumes permeability scales with r^2. Therefore, we again employ Equation (V.2) and use $W(r) = r^2$ along with the appropriate integration limits calculate the relative permeabilities of the liquid, $k_{\mathrm{r,L}}$, and gas, $k_{\mathrm{r,G}}$, respectively, as a function of P_{C}. $k_{\mathrm{r,L}}$ is calculated according to Equation (V.17) while $k_{\mathrm{r,G}}$ is calculated by Equation (V.18).

$$k_{\mathrm{r,L}} = S_{\mathrm{e}}^{n_{\mathrm{L}}} \frac{\displaystyle\int_0^{90} \Psi(\theta)\left\{\sum_k \frac{f_{r,k}}{2} r_{\mathrm{o},k}^2 \exp\left[2s_k^2\right]\left[1+\mathrm{erf}\left(\frac{\ln\left(r_{\mathrm{c}}\right)-\ln\left(r_{\mathrm{o},k}\right)}{s_k\sqrt{2}} - s_k\sqrt{2}\right)\right]\right\}d\theta + \int_{90}^{180} \Psi(\theta)\left\{\sum_k \frac{f_{r,k}}{2} r_{\mathrm{o},k}^2 \exp\left[2s_k^2\right]\left[1-\mathrm{erf}\left(\frac{\ln\left(r_{\mathrm{c}}\right)-\ln\left(r_{\mathrm{o},k}\right)}{s_k\sqrt{2}} - s_k\sqrt{2}\right)\right]\right\}d\theta}{\left\{\sum_k f_{r,k} r_{\mathrm{o},k}^2 \exp\left[2s_k^2\right]\right\}} \tag{V.17}$$

$$k_{\mathrm{r,G}} = \left(1-S\right)^{n_{\mathrm{G}}} \frac{\displaystyle\int_{0}^{90} \Psi(\theta)\left\{\sum_{k} \frac{f_{r,k}}{2} r_{\mathrm{o},k}^{2} \exp\left[2s_{k}^{2}\right]\left[1-\mathrm{erf}\left(\frac{\ln\left(r_{\mathrm{c}}\right)-\ln\left(r_{\mathrm{o},k}\right)}{s_{k}\sqrt{2}}-s_{k}\sqrt{2}\right)\right]\right\}d\theta + \int_{90}^{180} \Psi(\theta)\left\{\sum_{k} \frac{f_{r,k}}{2} r_{\mathrm{o},k}^{2} \exp\left[2s_{k}^{2}\right]\left[1+\mathrm{erf}\left(\frac{\ln\left(r_{\mathrm{c}}\right)-\ln\left(r_{\mathrm{o},k}\right)}{s_{k}\sqrt{2}}-s_{k}\sqrt{2}\right)\right]\right\}d\theta}{\left\{\sum_{k} f_{r,k} r_{\mathrm{o},k}^{2} \exp\left[2s_{k}^{2}\right]\right\}} \quad \text{(V.18)}$$

For this study I exponent values of $n_{\mathrm{G,CFS}} = 3$ and $n_{\mathrm{L,CFS}} = 4$ for the CFS and $n_{\mathrm{G,MPL}} = 3$ and $n_{\mathrm{L,MPL}} = 3.5$ for the MPL based on a validated PEFC model using similar fibrous CFS and MPL materials sets, respectively.[167] For any subsequent analyses using the Darcy permeability, we could assume that $k_{\mathrm{sat,CFS}} = 10^{-12}$ m^2 and $k_{\mathrm{sat,MPL}} = 10^{-15}$ m^2 based on the same report. Plots of the $k_{\mathrm{r,L}}$ and $k_{\mathrm{r,G}}$ as a function of P_{C} are provided for each GDE component in **Figure V-12** and **Figure V-13**, respectively.

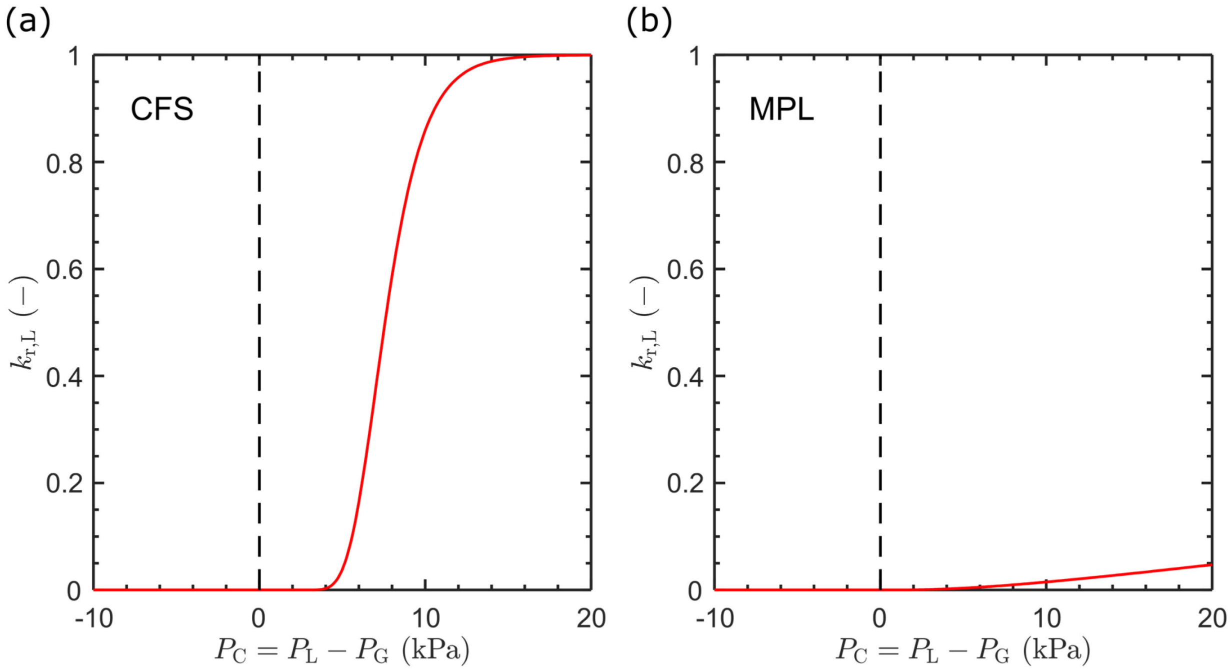

***Figure V-12**: Liquid relative permeability versus capillary pressure for each GDE component. Different permeability trends for the (a) CFS (H23) and (b) MPL are demonstrated by plotting their curves within the same pressure range.*

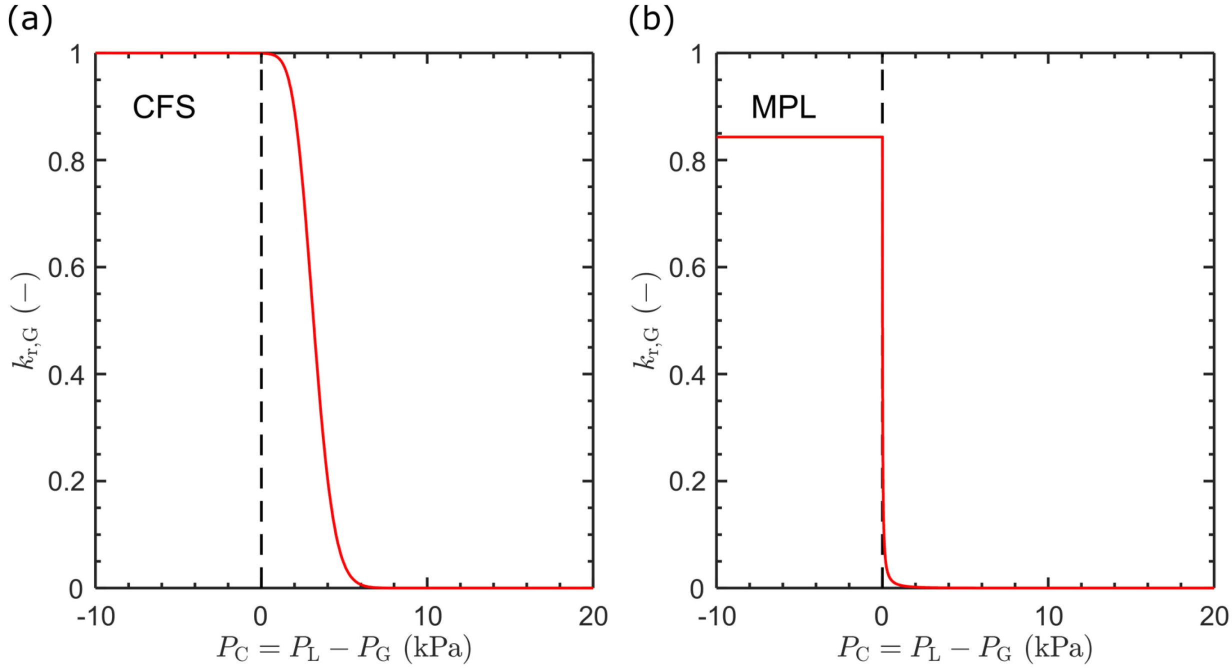

Figure V-13*: Gas relative permeability versus capillary pressure for each GDE component. Different permeability trends for the (a) CFS (H23) and (b) MPL are demonstrated by plotting their curves within the same pressure range.*

5. *Contact Angle Variability: Electrowetting and Aqueous-Organic Liquid Mixtures*

Exploring the implications of contact angle variability on GDE wettability is relevant for predicting how CO2R reaction environments might influence electrolyzer performance. Specifically, polarization-induced electrowetting and the generation of high concentrations of liquid CO2R products are both anticipated to lead to increased GDE wettability as previously discussed in Chapters III and IV, respectively. In this section, I show how general variations to characteristic contact angles, θ_o, within each component's CAD shift calculated electrode properties.

5.1. Electrowetting

Electrowetting is characterized by the decrease in contact angle between fluids and a polarizable substrate due to the application of a potential bias at the interface between them. In practice, harnessing electrocapillarity to manipulate small amounts of liquid on surfaces with a voltage input has many applications ranging from microfluidics, adjustable liquid lenses, and electronic display technologies.[171] Electrowetting on a dielectric (EWOD) technologies are prevalent for such use cases because the surfaces are coated with an insulating film, such as PTFE, to prevent faradaic charge transfer reactions. However, in the context of CO_2 electrolyzers, bare electrodes, most often composed of carbon and metals, constitute the polarizable surfaces. In gas fed GDE flow cells that use liquid electrolytes electrowetting is hypothesized to be responsible, to some degree, for unexpected electrode saturation at sufficiently high electrode potentials.[93,181] Recall from Chapter III that although increasing current density is associated with, and possibly contributes to, accelerated cathode flooding, the precise origin of GDE flooding was not completely determined. In this section, I attempt to simulate and then contextualize the hypothesized impact of electrowetting on GDE saturation by shifting the CAD.

To understand the electrowetting effect, we can consider the simple case of a liquid electrolyte droplet deposited onto a planar polarizable solid surface with a gaseous phase enveloping both the droplet and solid. As shown in **Figure V-14a**, the interfacial energy/surface tension between the phases are balanced by Young's relation as shown in Equation (V.19).

$$\gamma_{\mathrm{SG}} = \gamma_{\mathrm{SL}} + \gamma_{\mathrm{LG}} \cos(\theta) \tag{V.19}$$

The Lippman equation can then be introduced to describe the decrease in interfacial energy between the solid and liquid phases, γ_{SL}, as a function of the square of the applied surface potential, Φ^2, as shown in Equation (V.20).

$$\gamma_{\mathrm{SL}} = \gamma_{\mathrm{SL}}^{0} - \frac{C_{\mathrm{dl}}\Phi^2}{2} \tag{V.20}$$

This expression shows that the interfacial surface energy decreases no matter the sign of the polarization applied at the interface. The functional relationship between Φ and θ is determined from by combining the Young-Dupre and Lippmann relationships to produce the Young-Lippmann relation, which is expressed in Equation (V.21).[171]

$$\cos(\theta) = \cos(\theta_{\mathrm{o}}) + \frac{C_{\mathrm{dl}}}{2\gamma_{\mathrm{LG}}}\Phi^2 \tag{V.21}$$

If the interfacial tension between the liquid and gas phases, γ_{LG}, and the electrochemical double layer capacitance between the solid and liquid electrolyte phases, C_{dl}, are known, then we can estimate the impact of electrode polarization on electrode wettability. Note that the electrode polarization shown here is strictly defined as the applied surface potential relative to the "potential of zero charge", Φ_{pzc}, which is an equilibrium potential that spontaneous emerges to balance charge at the interface between the electrolyte and the polarizable solid. The electrowetting phenomenon on a planar surface is depicted qualitatively in **Figure V-14b**.

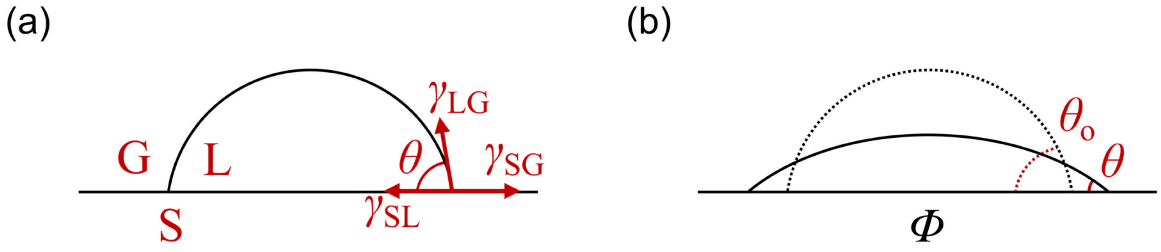

***Figure V-14**: Conceptual solid-liquid-gas contact angle and the electrowetting phenomenon. (a) The surface tensions, γ, at the interfaces between the solid (S), liquid (L), and gas (G) phases are balanced by Young's equation. (b) Polarizing the solid phase with an applied potential, Φ, results in a decrease in the contact angle from θ_o to θ according to the Young-Lippmann equation.*

The electrowetting (EW) equation presented in Equation (V.21) provides a means by which we can investigate the influence of electrode polarization on intrinsic wettability and, ultimately, spatially resolved saturation. Here I focus on carbon, since it constitutes the major polarizable component of the nominally non-wetting components of the GDE (i.e., CFS and MPL). The applied potentials required to induce EW effects depends on the exposed polarizable fraction, f_{EW}, inherent to each GDE component surface, but also on the C_{dl} inherent to each electrode-electrolyte pair. Measurable θ shifts have been observed when applying potentials as low as ~100 mV within a packed bed of glassy carbon particles.[172] Carbon fibers (CFS) and carbon black powders (MPL) are more graphitic in character than glassy carbon, as measured by their Raman spectra, and might exhibit different EW effects.[182]

For a baseline estimation of carbon EW, we could first assume a double layer capacitance, C_{dl}, of 20 μF cm^{-2}, which represents a bulk basal plane carbon surface reported by Shi.[183] However, it has been shown that capacitance varies notably according to carbon allotrope. Rabbow and Whitehead note that the edge sites of a carbon fiber may exhibit $C_{\mathrm{dl,edge}} \approx 132$ μF cm^{-2} while the basal edge of the fiber only exhibits $C_{\mathrm{dl,basal}} \approx 4.7$ μF cm^{-2}. This notable C_{dl} difference for different portions of the same carbon fiber implies that more targeted studies of EW effects on polarizable substrates with non-planar geometries and in porous media are warranted. Using these parameters and the surface tension of pure water, we can calculate the intrinsic contact angle, θ, as a function of applied potential, Φ. As shown by the array of curves in **Figure V-15**, inducing an initial 10° decrease in the θ would only require as low as ca. 100 mV on edge carbon surfaces (132 μF cm^{-2}) but as much as ca. 700 mV on basal carbon surfaces (4.7 μF cm^{-2}).

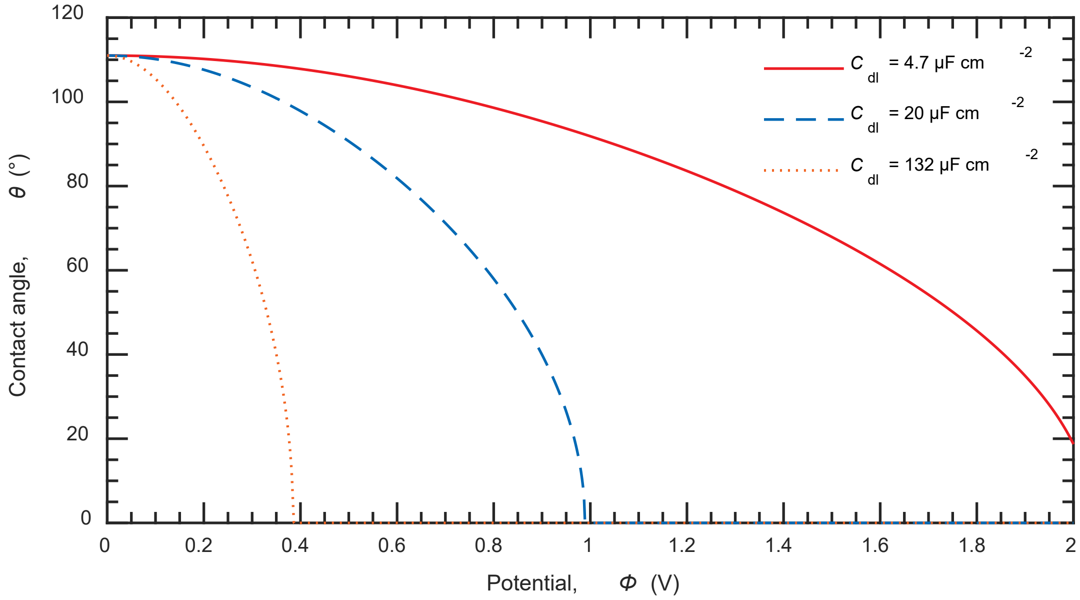

***Figure V-15**: Electrowetting voltages required to induce contact angle variation as a function of representative carbon specific double layer capacitance values. The baseline contact angle in this case is 112°.*

We can simulate the hypothetical impacts of EW on saturation of the CFS and MPL by shifting some fraction or the entire CAD distribution. Translating the range of θ values back to a values of Φ only requires Equation (V.21) along with an assumed (or measured) C_{dl} and $\gamma_{\mathrm{LG}} = 0.072$ N m^{-1}

to represent an aqueous electrolyte in contact with a carbon electrode surface. For the case of a bare porous carbon electrode (e.g., H23), we could assume that the entire surface is subject to EW effects. However, the wettable interior surfaces of the CFS and MPL pore volumes are likely to be partially or fully coated by binder and/or wet-proofing polymers such polytetrafluoroethylene (PTFE) or fluorinated ethylene propylene (FEP). As shown by the cross-section of the Ag-GDE cross-sectional elemental map in **Figure V-4**, a significant fraction of the carbon may be coated, but the distribution might be heterogeneous. Combining pore-resolved coating information with PNM models could be a promising means for evaluating how coating quality and distribution might change EW effects on saturation as a function of position within a porous electrode.

For an initial analysis, I consider the impacts of EW as a function of the uncoated fraction of the electrode surface and define the surface fraction accessible to EW as f_{EW}. This is handled by adding an EW-shifted CAD (Ψ_{EW}) weighted by f_{EW} to the original CAD (Ψ_0) weighted by $(1 - f_{EW})$, as shown in Equation (V.22).

$$\Psi(\theta) = (1 - f_{EW})\Psi_0(\theta) + f_{EW}\Psi_{EW}(\theta) \tag{V.22}$$

A series of simulated contact angle decrease simulations are reported for the CFS and the MPL in **Figure V-16** and **Figure V-17**, respectively. The four panels in each figure correspond to scenarios of increasing coating coverage in which f_{EW} = 100, 75, 50, or 25%, respectively. Visualizations of the CAD shifts associated with each f_{EW} are reported in **Figure V-29** (CFS) and **Figure V-30** (MPL) in Appendix D. The contours in each plot correspond to partial modifications of the CAD in 5° increments away from the baseline values of 111° and 110° for the CFS (H23) and MPL, respectively. Unsurprisingly, as the fraction of the pore surface covered by an insulator (i.e., PTFE) increases (i.e., f_{EW} decreases), the model predicts a diminishing impact of θ variation on the P_C-S

curves. Experiments should be conducted in the future to approximate values of f_{EW} for each material to fully evaluate the EW hypotheses proposed in this work. Additional plots showing the effects of a contact angle variation (f_{EW} = 100%) on the other calculated properties (r_{Kn}, $a_{\mathrm{v,LG}}$, $k_{\mathrm{r,L}}$, $k_{\mathrm{r,G}}$) are reported in **Figure V-31** (CFS) and **Figure V-32** (MPL) Appendix D. Accurate mapping of the distribution of electrode components in the pore spaces of a GDE would improve predictions of the possible influences of EW on GDE flooding when in contact with liquid electrolytes.

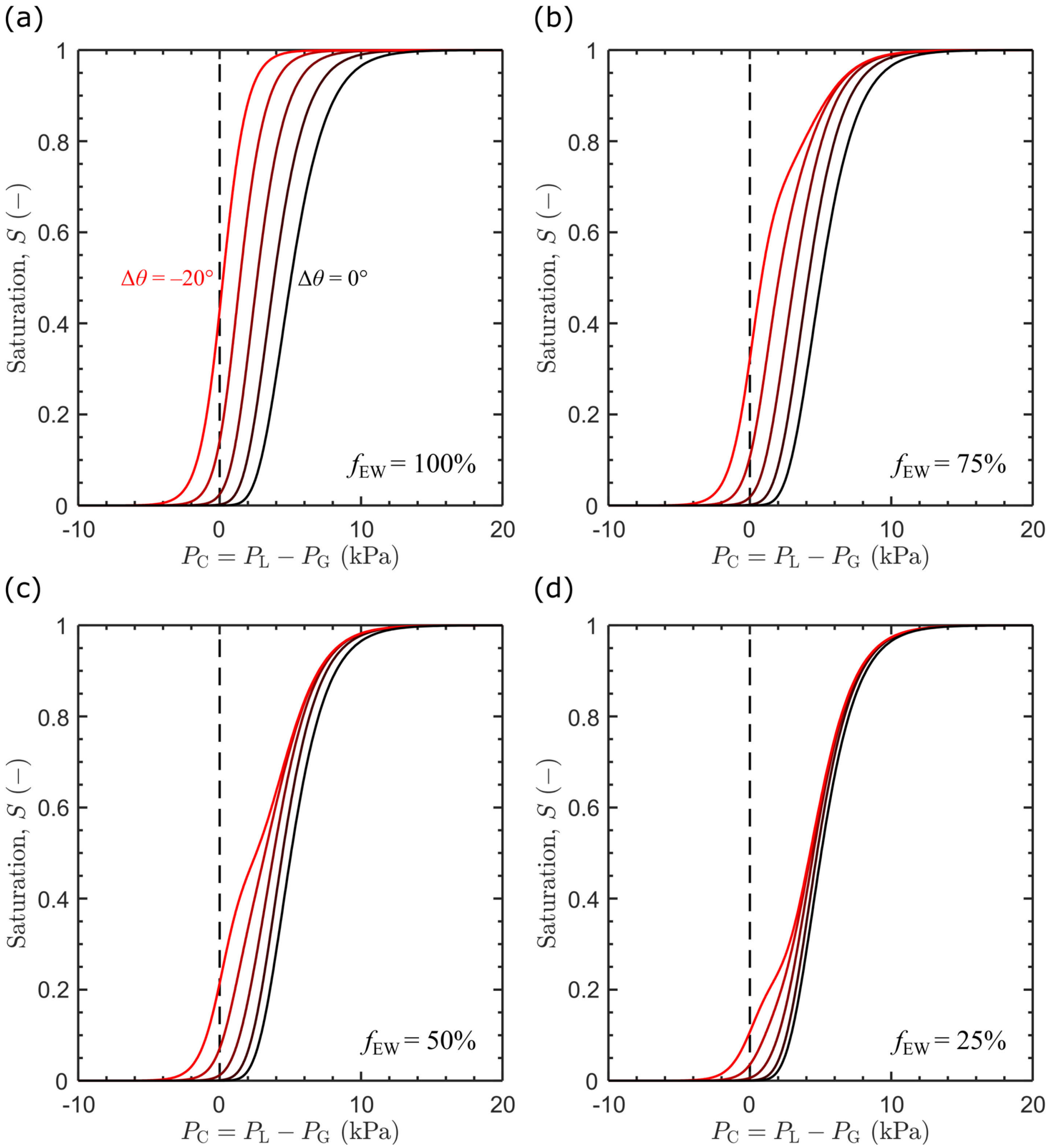

***Figure V-16**: Simulated electrowetting effect on the CFS P_C-S curves as a function of f_{EW}. Panels correspond to scenarios in which (a) 100, (b) 75, (c) 50, or (d) 25% of the pore wall area is polarizable and susceptible to electrowetting.*

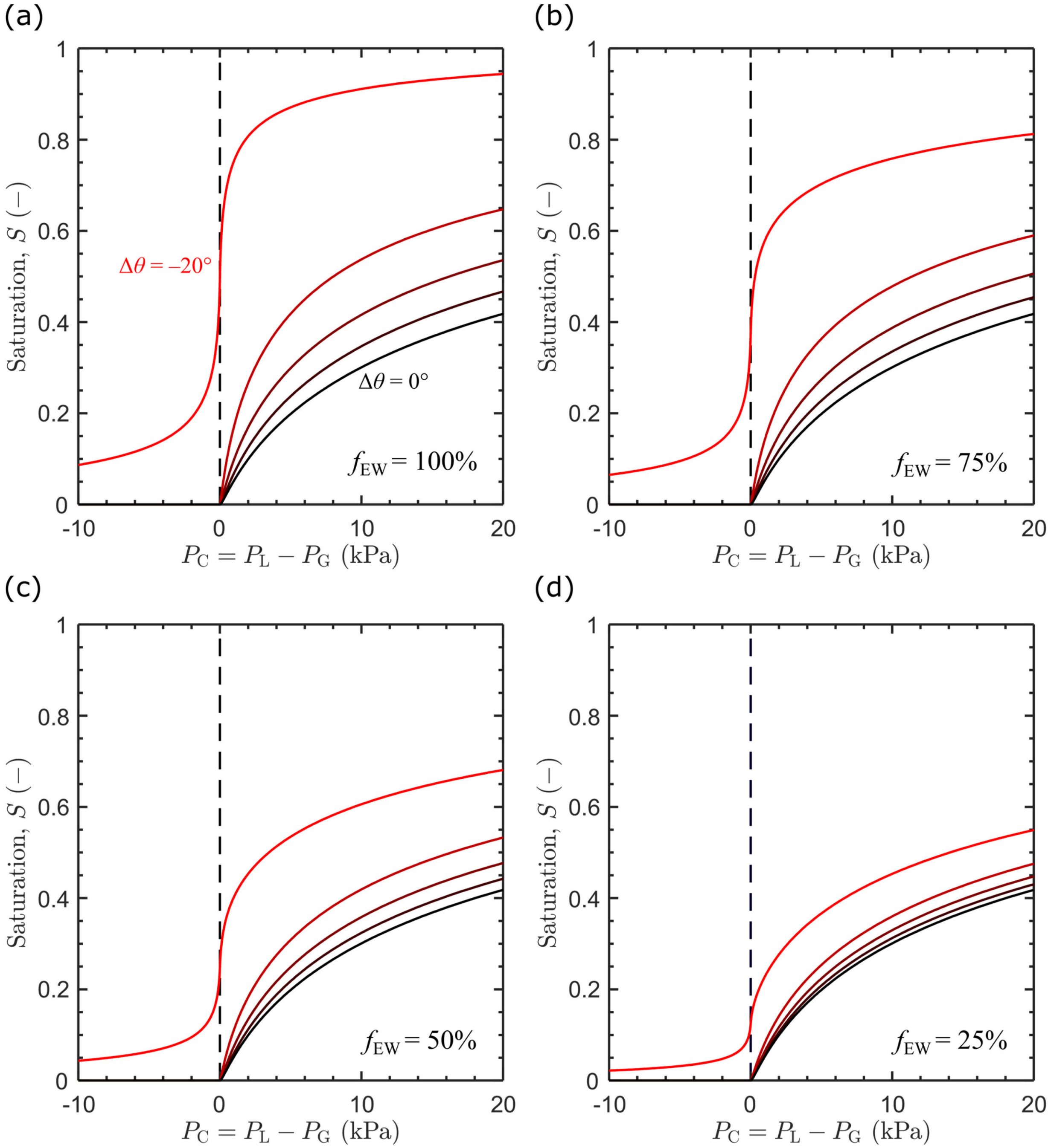

***Figure V-17**: Simulated electrowetting effect on the MPL P_C-S curves as a function of f_{EW}. Panels correspond to scenarios in which (a) 100, (b) 75, (c) 50, or (d) 25% of the pore wall area is polarizable and susceptible to electrowetting.*

While the effects of EW are most pronounced for systems with liquid electrolytes, high concentration liquid CO2R products are relevant for these systems and even for those using polymer membrane electrolytes. In the next section, I use this same modeling framework to predict GDE saturation trends that could emerge when facing aqueous-organic liquid mixtures, as first discussed in Chapter IV. While the increased wettability predicted by EW equation assumes that γ_{LG} is approximately constant as a function of Φ, the increased wettability due to liquid CO2R products must also consider the coupled nature of γ and θ.

5.2. Aqueous-Organic Liquid Mixtures

As discussed in Chapter IV, the liquid-gas surface tension of liquid mixture can be correlated to changes in the contact angle between droplets and solid surfaces. Here, I vary both the CAD and γ values used when calculating the CFS and MPL P_C-S curves. The γ-θ functional relationship is determined from previous sessile drop contact angle measurements of alcohol-water mixtures on a flat polytetrafluoroethylene (PTFE) surface.[173] The surface tension values used here start from that of a purely aqueous solution (0.072 N m^{-1}) and decrease towards numbers that represent mixtures enriched in organic species (0.032 N m^{-1}). I use the polynomial fit equation introduced in Chapter IV to predict liquid contact angles on PTFE, θ_{PTFE}, along with the corresponding alcohol mass fractions for methanol, ethanol, and 1-propanol. The mass fractions for each CO2R liquid product are calculated using the data **Figure IV-10b**. All relevant surface tension, alcohol mass fraction, and contact angle values are reported in **Table V-5**.

***Table V-5**: γ-θ equivalence data for simulating CO2R liquid product mixture wettability. Aqueous-alcohol mixture surface tensions are reported with equivalent concentrations of methanol, ethanol, and 1-propanol dilutions in water. The PTFE contact angle, θ_{PTFE}, predicted from a Zisman plot polynomial fit, as shown in **Figure IV-10b**.*

Surface tension, γ (N/m)	**Alcohol mass fraction (%)**			**Predicted* contact angle θ_{PTFE} (°)**
	Methanol	*Ethanol*	*1-Propanol*	
0.072	0	0	0	112.4
0.062	5.55	2.63	1.20	104.0
0.052	14.05	6.86	2.74	94.8
0.042	28.17	15.17	5.09	84.1
0.032	52.60	32.55	12.74	69.8
*Polynomial fit: $\gamma = 0.02865[1 - \cos(\theta_{PTFE})]^2 - 0.00332[1 - \cos(\theta_{PTFE})] + 0.02191$				

Taking these combinations of γ and θ, I simulate the saturation effects of CO2R liquid products on the CFS and MPL and report the P_C-S predictions in **Figure V-18** and **Figure V-19**, respectively. As noted in Chapter IV, I use the θ_{PTFE} values instead of carbon values for saturation analysis because PTFE is the less wettable electrode component and can provide an upper bound on flooding resilience in a GDE. Furthermore, analyzing P_C-S trends for GDE components composed primarily of PTFE might illuminate how even nominally "wet-proof" materials such as PTFE are challenged by liquid mixtures enriched in organic reaction products.

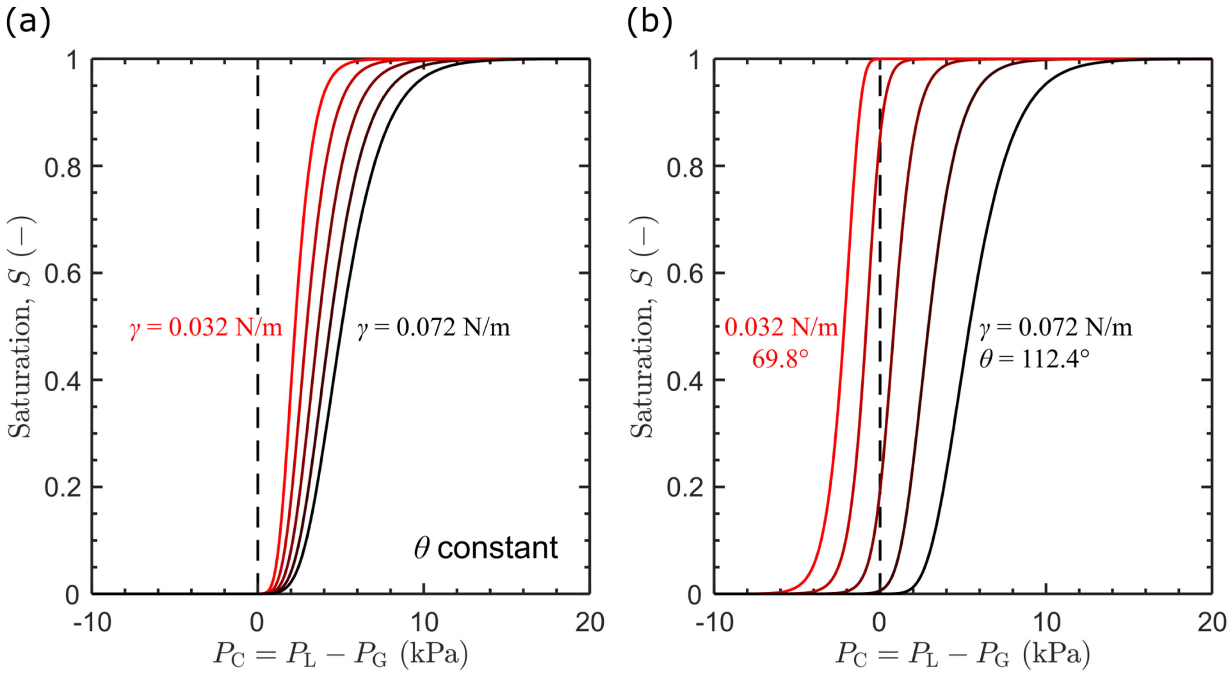

Figure V-18: *Simulated liquid CO2R product effect on CFS P_C-S curves considering variable (a) γ and (b) γ-θ.*

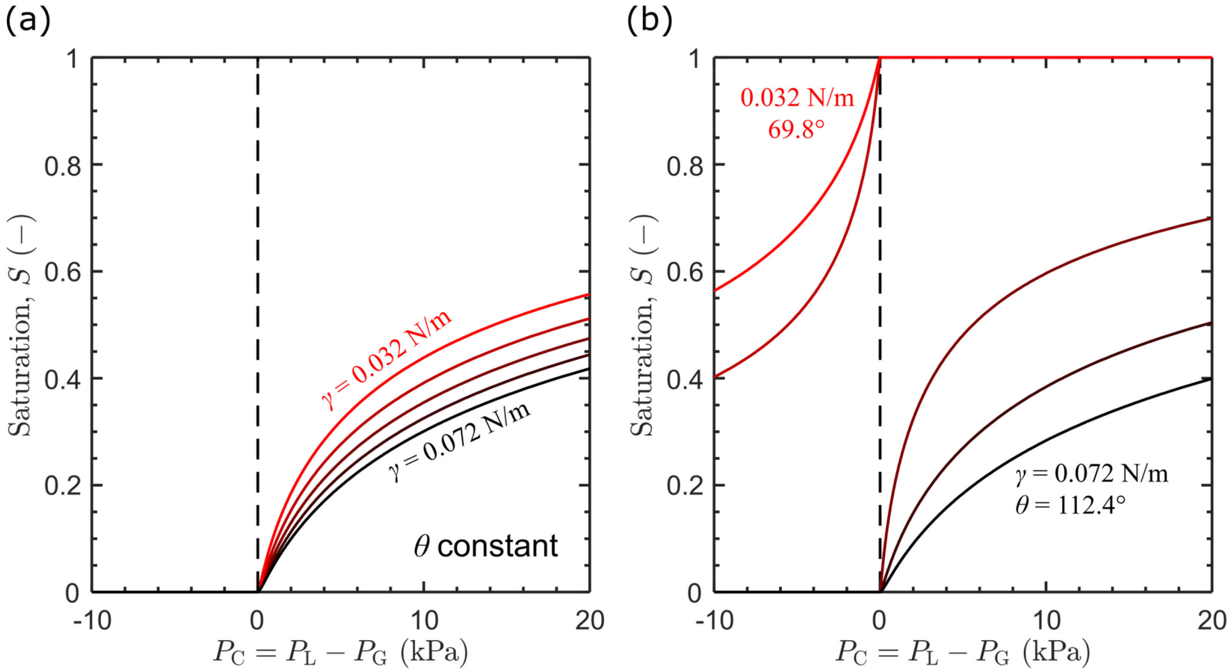

Figure V-19: *Simulated liquid CO2R product effect on MPL P_C-S curves considering variable (a) γ and (b) γ-θ.*

As can be seen from the results in **Figure V-18** and **Figure V-19**, shifting γ alone minimally changes saturation fraction at a given P_C. Shifting γ and θ together results in a more substantial change in the equilibrium saturation for both the CFS and MPL models. Both phenomena shift P_C-S towards more negative P_C, indicating an increasingly hydrophilic pore character and that minimizing liquid saturation, in practice, might require increasing P_G (or decreasing P_L). The changes in the CFS are considerably milder as compared to the MPL because the MPL has a much smaller characteristic pore sizes in its PSD. Thus, its hydrophobic pores are more difficult to fill and its hydrophilic pores are easier to fill. As CAD crosses 90° threshold for both materials, the S value at $P_C = 0$ kPa jumps from 0 to 100%.

Using this model, can understand qualitatively why GDE layers with smaller pores (i.e., MPL) would so rapidly and spontaneously imbibe aqueous-organic liquid mixtures at pressure balanced conditions (i.e., $P_C = 0$ kPa). In practice, if liquid CO2R products are not cleared from the catalyst layer, either by diffusing into the bulk electrolyte phase or by evaporating into the gas phase, low surface tension liquids would tend to spontaneously saturate the pore volume of the MPL, resulting in liquid percolation to the CFS and diminished gas species transport to the catalyst layer. The implications of increased MPL saturation are worth consideration by engineers and operators of future large-scale electrolyzers who might intend to target high concentration liquid product streams to reduce downstream separation costs.

6. *Simulating Flooding Events Due to Contact Angle Variability*

Transport models of GDEs are invaluable for predicting the impacts of electrode microstructure and wettability characteristics on CO2R performance. In this section, I use previously derived electrode properties to model Darcy flow of water through partially-saturated CFS and MPL layers of a GDE as a function of liquid channel pressure, P_{LC}, and intrinsic contact angles, θ, of the materials. We can use transient models to understand the propagation of liquid fronts through porous media and steady state solutions to quickly probe the average saturation of the GDE as a function of previous discussed wettability characteristics.

6.1. COMSOL Model Physics

To evaluate the impacts of contact angle variability on GDE component water saturation and gas transport properties (e.g., species diffusivities), I implement a Darcy flow transport model in COMSOL Multiphysics (version 5.6). The GDE components, CFS and MPL, are treated as 1D intervals with thicknesses of 200 μm and 50 μm, respectively, as shown in the model domain schematic in **Figure V-20**. Note that the CFS is shortened from 210 μm to 200 μm because some portion of the MPL is embedded within the CFS, effectively eliminating some portion of the fibrous character in that intermediate region. I set the porosities to $\varepsilon_{\mathrm{p,CFS}} = 0.7$ and $\varepsilon_{\mathrm{p,MPL}} = 0.4$ based on results from MIP for the CFS and an estimated value for the MPL based on a previous study.[166] I chose saturated permeabilities that are in line with a study by Zenyuk et al.[167] They are set to $k_{\mathrm{sat,CFS}} = 10^{-12}$ m^2 and $k_{\mathrm{sat,MPL}} = 10^{-15}$ m^2 for the CFS and MPL, respectively. The water properties, including density, ρ, and dynamic viscosity, μ, are taken from COMSOL's built-in property set. All calculations are performed using a system temperature of 298.15 K and with a reference pressure of 1 atm. All pressure values after this point are gauge pressures relative to the reference pressure unless otherwise specific as absolute or capillary pressures.

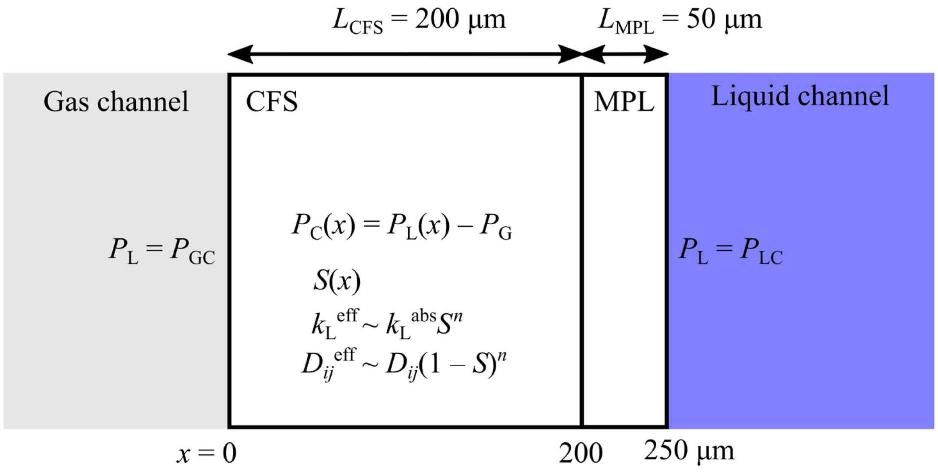

***Figure V-20**: 1D COMSOL transport model schematic for Darcy flow of water through partially saturated MPL and CFS layers.*

The velocity of liquid flow is modeled by Darcy's law, shown in Equation (V.15), with the overall transient conservation equation for the liquid is shown in Equation (V.23).

$$\frac{\partial}{\partial t}\left(\varepsilon_{\mathrm{p,L}}\rho\right) - \frac{\rho k_{\mathrm{L}}^{\mathrm{eff}}}{\mu}\frac{\partial^2 P_{\mathrm{L}}}{\partial x^2} = 0 \qquad \text{(V.23)}$$

In this expression, the liquid porosity, $\varepsilon_{\mathrm{p,L}}$, is defined as the overall porosity of the material multiplied by the liquid saturation, S, as shown in Equation (V.24).

$$\varepsilon_{\mathrm{p,L}} = \varepsilon_{\mathrm{p}} S \qquad \text{(V.24)}$$

The effective liquid permeability, $k_{\mathrm{L}}^{\mathrm{eff}}$, is determined as a function of P_{C} using Equation (V.16). In the future, the full conservation equation would be needed to analyze the time-varying evolution of the liquid front through the GDE. However, here I choose to focus on changes to the steady state liquid saturation profile as a function of liquid channel pressure (P_{LC}) and θ. For the steady state case, Equation (V.23) reduces to the form of Laplace's equation shown in Equation (V.25).

$$\frac{d^2 P_{\mathrm{L}}}{dx^2} = 0 \tag{V.25}$$

Gaseous species diffusivity is chosen as a representative transport property that is relevant as a proxy for electrolyzer CO2R performance. A bulk gas diffusivity, $D_{\mathrm{G}} = 10^{-5}\ \mathrm{m}^2\ \mathrm{s}^{-1}$, is assumed for the purposes of calculating effective diffusivity, $D_{\mathrm{G}}^{\mathrm{eff}}$, as a function of S using Equation (V.26).

$$D_{\mathrm{G}}^{\mathrm{eff}} = D_{\mathrm{G}}\left(1 - S\right)^{n_{\mathrm{G}}} \tag{V.26}$$

The gas species transport coefficients are chosen to be $n_{\mathrm{G,CFS}} = 3$ and $n_{\mathrm{G,MPL}} = 3$ based on a previous report in the literature.[167]

Pressure set points are used as the boundary conditions at the liquid channel (LC) and gas channel (GC). In the baseline case, the water pressure at the liquid channel interface is set to $P_{\mathrm{L}} = P_{\mathrm{LC}} = 0.1$ kPa, which is low enough that at standard wettability conditions the flux of water due to pressure driven flow through the material should be minimal. At the gas channel interface, the water pressure is set to $P_{\mathrm{L}} = P_{\mathrm{GC}} = 0$ kPa, indicating that liquid removal/droplet detachment into the gas channel would be trivial. When the CFS and MPL are both used together to simulate flow through a full GDE model, liquid pressure continuity is assumed between the domains.

6.2. Model Results and Discussion

First, I calculate the steady state distribution of water for the isolated CFS and MPL components. For a set P_{LC}, I gradually decrease the θ and record the average saturation across the material domain. As shown in **Figure V-21**, the average CFS water saturation starts at less than zero percent for $\theta_{\mathrm{CFS}} = 111°$ and steadily increases as the wettability of the material is increased (θ decreases). The plot of the average saturation which has a sigmoid shape like the constitutive P_{C}-S curve. As PLC is increased from 0.1 kPa to 1 kPa, the average saturation curve shifts towards higher θ values.

Analogous results for the isolated MPL are also shown in **Figure V-21**. Even sharper saturation transitions occur within the MPL as the θ approaches 90°. As the liquid pressure is increased from 0.1 to 1 kPa and then again from 1 to 10 kPa, we can see that the average baseline MPL saturation also shifts upward. The transition from a dry state to a saturated state occurs more sharply for the MPL than for CFS both due to the smaller pore sizes in the PSD but also due to a narrower CAD. Any changes to the intrinsic wettability (θ) of the MPL would be expected to appear later than for the CFS, but the changes could manifest more catastrophically.

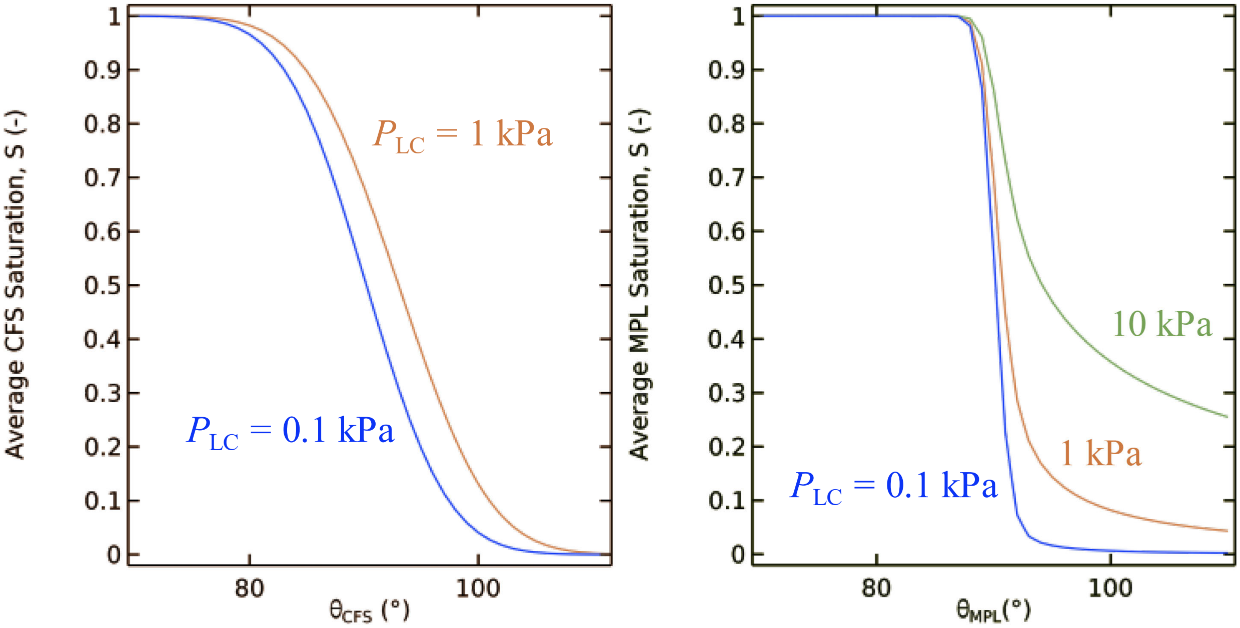

Figure V-21*: Average liquid saturation in isolated CFS and MPL layers as a function of θ and P_{LC}. As θ decreases, the saturation increases. The sharpness of the transition from dry to saturated occurs more sharply for the MPL than for CFS both due to the smaller pore sizes but also due to the narrower CAD in the MPL.*

D_G^{eff} for both the CFS and MPL are reported in **Figure V-22**. In general, the inverse correlation between the D_G^{eff} and saturation are evident. However due to the power law relationship between saturation and diffusivity, the diffusivities in both CFS and MPL decrease more quickly than the corresponding saturations increase. This example demonstrates how a material does not need to necessarily need to be highly saturated with liquid before transport coefficients diminish substantially.

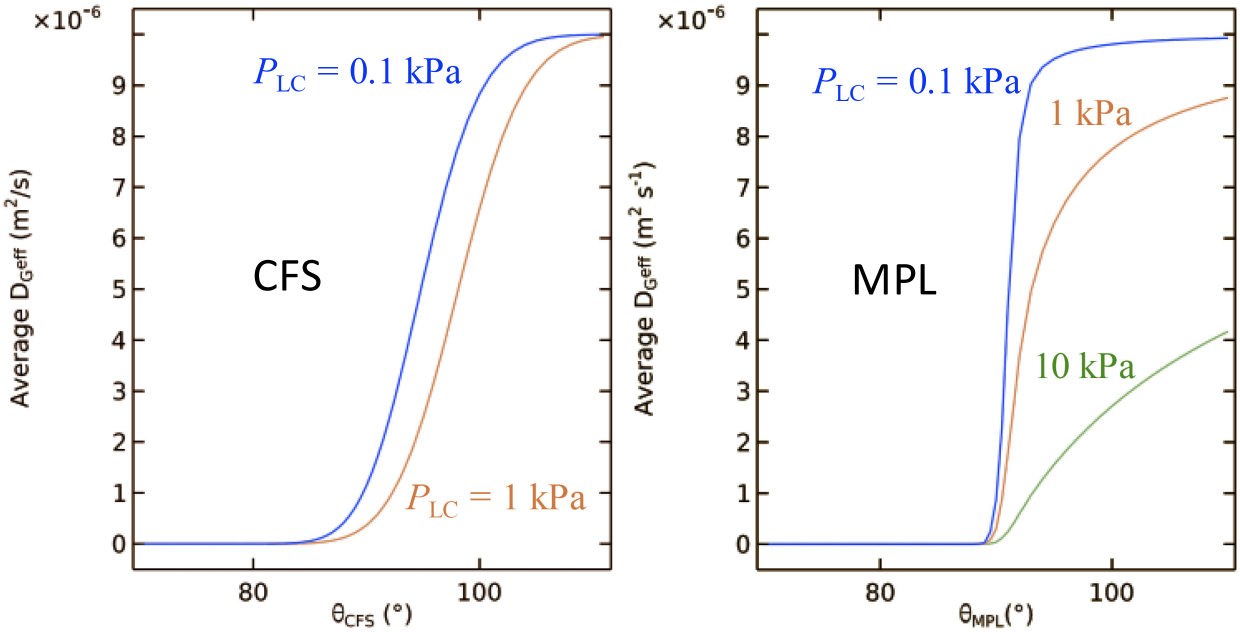

Figure V-22: *Average D_G^{eff} through isolated CFS and MPL layers as a function of θ and P_{LC}. Like the saturation profiles, the diffusivities undergo a transition as the layer wettabilities change. However due to the power law relationship between saturation and diffusivity, the diffusivities in both CFS and MPL decrease more quickly than the corresponding saturations increase.*

In full GDEs, the MPL functions as a protective barrier against excess flooding in the CFS. As in the isolated cases, varying the θ_{CFS} and θ_{MPL} together at a given applied pressure results in a similar sharp increase in the average saturation and a decrease in the average gas diffusivity as shown in **Figure V-23** and **Figure V-24**, respectively. A future step for this 1D model framework will be to conduct transient studies with this model framework to see if macro-homogeneous models can predict the decline of CO2R electrolyzer performance as a result of increased wettability. If this macro-homogeneous approach cannot capture the effects of liquid percolation on CO_2 transport through the GDE then perhaps models with pore-scale resolution might be better suited to a transient study. As mentioned previously, PNMs may be appropriate in that case.

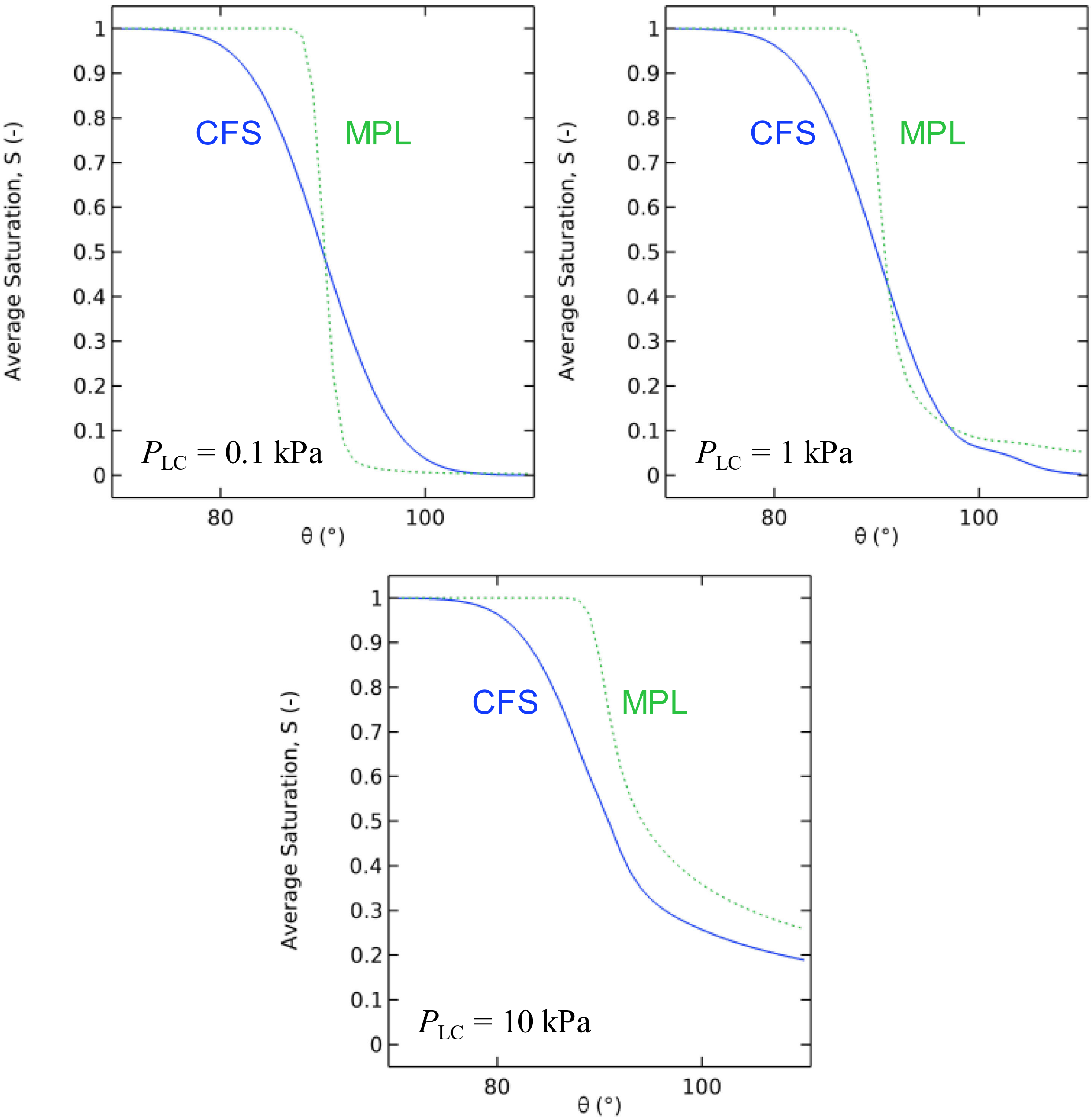

Figure V-23: *Average saturation for stacked CFS and MPL layers as a function of θ and P_{LC}. The CFS and MPL are indicated by solid (–) and dashed (---) lines, respectively.*

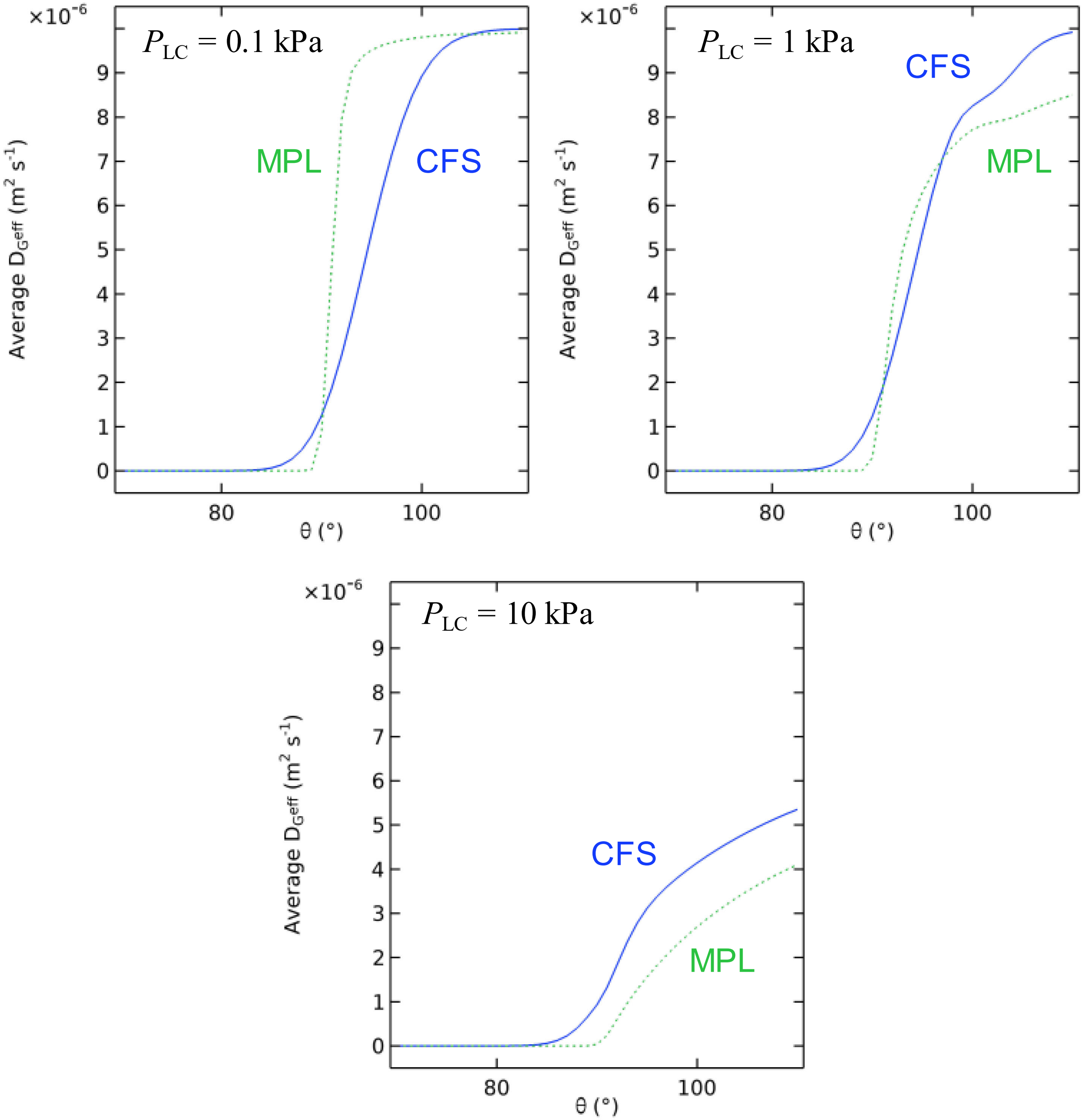

***Figure V-24**: Average D_G^{eff} for stacked CFS and MPL layers as a function of θ and P_{LC}. The CFS and MPL are indicated by solid (–) and dashed (---) lines, respectively.*

From this simple analysis we can see that contact angle varying effects (e.g., electrowetting) in the electrolyte facing portion of the GDE to be the one that limits gas species transport to the catalyst layer. This is important due to fact that the MPL has a low saturated permeability ($k_{sat,MPL} = 10^{-15}$

m^2) and must remain relatively dry to be effective. This is interesting to consider because MPLs are designed to be hydrophobic and known to improve the performance of cathode water management in PEFCs as they retain less water than the CFS layer. When an MPL is added to a CFS, water percolates from the catalyst layer to the gas channel at a lower overall GDL saturation than when a CFS is used in isolation.[44] This facilitates oxygen transport to the catalyst layer even at high current densities. However, when MPLs are exposed to CO2R reaction environments, the increased wettability due to EW or from enriched liquid products might alter the interactions between the liquid phase and the GDE. For these situations of decreased θ of the MPL becomes an obstacle to rather than a conduit for gas transport.

7. Conclusions

Macro-homogeneous electrode models enable inquiry into how variable wettability predictors (P_C, θ, and γ) might alter GDE saturation and, therefore, overall cell performance. Ultimately liquid filling curves simulated using this model framework need to be experimentally validated by fitting them against empirically measured P_C-S data both for electrodes under polarization and with aqueous-organic mixtures as the intruding fluids. Characterizing multi-phase flow and saturation within polarized porous media using conditions that are relevant to CO2R or even other electrochemical systems would extend the applicability of P_C-S curves to challenging scenarios such as those discussed in this thesis. Once validated, such models could be used to better calculate effective transport coefficients within partially saturated porous media. This improved understanding of CO_2 electrolyzer performance in extreme scenarios might inspire the development of new electrode components or even new operational approaches, such as in-cell separation strategies to enhance product recovery.

ACKNOWLEDGMENTS

This work was funded in part by the Joseph W. Richards Summer Research Fellowship of The Electrochemical Society and the Alfred P. Sloan Foundation. I would like to thank Dr. Yongwook Kim and Prof. Jeff Gostick at the University of Waterloo for collecting the empirical capillary pressure-saturation data and associated data for the porous electrode samples discussed in this chapter. I would also like to thank Kevin M. Tenny and Weiran (Sasha) Gao of the Brushett Research Group for the helpful discussions of regarding the construction of transport models. I would like to thank Pedro de Souza of the Bazant Research Group for enlightening discussions about the concepts of electrocapillarity and electrowetting as well as numerical transport modeling.

8. Appendix A: List of Symbols

Table V-6: *List of variables*

Variable	Unit	Description
a_c	m^{-1}	Cross-sectional area per unit volume
$a_{v,LG}$	m^{-1}	volume-specific liquid-gas interfacial area
C_{dl}	$F\ m^2$	Electrochemical double layer capacitance
D	$m^2\ s^{-1}$	Mass diffusivity
D^{eff}	$m^2\ s^{-1}$	Effective mass diffusivity
D_{Kn}	$m^2\ s^{-1}$	Knudsen mass diffusivity
f	-	Curve weight
f_{EW}	-	Fraction of electrowetting area
k	-	PSD curve index
k^{eff}	m^2	Effective fluid permeability
$k_{r,L}$	-	Relative permeability, liquid
$k_{r,G}$	-	Relative permeability, gas
k_{sat}	m^2	Saturated fluid permeability
L	m	Domain length
M	$g\ mol^{-1}$	Molar mass
n	-	CAD curve index
n_L	-	Liquid phase transport coefficient exponent
n_G	-	Gas phase transport coefficient exponent
P_C	Pa	Capillary pressure
P_L	Pa	Liquid phase pressure
P_{LC}	Pa	Liquid channel pressure
P_G	Pa	Gas phase pressure
P_{GC}	Pa	Gas channel pressure
r	m	Pore radius
r_c	m	Critical pore radius
r_o	m	Characteristic pore radius
r_{Kn}	m	Average Knudsen radius
s	-	Spread of log-normal distribution
S	-	Liquid saturation, scaled
S^*	-	Liquid saturation, unscaled
S_e	-	Effective liquid saturation
S_r	-	Residual liquid saturation
S_{max}	-	Maximum liquid saturation
t	s	Time coordinate

u	m s^{-1}	Fluid velocity
V	-	Normalized pore volume, pore size distribution (probability density function)
x	M	1D model length coordinate
W	(varies)	Weight function
Y	(varies)	Macro-homogeneous property

Table V-7: *List of Greek letter variables*

Variable	**Unit**	**Description**
γ	N m^{-1}	Surface tension
θ	°	Contact angle
θ_o	°	Characteristic contact angle
σ	-	Spread of normal distribution
Ψ	-	Contact angle distribution (probability density function)
Φ	V	Surface potential
ρ	kg m^{-3}	Fluid density
μ	kg m^{-1} s^{-1}	Dynamic fluid viscosity
ε	-	Porosity (pore volume fraction)

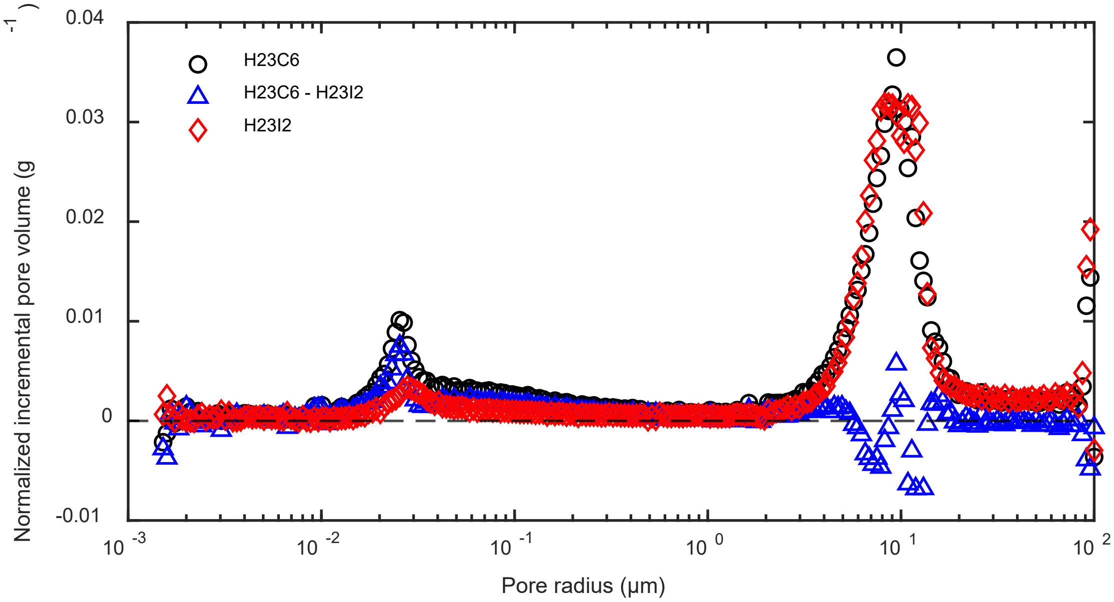

Figure V-25: *Incremental pore volume distributions for H23C6-class GDL components obtained using mercury intrusion porosimetry. The breakdown of the components, including the complete GDL (H23C6), the CFS (H23I2), and the computed MPL, which is taken to be the difference between the complete GDL and CFS curves.*

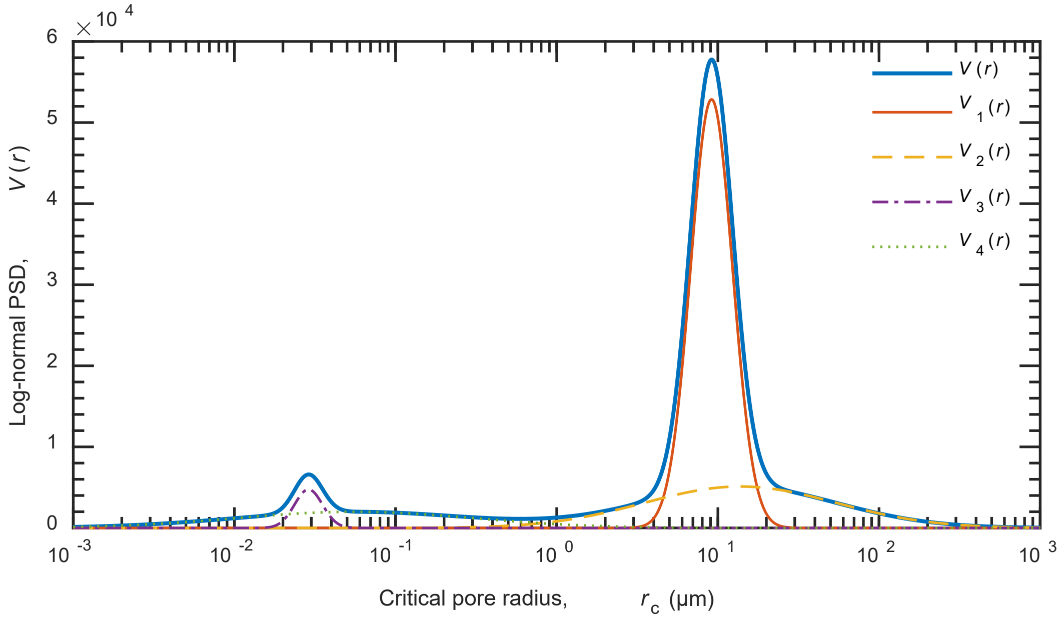

Figure V-26: *Initial log-normal distribution, V(r), for the CFS (H23I2)*

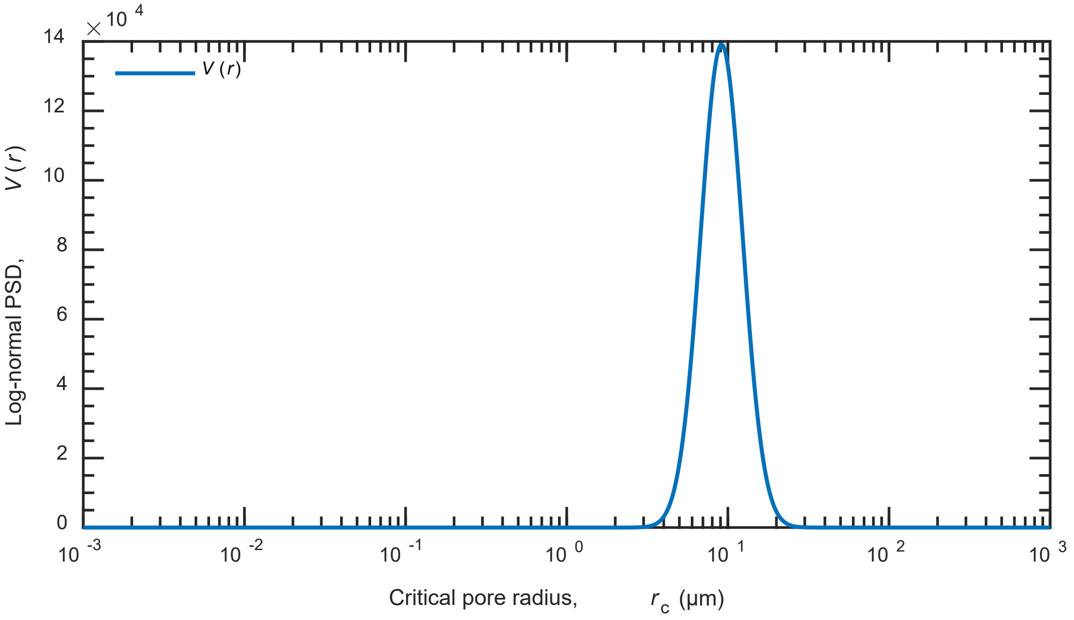

Figure V-27: *Simplified log-normal, V(r), for the CFS after CAD analysis*

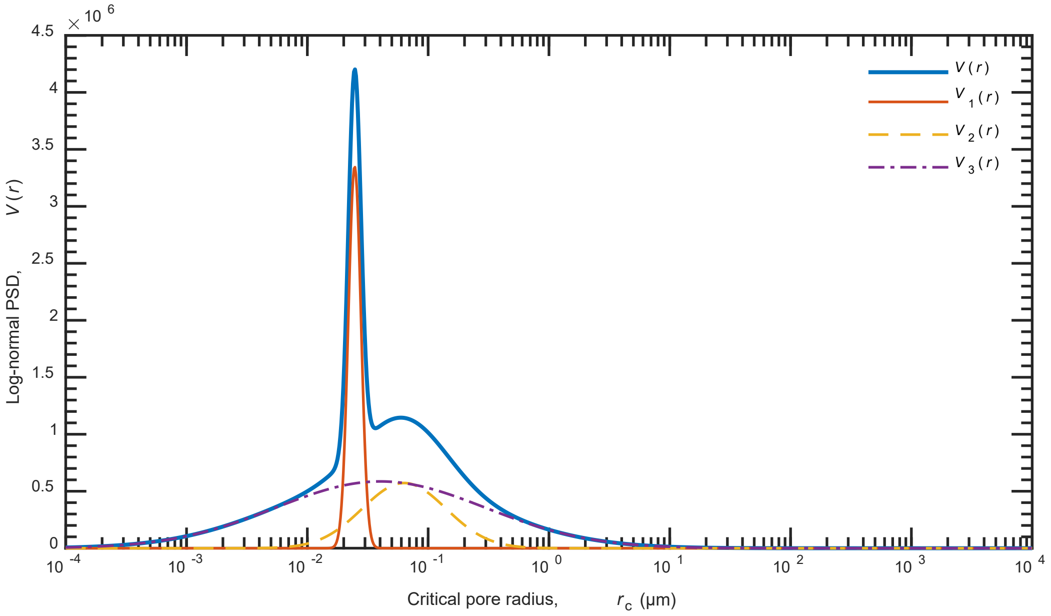

Figure V-28: *Log-normal distribution, V(r), for the MPL (H23C6 – H23I2)*

11. Appendix D: Contact Angle Variability Additional Plots

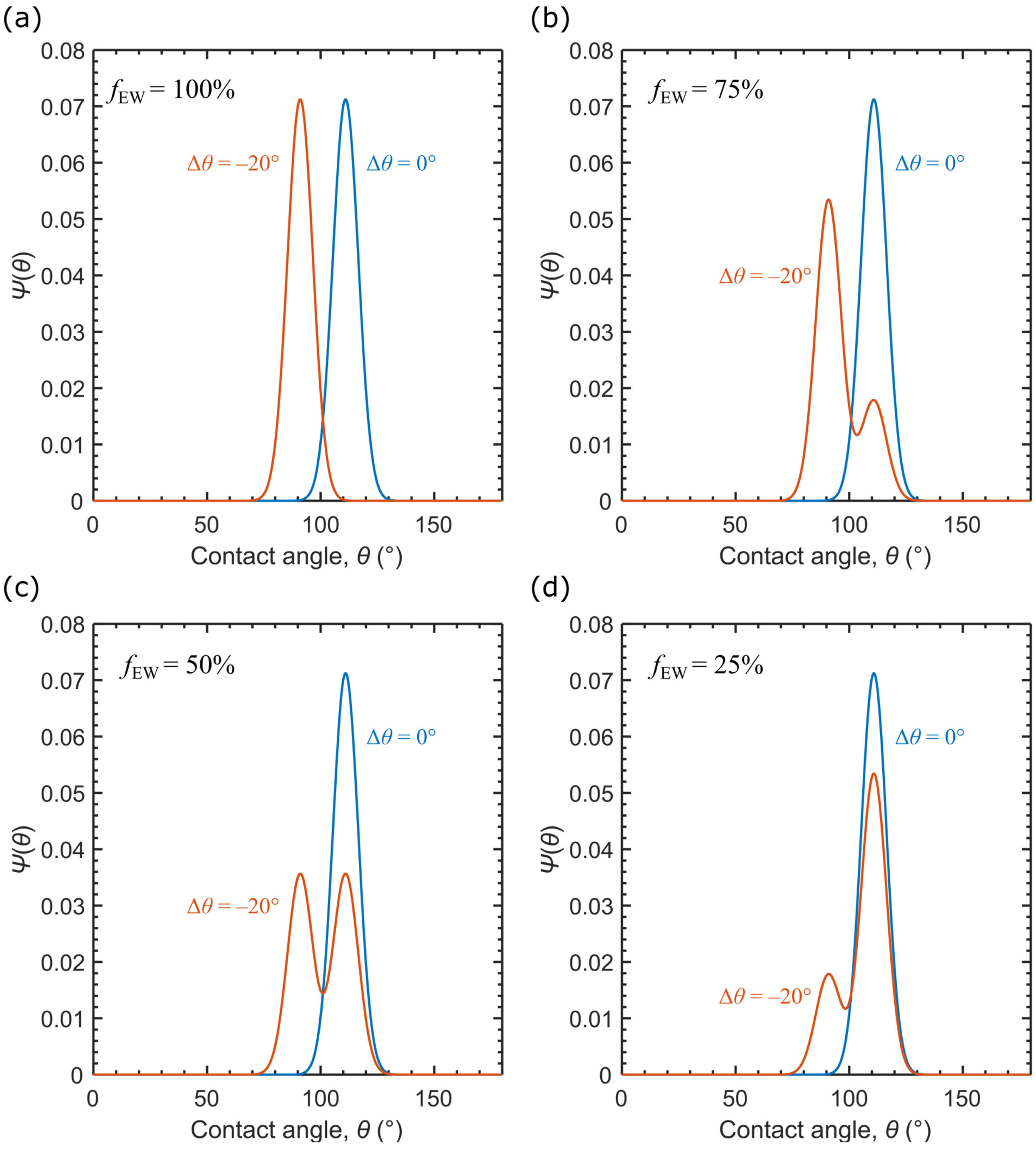

Figure V-29*: Simulated electrowetting effect on the CFS CAD as a function of f_{EW}. Panels correspond to scenarios in which (a) 100, (b) 75, (c) 50, or (d) 25% of the pore wall area is polarizable and susceptible to electrowetting.*

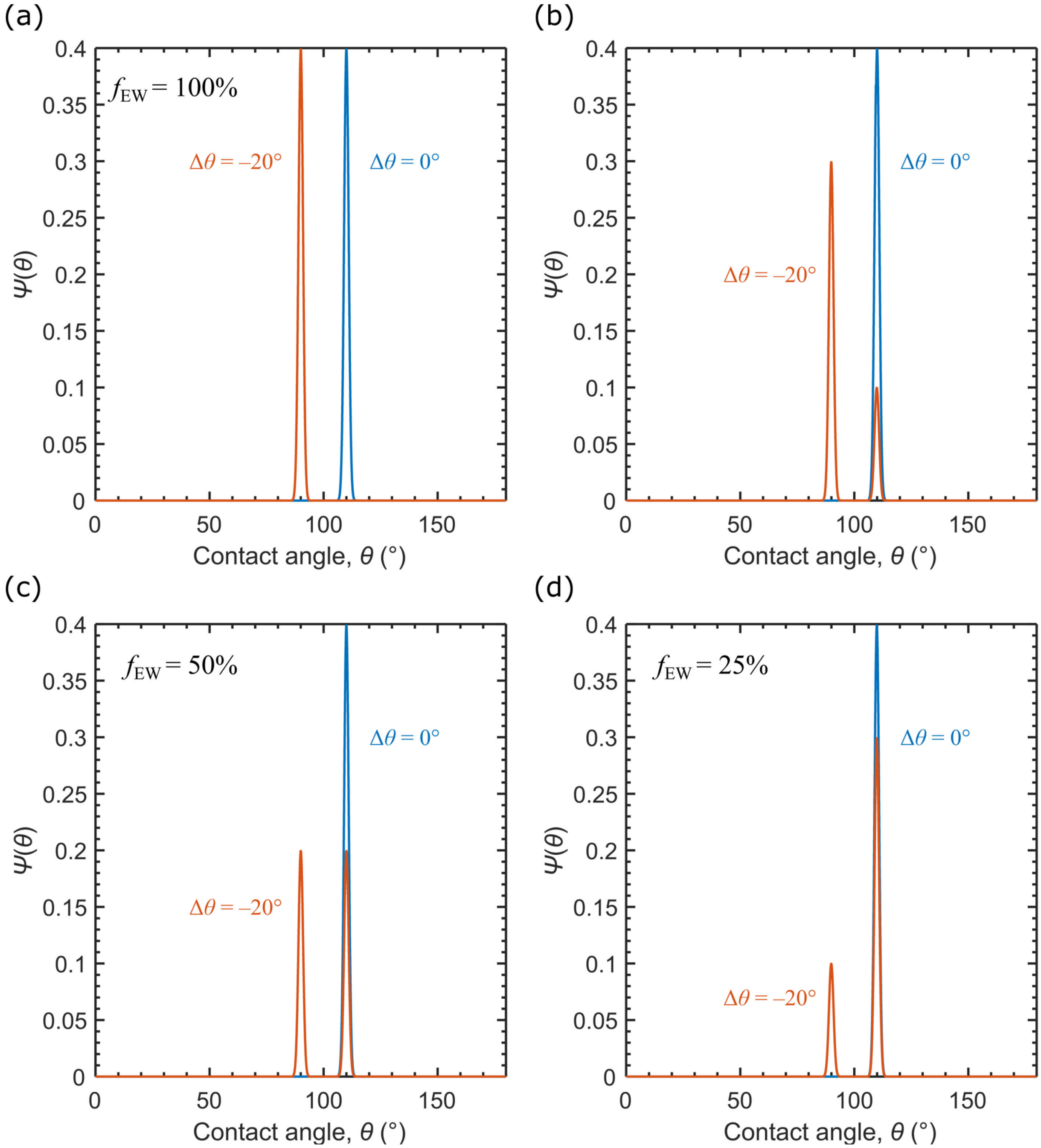

Figure V-30*: Simulated electrowetting effect on the MPL CAD as a function of f_{EW}. Panels correspond to scenarios in which (a) 100, (b) 75, (c) 50, or (d) 25% of the pore wall area is polarizable and susceptible to electrowetting.*

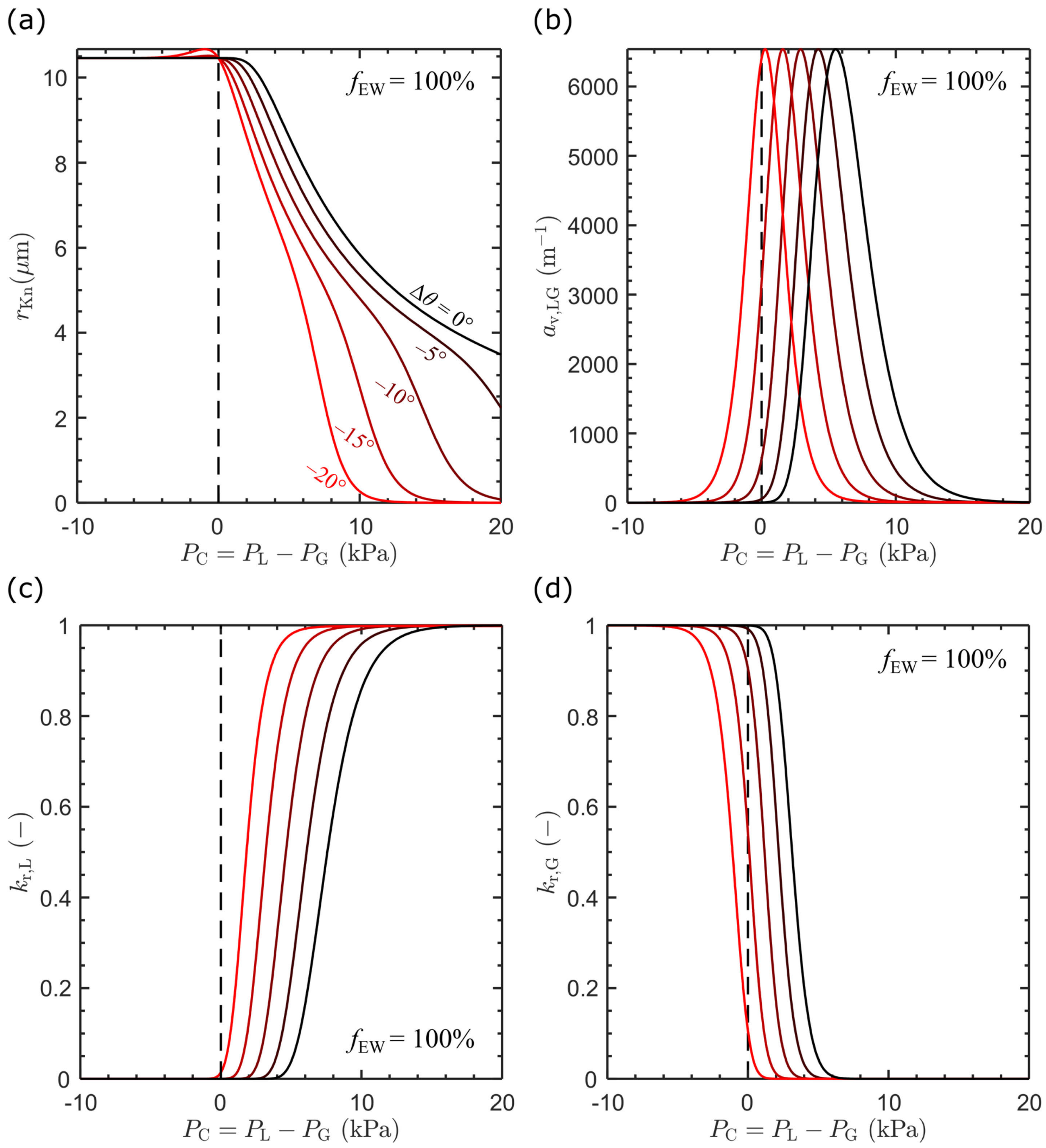

***Figure V-31**: CFS (H23) properties modified by contact angle variability with f_{EW} = 100%. (a) Knudsen radius, (b) volume-specific liquid-gas interfacial area, (c) relative liquid permeability, and (d) relative gas permeability are reported as functions of P_C. Contact angles decrease from θ_o = 111° in increments of 5°.*

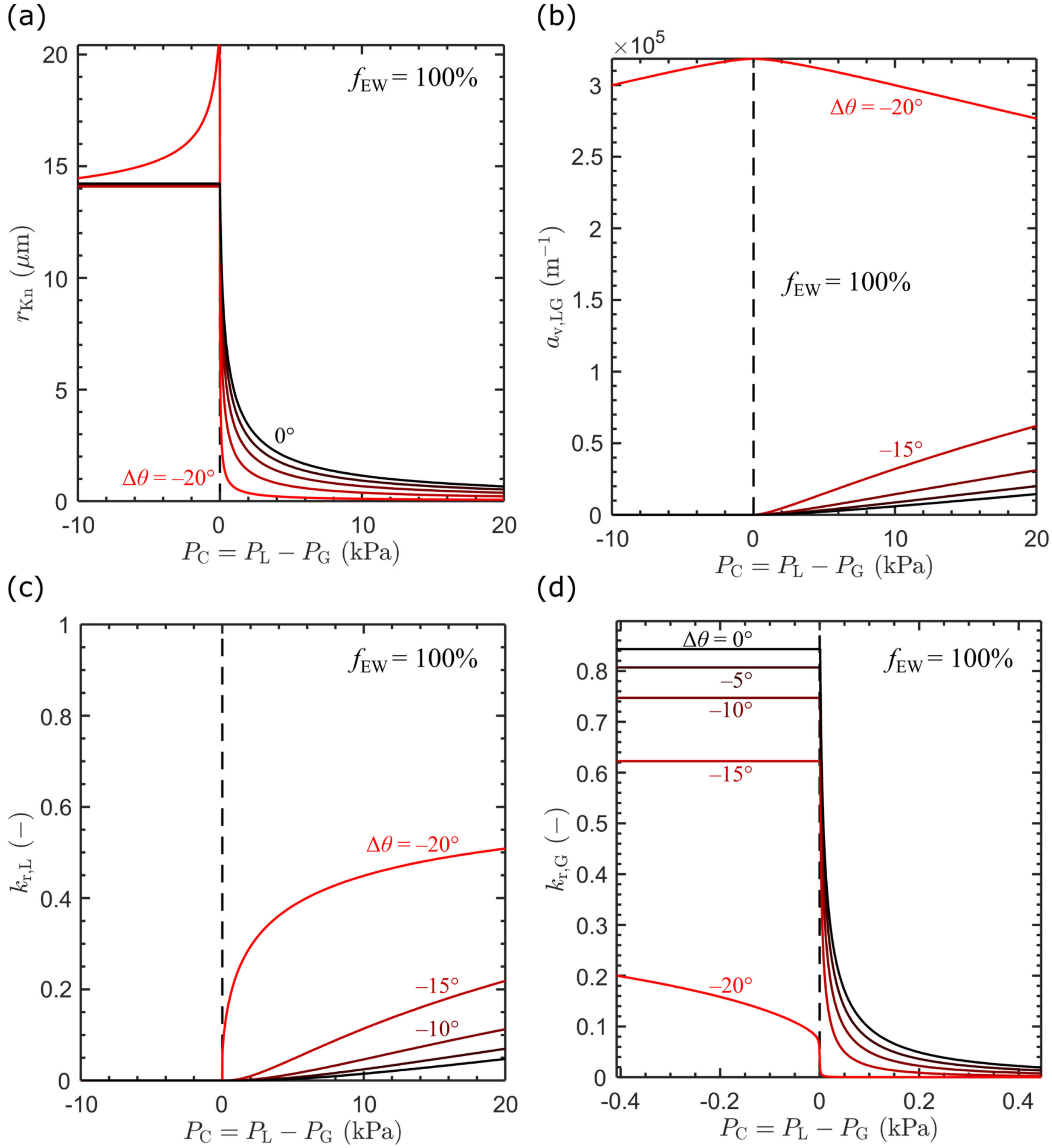

***Figure V-32**: MPL properties modified by contact angle variability with f_{EW} = 100%. (a) Knudsen radius, (b) volume-specific liquid-gas interfacial area, (c) relative liquid permeability, and (d) relative gas permeability are reported as functions of P_C. Contact angles decrease from θ_o = 110° in increments of 5°.*

VI. Conclusions & Future Work

Gas diffusion electrodes (GDEs) are becoming invaluable for improving the activity and selectivity of electrochemical CO_2 reduction (CO2R). Early implementations of these highly engineered porous materials in gas-fed flowing electrolyte CO_2 electrolyzers have shown both promising electrocatalytic performance, but also challenges largely related to electrolyte flooding. Through this thesis work, I have both demonstrated the benefits of using GDEs over planar electrocatalysts but also sought to understand current failure modes but also anticipate future challenges for this technology.

To understand the functional limits of deploying GDEs in flowing electrolyte configurations, I sought to identify some of the underlying mechanism responsible for GDE flooding. To do this I conducted a series of galvanostatic electrolysis experiments with Ag-GDEs. Simultaneously tracking the decline of CO2R selectivity and the increase in wetted electrode area through electrochemical double layer capacitance enabled the identification of current density correlated with the onset of GDE flooding. Directly engaging the physics underlying electrode flooding prompts discussions about the practical limitations of using GDEs in contact with liquid electrolytes. It also motivated further contemplations of the sources of flooding during CO2R and how we might choose different operating modes such as moving more towards polymer electrolyte membrane configurations.

Macro-homogeneous models have been proven to by other researchers to be useful for predicting GDE flooding at the cell level for PEFCs and, to some extent, CO_2 electrolyzers. However, now that baseline results have been obtained, future computational models for CO2R must evolve. Specifically, I would like to call attention to the need to study transient propagation of liquid fronts through GDEs for a variety of flooding scenarios encountered during CO2R. These future studies should be conducted both within the computationally expedient macro-homogeneous framework discussed in this thesis but also through other methods such as Pore Network Modeling (PNM), which can resolve pore-scale intrusion phenomena through 3D reconstruction of porous materials. Future transient studies involving wettability variations should be modeled and validated against operando experimental measurement of liquid saturation as enabled by advanced techniques such as neutron imaging, already used extensively for cathode flooding visualization in PEFCs.

Improving fundamental understanding of multiphase interactions within GDEs during CO2R will benefit from future efforts to evaluate the distribution of fluid phases within porous media. The same techniques that have been honed to study water transport within polymer electrolyte fuel cell gas diffusion layers should be applied to CO_2 electrolyzers, which face unique but analogous liquid flooding challenges. Repeating the studies presented in Chapter III, while using neutron imaging to resolve the saturation within each GDE layer would shed much needed light upon the origins of electrolyte flooding. Direct imaging of the water content within the component layers of the cathode GDE across a range of feed conditions and electrode polarizations/current densities might allow future researcher to deconvolute the relative contributions of pressure driven percolation, spontaneous electrowetting, and bicarbonate/carbonate salt precipitation near the gas-electrolyte interface.

In addition to in situ imaging of flooding during operation, we need more extensive measurements of capillary pressure-saturation and associated curves to predict GDE behaviors in the challenging fluidic environments inherent to CO2R. We often rightfully assume that capillary pressure-saturation information collected using mercury and water are representative of operating conditions. As shown in this thesis work, CO_2 electrolyzers sometimes involve liquid environments that are non-aqueous and liquid-solid interactions that change as a function of electrode polarization. Collecting and sharing new capillary pressure-saturation data for electrically polarized porous materials and with both electrolytes and mixtures of varied surface tension would help to validate some of the GDE flooding hypotheses developed in this this thesis.

Although I have largely discussed GDEs for CO2R in this thesis in the context of component failures, I have no doubt that continued contemplation of the physical mechanisms of electrode flooding will lead to engineered GDEs that uniquely tailored to electrochemical CO_2 upgrading. To date, many commonly used GDEs have been engineering for use in PEFCs, which is why they do not always suit the environments of CO2R. By continuing to expand our fundamental understanding of species and phases transport within complex porous materials we will perhaps be prepared to design novel material sets that are suited to CO2R or even more challenging reaction chemistries and fluid environments.

References

(1) *International Energy Outlook 2017*; Government DOE/EIA-0484(2017); EIA, 2017; pp 1–151.

(2) EPA. *U.S. Greenhouse Gas Inventory Report: 1990-2018*; 2020.

(3) Pletcher, D. The Cathodic Reduction of Carbon Dioxide—What Can It Realistically Achieve? A Mini Review. *Electrochem. Commun.* **2015**, *61*, 97–101. https://doi.org/10.1016/j.elecom.2015.10.006.

(4) Smith, W. A.; Burdyny, T.; Vermaas, D. A.; Geerlings, H. Pathways to Industrial-Scale Fuel Out of Thin Air from CO2 Electrolysis. *Joule* **2019**, *0* (0). https://doi.org/10.1016/j.joule.2019.07.009.

(5) IEA. *Energy Prices 2020*; IEA: Paris, 2020.

(6) Verma, S.; Kim, B.; Jhong, H.-R. "Molly"; Ma, S.; Kenis, P. J. A. A Gross-Margin Model for Defining Technoeconomic Benchmarks in the Electroreduction of CO2. *ChemSusChem* **2016**, n/a-n/a. https://doi.org/10.1002/cssc.201600394.

(7) U.S. Energy Information Administration (EIA). U.S. Electricity Prices by State, Sector http://www.eia.gov/electricity/data.cfm#sales (accessed Nov 12, 2016).

(8) BloombergNEF. Scale-up of Solar and Wind Puts Existing Coal, Gas at Risk. *BloombergNEF*, 2020.

(9) Bard, A. J.; Faulkner, L. R. *Electrochemical Methods: Fundamentals and Applications*, Second Edition.; Wiley: Hoboken, NJ, 2001.

(10) *CRC Handbook of Chemistry and Physics*, 99th Edition.; Rumble, J. R., Ed.; CRC Press/Taylor & Francis: Boca Raton, FL, 2018.

(11) McCrory, C. C. L.; Jung, S.; Peters, J. C.; Jaramillo, T. F. Benchmarking Heterogeneous Electrocatalysts for the Oxygen Evolution Reaction. *J. Am. Chem. Soc.* **2013**, *135* (45), 16977–16987. https://doi.org/10.1021/ja407115p.

(12) Minguzzi, A.; Fan, F.-R. F.; Vertova, A.; Rondinini, S.; Bard, A. J. Dynamic Potential–PH Diagrams Application to Electrocatalysts for Wateroxidation. *Chem Sci* **2012**, *3* (1), 217–229. https://doi.org/10.1039/C1SC00516B.

(13) Verma, S.; Lu, S.; Kenis, P. J. A. Co-Electrolysis of CO2 and Glycerol as a Pathway to Carbon Chemicals with Improved Technoeconomics Due to Low Electricity Consumption. *Nat. Energy* **2019**, *4* (6), 466–474. https://doi.org/10.1038/s41560-019-0374-6.

(14) Tsai, K. In 2020, U.S. natural gas prices were the lowest in decades - Today in Energy - U.S. Energy Information Administration (EIA) https://www.eia.gov/todayinenergy/detail.php?id=46376# (accessed Jan 19, 2021).

(15) Orella, M. J.; Brown, S. M.; Leonard, M. E.; Román-Leshkov, Y.; Brushett, F. R. A General Technoeconomic Model for Evaluating Emerging Electrolytic Processes. *Energy Technol.* **2020**, *n/a* (n/a), 1900994. https://doi.org/10.1002/ente.201900994.

(16) Moussallem, I.; Jörissen, J.; Kunz, U.; Pinnow, S.; Turek, T. Chlor-Alkali Electrolysis with Oxygen Depolarized Cathodes: History, Present Status and Future Prospects. *J. Appl. Electrochem.* **2008**, *38* (9), 1177–1194. https://doi.org/10.1007/s10800-008-9556-9.

(17) *Handbook of Fuel Cells : Fundamentals, Technology, and Applications*; Vielstich, W., Lamm, A., Gasteiger, H. A., Eds.; Wiley, 2003.

(18) Kuhl, K. P.; Cave, E. R.; Abram, D. N.; Jaramillo, T. F. New Insights into the Electrochemical Reduction of Carbon Dioxide on Metallic Copper Surfaces. *Energy Environ. Sci.* **2012**, *5* (5), 7050. https://doi.org/10.1039/c2ee21234j.

(19) Hatsukade, T.; Kuhl, K. P.; Cave, E. R.; Abram, D. N.; Jaramillo, T. F. Insights into the Electrocatalytic Reduction of CO $_2$ on Metallic Silver Surfaces. *Phys Chem Chem Phys* **2014**, *16* (27), 13814–13819. https://doi.org/10.1039/C4CP00692E.

(20) Hori, Y. Electrochemical CO2 Reduction on Metal Electrodes. In *Modern Aspects of Electrochemistry*; Springer: New York, NY, 2008; pp 89–189.

(21) Nitopi, S.; Bertheussen, E.; Scott, S. B.; Liu, X.; Engstfeld, A. K.; Horch, S.; Seger, B.; Stephens, I. E. L.; Chan, K.; Hahn, C.; Nørskov, J. K.; Jaramillo, T. F.; Chorkendorff, I. Progress and Perspectives of Electrochemical CO $_2$ Reduction on Copper in Aqueous Electrolyte. *Chem. Rev.* **2019**. https://doi.org/10.1021/acs.chemrev.8b00705.

(22) Zeng, J. S.; Corbin, N.; Williams, K.; Manthiram, K. Kinetic Analysis on the Role of Bicarbonate in Carbon Dioxide Electroreduction at Immobilized Cobalt Phthalocyanine. *ACS Catal.* **2020**, *10* (7), 4326–4336. https://doi.org/10.1021/acscatal.9b05272.

(23) Ma, M.; Trześniewski, B. J.; Xie, J.; Smith, W. A. Selective and Efficient Reduction of Carbon Dioxide to Carbon Monoxide on Oxide-Derived Nanostructured Silver Electrocatalysts. *Angew. Chem. Int. Ed.* **2016**, *55* (33), 9748–9752. https://doi.org/10.1002/anie.201604654.

(24) Weisenberger, S.; Schumpe, A. Estimation of Gas Solubilities in Salt Solutions at Temperatures from 273 K to 363 K. *AIChE J.* **1996**, *42* (1), 298–300. https://doi.org/10.1002/aic.690420130.

(25) Lobaccaro, P.; Singh, M. R.; Clark, E. L.; Kwon, Y.; Bell, A. T.; Ager, J. W. Effects of Temperature and Gas–Liquid Mass Transfer on the Operation of Small Electrochemical Cells for the Quantitative Evaluation of CO2 Reduction Electrocatalysts. *Phys. Chem. Chem. Phys.* **2016**, *18* (38), 26777–26785. https://doi.org/10.1039/C6CP05287H.

(26) Leonard, M. E.; Clarke, L. E.; Forner-Cuenca, A.; Brown, S. M.; Brushett, F. R. Investigating Electrode Flooding in a Flowing Electrolyte, Gas-Fed Carbon Dioxide Electrolyzer. *ChemSusChem* **2020**, *13* (2), 400–411. https://doi.org/10.1002/cssc.201902547.

(27) Sen, S.; Brown, S. M.; Leonard, M.; Brushett, F. R. Electroreduction of Carbon Dioxide to Formate at High Current Densities Using Tin and Tin Oxide Gas Diffusion Electrodes. *J. Appl. Electrochem.* **2019**, *49* (9), 917–928. https://doi.org/10.1007/s10800-019-01332-z.

(28) Sen, S.; Leonard, M.; Radhakrishnan, R.; Snyder, S.; Skinn, B.; Wang, D.; Hall, T.; Taylor, E. J.; Brushett, F. R. Pulse Plating of Copper onto Gas Diffusion Layers for the

Electroreduction of Carbon Dioxide. *MRS Adv.* **2018**, *3* (23), 1277–1284. https://doi.org/10.1557/adv.2017.623.

(29) Gabardo, C. M.; Seifitokaldani, A.; Edwards, J. P.; Dinh, C.-T.; Burdyny, T.; Kibria, M. G.; O'Brien, C. P.; Sargent, E. H.; Sinton, D. Combined High Alkalinity and Pressurization Enable Efficient CO2 Electroreduction to CO. *Energy Environ. Sci.* **2018**, *11* (9), 2531–2539. https://doi.org/10.1039/C8EE01684D.

(30) Luna, P. D.; Hahn, C.; Higgins, D.; Jaffer, S. A.; Jaramillo, T. F.; Sargent, E. H. What Would It Take for Renewably Powered Electrosynthesis to Displace Petrochemical Processes? *Science* **2019**, *364* (6438), eaav3506. https://doi.org/10.1126/science.aav3506.

(31) Carroll, J. J.; Slupsky, J. D.; Mather, A. E. The Solubility of Carbon Dioxide in Water at Low Pressure. *J. Phys. Chem. Ref. Data* **1991**, *20* (6), 1201–1209. https://doi.org/10.1063/1.555900.

(32) Weng, L.-C.; Bell, A. T.; Weber, A. Z. Modeling Gas-Diffusion Electrodes for CO2 Reduction. *Phys. Chem. Chem. Phys.* **2018**, *20* (25), 16973–16984. https://doi.org/10.1039/C8CP01319E.

(33) Chen, C.; Khosrowabadi Kotyk, J. F.; Sheehan, S. W. Progress toward Commercial Application of Electrochemical Carbon Dioxide Reduction. *Chem* **2018**, *4* (11), 2571–2586. https://doi.org/10.1016/j.chempr.2018.08.019.

(34) Cook, R. L.; MacDuff, R. C.; Sammells, A. F. High Rate Gas Phase CO 2 Reduction to Ethylene and Methane Using Gas Diffusion Electrodes. *J. Electrochem. Soc.* **1990**, *137* (2), 607–608. https://doi.org/10.1149/1.2086515.

(35) Endrődi, B.; Bencsik, G.; Darvas, F.; Jones, R.; Rajeshwar, K.; Janáky, C. Continuous-Flow Electroreduction of Carbon Dioxide. *Prog. Energy Combust. Sci.* **2017**, *62*, 133–154. https://doi.org/10.1016/j.pecs.2017.05.005.

(36) Dinh, C.-T.; Burdyny, T.; Kibria, M. G.; Seifitokaldani, A.; Gabardo, C. M.; Arquer, F. P. G. de; Kiani, A.; Edwards, J. P.; Luna, P. D.; Bushuyev, O. S.; Zou, C.; Quintero-Bermudez, R.; Pang, Y.; Sinton, D.; Sargent, E. H. CO2 Electroreduction to Ethylene via Hydroxide-Mediated Copper Catalysis at an Abrupt Interface. *Science* **2018**, *360* (6390), 783–787. https://doi.org/10.1126/science.aas9100.

(37) Dinh, C.-T.; García de Arquer, F. P.; Sinton, D.; Sargent, E. H. High Rate, Selective, and Stable Electroreduction of CO2 to CO in Basic and Neutral Media. *ACS Energy Lett.* **2018**, *3* (11), 2835–2840. https://doi.org/10.1021/acsenergylett.8b01734.

(38) Yang, H.; Kaczur, J. J.; Sajjad, S. D.; Masel, R. I. Electrochemical Conversion of CO2 to Formic Acid Utilizing Sustainion^{TM} Membranes. *J. CO2 Util.* **2017**, *20*, 208–217. https://doi.org/10.1016/j.jcou.2017.04.011.

(39) Liu, Z.; Yang, H.; Kutz, R.; Masel, R. I. CO2 Electrolysis to CO and O2 at High Selectivity, Stability and Efficiency Using Sustainion Membranes. *J. Electrochem. Soc.* **2018**, *165* (15), J3371–J3377. https://doi.org/10.1149/2.0501815jes.

(40) Verma, S.; Hamasaki, Y.; Kim, C.; Huang, W.; Lu, S.; Jhong, H.-R. M.; Gewirth, A. A.; Fujigaya, T.; Nakashima, N.; Kenis, P. J. A. Insights into the Low Overpotential Electroreduction of CO2 to CO on a Supported Gold Catalyst in an Alkaline Flow

Electrolyzer. *ACS Energy Lett.* **2018**, *3* (1), 193–198. https://doi.org/10.1021/acsenergylett.7b01096.

(41) Burdyny, T.; Smith, W. A. CO2 Reduction on Gas-Diffusion Electrodes and Why Catalytic Performance Must Be Assessed at Commercially-Relevant Conditions. *Energy Environ. Sci.* **2019**, *12* (5), 1442–1453. https://doi.org/10.1039/C8EE03134G.

(42) Weber, A. Z.; Newman, J. Modeling Transport in Polymer-Electrolyte Fuel Cells. *Chem. Rev.* **2004**, *104* (10), 4679–4726. https://doi.org/10.1021/cr020729l.

(43) Owejan, J. P.; Owejan, J. E.; Gu, W.; Trabold, T. A.; Tighe, T. W.; Mathias, M. F. Water Transport Mechanisms in PEMFC Gas Diffusion Layers. *J. Electrochem. Soc.* **2010**, *157* (10), B1456–B1464. https://doi.org/10.1149/1.3468615.

(44) Gostick, J. T.; Ioannidis, M. A.; Fowler, M. W.; Pritzker, M. D. On the Role of the Microporous Layer in PEMFC Operation. *Electrochem. Commun.* **2009**, *11* (3), 576–579. https://doi.org/10.1016/j.elecom.2008.12.053.

(45) Forner-Cuenca, A.; Manzi-Orezzoli, V.; Biesdorf, J.; Kazzi, M. E.; Streich, D.; Gubler, L.; Schmidt, T. J.; Boillat, P. Advanced Water Management in PEFCs: Diffusion Layers with Patterned Wettability I. Synthetic Routes, Wettability Tuning and Thermal Stability. *J. Electrochem. Soc.* **2016**, *163* (8), F788–F801. https://doi.org/10.1149/2.0271608jes.

(46) Forner-Cuenca, A.; Biesdorf, J.; Lamibrac, A.; Manzi-Orezzoli, V.; Büchi, F. N.; Gubler, L.; Schmidt, T. J.; Boillat, P. Advanced Water Management in PEFCs: Diffusion Layers with Patterned Wettability II. Measurement of Capillary Pressure Characteristic with Neutron and Synchrotron Imaging. *J. Electrochem. Soc.* **2016**, *163* (9), F1038–F1048.

(47) Forner-Cuenca, A.; Biesdorf, J.; Manzi-Orezzoli, V.; Gubler, L.; Schmidt, T. J.; Boillat, P. Advanced Water Management in PEFCs: Diffusion Layers with Patterned Wettability III. Operando Characterization with Neutron Imaging. *J. Electrochem. Soc.* **2016**, *163* (13), F1389–F1398. https://doi.org/10.1149/2.0891613jes.

(48) Oberholzer, P.; Boillat, P.; Siegrist, R.; Kästner, A.; Lehmann, E. H.; Scherer, G. G.; Wokaun, A. Simultaneous Neutron Imaging of Six Operating PEFCs: Experimental Set-up and Study of the MPL Effect. *Electrochem. Commun.* **2012**, *20*, 67–70. https://doi.org/10.1016/j.elecom.2012.03.038.

(49) Simon, C.; Kartouzian, D.; Müller, D.; Wilhelm, F.; Gasteiger, H. A. Impact of Microporous Layer Pore Properties on Liquid Water Transport in PEM Fuel Cells: Carbon Black Type and Perforation. *J. Electrochem. Soc.* **2017**, *164* (14), F1697–F1711. https://doi.org/10.1149/2.1321714jes.

(50) Boillat, P.; Lehmann, E. H.; Trtik, P.; Cochet, M. Neutron Imaging of Fuel Cells – Recent Trends and Future Prospects. *Curr. Opin. Electrochem.* **2017**, *5* (1), 3–10. https://doi.org/10.1016/j.coelec.2017.07.012.

(51) Nagai, Y.; Eller, J.; Hatanaka, T.; Yamaguchi, S.; Kato, S.; Kato, A.; Marone, F.; Xu, H.; Büchi, F. N. Improving Water Management in Fuel Cells through Microporous Layer Modifications: Fast Operando Tomographic Imaging of Liquid Water. *J. Power Sources* **2019**, *435*, 226809. https://doi.org/10.1016/j.jpowsour.2019.226809.

(52) Zenyuk, I. V.; Lamibrac, A.; Eller, J.; Parkinson, D. Y.; Marone, F.; Büchi, F. N.; Weber, A. Z. Investigating Evaporation in Gas Diffusion Layers for Fuel Cells with X-Ray Computed Tomography. *J. Phys. Chem. C* **2016**, *120* (50), 28701–28711. https://doi.org/10.1021/acs.jpcc.6b10658.

(53) Liu, K.; Smith, W. A.; Burdyny, T. Introductory Guide to Assembling and Operating Gas Diffusion Electrodes for Electrochemical CO2 Reduction. *ACS Energy Lett.* **2019**, 639–643. https://doi.org/10.1021/acsenergylett.9b00137.

(54) Kozbial, A.; Trouba, C.; Liu, H.; Li, L. Characterization of the Intrinsic Water Wettability of Graphite Using Contact Angle Measurements: Effect of Defects on Static and Dynamic Contact Angles. *Langmuir* **2017**, *33* (4), 959–967. https://doi.org/10.1021/acs.langmuir.6b04193.

(55) Qiu, S.; Fuentes, C. A.; Zhang, D.; Van Vuure, A. W.; Seveno, D. Wettability of a Single Carbon Fiber. *Langmuir* **2016**, *32* (38), 9697–9705. https://doi.org/10.1021/acs.langmuir.6b02072.

(56) FK; KO; TW. *Wettability of Carbon Fibers Using Single-Fiber Contact Angle Measurements – a Feasibility Study*; Application Report AR271e; KRÜSS GmbH: Hamburg, Germany, 2013; p 3.

(57) Wood, D. L.; Rulison, C.; Borup, R. L. Surface Properties of PEMFC Gas Diffusion Layers. *J. Electrochem. Soc.* **2010**, *157* (2), B195–B206. https://doi.org/10.1149/1.3261850.

(58) Taherian, F.; Marcon, V.; van der Vegt, N. F. A.; Leroy, F. What Is the Contact Angle of Water on Graphene? *Langmuir* **2013**, *29* (5), 1457–1465. https://doi.org/10.1021/la304645w.

(59) Kim, B.; Hillman, F.; Ariyoshi, M.; Fujikawa, S.; Kenis, P. J. A. Effects of Composition of the Micro Porous Layer and the Substrate on Performance in the Electrochemical Reduction of CO2 to CO. *J. Power Sources* **2016**, *312*, 192–198. https://doi.org/10.1016/j.jpowsour.2016.02.043.

(60) Sow, P. K.; Lu, Z.; Talebian, H.; Damron, L.; Mérida, W. Double Layer Capacitance Measurements To Characterize the Water Intrusion into Porous Materials. *J. Phys. Chem. C* **2016**, *120* (43), 24794–24802. https://doi.org/10.1021/acs.jpcc.6b07861.

(61) Rabbow, T. J.; Whitehead, A. H. Deconvolution of Electrochemical Double Layer Capacitance between Fractions of Active and Total Surface Area of Graphite Felts. *Carbon* **2017**, *111*, 782–788. https://doi.org/10.1016/j.carbon.2016.10.064.

(62) Milshtein, J. D.; Barton, J. L.; Darling, R. M.; Brushett, F. R. 4-Acetamido-2,2,6,6-Tetramethylpiperidine-1-Oxyl as a Model Organic Redox Active Compound for Nonaqueous Flow Batteries. *J. Power Sources* **2016**, *327* (Supplement C), 151–159. https://doi.org/10.1016/j.jpowsour.2016.06.125.

(63) Verma, S.; Lu, X.; Ma, S.; Masel, R. I.; Kenis, P. J. A. The Effect of Electrolyte Composition on the Electroreduction of CO2 to CO on Ag Based Gas Diffusion Electrodes. *Phys. Chem. Chem. Phys.* **2016**, *18* (10), 7075–7084. https://doi.org/10.1039/C5CP05665A.

(64) Salvatore, D. A.; Weekes, D. M.; He, J.; Dettelbach, K. E.; Li, Y. C.; Mallouk, T. E.; Berlinguette, C. P. Electrolysis of Gaseous CO2 to CO in a Flow Cell with a Bipolar

Membrane. *ACS Energy Lett.* **2018**, *3* (1), 149–154. https://doi.org/10.1021/acsenergylett.7b01017.

(65) Haas, T.; Krause, R.; Weber, R.; Demler, M.; Schmid, G. Technical Photosynthesis Involving CO2 Electrolysis and Fermentation. *Nat. Catal.* **2018**, *1* (1), 32–39. https://doi.org/10.1038/s41929-017-0005-1.

(66) Lee, J.; Lim, J.; Roh, C.-W.; Whang, H. S.; Lee, H. Electrochemical CO2 Reduction Using Alkaline Membrane Electrode Assembly on Various Metal Electrodes. *J. CO2 Util.* **2019**, *31*, 244–250. https://doi.org/10.1016/j.jcou.2019.03.022.

(67) El-kharouf, A.; Mason, T. J.; Brett, D. J. L.; Pollet, B. G. Ex-Situ Characterisation of Gas Diffusion Layers for Proton Exchange Membrane Fuel Cells. *J. Power Sources* **2012**, *218*, 393–404. https://doi.org/10.1016/j.jpowsour.2012.06.099.

(68) Ma, S.; Luo, R.; Moniri, S.; Lan, Y.; Kenis, P. J. A. Efficient Electrochemical Flow System with Improved Anode for the Conversion of CO2 to CO. *J. Electrochem. Soc.* **2014**, *161* (10), F1124–F1131. https://doi.org/10.1149/2.1201410jes.

(69) Kim, B.; Ma, S.; Molly Jhong, H.-R.; Kenis, P. J. A. Influence of Dilute Feed and PH on Electrochemical Reduction of CO2 to CO on Ag in a Continuous Flow Electrolyzer. *Electrochimica Acta* **2015**, *166*, 271–276. https://doi.org/10.1016/j.electacta.2015.03.064.

(70) Wu, K.; Birgersson, E.; Kim, B.; Kenis, P. J. A.; Karimi, I. A. Modeling and Experimental Validation of Electrochemical Reduction of CO2 to CO in a Microfluidic Cell. *J. Electrochem. Soc.* **2015**, *162* (1), F23–F32. https://doi.org/10.1149/2.1021414jes.

(71) Ma, S.; Sadakiyo, M.; Luo, R.; Heima, M.; Yamauchi, M.; Kenis, P. J. A. One-Step Electrosynthesis of Ethylene and Ethanol from CO 2 in an Alkaline Electrolyzer. *J. Power Sources* **2016**, *301*, 219–228. https://doi.org/10.1016/j.jpowsour.2015.09.124.

(72) Keith, D. W.; Holmes, G.; St. Angelo, D.; Heidel, K. A Process for Capturing CO2 from the Atmosphere. *Joule* **2018**, *2* (8), 1573–1594. https://doi.org/10.1016/j.joule.2018.05.006.

(73) Schulz, K. G.; Riebesell, U.; Rost, B.; Thoms, S.; Zeebe, R. E. Determination of the Rate Constants for the Carbon Dioxide to Bicarbonate Inter-Conversion in PH-Buffered Seawater Systems. *Mar. Chem.* **2006**, *100* (1), 53–65. https://doi.org/10.1016/j.marchem.2005.11.001.

(74) Santamaria, A. D.; Das, P. K.; MacDonald, J. C.; Weber, A. Z. Liquid-Water Interactions with Gas-Diffusion-Layer Surfaces. *J. Electrochem. Soc.* **2014**, *161* (12), F1184–F1193. https://doi.org/10.1149/2.0321412jes.

(75) Duan, Y.; Luebke, D. R.; Pennline, H. W.; Li, B.; Janik, M. J.; Halley, J. W. Ab Initio Thermodynamic Study of the CO2 Capture Properties of Potassium Carbonate Sesquihydrate, K2CO3·1.5H2O. *J. Phys. Chem. C* **2012**, *116* (27), 14461–14470. https://doi.org/10.1021/jp303844t.

(76) Eisaman, M. D.; Alvarado, L.; Larner, D.; Wang, P.; Garg, B.; Littau, K. A. CO2 Separation Using Bipolar Membrane Electrodialysis. *Energy Environ. Sci.* **2011**, *4* (4), 1319–1328. https://doi.org/10.1039/C0EE00303D.

(77) Watkins, J. D.; Siefert, N. S.; Zhou, X.; Myers, C. R.; Kitchin, J. R.; Hopkinson, D. P.; Nulwala, H. B. Redox-Mediated Separation of Carbon Dioxide from Flue Gas. *Energy Fuels* **2015**, *29* (11), 7508–7515. https://doi.org/10.1021/acs.energyfuels.5b01807.

(78) Rigdon, W. A.; Omasta, T. J.; Lewis, C.; Hickner, M. A.; Varcoe, J. R.; Renner, J. N.; Ayers, K. E.; Mustain, W. E. Carbonate Dynamics and Opportunities With Low Temperature, Anion Exchange Membrane-Based Electrochemical Carbon Dioxide Separators. *J. Electrochem. Energy Convers. Storage* **2017**, *14* (2), 020701-020701–020708. https://doi.org/10.1115/1.4033411.

(79) Rolla, A.; Sadkowski, A.; Wild, J.; Zóltowski, P. On the Problem of Ageing of Carbon—Air Electrodes in Alkaline Electrolytes. *J. Power Sources* **1980**, *5* (2), 189–196. https://doi.org/10.1016/0378-7753(80)80106-6.

(80) Veran-Tissoires, S.; Marcoux, M.; Prat, M. Discrete Salt Crystallization at the Surface of a Porous Medium. *Phys. Rev. Lett.* **2012**, *108* (5), 054502. https://doi.org/10.1103/PhysRevLett.108.054502.

(81) Weng, L.-C.; Bell, A. T.; Weber, A. Z. Towards Membrane-Electrode Assembly Systems for CO2 Reduction: A Modeling Study. *Energy Environ. Sci.* **2019**, *12* (6), 1950–1968. https://doi.org/10.1039/C9EE00909D.

(82) Dunlap, P. M.; Faris, S. R. Surface Tension of Aqueous Solutions of Potassium Hydroxide. *Nature* **1962**, *196* (4861), 1312–1313. https://doi.org/10.1038/1961312a0.

(83) Benziger, J.; Nehlsen, J.; Blackwell, D.; Brennan, T.; Itescu, J. Water Flow in the Gas Diffusion Layer of PEM Fuel Cells. *J. Membr. Sci.* **2005**, *261* (1), 98–106. https://doi.org/10.1016/j.memsci.2005.03.049.

(84) Gostick, J. T.; Fowler, M. W.; Ioannidis, M. A.; Pritzker, M. D.; Volfkovich, Y. M.; Sakars, A. Capillary Pressure and Hydrophilic Porosity in Gas Diffusion Layers for Polymer Electrolyte Fuel Cells. *J. Power Sources* **2006**, *156* (2), 375–387. https://doi.org/10.1016/j.jpowsour.2005.05.086.

(85) Gostick, J. T.; Ioannidis, M. A.; Fowler, M. W.; Pritzker, M. D. Direct Measurement of the Capillary Pressure Characteristics of Water–Air–Gas Diffusion Layer Systems for PEM Fuel Cells. *Electrochem. Commun.* **2008**, *10* (10), 1520–1523. https://doi.org/10.1016/j.elecom.2008.08.008.

(86) Tranter, T. G.; Gostick, J. T.; Burns, A. D.; Gale, W. F. Capillary Hysteresis in Neutrally Wettable Fibrous Media: A Pore Network Study of a Fuel Cell Electrode. *Transp. Porous Media* **2018**, *121* (3), 597–620. https://doi.org/10.1007/s11242-017-0973-2.

(87) Verma, S.; Nwabara, U. O.; Kenis, P. J. A. Carbon-Based Electrodes and Catalysts for the Electroreduction of Carbon Dioxide (CO2) to Value-Added Chemicals. In *Nanocarbons for Energy Conversion: Supramolecular Approaches*; Nakashima, N., Ed.; Springer International Publishing: Cham, 2019; pp 219–251. https://doi.org/10.1007/978-3-319-92917-0_10.

(88) Gostick, J. T.; Ioannidis, M. A.; Fowler, M. W.; Pritzker, M. D. Wettability and Capillary Behavior of Fibrous Gas Diffusion Media for Polymer Electrolyte Membrane Fuel Cells. *J. Power Sources* **2009**, *194* (1), 433–444. https://doi.org/10.1016/j.jpowsour.2009.04.052.

(89) Lamibrac, A.; Roth, J.; Toulec, M.; Marone, F.; Stampanoni, M.; Büchi, F. N. Characterization of Liquid Water Saturation in Gas Diffusion Layers by X-Ray Tomographic Microscopy. *J. Electrochem. Soc.* **2016**, *163* (3), F202–F209. https://doi.org/10.1149/2.0401603jes.

(90) Jhong, H.-R. "Molly"; Brushett, F. R.; Kenis, P. J. A. The Effects of Catalyst Layer Deposition Methodology on Electrode Performance. *Adv. Energy Mater.* **2013**, *3* (5), 589–599. https://doi.org/10.1002/aenm.201200759.

(91) Shapoval, G. S.; Pud, A. A.; Zamotayev, P. V.; Kachan, A. A. Degradation of Some Carbon-Chain Polymers by Electrochemical Reduction. *Polym. Sci. USSR* **1985**, *27* (10), 2427–2431. https://doi.org/10.1016/0032-3950(85)90325-9.

(92) Endrődi, B.; Kecsenovity, E.; Samu, A.; Darvas, F.; Jones, R. V.; Török, V.; Danyi, A.; Janáky, C. Multilayer Electrolyzer Stack Converts Carbon Dioxide to Gas Products at High Pressure with High Efficiency. *ACS Energy Lett.* **2019**, *4* (7), 1770–1777. https://doi.org/10.1021/acsenergylett.9b01142.

(93) De Mot, B.; Hereijgers, J.; Duarte, M.; Breugelmans, T. Influence of Flow and Pressure Distribution inside a Gas Diffusion Electrode on the Performance of a Flow-by CO2 Electrolyzer. *Chem. Eng. J.* **2019**, *378*, 122224. https://doi.org/10.1016/j.cej.2019.122224.

(94) Shahidzadeh-Bonn, N.; Desarnaud, J.; Bertrand, F.; Chateau, X.; Bonn, D. Damage in Porous Media Due to Salt Crystallization. *Phys. Rev. E* **2010**, *81* (6), 066110. https://doi.org/10.1103/PhysRevE.81.066110.

(95) Lamminen, J.; Kivisaari, J.; Lampinen, M. J.; Viitanen, M.; Vuorisalo, J. Preparation of Air Electrodes and Long Run Tests. *J. Electrochem. Soc.* **1991**, *138* (4), 905–908. https://doi.org/10.1149/1.2085745.

(96) Al-Saleh, M. A.; Gültekin, S.; Al-Zakri, A. S.; Celiker, H. Effect of Carbon Dioxide on the Performance of Ni/PTFE and Ag/PTFE Electrodes in an Alkaline Fuel Cell. *J. Appl. Electrochem.* **1994**, *24* (6), 575–580. https://doi.org/10.1007/BF00249861.

(97) Naughton, M. S.; Brushett, F. R.; Kenis, P. J. A. Carbonate Resilience of Flowing Electrolyte-Based Alkaline Fuel Cells. *J. Power Sources* **2011**, *196* (4), 1762–1768. https://doi.org/10.1016/j.jpowsour.2010.09.114.

(98) Behling, N. H. Chapter 3 - History of Alkaline Fuel Cells. In *Fuel Cells*; Behling, N. H., Ed.; Elsevier, 2013; pp 37–51. https://doi.org/10.1016/B978-0-444-56325-5.00003-X.

(99) Perry, M. L.; Fuller, T. F. A Historical Perspective of Fuel Cell Technology in the 20th Century. *J. Electrochem. Soc.* **2002**, *149* (7), S59–S67. https://doi.org/10.1149/1.1488651.

(100) Larrazábal, G. O.; Strøm-Hansen, P.; Heli, J. P.; Zeiter, K.; Therkildsen, K. T.; Chorkendorff, I.; Seger, B. Analysis of Mass Flows and Membrane Crossover in CO2 Reduction at High Current Densities in a MEA-Type Electrolyzer. *ACS Appl. Mater. Interfaces* **2019**. https://doi.org/10.1021/acsami.9b13081.

(101) Yin, Z.; Peng, H.; Wei, X.; Zhou, H.; Gong, J.; Huai, M.; Xiao, L.; Wang, G.; Lu, J.; Zhuang, L. An Alkaline Polymer Electrolyte CO2 Electrolyzer Operated with Pure Water. *Energy Environ. Sci.* **2019**, *12* (8), 2455–2462. https://doi.org/10.1039/C9EE01204D.

(102) Smith, W. A.; Burdyny, T.; Vermaas, D. A.; Geerlings, H. Pathways to Industrial-Scale Fuel Out of Thin Air from CO2 Electrolysis. *Joule* **2019**, *3* (8), 1822–1834. https://doi.org/10.1016/j.joule.2019.07.009.

(103) Darling, R. M.; Gallagher, K. G.; Kowalski, J. A.; Ha, S.; Brushett, F. R. Pathways to Low-Cost Electrochemical Energy Storage: A Comparison of Aqueous and Nonaqueous Flow Batteries. *Energy Environ. Sci.* **2014**, *7* (11), 3459–3477. https://doi.org/10.1039/C4EE02158D.

(104) Feaster, J. T.; Shi, C.; Cave, E. R.; Hatsukade, T.; Abram, D. N.; Kuhl, K. P.; Hahn, C.; Nørskov, J. K.; Jaramillo, T. F. Understanding Selectivity for the Electrochemical Reduction of Carbon Dioxide to Formic Acid and Carbon Monoxide on Metal Electrodes. *ACS Catal.* **2017**, *7* (7), 4822–4827. https://doi.org/10.1021/acscatal.7b00687.

(105) Ringe, S.; Clark, E. L.; Resasco, J.; Walton, A.; Seger, B.; Bell, A. T.; Chan, K. Understanding Cation Effects in Electrochemical CO2 Reduction. *Energy Environ. Sci.* **2019**. https://doi.org/10.1039/C9EE01341E.

(106) Weng, L.-C.; Bell, A. T.; Weber, A. Z. Modeling Gas-Diffusion Electrodes for CO2 Reduction. *Phys. Chem. Chem. Phys.* **2018**, *20* (25), 16973–16984. https://doi.org/10.1039/C8CP01319E.

(107) Thorson, M. R.; Siil, K. I.; Kenis, P. J. A. Effect of Cations on the Electrochemical Conversion of CO2 to CO. *J. Electrochem. Soc.* **2013**, *160* (1), F69–F74. https://doi.org/10.1149/2.052301jes.

(108) Larrazábal, G. O.; Strøm-Hansen, P.; Heli, J. P.; Zeiter, K.; Therkildsen, K. T.; Chorkendorff, I.; Seger, B. Analysis of Mass Flows and Membrane Cross-over in CO2 Reduction at High Current Densities in an MEA-Type Electrolyzer. *ACS Appl. Mater. Interfaces* **2019**, *11* (44), 41281–41288. https://doi.org/10.1021/acsami.9b13081.

(109) Liu, Z.; Yang, H.; Kutz, R.; Masel, R. I. CO $_2$ Electrolysis to CO and O $_2$ at High Selectivity, Stability and Efficiency Using Sustainion Membranes. *J. Electrochem. Soc.* **2018**, *165* (15), J3371–J3377. https://doi.org/10.1149/2.0501815jes.

(110) Fogler, H. S. *Elements of Chemical Reaction Engineering*, 4th ed.; Prentice Hall International Series in the Physical and Chemical Engineering Sciences; Pearson Education, Inc.: Boston, MA, 2006.

(111) Arquer, F. P. G. de; Dinh, C.-T.; Ozden, A.; Wicks, J.; McCallum, C.; Kirmani, A. R.; Nam, D.-H.; Gabardo, C.; Seifitokaldani, A.; Wang, X.; Li, Y. C.; Li, F.; Edwards, J.; Richter, L. J.; Thorpe, S. J.; Sinton, D.; Sargent, E. H. CO2 Electrolysis to Multicarbon Products at Activities Greater than 1 A Cm−2. *Science* **2020**, *367* (6478), 661–666. https://doi.org/10.1126/science.aay4217.

(112) Gabardo, C. M.; O'Brien, C. P.; Edwards, J. P.; McCallum, C.; Xu, Y.; Dinh, C.-T.; Li, J.; Sargent, E. H.; Sinton, D. Continuous Carbon Dioxide Electroreduction to Concentrated Multi-Carbon Products Using a Membrane Electrode Assembly. *Joule* **2019**. https://doi.org/10.1016/j.joule.2019.07.021.

(113) Ripatti, D. S.; Veltman, T. R.; Kanan, M. W. Carbon Monoxide Gas Diffusion Electrolysis That Produces Concentrated C2 Products with High Single-Pass Conversion. *Joule* **2019**, *3* (1), 240–256. https://doi.org/10.1016/j.joule.2018.10.007.

(114) Pinnow, S.; Chavan, N.; Turek, T. Thin-Film Flooded Agglomerate Model for Silver-Based Oxygen Depolarized Cathodes. *J. Appl. Electrochem.* **2011**, *41* (9), 1053–1064. https://doi.org/10.1007/s10800-011-0311-2.

(115) Haas, T.; Krause, R.; Weber, R.; Demler, M.; Schmid, G. Technical Photosynthesis Involving CO 2 Electrolysis and Fermentation. *Nat. Catal.* **2018**, *1* (1), 32–39. https://doi.org/10.1038/s41929-017-0005-1.

(116) Washburn, E. W. The Dynamics of Capillary Flow. *Phys. Rev.* **1921**, *17* (3), 273–283. https://doi.org/10.1103/PhysRev.17.273.

(117) Deen, W. M. *Analysis of Transport Phenomena*, 2nd ed.; Oxford University Press: New York, NY, 2011.

(118) Gu, Z.; Bazant, M. Z. Microscopic Theory of Capillary Pressure Hysteresis Based on Pore-Space Accessivity and Radius-Resolved Saturation. *Chem. Eng. Sci.* **2019**, *196*, 225–246. https://doi.org/10.1016/j.ces.2018.10.054.

(119) Gennes, P.-G. de; Brochard-Wyart, F.; Quéré, D. *Capillarity and Wetting Phenomena: Drops, Bubbles, Pearls, Waves*; Springer: New York, NY, 2010.

(120) Zisman, W. A. Relation of the Equilibrium Contact Angle to Liquid and Solid Constitution. In *Contact Angle, Wettability, and Adhesion*; Advances in Chemistry; AMERICAN CHEMICAL SOCIETY, 1964; Vol. 43, pp 1–51. https://doi.org/10.1021/ba-1964-0043.ch001.

(121) Weissenborn, P. K.; Pugh, R. J. Surface Tension of Aqueous Solutions of Electrolytes: Relationship with Ion Hydration, Oxygen Solubility, and Bubble Coalescence. *J. Colloid Interface Sci.* **1996**, *184* (2), 550–563. https://doi.org/10.1006/jcis.1996.0651.

(122) Álvarez, E.; Vázquez, G.; Sánchez-Vilas, M.; Sanjurjo, B.; Navaza, J. M. Surface Tension of Organic Acids + Water Binary Mixtures from 20 °C to 50 °C. *J. Chem. Eng. Data* **1997**, *42* (5), 957–960. https://doi.org/10.1021/je970025m.

(123) Li, Z.-B.; Li, Y.-G.; Lu, J.-F. Surface Tension Model for Concentrated Electrolyte Aqueous Solutions by the Pitzer Equation. *Ind. Eng. Chem. Res.* **1999**, *38* (3), 1133–1139. https://doi.org/10.1021/ie980465m.

(124) Ohshima, H.; Matsubara, H. Surface Tension of Electrolyte Solutions. *Colloid Polym. Sci.* **2004**, *282* (9), 1044–1048. https://doi.org/10.1007/s00396-003-1024-9.

(125) Young, T. III. An Essay on the Cohesion of Fluids. *Philos. Trans. R. Soc. Lond.* **1805**, *95*, 65–87. https://doi.org/10.1098/rstl.1805.0005.

(126) Wenzel, R. N. RESISTANCE OF SOLID SURFACES TO WETTING BY WATER. *Ind. Eng. Chem.* **1936**, *28* (8), 988–994. https://doi.org/10.1021/ie50320a024.

(127) Cassie, A. B. D.; Baxter, S. Wettability of Porous Surfaces. *Trans. Faraday Soc.* **1944**, *40*, 546. https://doi.org/10.1039/tf9444000546.

(128) *ISO 4920:2012, Textile Fabrics — Determination of Resistance to Surface Wetting (Spray Test)*; International Organization for Standardization: Geneva, Switzerland, 2012.

(129) *ISO 9073-17:2008, Textiles — Test Methods for Nonwovens — Part 17: Determination of Water Penetration (Spray Impact)*; International Organization for Standardization: Geneva, Switzerland, 2008.

(130) Fishman, J. Z.; Leung, H.; Bazylak, A. Droplet Pinning by PEM Fuel Cell GDL Surfaces. *Int. J. Hydrog. Energy* **2010**, *35* (17), 9144–9150. https://doi.org/10.1016/j.ijhydene.2010.06.027.

(131) Parry, V.; Berthomé, G.; Joud, J.-C. Wetting Properties of Gas Diffusion Layers: Application of the Cassie–Baxter and Wenzel Equations. *Appl. Surf. Sci.* **2012**, *258* (15), 5619–5627. https://doi.org/10.1016/j.apsusc.2012.02.038.

(132) Shi, R.; Guo, J.; Zhang, X.; Waterhouse, G. I. N.; Han, Z.; Zhao, Y.; Shang, L.; Zhou, C.; Jiang, L.; Zhang, T. Efficient Wettability-Controlled Electroreduction of CO2 to CO at Au/C Interfaces. *Nat. Commun.* **2020**, *11* (1), 3028. https://doi.org/10.1038/s41467-020-16847-9.

(133) Xia, C.; Zhu, P.; Jiang, Q.; Pan, Y.; Liang, W.; Stavitski, E.; Alshareef, H. N.; Wang, H. Continuous Production of Pure Liquid Fuel Solutions via Electrocatalytic CO 2 Reduction Using Solid-Electrolyte Devices. *Nat. Energy* **2019**, *4* (9), 776–785. https://doi.org/10.1038/s41560-019-0451-x.

(134) SK. *Effect of Drop Volume on Static Contact Angles*; Technical Note TN310e; KRÜSS GmbH: Hamburg, Germany, 2004; p 2.

(135) Orella, M. J. *DropPy*; 2020.

(136) Lee, S.; Park, J.-S.; Lee, T. R. The Wettability of Fluoropolymer Surfaces: Influence of Surface Dipoles. *Langmuir* **2008**, *24* (9), 4817–4826. https://doi.org/10.1021/la700902h.

(137) Delacourt, C.; Ridgway, P. L.; Kerr, J. B.; Newman, J. Design of an Electrochemical Cell Making Syngas (CO+H[Sub 2]) from CO[Sub 2] and H[Sub 2]O Reduction at Room Temperature. *J. Electrochem. Soc.* **2008**, *155* (1), B42. https://doi.org/10.1149/1.2801871.

(138) Naughton, M. S.; Brushett, F. R.; Kenis, P. J. A. Carbonate Resilience of Flowing Electrolyte-Based Alkaline Fuel Cells. *J. Power Sources* **2011**, *196* (4), 1762–1768. https://doi.org/10.1016/j.jpowsour.2010.09.114.

(139) Brushett, F. R.; Naughton, M. S.; Ng, J. W. D.; Yin, L.; Kenis, P. J. A. Analysis of Pt/C Electrode Performance in a Flowing-Electrolyte Alkaline Fuel Cell. *Int. J. Hydrog. Energy* **2012**, *37* (3), 2559–2570. https://doi.org/10.1016/j.ijhydene.2011.10.078.

(140) Naughton, M. S.; Gu, G. H.; Moradia, A. A.; Kenis, P. J. A. Tailoring Electrode Hydrophobicity to Improve Anode Performance in Alkaline Media. *J. Power Sources* **2013**, *242*, 581–588. https://doi.org/10.1016/j.jpowsour.2013.05.054.

(141) Verma, S.; Lu, X.; Ma, S.; Masel, R. I.; Kenis, P. J. A. The Effect of Electrolyte Composition on the Electroreduction of CO2 to CO on Ag Based Gas Diffusion Electrodes. *Phys. Chem. Chem. Phys.* **2016**, *18* (10), 7075–7084. https://doi.org/10.1039/C5CP05665A.

(142) Kim, B.; Hillman, F.; Ariyoshi, M.; Fujikawa, S.; Kenis, P. J. A. Effects of Composition of the Micro Porous Layer and the Substrate on Performance in the Electrochemical Reduction of CO2 to CO. *J. Power Sources* **2016**, *312*, 192–198. https://doi.org/10.1016/j.jpowsour.2016.02.043.

(143) Liu, K.; Smith, W. A.; Burdyny, T. Introductory Guide to Assembling and Operating Gas Diffusion Electrodes for Electrochemical CO2 Reduction. *ACS Energy Lett.* **2019**, 639–643. https://doi.org/10.1021/acsenergylett.9b00137.

(144) Salvatore, D.; Berlinguette, C. P. Voltage Matters When Reducing CO2 in an Electrochemical Flow Cell. *ACS Energy Lett.* **2019**, 215–220. https://doi.org/10.1021/acsenergylett.9b02356.

(145) Xu, Y.; Edwards, J. P.; Zhong, J.; O'Brien, C. P.; Gabardo, C. M.; McCallum, C.; Li, J.; Dinh, C.-T.; Sargent, E. H.; Sinton, D. Oxygen-Tolerant Electroproduction of C2 Products from Simulated Flue Gas. *Energy Environ. Sci.* **2019**. https://doi.org/10.1039/C9EE03077H.

(146) Edwards, J. P.; Xu, Y.; Gabardo, C. M.; Dinh, C.-T.; Li, J.; Qi, Z.; Ozden, A.; Sargent, E. H.; Sinton, D. Efficient Electrocatalytic Conversion of Carbon Dioxide in a Low-Resistance Pressurized Alkaline Electrolyzer. *Appl. Energy* **2020**, *261*, 114305. https://doi.org/10.1016/j.apenergy.2019.114305.

(147) Kutana, A.; Giapis, K. P. Atomistic Simulations of Electrowetting in Carbon Nanotubes. *Nano Lett.* **2006**, *6* (4), 656–661. https://doi.org/10.1021/nl052393b.

(148) J. Lomax, D.; Kant, P.; T. Williams, A.; V. Patten, H.; Zou, Y.; Juel, A.; W. Dryfe, R. A. Ultra-Low Voltage Electrowetting Using Graphite Surfaces. *Soft Matter* **2016**, *12* (42), 8798–8804. https://doi.org/10.1039/C6SM01565D.

(149) Purcell, W. R. Interpretation of Capillary Pressure Data. *J. Pet. Technol.* **1950**, *2* (08), 11–12. https://doi.org/10.2118/950369-G.

(150) Ge, N.; Chevalier, S.; Lee, J.; Yip, R.; Banerjee, R.; George, M. G.; Liu, H.; Lee, C.; Fazeli, M.; Antonacci, P.; Kotaka, T.; Tabuchi, Y.; Bazylak, A. Non-Isothermal Two-Phase Transport in a Polymer Electrolyte Membrane Fuel Cell with Crack-Free Microporous Layers. *Int. J. Heat Mass Transf.* **2017**, *107*, 418–431. https://doi.org/10.1016/j.ijheatmasstransfer.2016.11.045.

(151) Mason, G.; Morrow, N. R. Effect of Contact Angle on Capillary Displacement Curvatures in Pore Throats Formed by Spheres. *J. Colloid Interface Sci.* **1994**, *168* (1), 130–141. https://doi.org/10.1006/jcis.1994.1402.

(152) Tranter, T. G.; Boillat, P.; Mularczyk, A.; Manzi-Orezzoli, V.; Shearing, P. R.; Brett, D.; Eller, J.; Gostick, J.; Forner-Cuenca, A. Pore Network Modelling of Capillary Transport and Relative Diffusivity in Gas Diffusion Layers with Patterned Wettability. *J. Electrochem. Soc.* **2020**. https://doi.org/10.1149/1945-7111/ab9d61.

(153) Gostick, J. T.; Fowler, M. W.; Pritzker, M. D.; Ioannidis, M. A.; Behra, L. M. In-Plane and through-Plane Gas Permeability of Carbon Fiber Electrode Backing Layers. *J. Power Sources* **2006**, *162* (1), 228–238. https://doi.org/10.1016/j.jpowsour.2006.06.096.

(154) Virtek IP-rated PTFE vents | sintered PTFE material | sealed enclosures https://www.porex.com/markets/electronics/ip-rated-protection-vents/ (accessed Feb 29, 2020).

(155) Gurau, V.; Bluemle, M. J.; De Castro, E. S.; Tsou, Y.-M.; Mann, J. A.; Zawodzinski, T. A. Characterization of Transport Properties in Gas Diffusion Layers for Proton Exchange Membrane Fuel Cells: 1. Wettability (Internal Contact Angle to Water and Surface Energy of GDL Fibers). *J. Power Sources* **2006**, *160* (2), 1156–1162. https://doi.org/10.1016/j.jpowsour.2006.03.016.

(156) Yao, L. Water and Oil Repellent Porous Particles and Methods for Making the Same. US20040028890A1, February 12, 2004.

(157) Deng, B.; Cai, R.; Yu, Y.; Jiang, H.; Wang, C.; Li, J.; Li, L.; Yu, M.; Li, J.; Xie, L.; Huang, Q.; Fan, C. Laundering Durability of Superhydrophobic Cotton Fabric. *Adv. Mater.* **2010**, *22* (48), 5473–5477. https://doi.org/10.1002/adma.201002614.

(158) Adiletta, J. G. Hydrophobic-Oleophobic Fluoropolymer Compositions. US5981614A, November 9, 1999.

(159) Thottupurathu, G. Process to Increase the Oleophobicity of PTFE, and Resulting Oleophobic Articles. US8088445B2, January 3, 2012.

(160) Liu, H.; George, M. G.; Messerschmidt, M.; Zeis, R.; Kramer, D.; Scholta, J.; Bazylak, A. Accelerated Degradation of Polymer Electrolyte Membrane Fuel Cell Gas Diffusion Layers. *J. Electrochem. Soc.* **2017**, *164* (7), F695. https://doi.org/10.1149/2.0071707jes.

(161) Ellinas, K.; Tserepi, A.; Gogolides, E. Durable Superhydrophobic and Superamphiphobic Polymeric Surfaces and Their Applications: A Review. *Adv. Colloid Interface Sci.* **2017**, *250*, 132–157. https://doi.org/10.1016/j.cis.2017.09.003.

(162) Orella, M.; Leonard, M.; Román-Leshkov, Y.; Brushett, F. Automated Analysis of Contact Angle Goniometry Data Using DropPy. *ChemRxiv* **2020**. https://doi.org/10.26434/chemrxiv.11916336.v1.

(163) Law, K.-Y. Definitions for Hydrophilicity, Hydrophobicity, and Superhydrophobicity: Getting the Basics Right. *J. Phys. Chem. Lett.* **2014**, *5* (4), 686–688. https://doi.org/10.1021/jz402762h.

(164) Weng, L.-C.; Bell, A. T.; Weber, A. Z. Modeling Gas-Diffusion Electrodes for CO2 Reduction. *Phys. Chem. Chem. Phys.* **2018**, *20* (25), 16973–16984. https://doi.org/10.1039/C8CP01319E.

(165) Weber, A. Z.; Darling, R. M.; Newman, J. Modeling Two-Phase Behavior in PEFCs. *J. Electrochem. Soc.* **2004**, *151* (10), A1715. https://doi.org/10.1149/1.1792891.

(166) Weber, A. Z. Improved Modeling and Understanding of Diffusion-Media Wettability on Polymer-Electrolyte-Fuel-Cell Performance. *J. Power Sources* **2010**, *195* (16), 5292–5304. https://doi.org/10.1016/j.jpowsour.2010.03.011.

(167) Zenyuk, I. V.; Das, P. K.; Weber, A. Z. Understanding Impacts of Catalyst-Layer Thickness on Fuel-Cell Performance via Mathematical Modeling. *J. Electrochem. Soc.* **2016**, *163* (7), F691. https://doi.org/10.1149/2.1161607jes.

(168) Zhou, J.; Putz, A.; Secanell, M. A Mixed Wettability Pore Size Distribution Based Mathematical Model for Analyzing Two-Phase Flow in Porous Electrodes: I. Mathematical Model. *J. Electrochem. Soc.* **2017**, *164* (6), F530–F539. https://doi.org/10.1149/2.0381706jes.

(169) Zhou, J.; Stanier, D.; Putz, A.; Secanell, M. A Mixed Wettability Pore Size Distribution Based Mathematical Model for Analyzing Two-Phase Flow in Porous Electrodes: II. Model Validation and Analysis of Micro-Structural Parameters. *J. Electrochem. Soc.* **2017**, *164* (6), F540. https://doi.org/10.1149/2.0391706jes.

(170) Weng, L.-C.; Bell, A. T.; Weber, A. Z. A Systematic Analysis of Cu-Based Membrane-Electrode Assemblies for CO2 Reduction through Multiphysics Simulation. *Energy Environ. Sci.* **2020**. https://doi.org/10.1039/D0EE01604G.

(171) Mugele, F.; Baret, J.-C. Electrowetting: From Basics to Applications. *J. Phys. Condens. Matter* **2005**, *17* (28), R705–R774. https://doi.org/10.1088/0953-8984/17/28/R01.

(172) Schwaminger, S. P.; Begovic, B.; Schick, L.; Jumani, N. A.; Brammen, M. W.; Fraga-García, P.; Berensmeier, S. Potential-Controlled Tensiometry: A Tool for Understanding Wetting and Surface Properties of Conductive Powders by Electroimbibition. *Anal. Chem.* **2018**, *90* (24), 14131–14136. https://doi.org/10.1021/acs.analchem.8b03475.

(173) Leonard, M. E.; Orella, M. J.; Aiello, N.; Román-Leshkov, Y.; Forner-Cuenca, A.; Brushett, F. R. Editors' Choice—Flooded by Success: On the Role of Electrode Wettability in CO2 Electrolyzers That Generate Liquid Products. *J. Electrochem. Soc.* **2020**, *167* (12), 124521. https://doi.org/10.1149/1945-7111/abaa1a.

(174) García-Salaberri, P. A.; Gostick, J. T.; Hwang, G.; Weber, A. Z.; Vera, M. Effective Diffusivity in Partially-Saturated Carbon-Fiber Gas Diffusion Layers: Effect of Local Saturation and Application to Macroscopic Continuum Models. *J. Power Sources* **2015**, *296*, 440–453. https://doi.org/10.1016/j.jpowsour.2015.07.034.

(175) García-Salaberri, P. A.; Hwang, G.; Vera, M.; Weber, A. Z.; Gostick, J. T. Effective Diffusivity in Partially-Saturated Carbon-Fiber Gas Diffusion Layers: Effect of through-Plane Saturation Distribution. *Int. J. Heat Mass Transf.* **2015**, *86*, 319–333. https://doi.org/10.1016/j.ijheatmasstransfer.2015.02.073.

(176) Gostick, J.; Aghighi, M.; Hinebaugh, J.; Tranter, T.; Hoeh, M. A.; Day, H.; Spellacy, B.; Sharqawy, M. H.; Bazylak, A.; Burns, A.; Lehnert, W.; Putz, A. OpenPNM: A Pore Network Modeling Package. *Comput. Sci. Eng.* **2016**, *18* (4), 60–74. https://doi.org/10.1109/MCSE.2016.49.

(177) Dashtian, H.; Shokri, N.; Sahimi, M. Pore-Network Model of Evaporation-Induced Salt Precipitation in Porous Media: The Effect of Correlations and Heterogeneity. *Adv. Water Resour.* **2018**, *112*, 59–71. https://doi.org/10.1016/j.advwatres.2017.12.004.

(178) Pore Volume Measurement Services | Particle Testing Authority.

(179) Gostick, J. T.; Khan, Z. A.; Tranter, T. G.; Kok, M. D. r; Agnaou, M.; Sadeghi, M.; Jervis, R. PoreSpy: A Python Toolkit for Quantitative Analysis of Porous Media Images. *J. Open Source Softw.* **2019**, *4* (37), 1296. https://doi.org/10.21105/joss.01296.

(180) Weber, A. Z.; Borup, R. L.; Darling, R. M.; Das, P. K.; Dursch, T. J.; Gu, W.; Harvey, D.; Kusoglu, A.; Litster, S.; Mench, M. M.; Mukundan, R.; Owejan, J. P.; Pharoah, J. G.; Secanell, M.; Zenyuk, I. V. A Critical Review of Modeling Transport Phenomena in Polymer-Electrolyte Fuel Cells. *J. Electrochem. Soc.* **2014**, *161* (12), F1254. https://doi.org/10.1149/2.0751412jes.

(181) Yang, K.; Kas, R.; Smith, W. A.; Burdyny, T. Role of the Carbon-Based Gas Diffusion Layer on Flooding in a Gas Diffusion Electrode Cell for Electrochemical CO2 Reduction. *ACS Energy Lett.* **2020**, 33–40. https://doi.org/10.1021/acsenergylett.0c02184.

(182) Hodkiewicz, J. *Characterizing Carbon Materials with Raman Spectroscopy*; Application Note: 51901; Thermo Fisher Scientific: Madison, WI; p 5.

(183) Shi, H. Activated Carbons and Double Layer Capacitance. *Electrochimica Acta* **1996**, *41* (10), 1633–1639. https://doi.org/10.1016/0013-4686(95)00416-5.

Permissions

Chapter II contains figures adapted from two previously published works. The first was originally published by Springer Nature on behalf of Journal of Applied Electrochemistry: S. Sen, S. M. Brown, M. Leonard, F. R. Brushett, Electroreduction of carbon dioxide to formate at high current densities using tin and tin oxide gas diffusion electrodes, *Journal of Applied Electrochemistry* **2019** *49* (9), 917–928. The second was originally published by Cambridge University Press on behalf of MRS Advances: S. Sen, M. Leonard, R. Radhakrishnan, S. Snyder, B. Skinn, D. Wang, T. Hall, E. J. Taylor, F. R. Brushett, Pulse Plating of Copper onto Gas Diffusion Layers for the Electroreduction of Carbon Dioxide, *MRS Advances* **2017** *3* (23), 1277–1284. **Chapter III** was reproduced from work previously published by Wiley-VCH on behalf of ChemSusChem: M. E. Leonard, L. E. Clarke, A. Forner-Cuenca, S. M. Brown, F. R. Brushett, Investigating Electrode Flooding in a Flowing Electrolyte, Gas-Fed Carbon Dioxide Electrolyzer, *ChemSusChem* **2019** *13* (2), 400–411. **Chapter IV** was reproduced from an open-access article published by IOP Publishing on behalf of Journal of the Electrochemical Society: M. E. Leonard, M. J. Orella, N. Aiello, Y. Román-Leshkov, A. Forner-Cuenca, F. R. Brushett, Editors' Choice—Flooded by Success: On the Role of Electrode Wettability in CO_2 Electrolyzers that Generate Liquid Products, *Journal of the Electrochemical Society* **2020** *167* (12), 124521. **Chapter V** contains results that, in some form, may be submitted for publication in a peer-reviewed journal in the future.